

Spring 5-2017

# Influence of Multiwall Carbon Nanotubes on Corrosion Performance and Water Hydrogen Bonding of Epoxy-Amine Thin Films

Greg William Curtzwiler  
*University of Southern Mississippi*

Follow this and additional works at: <https://aquila.usm.edu/dissertations>

 Part of the [Materials Chemistry Commons](#), and the [Polymer Chemistry Commons](#)

---

## Recommended Citation

Curtzwiler, Greg William, "Influence of Multiwall Carbon Nanotubes on Corrosion Performance and Water Hydrogen Bonding of Epoxy-Amine Thin Films" (2017). *Dissertations*. 1383.  
<https://aquila.usm.edu/dissertations/1383>

This Dissertation is brought to you for free and open access by The Aquila Digital Community. It has been accepted for inclusion in Dissertations by an authorized administrator of The Aquila Digital Community. For more information, please contact [aquilastaff@usm.edu](mailto:aquilastaff@usm.edu).

INFLUENCE OF MULTIWALL CARBON NANOTUBES ON CORROSION  
PERFORMANCE AND WATER HYDROGEN BONDING OF  
EPOXY-AMINE THIN FILMS

by

Greg William Curtzwiler

A Dissertation  
Submitted to the Graduate School,  
the College of Science and Technology,  
and the School of Polymers and High Performance Materials  
at The University of Southern Mississippi  
in Partial Fulfillment of the Requirements  
for the Degree of Doctor of Philosophy

May 2017

INFLUENCE OF MULTIWALL CARBON NANOTUBES ON CORROSION  
PERFORMANCE AND WATER HYDROGEN BONDING OF  
EPOXY-AMINE THIN FILMS

by Greg William Curtzwiler

May 2017

Approved by:

---

Dr. James Rawlins, Committee Chair  
Associate Professor, Polymers and High Performance Materials

---

Dr. Jeffery Wiggins, Committee Member  
Associate Professor, Polymers and High Performance Materials

---

Dr. Derek Patton, Committee Member  
Associate Professor, Polymers and High Performance Materials

---

Dr. Sarah Morgan, Committee Member  
Professor, Polymers and High Performance Materials

---

Dr. Gopinath Subramanian, Committee Member  
Assistant Professor, Polymers and High Performance Materials

---

Dr. Jeffery Wiggins  
Director, School of Polymers and High Performance Materials

---

Dr. Karen S. Coats  
Dean of the Graduate School

COPYRIGHT BY

Greg William Curtzwiler

2017

*Published by the Graduate School*



THE UNIVERSITY OF  
**SOUTHERN**  
**MISSISSIPPI.**

## ABSTRACT

# INFLUENCE OF MULTIWALL CARBON NANOTUBES ON CORROSION PERFORMANCE AND WATER HYDROGEN BONDING OF EPOXY-AMINE THIN FILMS

by Greg William Curtzwiler

May 2017

This dissertation research sought to provide a fundamental basis of understanding to commence the systematic investigation of developing economically viable fully formulated epoxy-amine coating systems containing multiwall carbon nanotubes (MWCNT). Namely, a facile and rapid method for multiwall carbon nanotube surface modification and molecular structure interpretation was developed to assist in designing MWCNT-polymer interactions and achieving high levels of dispersion. Additionally, a rapid and quantitative method was developed to investigate the dispersibility potential of MWCNTs possessing a given surface modification in combination with a dispersion protocol which can further be utilized as a quality control metric in commercial applications. It was observed and quantified that multiwall carbon nanotubes altered the average water hydrogen bonding distribution within an epoxy-amine polymer thin film. These measured differences in water hydrogen bonding interactions correlated consistently and well with reduced corrosion rates of epoxy-amine coated steel substrates with intentionally created defects. To create further understanding, additional nano-carbon allotropes (carbon black, MWCNT, graphene) were utilized in an attempt to establish a relationship between water hydrogen bonding interactions within an epoxy-amine matrix coated over a steel substrate and the corrosion performance; specifically,

when the relative concentration of bound water increased and the relative concentration of free water decreased, the overall rate of corrosion decreased in each of the systems studied. A simple and experimentally-derived equation proved capable of predicting ~91% of the variation in the measured corrosion rates from the established water hydrogen bonding interactions measured at ambient from pre-corrosion testing conditions,  $t=0$ , using a stepwise multivariable regression analysis approach and incorporating each of the varying nano-carbon allotrope systems.

## ACKNOWLEDGMENTS

I would like to thank my adviser, Dr. James Rawlins, for his continued support and encouraging me to follow my passion to advance the science of carbon nanotubes. The process of conducting carbon nanotube research under his guidance, support, and advice has resulted in creating a tremendous wealth of skills invaluable to the pursuit of a highly productive career as a fundamental research scientist. I would also like to thank my advisory committee Dr. Jeffery Wiggins, Dr. Sarah Morgan, Dr. Derek Patton, and Dr. Gopinath Subramanian for their time and consideration of my work. Also, I would like to thank Dr. Eric Williams, whom co-authored several manuscripts, for his endless availability and long discussions regarding my work. I would also like to thank Sharathkumar Mendon for his expert editing and quick turnaround of documents that needed to be submitted with little remaining time.

Finally, I must acknowledge the financial support of the United States Air Force Academy (FA7000-12-2-0016) through funding by the Department of Defense and collaborative efforts for Corrosion Prevention and Understanding via the Technical Corrosion Collaboration working group comprised of The University of Virginia, The University of Hawaii, The Ohio State University, the Air Force Academy, The University of Akron, The University of Southern Mississippi, the Air Force Institute of Technology, the Naval Postgraduate School, and the US Naval Academy.

## DEDICATION

This dissertation is dedicated to all Curtzwilers, past, present, and future. I hope this work brings honor and respect to our name. I must thank my wife, Brittany, as, without her love and support, I would have not have had the strength to finish; my mom, Lisa, who instilled into me the concept of “nothing less than your best”; my dad, Bill, who taught me to endure, sacrifice, and work hard to provide for your family.

I would also like to acknowledge Jim Kurinsky who gave a young biochemist with no experience an opportunity to perform research in carbon nanotube nanocomposites. This experience commenced a cascade of events that lead my research interests away from biochemistry towards nanotechnology and polymers which subsequently landed me here at the University of Southern Mississippi to pursue a Doctorate of Philosophy in Polymer Science and Engineering.

In a career of investigation and innovation, there is nothing more certain than failure. Throughout my childhood, a handwritten note was attached to the refrigerator, always in view, to remind me that failure is nothing more than a learning experience. When Thomas Edison was asked to comment about the 10,000 times he failed to invent the light bulb, he replied,

I have not failed 10,000 times. I have not failed once. I have succeeded in proving that those 10,000 ways will not work. When I have eliminated the ways that will not work, I will find the way that will work.

-Thomas Edison<sup>1</sup>

---

<sup>1</sup> Furr, N. How Failure Taught Edison to Repeatedly Innovate 2011. <http://www.forbes.com/sites/nathanfurr/2011/06/09/how-failure-taught-edison-to-repeatedly-innovate/#1d0f530b38f5> (accessed 2016 December 11).

Corbin, my son, as you have just entered into this world, please remember that failure is guaranteed, it is how you continue on that will define who you are.

## TABLE OF CONTENTS

ABSTRACT .....	ii
ACKNOWLEDGMENTS .....	iv
DEDICATION .....	v
LIST OF TABLES .....	xv
LIST OF ILLUSTRATIONS .....	xvi
LIST OF SCHEMES.....	xxv
LIST OF ABBREVIATIONS.....	xxvi
CHAPTER I - INTRODUCTION .....	1
1.1 Motivation of Research.....	1
1.1.1 Corrosion of Steel Substrates.....	1
1.1.2 Water Hydrogen Bonding Interactions in Polymers .....	4
1.1.3 Carbon Nanotubes as Corrosion Control Materials .....	7
1.2 Introduction to Carbon Nanotubes.....	8
1.3 Dissertation Objectives and Outline .....	10
1.4 References.....	15
CHAPTER II – DEVELOPMENT OF A MORE STANDARDIZED DECONVOLUTION PROTOCOL FOR RAMAN SPECTRA OF MULTIWALL CARBON NANOTUBES.....	19
2.1 Abstract.....	19



3.1 Abstract.....	59
3.2 Introduction.....	60
3.3 Experimental.....	64
3.3.1 Materials .....	64
3.3.2 Surface Modification of MWCNTs .....	65
3.3.3 Characterization of Functionalized MWCNTs .....	66
3.3.4 Waterborne Epoxy-Amine Thin Film Material Combination, Free Film Fabrication, and Coating Application.....	67
3.3.5 MWCNT Dispersion Analysis.....	68
3.3.6 Statistical Analysis.....	69
3.4 Results.....	70
3.4.2 MWCNT Dispersion in Epoxy-Amine Coatings.....	72
3.4.3 Free Film Absorbance and Blackness/Opacity of Steel Bound Coatings .....	84
3.5 Discussion.....	89
3.6 Conclusions.....	92
3.7 References.....	94
 CHAPTER IV – COMPARISON OF THE ADDED VALUE FOR CORROSION PERFORMANCE OF CHEMICALLY MODIFIED MULTIWALL CARBON NANOTUBE EPOXY-AMINE COATING SYSTEMS ON STEEL SUBSTRATES ....	
4.1 Abstract.....	98

4.2 Introduction.....	99
4.2.2 Ultrasonication.....	100
4.3 Experimental.....	102
4.3.1 Materials .....	102
4.3.2 Chemical Modification of Multiwall Carbon Nanotubes .....	103
4.3.2.1 Radical Addition to MWCNT.....	103
4.3.2.2 Subsequent Chemical Modification of ABCVA and AMP MWCNTs ..	103
4.3.3 Characterization of MWCNT Functionalization .....	105
4.3.4 Fabrication of Model Epoxy-Amine Coating and Free Films Containing Functionalized MWCNTs.....	106
4.3.5 Coating Characterization .....	108
4.3.6 Corrosion Analysis.....	110
4.3.7 Water Hydrogen Bonding States .....	111
4.3.8 Post-Exposure Analysis .....	112
4.3.9 Statistical Analysis.....	113
4.4 Results.....	113
4.4.1 MWCNT Characterization.....	113
4.4.2 Coating Microstructure and Carbon Nanotube Dispersion.....	114
4.4.3 Polymer-MWCNT Interactions via Vibrational Spectroscopy.....	116
4.4.4 Coating Performance Characteristics.....	120

4.4.5 Corrosion Performance of MWCNT Coatings on Steel Substrates.....	122
4.4.6 Water Hydrogen Bonding Interactions .....	126
4.5 Discussion.....	128
4.6 Conclusions.....	129
4.7 References.....	131
CHAPTER V – MEASUREABLE AND INFLUENTIAL PARAMETERS THAT INFLUENCE CORROSION PERFORMANCE DIFFERENCES BETWEEN MULTIWALL CARBON NANOTUBE COATING MATERIAL COMBINATIONS AND MODEL PARENT MATERIAL COMBINATIONS DERIVED FROM EPOXY- AMINE MATRIX MATERIALS .....	135
5.1 Abstract.....	135
5.2 Introduction.....	136
5.3 Experimental.....	139
5.3.1 Materials and Methods.....	139
5.3.2 Characterization of MWCNT Functionalization .....	139
5.3.3 Model Epoxy-Amine Steel Bound and Free Films Containing MWCNTs ...	140
5.3.4 Coating Characterization .....	140
5.3.5 Corrosion Analysis.....	140
5.3.6 Water Hydrogen Bonding Interactions .....	141
5.3.7 Post-Exposure Analysis .....	142

5.3.8 Statistical Analysis.....	142
5.4 Results.....	143
5.4.1 MWCNT Characterization.....	143
5.4.2 Carbon Nanotube Dispersion of Free Films and Their Properties.....	144
5.4.3 Influence of MWCNTs on Water Type Distributions at Ambient Conditions .....	150
5.4.4 Influence of MWCNTs on the Water Hydrogen Bonding Interactions Distribution after 168 Hours of Salt Fog Exposure .....	154
5.4.5 Influence of MWCNTs on the Corrosion Performance of Epoxy-Amine Thin Films on Steel Substrates .....	157
5.4.6 Post-Exposure Analysis of Coated Panels Subjected to Accelerated Corrosion Conditions .....	161
5.4.7 Influence of Water Hydrogen Bonding on Corrosion Performance of MWCNT/Epoxy-Amine Thin Films.....	162
5.5 Discussion.....	166
5.6 Conclusions.....	170
5.7 References.....	171
 CHAPTER VI – PREDICTION OF EPOXY-AMINE CORROSION PERFORMANCE ON STEEL IN A SALT FOG ENVIRONMENT USING PRE-EXPOSURE MEASUREMENTS AND STEPWISE REGRESSION ANALYSIS.....	
6.1 Abstract.....	175

6.2 Introduction.....	176
6.3 Experimental.....	179
6.3.1 Materials and Methods.....	179
6.3.2 Characterization of MWCNT Functionalization .....	179
6.3.3 Fabrication of Model Epoxy-Amine Steel Bound Polymer Thin Film and Free Films Containing Nano-Carbon Allotropes .....	179
6.3.4 Coating Characterization .....	180
6.3.5 Corrosion Analysis.....	180
6.3.6 Water Hydrogen Bonding Interactions .....	181
6.3.7 Post-Exposure Analysis .....	182
6.3.8 Statistical Analysis.....	182
6.4 Results and Discussion .....	183
6.4.2 Potential Predictor Input Parameters for Stepwise Multivariable Regression Analysis.....	185
6.4.2.1 Glass Transition Temperature.....	185
6.4.2.2 Water Vapor Desorption, Diffusivity, and Equilibrium Saturation .....	186
6.4.2.3 Water Hydrogen Bonding Interactions at $t=0$ , <i>ambient</i> .....	188
6.4.3 Corrosion Rate .....	192
6.4.4 Stepwise Multivariable Regression Analysis.....	196
6.4.5 Discussion .....	198

6.5 Conclusions.....	202
6.6 References.....	203
CHAPTER VII – DISSERTATION SUMMARY AND FUTURE OUTLOOK.....	206
APPENDIX A – Supplemental Figures for Chapter II.....	211
A.1 Raman Spectral Properties.....	211
A.1.1 Relationship between D/G and D'/G Raman Spectral Calculations.....	211
A.1.2 D'/G Ratios.....	213
A.2 Correlation of thermogravimetric analysis with Raman spectral properties.....	215
A.3 Correlation between X-ray photoelectron spectroscopy and Raman spectral properties.....	220
REFERENCES.....	229

## LIST OF TABLES

Table 2.1 List of band assignments for deconvolution of MWCNT Raman spectra.....	30
Table 2.2 List of peak assignments for deconvolution of MWCNT high-resolution C 1s X-ray photoelectron spectra.....	31

## LIST OF ILLUSTRATIONS

Figure 1.1 The corrosion triangle exhibiting the most common requirements for corrosion under aerobic, wet conditions. ....	2
Figure 1.2 Representative scheme of the cathodic delamination mechanism of coated steel. ....	4
Figure 1.3 Orientation of water molecules for direct interaction with solvated anions (left) and cations (right). ....	6
Figure 1.4 Estimated location of carbon nanotube technology on the Gartner “Hype Cycle of Innovation” curve. ....	9
Figure 2.1 General molecular structure of carbon nanotubes. ....	22
Figure 2.2 Example defects in the molecular structure of carbon nanotubes. ....	23
Figure 2.3 Example physical bond vibrations representative of the transverse optical (TO) and longitudinal optical (LO) phonons. ....	26
Figure 2.4 Flow chart describing MWCNTs radical and air oxidation treatments. ....	29
Figure 2.5 Representative deconvolution of first order MWCNT Raman spectra. ....	33
Figure 2.6 Average values of subtraction curve as a function of treatment and number of deconvoluted peaks. ....	34
Figure 2.7 Standard deviation of subtraction curve as a function of treatment and number of deconvoluted peaks. ....	35
Figure 2.8 Representative subtraction curves of HAMWCNT unmodified sample type as a function of the number of deconvoluted peaks. ....	36
Figure 2.9 Pearson product moment correlation coefficients for area and intensity based calculations of the D/G ratio as a function of the number of deconvoluted peaks. ....	37

Figure 2.10 Pearson product moment correlation coefficients for area and intensity based calculations of the D'/G ratio as a function of employed deconvoluted peaks. ....	38
Figure 2.11 Peak intensity and area based D'/G ratio calculations as a function of the number of deconvoluted peaks for first order Raman spectra. ....	40
Figure 2.12 Calculated defect density as a function of the number of deconvoluted peaks. ....	42
Figure 2.13 Area based D'/G values for LAMWCNT as a function of the number of deconvoluted peaks. ....	43
Figure 2.14 Pearson product moment correlation coefficient between Raman spectral properties and thermal degradation properties. ....	45
Figure 2.15 Representative deconvolution of MWCNT X-ray photoelectron spectra. ....	46
Figure 2.16 Pearson product moment correlation coefficient between Raman spectral properties and XPS. ....	47
Figure 2.17 Pearson product moment correlation coefficient between X-ray photoelectron spectroscopy and thermal degradation properties. ....	48
Figure 3.1 Representative optical images of waterborne epoxy-amine thin films comprised of different MWCNT surface chemistry-concentration combinations. ....	61
Figure 3.2 Katura plot exhibiting the effect of carbon nanotube diameter on the energy of electronic transitions in the electronic density of states. ....	63
Figure 3.3 Average D'/G values calculated employing a four peak deconvolution protocol for unmodified MWCNTs, hydroxyl MWCNTs, and amine MWCNTs. ....	70
Figure 3.4 Average meq hydroxyl/g MWCNT and average meq amine/g MWCNT. ....	71

Figure 3.5 Optical (left) and scanning electron micrographs (right) of MWCNT/waterborne epoxy-amine thin films at a 0.25 wt% MWCNTs loading level. ..	73
Figure 3.6 Optical (left) and scanning electron micrographs (right) of MWCNT/waterborne epoxy-amine thin films at a 0.50 wt% MWCNTs loading level. ..	74
Figure 3.7 Optical (left) and scanning electron micrographs (right) of MWCNT/waterborne epoxy-amine thin films at a 1.0 wt% MWCNTs loading level. ....	75
Figure 3.8 Optical (left) and scanning electron micrographs (right) of MWCNT/waterborne epoxy-amine thin films at a 1.5 wt% MWCNTs loading level. ....	76
Figure 3.9 Calculated dispersion index as a function of MWCNT concentration by surface chemistry. ....	78
Figure 3.10 Absorbance of MWCNT/waterborne epoxy-amine thin films as a function of concentration by MWCNT treatment. ....	80
Figure 3.11 Representative visible light absorption spectra of MWCNT/waterborne epoxy-amine thin films. ....	81
Figure 3.12 Thickness normalized absorbance of MWCNT/waterborne epoxy-amine thin films as a function of concentration by MWCNT treatment. ....	84
Figure 3.13 Blackness ( $M_y$ ) values (a), jetness ( $M_c$ ) values (b) and the undertone ( $d_M$ ) properties (c) of epoxy-amine thin films applied to steel substrates. ....	86
Figure 3.14 Blackness (a) and jetness (b) values of MWCNT waterborne epoxy-amine thin films as a function of the thickness normalized absorbance at 500 nm of the corresponding free film. ....	88
Figure 4.1 Synthetic approaches to functionalize the surface of carbon nanotubes. ....	100

Figure 4.2 Representative panel for the semi-quantitative corrosion area determination and location of ATR-FTIR analyses. ....	111
Figure 4.3 Representative deconvolution of the subtracted ATR-FTIR spectral hydroxyl region into various water interactions. ....	112
Figure 4.4 D'/G ratio of the unmodified and hydroxyl surface modified MWCNTs employing a four peak deconvolution protocol. ....	114
Figure 4.5 Scanning electron micrographs of epoxy-amine coatings containing MWCNTs displaying the degree of dispersion. ....	115
Figure 4.6 Absorbance values at 500 nm of epoxy-amine free films formulated with MWCNTs containing various functional groups. ....	116
Figure 4.7 Representative Raman spectra associated with the out-of-plane bending moments of an asymmetric benzene ring (a) and ATR-FTIR subtraction spectra of the aromatic ether region (b). ....	117
Figure 4.8 Change in Raman peak position of the D, G and G' bands due to incorporation of MWCNTs with different surface chemistries. ....	118
Figure 4.9 Internal stress measurements via the cantilever method. ....	120
Figure 4.10 Difference in the $T_g$ measured by DSC for crosslinked epoxy-amine thin films containing MWCNTs with different chemical functionalities. ....	121
Figure 4.11 Percent corrosion area of epoxy-amine polymer thin films on steel substrates formulated with MWCNTs of various chemical functionalities as a function of salt fog accelerated corrosion exposure time (a) and representative panels after 168 hours of exposure (b). ....	124

Figure 4.12 Scanning electron micrographs of the polymer at the polymer/substrate interface.....	125
Figure 4.13 Scanning electron micrographs of the polymer cross-section after ASTM B117 salt fog exposure.....	126
Figure 4.14 Water hydrogen bonding interactions at the air/polymer interface of epoxy-amine material combination after 168 hours of 5% NaCl fog exposure.....	127
Figure 4.15 Relationship between the corrosion area and water hydrogen bonding interactions at the polymer/air interface after 168 hours of salt fog exposure.....	128
Figure 5.1 Determination of the cathodic corrosion area by quantitative image analysis. ....	141
Figure 5.2 D'/G ratio of the unmodified and hydroxyl surface modified MWCNTs employing a four peak deconvolution protocol. ....	143
Figure 5.3 Scanning electron micrographs of epoxy-amine coatings containing MWCNTs (~20kx magnification). Scale bar for each micrograph is 500 nm. ....	145
Figure 5.4 Blackness (a) and undertone (b) properties for epoxy-amine material combinations containing various nano-carbon allotropes at concentrations of 0.50, 0.75, and 1.0 wt%. ....	146
Figure 5.5 The glass transition temperature of MWCNT/epoxy-amine material combinations with various concentrations of multiwall carbon nanotubes.....	148
Figure 5.6 Measured water vapor sorption properties for epoxy-amine free films containing multiwall carbon nanotubes. ....	150
Figure 5.7 Relative concentration of water vapor hydrogen bonding interactions within MWCNT/epoxy-amine thin films at t=0 hr, ambient. ....	152

Figure 5.8 Relative concentration of water hydrogen bonding interactions within MWCNT/epoxy-amine material combinations after 168 hours of salt fog exposure.....	157
Figure 5.9 Representative scanning electron micrograph and energy dispersive X-ray elemental map of the polymer/substrate interface of the coating after 168 hours of salt fog exposure. ....	158
Figure 5.10 Corrosion rate for epoxy-amine coatings on steel substrates formulated without/with multiwall carbon nanotubes (a) and representative panels after 168 hours of salt fog exposure (b).....	160
Figure 5.11 Representative scanning electron micrographs of the coating at the polymer/substrate interface away from the scribe after 168 hours of salt fog exposure.	162
Figure 5.12 Experimental corrosion rate as a function of the relative water hydrogen bonding concentration of after 168 hours of salt fog exposure including all material combinations and including only the MWCNT material combinations. ....	164
Figure 5.13 Corrosion rate of epoxy-amine coating thin films as a function of the relative water hydrogen bonding concentration of at ambient conditions before exposure. ....	166
Figure 6.1 Determination of the cathodic corrosion area by quantitative image analysis. ....	181
Figure 6.2 Scanning electron micrographs of epoxy-amine coatings containing MWCNTs (~20kx magnification). ....	184
Figure 6.3 Glass transition temperature of epoxy-amine coating thin films containing various nano-carbon allotropes and concentrations. ....	186

Figure 6.4 Ambient water concentration (a), water vapor diffusivity (b), and water vapor saturation at equilibrium (c) for epoxy-amine free films containing various nano carbon allotropes.....	188
Figure 6.5 Relative concentration of water hydrogen bonding interactions within epoxy-amine material combinations at $t=0$ Hr, ambient. ....	191
Figure 6.6 Average corrosion rate for epoxy-amine coatings on steel substrates formulated with various nano-carbon allotropes. ....	193
Figure 6.7 Experimental corrosion rate of epoxy-amine material combinations compared to the relative concentration of water hydrogen bonding interactions.....	195
Figure 6.8 Experimental corrosion rate compared to the predicted corrosion rate from pre-exposure measurements.....	197
Figure A.1 Pearson product moment correlation coefficient as a probe of the relationship between the intensity based D/G and D'/G calculations for HAMWCNT and LAMWCNT types. ....	211
Figure A.2 Pearson product moment correlation coefficient as a probe of the relationship between the area based D/G and D'/G calculations for HAMWCNT and LAMWCNT types. ....	212
Figure A.3 Area and intensity based D'/G ratios as a function of the number of deconvoluted peaks for HAMWCNT. ....	213
Figure A.4 Area and intensity based D'/G ratios as a function of the number of deconvoluted peaks for LAMWCNT.....	214

Figure A.5 Pearson product moment correlation coefficient between spectrum intensity based calculations and thermal degradation properties for HAMWCNT and LAMWCNT types. ....	215
Figure A.6 Pearson product moment correlation coefficient between the intensity/area based calculations from a two peak deconvolution and thermal degradation properties for HAMWCNT and LAMWCNT types.....	216
Figure A.7 Pearson product moment correlation coefficient between the intensity/area based calculations from a three peak deconvolution and thermal degradation properties for HAMWCNT and LAMWCNT types.....	217
Figure A.8 Pearson product moment correlation coefficient between the intensity based calculations from a four peak deconvolution and thermal degradation properties for HAMWCNT and LAMWCNT types.....	218
Figure A.9 Pearson product moment correlation coefficient between the area based calculations from a five peak deconvolution and thermal degradation properties for HAMWCNT and LAMWCNT types.....	219
Figure A.10 Pearson product moment correlation coefficient for the spectrum intensity based calculations and XPS calculations for HAMWCNT and LAMWCNT types. ....	220
Figure A.11 Pearson product moment correlation coefficient for intensity based Raman spectral properties determined with two deconvoluted peaks as a function of X-ray photoelectron spectral properties for HAMWCNT and LAMWCNT.....	221
Figure A.12 Pearson product moment correlation coefficient for area based Raman spectral properties determined with two deconvoluted peaks as a function of X-ray photoelectron spectral properties for HAMWCNT and LAMWCNT.....	222

Figure A.13 Pearson product moment correlation coefficient for intensity based Raman spectral properties determined with three deconvoluted peaks as a function of X-ray photoelectron spectral properties for HAMWCNT and LAMWCNT.....	223
Figure A.14 Pearson product moment correlation coefficient for area based Raman spectral properties determined with three deconvoluted peaks as a function of X-ray photoelectron spectral properties for HAMWCNT and LAMWCNT.....	224
Figure A.15 Pearson product moment correlation coefficient for intensity based Raman spectral properties determined with four deconvoluted peaks as a function of X-ray photoelectron spectral properties for HAMWCNT and LAMWCNT.....	225
Figure A.16 Pearson product moment correlation coefficient for area based Raman spectral properties determined with four deconvoluted peaks as a function of X-ray photoelectron spectral properties for HAMWCNT and LAMWCNT.....	226
Figure A.17 Pearson product moment correlation coefficient for intensity based Raman spectral properties determined with five deconvoluted peaks as a function of X-ray photoelectron spectral properties for HAMWCNT and LAMWCNT.....	227
Figure A.18 Pearson product moment correlation coefficient for area based Raman spectral properties determined with five deconvoluted peaks as a function of X-ray photoelectron spectral properties for HAMWCNT and LAMWCNT.....	228

LIST OF SCHEMES

Scheme 3.1 Synthetic scheme for surface modification of MWCNTs..... 66

Scheme 4.1 Synthetic scheme for chemical modification of MWCNTs to produce surface modified MWCNTs. .... 105

Scheme 4.2 Epoxy-amine thin polymer film material combination and structures..... 107

Scheme 4.3 Fabrication scheme of multiwall carbon nanotube epoxy-amine free films and coated steel panels. .... 107

Scheme 4.4 Protocol to determine ambient moisture content, water vapor diffusivity, and water vapor saturation by dynamic vapor sorption analysis. .... 110

Scheme 4.5 Protocol for post-exposure coating analysis after 168 hours of salt fog exposure. .... 113

Scheme 5.1 Protocol for post-exposure coating analysis after 168 hours of salt fog exposure. .... 142

## LIST OF ABBREVIATIONS

<i>2PD</i>	two peak deconvolution
<i>3PD</i>	three peak deconvolution
<i>4PD</i>	four peak deconvolution
<i>5PD</i>	five peak deconvolution
<i>ABCVA</i>	4,4'-azobis(4-cyanovaleric acid)
<i>AFM</i>	atomic force microscopy
<i>AMP</i>	2,2'-Azobis[2-methyl- <i>N</i> -(2-hydroxyethyl) propionamide]
<i>ATR</i>	attenuated total reflectance
<i>CNT</i>	carbon nanotube
<i>DI</i>	deionized
<i>DGEBA</i>	diglycidyl ether of bisphenol-A
<i>DSC</i>	differential scanning calorimetry
<i>DVS</i>	dynamic vapor sorption
<i>EDS</i>	energy dispersive X-ray spectroscopy
<i>EEW</i>	epoxy equivalent weight
<i>EM</i>	electron microscopy
<i>EOAC</i>	effective optical absorption coefficient
<i>FE-SEM</i>	field emission scanning electron microscopy
<i>FTIR</i>	Fourier-transform infrared spectroscopy
<i>HAMWCNT</i>	high aspect ratio multiwall carbon nanotube
<i>LAMWCNT</i>	low aspect ratio multiwall carbon nanotube

<i>LO</i>	longitudinal optical phonon
<i>MPMD</i>	2-methylpentamethylenediamine
<i>MWCNT</i>	multiwall carbon nanotube
<i>OTD</i>	onset of thermal degradation
<i>PCBTF</i>	Parachlorobenzotrifluoride
<i>PC</i>	Pearson product moment correlation coefficient
<i>RBF</i>	round bottom flask
<i>RH</i>	relative humidity
<i>SWCNT</i>	single wall carbon nanotube
<i>TD</i>	thermal degradation
<i>TDI</i>	toluene diisocyanate
$T_g$	glass transition temperature
<i>TGA</i>	thermogravimetric analysis
<i>THF</i>	tetrahydrofuran
<i>TO</i>	tangential optical phonon
<i>UV-vis</i>	ultraviolet-visible spectroscopy
<i>XPS</i>	X-ray photoelectron spectroscopy

## CHAPTER I - INTRODUCTION

### 1.1 Motivation of Research

Maintenance costs and loss of assets due to corrosion were estimated to cost ~2.5 trillion USD globally in 2013.<sup>2</sup> For example, as construction of the new San Francisco Bay Bridge was near completion, workers tightened the steel bolts designed to stabilize the bridge during an earthquake event which cracked during installation. Investigations indicated that the failure was attributed to hydrogen embrittlement caused by corrosion events prior to installation. Replacement of the bolts and other materials due to corrosion during construction cost an additional 23 million USD which necessitated an increased bridge toll to offset the costs.<sup>3</sup> Beyond economic considerations is the potential for loss of life and detrimental environmental events. The Fukushima nuclear power plant meltdown in Japan necessitated the introduction of groundwater into the remaining reactors to prevent additional meltdowns; this generated ~400 tons of radioactively contaminated water per day which was collected and stored in steel tanks. Leaking of the storage tanks has resulted in an estimated 300 tons of the contaminated water to leak into the ocean daily resulting in mass contamination of the ocean with radioactive material. The Japanese power company attributed the leak to corrosion of the steel tank at the seal/tank interface.<sup>4</sup> These situations exemplify the need for continuous development of new materials and formulations to increase the corrosion resistance of metal substrates.

#### 1.1.1 Corrosion of Steel Substrates

Corrosion of steel substrates occurs spontaneously in the presence and accumulation of oxygen, water, and conductive electrolyte species (Figure 1.1), thus, proper management of these environmental contaminants will reduce corrosion rates.<sup>5-6</sup>

The corrosion of steel substrates with defect-free organic coatings commences due to the eventual and generally inevitable, delivery of environmental contaminants (e.g., sodium chloride) to the substrate. Initially, conductive pathways are developed between the environment and the substrate due to water ingress which enables ion diffusion to and from the substrate. A local anode and cathode develops at the steel substrate which establishes a galvanic cell and drives the corrosion process. At the cathode, oxygen is reduced at the surface of the steel substrate largely producing hydroxyl moieties, but can also generate peroxides, superoxides, and radicals.<sup>6</sup> Metal dissolution, i.e., the production of ferrous ions and electrons, occurs at the anode; the dissolved ferrous ions are then involved in a cascade of subsequent reactions to yield iron chloride and finally iron oxide species (rust).<sup>6-7</sup>

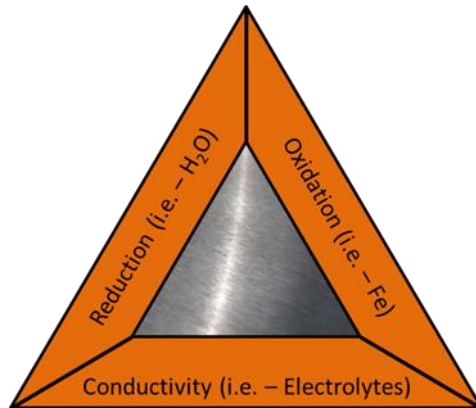


Figure 1.1 The corrosion triangle exhibiting the most common requirements for corrosion under aerobic, wet conditions.

To balance the negative charge produced by the cathodic reactions, solvated cations (commonly sodium ions) migrate through the coating or, most often, along the thin polymer thin film/substrate interface in a process known as cathodic delamination. Ion diffusion through the thin polymer film has been found to be much slower than along

the polymer thin film/substrate interface even though the ions are thought to travel through a swollen gel-like polymer state at the polymer coating/substrate interface;<sup>7</sup> thus, ion migration along the interface is generally the rate limiting step and follows Fick's law.<sup>6-7</sup>

The cathodic delamination corrosion mechanism of steel in the presence of water-solvated sodium and chlorine ions creates conditions that produce a relatively higher concentration of iron and chlorine near the local anode and a higher concentration of sodium moving away from the anode (Figure 1.2). The corrosion rate of steel substrates in real-world applications is significantly accelerated when the thin polymer film contains defects or macroscopic breaches from in-service abuse as environmental contaminants have direct access to the substrate; thus, much attention has been paid to the development of technologies that inhibit the corrosion events of coated substrates with macroscopic breaches.<sup>5-6, 8-9</sup> In the case of coated substrates with intentionally created defects, as is common for corrosion performance investigations of polymer coating formulations, the higher concentration of iron and chlorine is spatially observed in the scribed area (anode) and the higher concentration of sodium is away from the scribe (cathode).

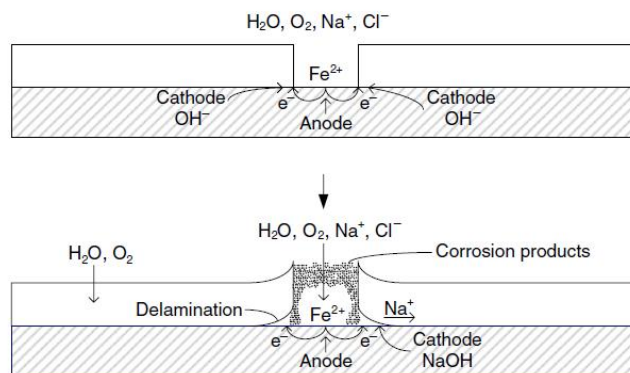


Figure 1.2 Representative scheme of the cathodic delamination mechanism of coated steel.

Note: image was adapted from reference Sørensen and co-workers.<sup>6</sup>

Organic polymer thin films (coatings) combined with various organic and inorganic fillers reduce corrosion rates of metal substrates via formation of a barrier from environmental contaminants and/or providing water-solvated ions of sparingly water-soluble pigments that passivate anodic reactions and/or repolarize the cathode, e.g., strontium chromate.<sup>5, 8</sup> Although strontium chromate is a very effective corrosion inhibiting pigment, the water solubility and toxicity of the solvated ions cast environmental concerns on the continued and long-term use of hexavalent chrome, and in some cases continued use in coating formulations is already prohibited.<sup>10</sup> As a result, alternative corrosion inhibiting and corrosion rate reducing technologies have been the subject of a large number of investigations with limited success towards replacing chromate based inhibitors and eliminating toxicity.<sup>10-13</sup>

### 1.1.2 Water Hydrogen Bonding Interactions in Polymers

The distribution of water hydrogen bonding interactions (i.e., whether it is free or bound) within a polymer can significantly impact the instantaneous material polymer performance characteristics;<sup>14-18</sup> for some polymers, the free to bound water ratio can

have a larger impact on properties than the overall bulk water absorption.<sup>16</sup> Free and bound water hydrogen bonding interactions is generally investigated via spectroscopic techniques (e.g., nuclear magnetic resonance spectroscopy, near infrared spectroscopy, dielectric spectroscopy, and mid-infrared spectroscopy).<sup>14, 16, 18-21</sup> In the literature, water has been classified discretely by the number of hydrogen bonds with the polymer matrix or another water molecule: singly-bound and multi-bound states are hydrogen bound via one and two hydrogen bonds, respectively.<sup>15-16</sup> Free water does not directly hydrogen bond with the polymer matrix nor another water molecule.<sup>15-16</sup>

Li and co-workers identified and further classified multi-bound water into loosely-bound and tightly-bound water.<sup>21</sup> Loosely-bound water was considered to exist when a water molecule hydrogen bonds to weak polar groups such as tertiary amines or sulfone groups or hydrogen bonds to highly polar, but sterically hindered groups.<sup>21</sup> Comparatively, tightly hydrogen bound water was strongly bound to hydroxyl groups whether it be to another water molecule or the polymer network.<sup>21</sup> Although the distribution of water states is typically described in the open literature as discrete states, it is important to note the rapid and dynamic nature of water molecule hydrogen bonding (on the order of picoseconds) and that the experimental time scales of most investigations (spectroscopic scans) is typically several orders of magnitude longer.<sup>22</sup>

Water-solvated sodium and chloride ions are the most common environmental contaminants attributed to corrosion initiation and propagation. Although polymers have been shown to be effective ion barriers in the absence of a macroscopic breach or detectable coating defect by some examples, most studies validate that ions and other corrosion inducing (or inhibiting) species are readily and rapidly transported through

polymeric materials.<sup>23-24</sup> However, in the case of macroscopically breached polymers, the concentration of corrosion inducing species at the substrate rapidly reaches equilibrium with the environment in the absence of any barrier to inhibit direct interaction with environmental elements. Importantly, it has been demonstrated that differences in polymer-ion diffusion properties exist at similar equilibrium water saturation levels from a variety of systems.<sup>23</sup> Water hydration shells, most often derived from free water, are required for ion transport through/within polymeric materials, however, the extent of ion hydration in polymers and the effective overall volume of solvated ions may be lower than observed in dilute aqueous solutions.<sup>23, 25</sup> Researchers have validated in some limited examples that specific water molecule orientation is required for ion solvation and mobility; i.e., O-H $\cdots$ X $^-$  for anionic species and for cationic species the O-H group points away from the cation (Figure 1.3).<sup>26</sup> Therefore, each 1) the water concentration and 2) the water hydrogen bonding interactions states, i.e., free and bound, affects their ability to participate in ion hydration shells and are shown in the literature to directly influence ion diffusion and ion activity.<sup>24, 27-28</sup>

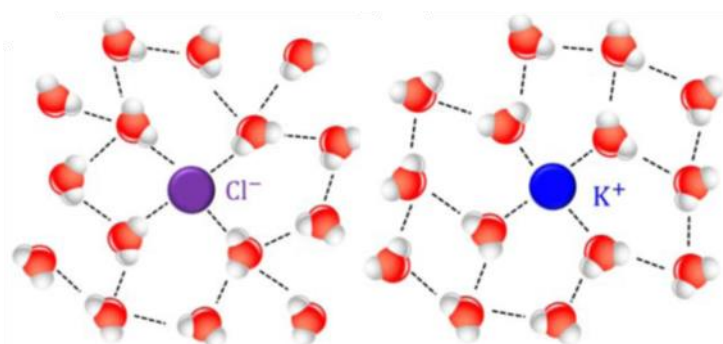


Figure 1.3 Orientation of water molecules for direct interaction with solvated anions (left) and cations (right).

Note: image adapted from Kropman and co-workers.<sup>26</sup>

### 1.1.3 Carbon Nanotubes as Corrosion Control Materials

In addition to electroactive materials for corrosion control, e.g., conductive polymers and sparingly water-soluble inorganic pigments, other materials such as carbon nanotubes (CNTs) dispersed into polymer matrix materials have resulted in diminished corrosion rates.<sup>29-33</sup> CNTs are quasi-one-dimensional high aspect ratio graphene nanostructures with unique electrical and physical properties.<sup>34-37</sup> Although the examples are limited, the improved corrosion performance of CNT-polymer blends were attributed to, singularly or in combination, increased barrier properties (tortuosity), increased adhesion and improved mechanical properties, and/or the formation of electrically conducting networks commonly described and measured as able to facilitate electrochemical reactions at low concentrations.<sup>10, 13, 29, 33, 38-39</sup> Calculations have also indicated that environmental contaminants and corrosion by-products (e.g., chlorine, oxygen, hydroxyl ions, and sulfates) adsorb to the CNT sidewall and end-caps which contributes to reducing migration through coatings and limits the concentration of these species at the polymer/metal interface.<sup>32</sup> Thought to be critically important to the present work, however, some studies have also shown that the water diffusivity and water absorption at saturation for a given MWCNT concentration remain, within detection limits, constant and yet similar systems also exhibit reduced corrosion rates;<sup>40-41</sup> hence, additional parameters and/or mechanisms must also exist which directly contributes to the overall corrosion performance, i.e., additional mechanistic considerations are missing from understanding the overall corrosion process of coated substrates. It is the main goal of this work to determine and understand this alternative mechanism that has so far been evasive in the open literature.

## 1.2 Introduction to Carbon Nanotubes

Over 180,000 peer reviewed papers, reports, reviews and patents have been generated since the seminal article in Nature on carbon nanotubes (CNTs) in 1991 by Iijima.<sup>42</sup> Surprisingly, CNTs have not been adopted into mainstream applications even though commercial scale production and sales of the raw CNTs and functionalized variants have been realized. Carbon nanotubes are quasi-one dimensional graphene structures with unique physical properties: one-dimensional ballistic conductivity (approximately  $10^5$  to  $10^7$  S/m with carrier density greater than  $10^9$  A/cm<sup>2</sup>), excellent thermal conductivity (theoretically 6600 W/mK at room temperature), and high strength being ~100 times stronger than steel (modulus over 1 TPa, tensile strength up to 160 GPa) and 5-7 times lighter.<sup>35-36, 43-46</sup> The chemical and physical properties of CNTs strongly depend on the production method which determines tube diameter, length, and sidewall chirality.<sup>45, 47</sup>

Upon the discovery of carbon nanotubes and the increased understanding of their unique physical properties, there was a large intellectual and economic investment into making use of these relatively unexplored materials – the technology trigger. Generally, early investigations simply mixed carbon nanotubes into polymer matrix materials in an attempt to impart the electrical and mechanical properties of CNTs to the overall structure which rapidly produced a number of patents and products. However, the “pixie dust” approach to producing new high performance materials generally resulted in negligible performance gains with high prices which lead to negative impressions on the usefulness of carbon nanotubes beyond the most specialized applications. It has been suggested that carbon nanotube technologies are in the local minimum – the trough of

disillusionment - of the Gartner “Hype Cycle of Innovation” curve (Figure 1.4).<sup>48-51</sup> As carbon nanotubes are now available in kilogram quantities at costs that are economically feasible (~\$0.20 per gram for industrial multiwall carbon nanotubes)<sup>52</sup>, there is a large potential for these materials to move through the slope of enlightenment and take place in disruptive innovations in the near future.

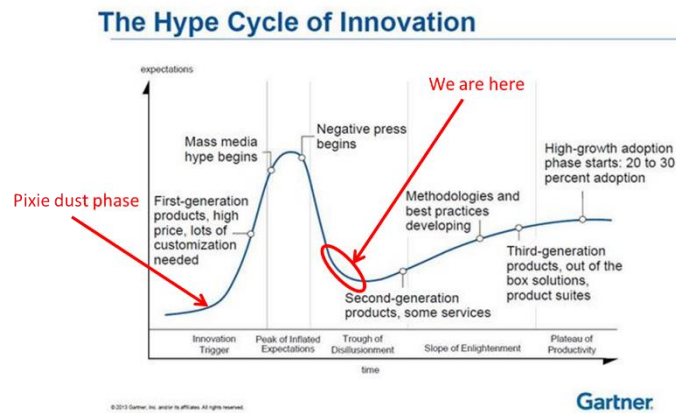


Figure 1.4 Estimated location of carbon nanotube technology on the Gartner “Hype Cycle of Innovation” curve.

Note: the interpretation of the curve was in November 2015 at the Nano for Defense Conference, City of Industry, CA.

Although CNTs have unique attributes, their high aspect ratio, surface area (> 100 m<sup>2</sup> per gram), and the high polarizability of the extended  $\pi$ -electron cloud yields large van der Waals forces (estimated to be 500 eV/micron of tube length) causing agglomeration/bundling; this presents the complete exfoliation and dispersion of bundled nanotubes a difficult challenge.<sup>45, 53-54</sup> Carbon nanotubes possess limited reactivity and do not readily interact with organic or aqueous media, which leads to poor exfoliation and dispersion detrimentally affecting the composite performance.<sup>36, 45, 53</sup> Studies have indicated that CNTs must be completely exfoliated with strong polymer-particle interfacial interactions to realize the full potential of CNT-polymer composites.<sup>36, 45, 47, 55</sup>

Several factors must be considered when attempting to disperse particles in liquid media, which is the case for most coating systems. Particle aggregation occurs when the interparticle interactions are stronger than the particle-solvent interactions which subsequently increases the sedimentation potential.<sup>56-57</sup> Highly dispersed CNT systems commonly include a deagglomeration process (ultrasonication, ball milling, calendaring, etc.) followed by chemical/physical modification to increase CNT-media interactions, increase dispersion, and reduce reagglomeration during processing.

### **1.3 Dissertation Objectives and Outline**

In the context of corrosion control coating systems, water, ion, and oxygen transport are of great concern as they collectively participate in the corrosion of steel.<sup>58</sup> It has been shown that traditional organic coatings cannot sufficiently hinder oxygen and water permeation to prevent thin polymer coating delamination due to these species reaching the substrate, thus, proper control of ionic species by a coating is required to limit the cathodic delamination process.<sup>6</sup> The initial hypothesis of the work was that incorporating MWCNTs into thin film material combinations provides a more tortuous path for corrosion inducing species to reach the substrate thereby reducing corrosion rates concurrently. To ideally and properly investigate this hypothesis, the MWCNTs must be highly exfoliated and deagglomerated with sufficient polymer interactions and oriented parallel to the substrate. MWCNTs were chemically modified then dispersed in a model crosslinked parent epoxy-amine material combination in an attempt to investigate the tortuosity mechanism. However, preliminary experimental evidence of the current MWCNT/epoxy-amine material combinations indicated an alternative mechanism dominated the corrosion propagation properties. These data combined with an in-depth

investigation of the open literature identified critical gaps in knowledge which gives rise to specific key questions and observations:

- Raman spectroscopy has been one of the most widely used investigative tools for monitoring changes in MWCNT molecular structure, yet no standardized approach for interpreting spectra currently exists. Thus, of the various reported protocols for the deconvolution of MWCNT Raman spectra in the literature, which reported protocol is most representative of changes in MWCNT molecular structure of the outer tube due to chemical modification?
- Literature protocols for quantifying and differentiating variations in MWCNT dispersion states were not universal nor practical in all applications and some protocols required investigator chosen assumptions that may produce misleading results. These protocols appear to not be generally applicable for non-transparent substrate bound polymer systems. Could a simple method be developed that can reliably and reproducibly quantify the dispersion states of non-transparent substrate bound polymers reducing the potential for experimental and investigator bias?
- Chemical and physical surface modification of MWCNTs have been shown to increase the dispersion quality and influence polymer performance characteristics, yet the effect of MWCNT surface chemistry on corrosion performance has not been systematically investigated. How does the MWCNT surface chemistry affect the dispersion, critical

performance characteristics, and the corrosion rates of epoxy-amine coated steel substrates?

- Additionally, how does varying MWCNT concentration affect the corrosion rates of epoxy-amine coating steel substrates and what is the underlying mechanism of increased corrosion rate control if increased barrier properties are not realized?

Preliminary data suggested that increased barrier properties (tortuosity) was likely not the mechanism of increased corrosion rate control for the systems evaluated in this work, thus, the initial hypothesis of the MWCNT corrosion protection mechanism was further refined: **the corrosion performance of MWCNT/epoxy-amine material blends is directly related to the ability of the combined materials, and more specifically the MWCNTs, to manage water hydrogen bonding states within substrate bound polymer thin films (i.e., free versus bound water states); specifically, the potential of each water molecule in a specific hydrogen bonding state to contribute to ion hydration shells and readily transport corrosion inducing environmental contaminants and corrosion products to and from the substrate directly influences the corrosion rate.** The observations and questions above were the main focal drivers for the research reported herein and the goal was to provide a more fundamental understanding such that MWCNTs were able to usefully be utilized for corrosion control applications.

With the goal of developing a more accurate and revised hypothesis, and simultaneously increase the understanding on the effects of water hydrogen bonding interactions within thin polymer films applied to metallic substrates on the corrosion

performance, the corrosion rates of MWCNT/epoxy-amine coated steel substrates were quantified and compared to the relative concentration distribution of free versus bound water within the thin polymer film. Experimental corrosion rates for short but adequate durations of up to 168 hours of standard neutral salt fog exposure correlated well with the measured relative concentrations of each, free water, singly-bound water, and multi-bound water within each MWCNT/epoxy-amine material combination. The trendline slopes of these relationships indicated that both the free and singly-bound water states contributed to increasing the corrosion rate and that multi-bound water reduced the corrosion rate. These relationships were further validated via loading graphene and carbon black particles into the same parent epoxy-amine polymer matrix to increase the number of material combinations with various distributions of water hydrogen bonding interactions and corrosion rates. Each question above provided the basis of several distinct and independent objectives which were divided into the various chapters of this dissertation. The specific goal of each chapter was to:

- develop a more reliable and standardized deconvolution protocol for first-order Raman spectra of MWCNTs,
- develop a rapid quantitative protocol for measuring MWCNT degree of dispersion in non-transparent and substrate bound polymers,
- investigate the effect of MWCNT surface chemistry on the corrosion performance of epoxy-amine coating systems on steel substrates,
- determine and validate the mechanism of increased corrosion control of MWCNT/epoxy-amine material combinations, and

- understand the influence of water hydrogen bonding interactions on corrosion performance and develop an equation capable of predicting the experimental corrosion rate of epoxy-amine coating material combinations applied to steel substrates in a salt fog environment using pre-exposure measurements.

These research results support the overarching concept that MWCNTs alter ion transport characteristics which is hypothesized to be attributed to increased surface area and surface interactions from which MWCNTs manage water hydrogen bonding interactions within polymer thin films. Serendipitously, a critical and direct understanding of the influence of free and bound water states on the corrosion rates of coated steel substrates was developed. These observed relationships prompted the investigation and the development of utilizing pre-exposure measurements to predict the experimental corrosion rates of coated steel substrates. It is surmised that the incorporation of MWCNTs into epoxy-amine thin film material combinations for corrosion rate reduction is applicable to other substrates in which ionic species initiate, propagate, and/or accelerate corrosion events. Additionally, determination of the relative concentration of water types within a coating as a function of real world exposure may provide insight into more accurate lifetime modeling, maintenance schedules, and provide a protocol for real-time “damage” assessment.<sup>59</sup>

## 1.4 References

2. Koch, G.; Varney, J.; Thompson, N.; Moghissi, O.; Gould, M.; Payer, J. *International Measures of Prevention, Application, and Economics of Corrosion Technologies Study*; NACE International: Houston, 2016.
3. Corrosion Failures: San Francisco Bay Bridge Bolt Failure. <http://www.nace.org/CORROSION-FAILURES-San-Francisco-Bay-Bridge-Bolt-Failure.aspx> (accessed 30 September).
4. Corrosion Failures: Fukushima Nuclear Plant Tank Leak. <http://www.nace.org/CORROSION-FAILURES-Fukushima-Nuclear-Plant-Tank-Leak.aspx> (accessed 30 September).
5. Revie, W. R., *Uhlig's Corrosion Handbook*. 3rd ed.; John Wiley & Sons, Inc.: Hoboken, 2011; p 1253.
6. Sørensen, P. A.; Kiil, S.; Dam-Johansen, K.; Weinell, C. E., Anticorrosive Coatings: A Review. *Journal of Coatings Technology and Research* **2009**, 6 (2), 135-176.
7. Leng, A.; Streckel, H.; Stratmann, M., The Delamination of Polymeric Coatings from Steel. Part 2: First Stage of Delamination, Effect of Type and Concentration of Cations on Delamination, Chemical Analysis of the Interface. *Corrosion Science* **1998**, 41 (3), 579-597.
8. Sander, J.; Kirmaier, L.; Manea, M.; Shchukin, D.; Skorb, E., *Anticorrosive Coatings: Fundamentals and New Concepts*. Vincentz Network GmbH & Co.: Hannover, 2010.
9. *Protective Organic Coatings*. ASM International: Materials Park, OH, 2015; Vol. 5B.
10. Pruna, A., Advances in Carbon Nanotube Technology for Corrosion Applications. In *Handbook of Polymer Nanocomposites. Processing, Performance and Application: Volume B: Carbon Nanotube Based Polymer Composites*, Kar, K. K.; Pandey, K. J.; Rana, S., Eds. Springer Berlin Heidelberg: Berlin, Heidelberg, 2015; pp 335-359.
11. Sharma, S. K.; Peter, A.; Obot, I. B., Potential of Azadirachta Indica as a Green Corrosion Inhibitor against Mild Steel, Aluminum, and Tin: A Review. *Journal of Analytical Science and Technology* **2015**, 6 (1), 1-16.
12. Rani, A. B. E.; Basu, B. B. J., Green Inhibitors for Corrosion Protection of Metals and Alloys: An Overview. *International Journal of Corrosion* **2012**, 2012, 15.
13. Anonymous, Chromate Primer Alternative Uses Carbon Nanotubes Modified with Corrosion Inhibitors. *Materials Performance* 1 April 2016, 2016.
14. Morsch, S.; Lyon, S.; Greensmith, P.; Smith, S. D.; Gibbon, S. R., Water Transport in an Epoxy–Phenolic Coating. *Progress in Organic Coatings* **2015**, 78, 293-299.
15. Cotugno, S.; Larobina, D.; Mensitieri, G.; Musto, P.; Ragosta, G., A Novel Spectroscopic Approach to Investigate Transport Processes in Polymers: The Case of Water–Epoxy System. *Polymer* **2001**, 42 (15), 6431-6438.
16. Musto, P.; Ragosta, G.; Mascia, L., Vibrational Spectroscopy Evidence for the Dual Nature of Water Sorbed into Epoxy Resins. *Chemistry of Materials* **2000**, 12 (5), 1331-1341.

17. Soles, C. L.; Yee, A. F., A Discussion of the Molecular Mechanisms of Moisture Transport in Epoxy Resins. *Journal of Polymer Science Part B: Polymer Physics* **2000**, *38* (5), 792-802.
18. Mijović, J.; Zhang, H., Local Dynamics and Molecular Origin of Polymer Network–Water Interactions as Studied by Broadband Dielectric Relaxation Spectroscopy, Ftir, and Molecular Simulations. *Macromolecules* **2003**, *36* (4), 1279-1288.
19. Takeshita, Y.; Becker, E.; Sakata, S.; Miwa, T.; Sawada, T., States of Water Absorbed in Water-Borne Urethane/Epoxy Coatings. *Polymer* **2014**, *55* (10), 2505-2513.
20. Lee, D. K.; Saito, T.; Benesi, A. J.; Hickner, M. A.; Allcock, H. R., Characterization of Water in Proton-Conducting Membranes by Deuterium Nmr T1 Relaxation. *The Journal of Physical Chemistry B* **2011**, *115* (5), 776-783.
21. Li, L.; Yu, Y.; Su, H.; Zhan, G.; Li, S.; Wu, P., The Diffusion Mechanism of Water Transport in Amine-Cured Epoxy Networks. *Applied Spectroscopy* **2010**, *64* (4), 458-466.
22. Barati Farimani, A.; Aluru, N. R., Existence of Multiple Phases of Water at Nanotube Interfaces. *The Journal of Physical Chemistry C* **2016**, *120* (41), 23763-23771.
23. Geise, G. M.; Paul, D. R.; Freeman, B. D., Fundamental Water and Salt Transport Properties of Polymeric Materials. *Progress in Polymer Science* **2014**, *39* (1), 1-42.
24. Dias, C. R.; Rosa, M. J.; de Pinho, M. N., Structure of Water in Asymmetric Cellulose Ester Membranes — and Atr-Ftir Study. *Journal of Membrane Science* **1998**, *138* (2), 259-267.
25. Posner, R.; Titz, T.; Wapner, K.; Stratmann, M.; Grundmeier, G., Transport Processes of Hydrated Ions at Polymer/Oxide/Metal Interfaces: Part 2. Transport on Oxide Covered Iron and Zinc Surfaces. *Electrochimica Acta* **2009**, *54* (3), 900-908.
26. Kropman, M. F.; Bakker, H. J., Dynamics of Water Molecules in Aqueous Solvation Shells. *Science* **2001**, *291* (5511), 2118-2120.
27. Gao, X.; Zhao, T.; Li, Z., Effects of Ions on the Diffusion Coefficient of Water in Carbon Nanotubes. *Journal of Applied Physics* **2014**, *116* (5), 054311.
28. Murphy, D.; de Pinho, M. N., An Atr-Ftir Study of Water in Cellulose Acetate Membranes Prepared by Phase Inversion. *Journal of Membrane Science* **1995**, *106* (3), 245-257.
29. Deyab, M. A., Effect of Carbon Nano-Tubes on the Corrosion Resistance of Alkyd Coating Immersed in Sodium Chloride Solution. *Progress in Organic Coatings* **2015**, *85*, 146-150.
30. Jeon, H.; Park, J.; Shon, M., Corrosion Protection by Epoxy Coating Containing Multi-Walled Carbon Nanotubes. *Journal of Industrial and Engineering Chemistry* **2013**, *19* (3), 849-853.
31. Cubides, Y.; Castaneda, H., Corrosion Protection Mechanisms of Carbon Nanotube and Zinc-Rich Epoxy Primers on Carbon Steel in Simulated Concrete Pore Solutions in the Presence of Chloride Ions. *Corrosion Science* **2016**, *109*, 145-161.
32. Butyrskaya, E. V.; Nechaeva, L. S.; Zapryagaev, S. A., Theoretical Study of the Corrosion Protection Mechanism by Carbon Nanotubes. *Computational and Theoretical Chemistry* **2016**, *1090*, 1-5.

33. Gergely, A.; Pászti, Z.; Hakkel, O.; Drotár, E.; Mihály, J.; Kálmán, E., Corrosion Protection of Cold-Rolled Steel with Alkyd Paint Coatings Compositing with Submicron-Structure Types Polypyrrole-Modified Nano-Size Alumina and Carbon Nanotubes. *Materials Science and Engineering: B* **2012**, *177* (18), 1571-1582.
34. Burchell, T. D., *Carbon Materials for Advanced Technologies*. Elsevier: Amsterdam, 1999; p 558.
35. Burghard, M., Electronic and Vibrational Properties of Chemically Modified Single-Wall Carbon Nanotubes. *Surface Science Reports* **2005**, *58* (1–4), 1-109.
36. Chou, T.-W.; Gao, L.; Thostenson, E. T.; Zhang, Z.; Byun, J.-H., An Assessment of the Science and Technology of Carbon Nanotube-Based Fibers and Composites. *Composites Science and Technology* **2010**, *70* (1), 1-19.
37. Spitalsky, Z.; Tasis, D.; Papagelis, K.; Galiotis, C., Carbon Nanotube–Polymer Composites: Chemistry, Processing, Mechanical and Electrical Properties. *Progress in Polymer Science* **2010**, *35* (3), 357-401.
38. Gergely, A.; Pászti, Z.; Mihály, J.; Drotár, E.; Török, T., Galvanic Function of Zinc-Rich Coatings Facilitated by Percolating Structure of the Carbon Nanotubes. Part II: Protection Properties and Mechanism of the Hybrid Coatings. *Progress in Organic Coatings* **2014**, *77* (2), 412-424.
39. Khun, N. W.; Frankel, G. S., Cathodic Delamination of Polyurethane/Multiwalled Carbon Nanotube Composite Coatings from Steel Substrates. *Progress in Organic Coatings* **2016**, *99*, 55-60.
40. Starkova, O.; Buschhorn, S. T.; Mannov, E.; Schulte, K.; Aniskevich, A., Water Transport in Epoxy/Mwcnt Composites. *European Polymer Journal* **2013**, *49* (8), 2138-2148.
41. Curtzwiler, G. W.; Williams, E. B.; Konecki, C. M.; Wand, S. W.; Rawlins, J. W., Comparison of the Added Value for Corrosion Performance of Chemically Modified Multiwall Carbon Nanotube Epoxy-Amine Coating Systems on Steel Substrates. In *The Waterborne Symposium*, New Orleans, LA, 2016.
42. Iijima, S., Helical Microtubules of Graphitic Carbon. *Nature (London)* **1991**, *354*, 56-8.
43. Kyrylyuk, A. V.; Hermant, M. C.; Schilling, T.; Klumperman, B.; Koning, C. E.; van, d. S. P., Controlling Electrical Percolation in Multicomponent Carbon Nanotube Dispersions. *Nature Nanotechnology* **2011**, *6*, 364-369.
44. Li, X.; Wong, S. Y.; Tjui, W. C.; Lyons, B. P.; Oh, S. A.; He, C. B., Non-Covalent Functionalization of Multiwalled Carbon Nanotubes and Their Application for Conductive Composites. *Carbon* **2008**, *46*, 829-831.
45. Bose, S.; Khare, R. A.; Moldenaers, P., Assessing the Strengths and Weaknesses of Various Types of Pre-Treatments of Carbon Nanotubes on the Properties of Polymer/Carbon Nanotubes Composites: A Critical Review. *Polymer* **2010**, *51* (5), 975-993.
46. Hernández-Pérez, A.; Avilés, F.; May-Pat, A.; Valadez-González, A.; Herrera-Franco, P. J.; Bartolo-Pérez, P., Effective Properties of Multiwalled Carbon Nanotube/Epoxy Composites Using Two Different Tubes. *Composites Science and Technology* **2008**, *68* (6), 1422-1431.

47. Ma, P.-C.; Siddiqui, N. A.; Marom, G.; Kim, J.-K., Dispersion and Functionalization of Carbon Nanotubes for Polymer-Based Nanocomposites: A Review. *Composites Part A: Applied Science and Manufacturing* **2010**, *41* (10), 1345-1367.
48. Lajoie, E.; Bridges, L., Innovation Decisions: Using the Gartner Hype Cycle. *Library Leadership & Management* **2014**, *28* (4), 7.
49. Anonymous Gartner Hype Cycle. <http://www.gartner.com/technology/research/methodologies/hype-cycle.jsp> (accessed 12/01/2015).
50. Duchesne, L. Graphene Is Here to Stay. <http://investorintel.com/technology-metals-intel/graphene-is-here-to-stay/> (accessed 12/1/2015).
51. Anonymous Graphene, 2d Materials and Carbon Nanotubes: Markets, Technologies and Opportunities 2015-2025. <http://www.prnewswire.com/news-releases/graphene-2d-materials-and-carbon-nanotubes-markets-technologies-and-opportunities-2015-2025-300180496.html> (accessed 12/01/2015).
52. Multi Walled Carbon Nanotubes Products. <https://www.cheaptubes.com/product-category/multi-walled-carbon-nanotubes/> (accessed 26 October).
53. Grossiord, N.; Loos, J.; Regev, O.; Koning, C. E., Toolbox for Dispersing Carbon Nanotubes into Polymers to Get Conductive Nanocomposites. *Chemistry of Materials* **2006**, *18* (5), 1089-1099.
54. Leonard, F., *Physics of Carbon Nanotube Devices*. William Andrew: 2009.
55. Gojny, F. H.; Nastalczyk, J.; Roslaniec, Z.; Schulte, K., Surface Modified Multi-Walled Carbon Nanotubes in Cnt/Epoxy-Composites. *Chemical Physics Letters* **2003**, *370* (5-6), 820-824.
56. Butt, H.-J.; Graf, K.; Kappl, M., *Physics and Chemistry of Interfaces*. John Wiley and Sons Inc: New York, NY, 2006.
57. Morrison, I.; Ross, S., *Colloidal Dispersion: Suspension, Emulsion, and Foams*. Wiley and Sons Inc: New York, NY, 2002.
58. Fontana, M., *Corrosion Engineering*. 3 ed.; McGraw-Hill, Inc: Singapore, 1986.
59. Cheng, H. K. F.; Basu, T.; Sahoo, N. G.; Li, L.; Chan, S. H., Current Advances in the Carbon Nanotube/Thermotropic Main-Chain Liquid Crystalline Polymer Nanocomposites and Their Blends. *Polymers* **2012**, *4* (2), 889-912.

CHAPTER II – DEVELOPMENT OF A MORE STANDARDIZED  
DECONVOLUTION PROTOCOL FOR RAMAN SPECTRA OF  
MULTIWALL CARBON NANOTUBES

**2.1 Abstract**

Carbon nanotubes (CNT) have an inherent tendency to aggregate in low viscosity media; thus, for optimal dispersion and distribution in a polymer matrix, CNTs are often modified chemically and/or physically. Much of the literature present quantifiable differences in CNT molecular structure changes between control and varying degrees of chemical modification via Raman spectroscopy. Even though a variety of mathematical methods have been employed for deconvolution of CNT first order Raman spectra to calculate D/G band ratios, there is no consensus on a standardized protocol. In this Chapter, Raman spectral properties of two multiwall CNTs (MWCNTs) with varying aspect ratios and two modification treatments (carbon-centered free radicals and thermal oxidation) were compared with thermogravimetric analysis (TGA) and X-ray photoelectron spectroscopy (XPS) measurements. It was noted that random selection of deconvolution protocols provided unpredictable and potentially misleading results. On the other hand, employing a four peak deconvolution protocol of first order MWCNT Raman spectra provided quantifiable results with the highest statistical confidence in correlating with TGA and XPS analyses and provided the greatest confidence in understanding the connection between Raman spectra and the MWCNT molecular structure.

## 2.2 Introduction

The mainstream application of multiwall carbon nanotubes (MWCNT) requires facile and reliable quantification of its chemical modifications. Although the outer tube of MWCNTs constitutes < 5% of the total mass, it predominantly determines the MWCNT's interfacial interactions with solvents and polymers. Therefore, it is critical to investigate whether the measured spectral properties correlate with measurements made by other analytical techniques related to the MWCNT outer tube to confirm surface chemistry modification. Raman spectroscopy has been widely used for non-destructive and rapid characterization of carbon nanotubes (CNTs) and has been the workhorse for qualifying, quantifying, and correlating molecular structure modifications of MWCNTs, often in the absence of supporting methods to verify whether changes in MWCNT molecular structure have definitively occurred. Interpretation and deconvolution of the first order Raman spectrum into the tangential order band (G band) and disorder band (D-band) has been common for discerning CNT chemical modifications with changes in molecular structure.

### 2.2.1 Carbon Nanotube Synthesis

Several methods have been employed to produce carbon nanotubes; mainly, arc discharge and catalytic chemical vapor deposition.<sup>53, 60</sup> Arc discharge utilizes two graphite rods as the anode and cathode.<sup>61</sup> The catalyst (typically Ni, Co, Fe, Y, or a mixture thereof) and graphite powder is loaded into the anode cavity and potassium chloride, iron sulfide powder, and graphite powder are loaded into the cathode cavity.<sup>61</sup> An arc is generated under a hydrogen atmosphere via a continuous current which produces CNTs with relatively low defects and high physical properties.<sup>61</sup> Catalytic

chemical vapor deposition (CCVD) injects a gaseous carbon source (e.g., acetylene, pure ethanol, or a mixture of methane and hydrogen) into a tubular oven in the presence of transitional metal catalysts; the size of the catalyst determines the diameter of the tube and the density of the particles controls the distance between the tubes.<sup>53, 62</sup> The arc discharge method is more costly than CCVD, but produces CNTs with better mechanical and electrical properties due to fewer defects.<sup>62</sup> Generally, CNTs synthesized via CCVD are, at present, the only ones of commercial importance as this method can produce large amount of CNTs in a commercially viable manner.<sup>63</sup>

### **2.2.2 Carbon Nanotube Structure**

Carbon nanotubes (CNTs) are tubular graphitic nanostructures comprised of a single wall (SWCNTs), two walls (DWCNTs), or multiple walls (MWCNTs) in which each wall is concentrically oriented.<sup>35, 54, 64-66</sup> The lowest energy geometric structure of these  $sp^2$  hybridized carbon structures is hexagonal in which the alignment of repeat structures ideally generates straight tubes of conjugated carbon (Figure 2.1). The distance between each tube wall has been measured to be  $\sim 0.34$  nm which is slightly greater than the spacing in graphite due to the curvature of the graphene wall although increased spacing has been observed in small diameter MWCNTs.<sup>54, 67-69</sup> Most synthetic methods for CNTs result in lengths in the tens to hundreds of microns with diameters from 0.7 to 2 nm for SWCNTs up to several tens of nanometers for MWCNTs.<sup>67</sup>

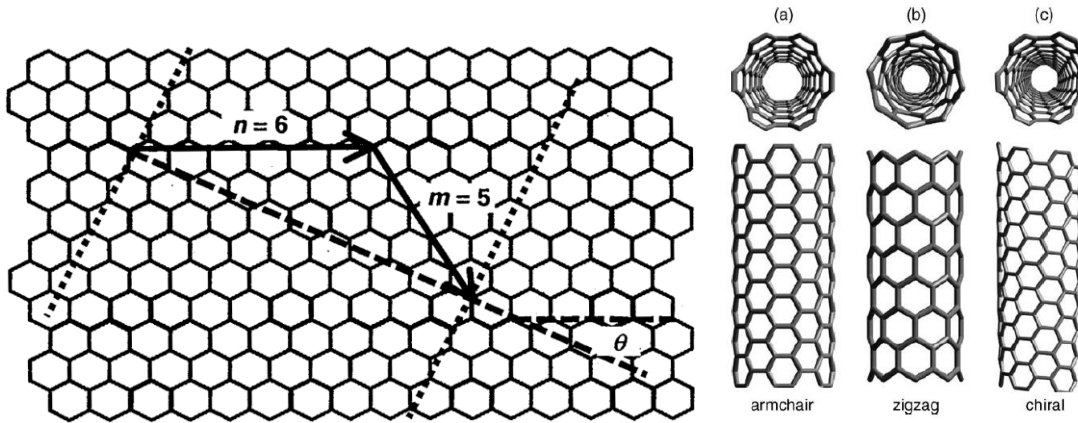


Figure 2.1 General molecular structure of carbon nanotubes.

Note: Designation of the  $n$  and  $m$  parameters for identifying the chiral vector of carbon nanotubes.<sup>35, 54, 67</sup>

Carbon nanotubes properties are strongly dependent upon the tube's chirality. CNT chirality is described using the  $(n,m)$  notation or by its diameter and chiral angle as both describe the vector in which the hexagonal repeat units are arranged around the tube (Figure 2.1).<sup>35, 54, 67</sup> The concentric tubes in double and multiwall carbon nanotubes are not required to have similar chiral vectors<sup>35, 65, 67</sup>; however, the chiralities of the tubes cannot be random since the interplanar spacing in defect-free regions of the tube remains approximately constant, and thus, a finite number of chiral vectors of adjacent walls are possible.<sup>67</sup>

### 2.2.3 Carbon Nanotube Defects

Defects present in carbon nanotubes significantly influences their physicochemical properties. The most common defects in CNTs include heptagon-pentagon pairs (Thrower-Stone-Wales, TSW), lattice vacancies, and interstitial moieties (Figure 2.2).<sup>45, 70</sup> While TSW defects preserve the continuous  $sp^2$  hybridization of carbon nanotubes, vacancies, and interstitial defects reduce conjugation in the structure thereby reducing the electrical/thermal conductivity and mechanical properties.<sup>70</sup> The

imperfections can induce morphological distortions resulting in physical curvature and are a result of the presence of pentagons, heptagons, and octagons within the  $sp^2$  lattice (Figure 2.2).<sup>45, 70</sup> These defects increase localized strain due to out of plane bending and increases reactivity making these sites more susceptible to chemical reactions and oxidation. As a result, more defects decrease CNT thermal stability. However, annealing at high temperature under vacuum reduces the number of defects improving the physical properties, such as electrical conductivity and mechanical strength.<sup>63</sup>

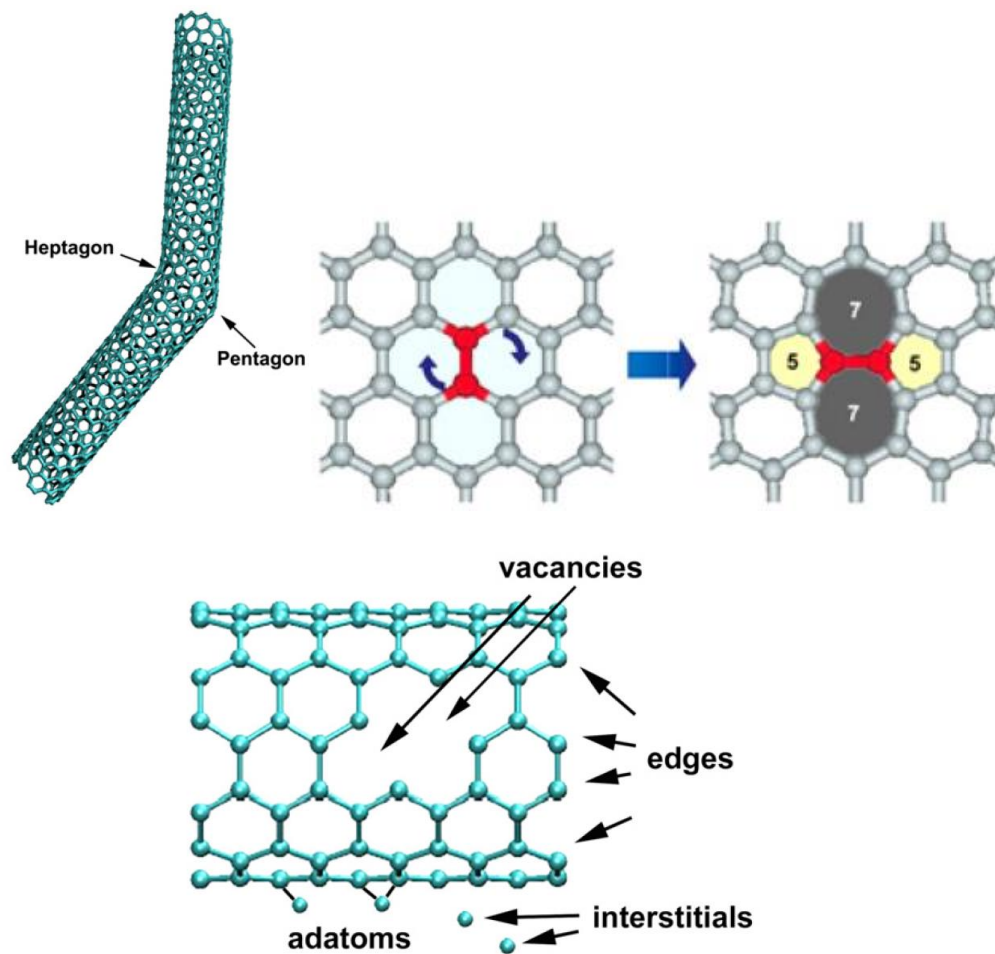


Figure 2.2 Example defects in the molecular structure of carbon nanotubes.

Note: These images were adapted from Lehman and co-workers.<sup>70</sup>

## 2.2.4 Electronic Structure of Graphene and Carbon Nanotubes

The electronic  $\sigma$  bands are responsible for strong in-plane covalent bonds within a single wall and the  $\pi$  bands produce the relatively weaker van der Waals inter- and intra-tube interactions.<sup>54, 65</sup> The cylindrical shape of CNTs yields discrete wave functions along the tube circumference (tangential direction), whereas the wave vector along the axis of an infinitely long tube remains continuous.<sup>35, 54</sup> The high curvature of small diameter nanotubes alters the carbon-carbon bond distances causing  $\sigma$  and  $\pi$  bond mixing.<sup>35, 65</sup> When the CNT diameter is sufficiently large to avoid sigma/pi overlap, the  $\pi$  bands are close to the Fermi level which enables optical excitation of electrons from the valence to conduction bands and gives rise to the characteristic bands in UV-Vis spectra.<sup>54, 65</sup>

MWCNT molecular structure has been most commonly investigated with the first order Raman spectra comprising of multiple characteristic bands related to the D and G bands of carbon allotropes. The G band ( $\sim 1580\text{ cm}^{-1}$ ) signal is representative of several tangential modes due to out-of-phase stretching vibrations of the carbon-carbon bonds in the CNT sidewall ( $E_{2g}$  symmetry; Figure 2.3) and has been typically associated with the graphitic nature (crystallinity, pristine arrangement of atoms).<sup>71</sup> The D band ( $\sim 1350\text{ cm}^{-1}$ ) has been attributed to finite size effects, disordered  $sp^3$  hybridized carbon atoms found in amorphous carbon impurities, and CNT defects (e.g., pentagon-heptagon pairs, grain boundaries, other in-plane topological defects).<sup>70-71</sup> This Raman mode is related to activation of the hexagonal ring breathing mode due to the loss of translational symmetry.<sup>71</sup> The D' band, observed as a broad shoulder of the G peak ( $\sim 1610\text{ cm}^{-1}$ ), has been associated with the degree of disorder/defects in the crystalline structure of MWCNTs.<sup>70</sup> Since this mode has been attributed to defects and strain along the tube

walls that affects the  $E_{2g}$  vibrational mode, it facilitates direct investigation of the changes in the defects of MWCNT tube walls and is independent of amorphous carbon impurities.<sup>70, 72</sup>

It has been widely accepted that the relative amounts of defects within CNTs can be investigated using the intrinsically normalized intensity ratio of the D band (related to disorder) to the G band (related to order and crystallinity), designated as  $I_D/I_G$ . While it was first proposed by Tuinstra and Koenig in 1970 for graphite and carbon fiber systems, it has been recently employed to measure CNT purity, purification efficiency, and to track chemical functionalization via substitution into empirical equations.<sup>64, 73-76</sup> As CNTs become purer (more structured), the  $I_D/I_G$  ratio decreases in accordance with the decreasing ratio of disordered  $sp^3$  carbons to more ordered  $sp^2$  carbons. However, there has been no definable standardized protocol for calculating the D/G ratio from Raman spectra of MWCNTs. A literature survey regarding protocols for calculating the D/G ratio indicated the use of: 1) the raw spectrum intensity ( $\sim 40\%$ )<sup>63-64, 77-98</sup> or 2) spectral deconvolution protocols employing two ( $\sim 21\%$ )<sup>99-111</sup>, three ( $\sim 25\%$ )<sup>72, 75, 112-123</sup>, five ( $\sim 12\%$ )<sup>124-130</sup>, or more than five ( $\sim 2\%$ )<sup>131</sup> peaks, utilizing either the peak intensity ( $\sim 48\%$ )<sup>72, 75, 107, 112, 114, 116, 118, 120, 122, 124-129, 131-132</sup> or peak area ( $\sim 52\%$ )<sup>99-101, 103-111, 113, 115, 119, 121, 130</sup>. These spectral deconvolution parameters require definitive methods/protocols to support broader utility and depth of understanding.

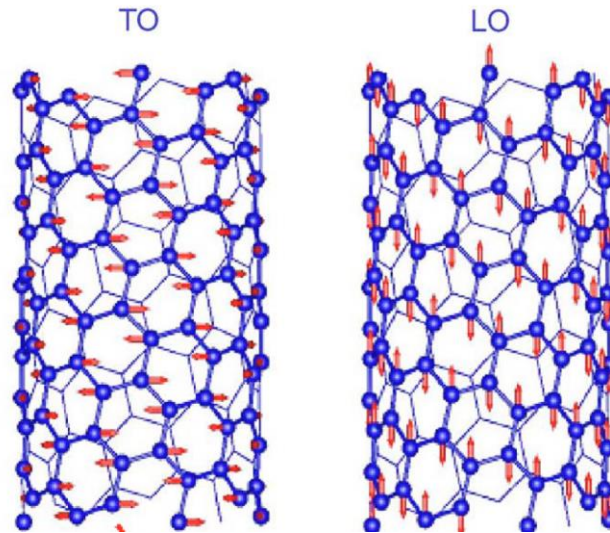


Figure 2.3 Example physical bond vibrations representative of the transverse optical (TO) and longitudinal optical (LO) phonons.

Note: This images was adapted from Piscane and coworkers.<sup>133</sup>

Thermogravimetric analysis (TGA) is a complementary tool to investigate the crystalline structure and defects of CNTs and has been employed industrially for quality control between batches.<sup>70</sup> Thermal oxidation properties are directly attributed to the degree of aromaticity within the MWCNT structure and can be influenced by the number of walls, tube diameter (strain), defects, and the composition and amount of residual catalyst present.<sup>70</sup> As a result, this technique can provide valuable information of the chemical nature of MWCNTs provided that all other variables are held constant. The oxidation temperature in an oxygenated atmosphere of MWCNTs has been shown to occur between 400 and 650 °C, single wall carbon nanotubes (SWCNTs) between 350 and 500 °C, and amorphous carbon between 200 and 300 °C.<sup>70</sup> Annealing was demonstrated to improve the molecular order of CNTs and increase the thermal degradation temperature; conversely, chemical modification interrupted the aromatic framework and reduced the thermal degradation temperature.<sup>70, 75, 121</sup>

X-ray photoelectron spectroscopy (XPS) is a surface specific analytical technique (i.e., 5-10 Å mean free electron escape path for carbon with a binding energy of ~285 eV<sup>134-135</sup>). Thus, changes in the molecular structure of the MWCNT outer tubes due to chemical functionalization is expected to be characterized accurately via XPS. However, quantification via XPS is complicated in that there are no absolute values for the XPS peak positions. Numerous databases and handbooks (provided by instrument manufacturers) report peak positions for all elements, but they are an accumulation of references and the data are dependent upon the instrument used, sample preparation, and other factors. With improved peak definition and resolution, there is general agreement in the literature regarding peak assignments.<sup>115, 136-144</sup>

The main objective of this Chapter was to quantify and understand the effects of varying the number of peaks utilized for deconvolution of first-order Raman spectra on the: 1) reported value of the D/G and D'/G ratios of chemically modified MWCNTs, and 2) to seek a consistent and reliable interpretation of MWCNT molecular structural feature/changes due to chemical modification via correlation of Raman spectral properties with TGA and XPS. Two types of MWCNTs were studied, each with the same approximate diameter but possessing different lengths (different aspect ratios); each type was treated singularly with either carbon-centered radicals or air oxidation. Each MWCNT aspect ratio and treatment was characterized via TGA, XPS, and Raman spectroscopy, and each Raman spectrum was deconvoluted via two, three, four, and five peaks.

## **2.3 Experimental**

### **2.3.1 Materials**

Low aspect ratio multiwall carbon nanotubes (LAMWCNT;  $l/d \sim 30$ ) (Cheap Tubes Inc.) and high aspect ratio multiwall carbon nanotubes (HAMWCNT;  $l/d \sim 650$ ) (Ahwahnee Technology) were analyzed as-received (unmodified) and upon modification as described below. HPLC grade tetrahydrofuran (THF), 4,4'-azobis(4-cyanovaleric acid) (ABCVA), and acetone were used as received from Sigma Aldrich and Fisher Scientific.

### **2.3.2 MWCNT Functionalization with 4,4'-azobis-(4-cyanovaleric acid)**

In a typical experiment, THF (30 mL) was added to a MWCNT type (250 mg) in a round bottom flask (RBF) and tip sonicated (20 kHz, 20 W) for 5 minutes. ABCVA (1.0 g) was dissolved in THF (5 mL) and added to the RBF after the MWCNT suspension cooled to room temperature. The RBF was sealed and purged with nitrogen for 10 minutes, and then heated to 60 °C for 72 hours on a heating mantle. The system was washed via four centrifugation/suspension cycles with THF prior to characterization (this treatment is denoted ABCVA). Control synthesis experiments were repeated for each MWCNT aspect ratio without ABCVA in the RBF (ABCVA control; Figure 2.4).

### **2.3.3 Air Oxidation of MWCNTs**

In a typical experiment, 10 mL of a 50 v/v acetone/deionized (DI) water blend was added to a MWCNT type (250 mg; HAMWCNT or LAMWCNT) in a scintillation vial and tip sonicated for 2 minutes at 20 W. Each system was placed in a furnace oven, heated to 400 °C at a ramp rate of 10 °C/minute, and held at 400 °C for 50 minutes for a total oven time of 1.5 hours. Control experiments were repeated without heating in an oven (0 hr; Figure 2.4).

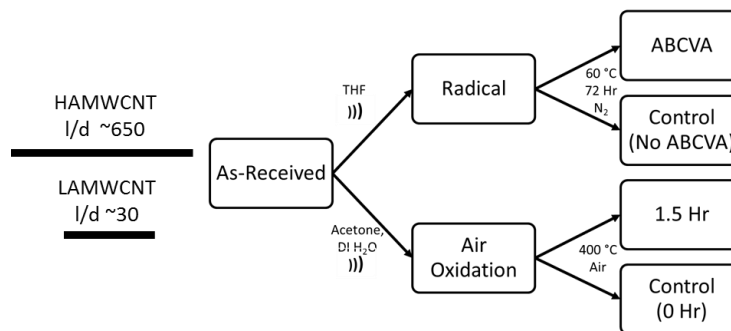


Figure 2.4 Flow chart describing MWCNTs radical and air oxidation treatments.

### 2.3.4 MWCNT Characterization

Raman spectra were collected with a Thermo Scientific DXR Raman microscope equipped with a 532 nm excitation laser through a 10x optical lens (spot size ~ 2  $\mu\text{m}$ ). The detector was set to auto-exposure to achieve a signal to noise ratio greater than 100. Each MWCNT aspect ratio - treatment combination was characterized using 40 separately acquired spectra. Each spectrum was baseline corrected and deconvoluted with each a two, a three, a four, and a five peak protocol using OMNIC for Dispersive Raman 8.2 software. The band positions and literature assignments are listed in Table 2.1 and Figure 2.5. Lorentzian distributions were employed for each peak for all deconvolution protocols except that a Gaussian distribution was used for the D' band when applicable.<sup>75</sup> The properties for each spectrum were calculated singularly and reported as the average of each separately acquired 40 spectra.

Table 2.1

List of band assignments for deconvolution of MWCNT Raman spectra.

Band Assignment	Wavenumber (cm <sup>-1</sup> )	Description
2 Peaks (2PD)		
D	1350	Disorder/defect Band
G	1580	Graphitic band (tangential E <sub>2g</sub> )
3 Peaks (3PD)		
D	1350	Disorder/defect Band
G	1575	Graphitic Band (tangential E <sub>2g</sub> )
D'	1615	E <sub>2g</sub> Disorder Band
4 Peaks (4PD)		
D	1350	Disorder/defect Band
LO	1450	Longitudinal Optical Phonon
G	1575	Graphitic Band (tangential E <sub>2g</sub> )
D'	1615	E <sub>2g</sub> Disorder Band
5 Peaks (5PD)		
D	1350	Disorder/defect Band
LO	1450	Longitudinal Optical Phonon
G(m)	1550	Metallic Band
G(s)	1570	Semiconducting Band
D'	1615	E <sub>2g</sub> Disorder Band

Note: Band assignments were retrieved from literature examples.<sup>75, 104, 107, 121, 145-146</sup>

The onset of thermal degradation (OTD) and thermal degradation (TD) temperatures were determined via thermogravimetric analysis (TGA) in air at a heating rate of 5 °C/minute from ambient to 800 °C in a TA Instruments Q500 thermogravimetric analyzer, following the recommended procedure reported by NIST for SWCNT characterization.<sup>147</sup> Five thermograms were obtained per MWCNT aspect ratio – treatment combination with each analysis having a nominal mass of 3 - 6 mg. All thermograms were normalized to the weight percent at 200 °C following the procedure of Osswald and co-workers, and the OTD and TD were determined according to methods reported by NIST.<sup>75, 147</sup>

X-ray photoelectron spectroscopy (XPS) analyses were performed on a Thermo Scientific K-Alpha X-ray spectrometer at a maximum background pressure of  $2 \times 10^{-9}$  mbar. The X-ray source utilizes an Al anode emitting Al K $\alpha$  X-rays (1486.6 eV) focused into a spot size of 400  $\mu\text{m}$ . Wide survey scans were collected at a pass energy of 200 eV at 1 eV steps and 50 ms dwell time. Narrow scans over the C1s peak of interest were collected with a higher energy resolution of 50 eV pass energy at 0.1 eV steps and 50 ms dwell time. During the analyses, a flood gun was used to counter any charging of the samples, operating at 0.2 V and 150  $\mu\text{A}$  emission current. The collected spectra were analyzed using the Thermo Scientific Advantage processing software and quantified using vendor supplied sensitivity factors (Table 2.2). The quantification is expressed in relative atomic percent with a sensitivity of 0.5 - 1 At %.

Table 2.2

List of peak assignments for deconvolution of MWCNT high-resolution C 1s X-ray photoelectron spectra.

<u>Band Assignment</u>	<u>Binding Energy (eV)</u>
sp <sup>2</sup> hybridized carbon	284.5
sp <sup>3</sup> hybridized carbon	285.4
C-O	286.2
C=O	287.1
O-C-O	288.9
$\pi$ - $\pi^*$ transition	291.2

Note: Band assignments were retrieved from literature examples.<sup>115, 136-144</sup>

### 2.3.5 Statistical Analysis

The Pearson product moment correlation coefficient (PC) was calculated via Minitab 17 software as a quantitative metric to investigate statistical linear correlations between two sets of measurements, e.g., Raman and XPS measurements.<sup>148</sup> Critical PC values corresponding to an  $\alpha = 0.05, 0.10,$  and  $0.20$  were employed for a statistical

correlation at 95%, 90%, and 80% confidence, respectively.<sup>148</sup> Bar graph borders with a solid line (————), dashed line (-----), or double dashed line (— . . —) correspond to statistical correlations at  $\alpha = 0.05$ , 0.10, and 0.20, respectively.

Measurement combinations between two techniques that were not statistically relevant at the employed confidence levels were omitted from the results for clarity.

## **2.4 Results**

### **2.4.1 Deconvolution of MWCNT Raman Spectra with Different Protocols**

Each Raman spectrum was individually deconvoluted into two (2PD), three (3PD), four (4PD), and five peaks (5PD), and the analyses were further refined for quantification of spectral properties using the peak intensity or the peak area for each deconvoluted peak (Table 2.1 and Figure 2.5 show the peak assignments). Literature studies report either the peak intensity or area to calculate the D/G ratio. In this Chapter, ratios and spectrum properties calculated with the peak intensity are designated with an “I” (e.g.,  $I_D/I_G$ ) and the peak area with an “A” (e.g.,  $A_D/A_G$ ). The quality of fit for each deconvolution protocol was quantified via investigation of the curve generated by subtracting the sum of the deconvoluted peaks from the measured spectrum.

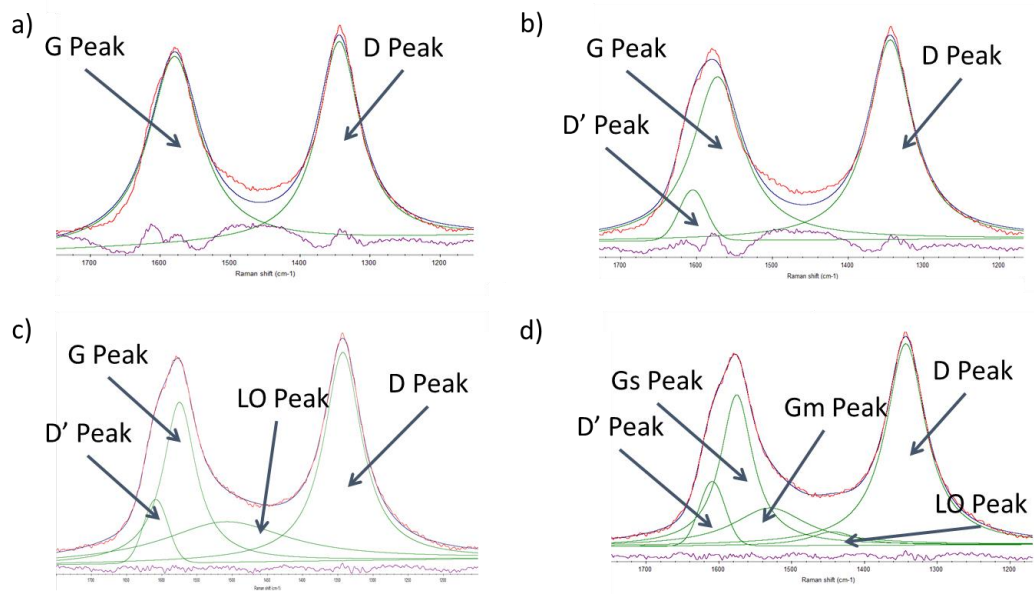


Figure 2.5 Representative deconvolution of first order MWCNT Raman spectra.

Note: employing two peaks (a), three peaks (b), four peaks (c), and five peaks (d).

To quantify the effects of utilizing different deconvolution protocols for first order MWCNT Raman spectra on the ability of the composite spectrum (sum of deconvoluted peaks) to fit the measured spectrum (“quality of fit”), the composite spectrum was subtracted from the measured spectrum between 1150 and 1750  $\text{cm}^{-1}$  and plotted (subtraction curve, purple line Figure 2.5). Positive and negative peaks of the subtraction curve represent the under-estimated and over-estimated composite spectrum, respectively. In general, the average value of the subtraction curve was near zero (less than 0.1% of G peak signal for all MWCNT types), suggesting that each resulting composite spectrum had an average total area close to the measured spectrum employing either 2PD, 3PD, 4PD, and 5PD (Figure 2.6).

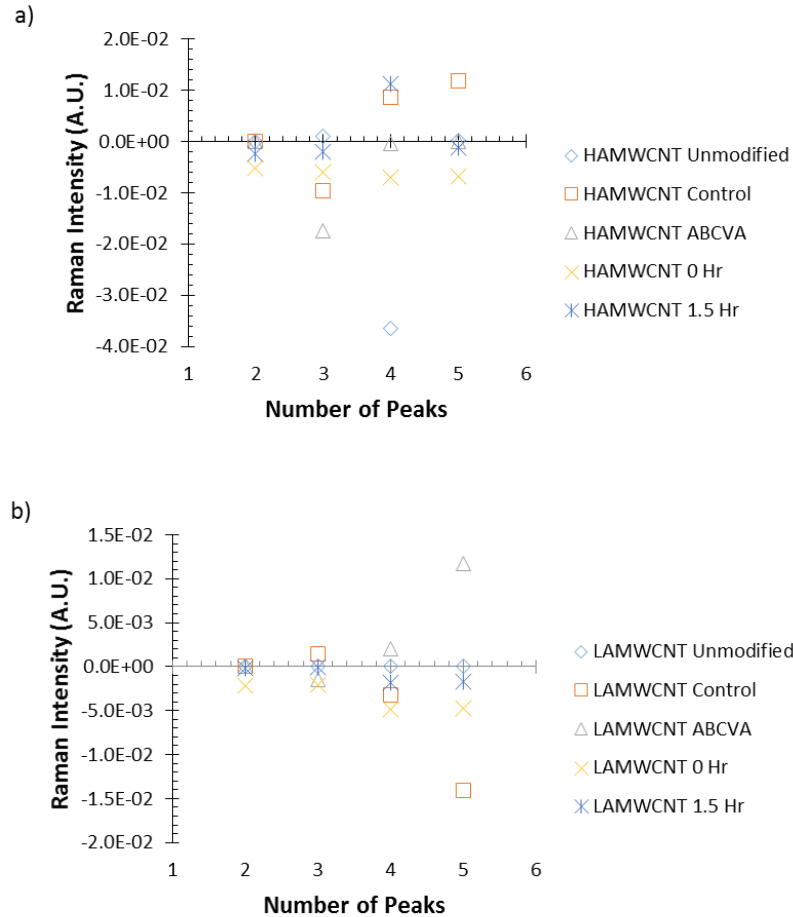


Figure 2.6 Average values of subtraction curve as a function of treatment and number of deconvoluted peaks.

Note: for HAMWCNT (a) and LAMWCNT (b).

The standard deviation of the subtraction curve decreased dramatically as the number of deconvoluted peaks increased; most noticeably from 3PD to 4PD (Figure 2.7). This indicated that employing more than 3PD enabled a better fit of the measured spectrum with the composite spectrum for first order derived MWCNT Raman spectra. Such an observation was expected as increasing the number of deconvolution peaks allowed for more degrees of freedom to adjust the composite spectrum to fit the measured spectrum.

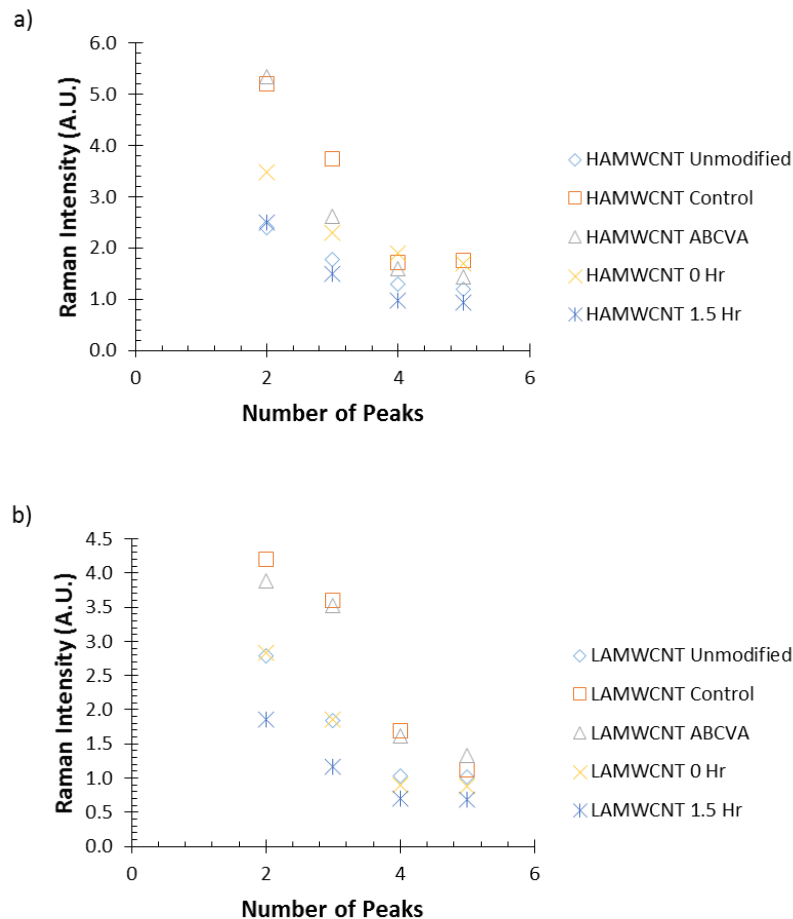


Figure 2.7 Standard deviation of subtraction curve as a function of treatment and number of deconvoluted peaks.

Note: for HAMWCNT (a) and LAMWCNT (b).

A broad peak was observed in all subtraction curves for all MWCNT types for 2PD and 3PD centered at  $\sim 1450 \text{ cm}^{-1}$  (LO phonon), but was accounted for with 4PD or 5PD (Figure 2.8). The amplitude of the subtraction curve reaches a maximum for 2PD where the D' band would be identified and a noticeable peak was observed for some MWCNT types at the peak maximum of the G band (Figure 2.8). This observation demonstrated the inability of 2PD to account for the asymmetric peak shape of the G band due to the presence of the disorder-based D' band, and resulted in a G band blue

shift which suggests increased functionalization.<sup>75</sup> This effect was less noticeable when 3PD is employed, and was effectively negligible for deconvolutions with 4PD and 5PD.

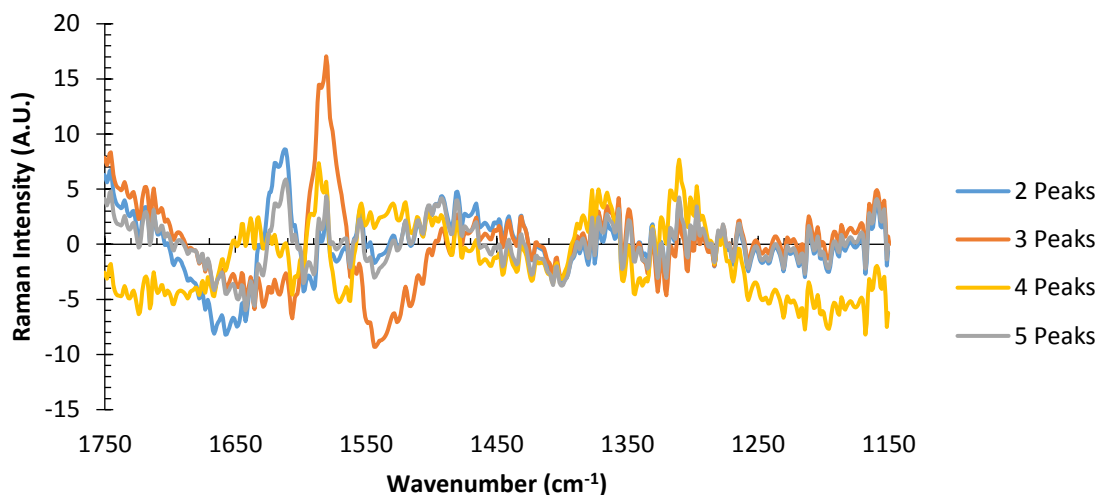


Figure 2.8 Representative subtraction curves of HAMWCNT unmodified sample type as a function of the number of deconvoluted peaks.

Note: The subtraction curves for other MWCNT types and treatments are similar.

Literature opinion is divided as to whether peak area or peak intensity should be used to calculate the D/G ratio. The  $A_D/A_G$  ratio was plotted as a function of the  $I_D/I_G$  ratio and the Pearson product moment correlation coefficient (PC) was calculated to determine the statistical significance of their relationship (Figure 2.9). The area/intensity of the D' band was omitted from the G band for calculations above 2PD as it has been most often attributed to defects and has not been traditionally included in literature calculations. The calculated PCs indicated that the area and intensity based D/G calculations (2PD-5PD) were statistically correlated with a 95% confidence ( $\alpha = 0.05$ ) for both HAMWCNT and LAMWCNT, except for LAMWCNT 3PD (not statistically relevant) and 5PD ( $\alpha = 0.10$ ) (Figure 2.9). However, a linear trendline slope less than one for all deconvolution protocols indicated that the  $A_D/A_G$  value was lower than the

corresponding  $I_D/I_G$  value, and emphasized the lack of interchangeability between area and intensity for various deconvolution parameters of MWCNT Raman spectra, and does not favor either spectral property for calculating the D/G ratio nor for direct substitution into empirical formulas (e.g., purity, crystal size estimation, defect density, perfect fringe length).<sup>64, 73-76</sup>

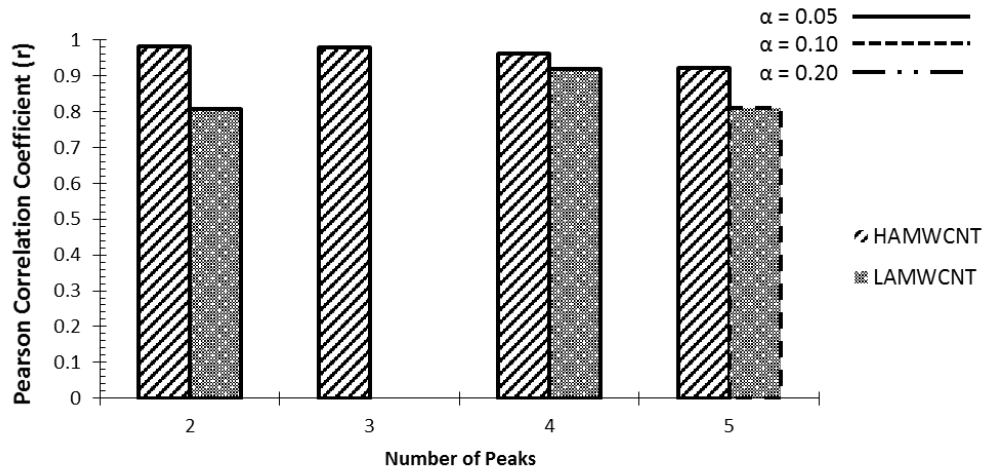


Figure 2.9 Pearson product moment correlation coefficients for area and intensity based calculations of the D/G ratio as a function of the number of deconvoluted peaks.

Note: Only the correlations that were statistically significant are shown in the figure.

Similarly, the area and intensity based D'/G ratios for both HAMWCNT and LAMWCNT were determined to be statistically correlated ( $\alpha = 0.05$ ) for all deconvolution protocols except HAMWCNT 5PD (Figure 2.10).

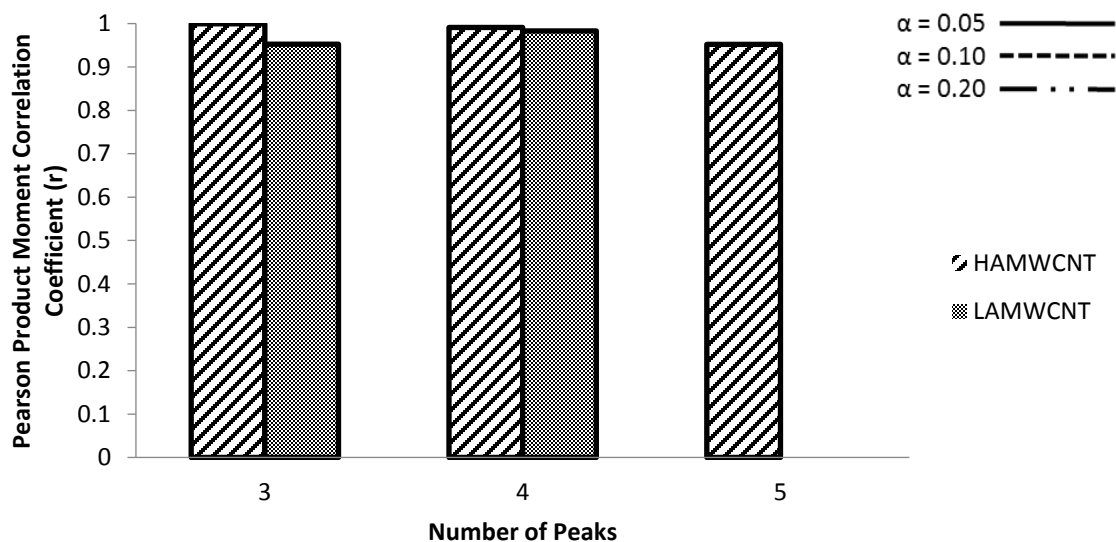
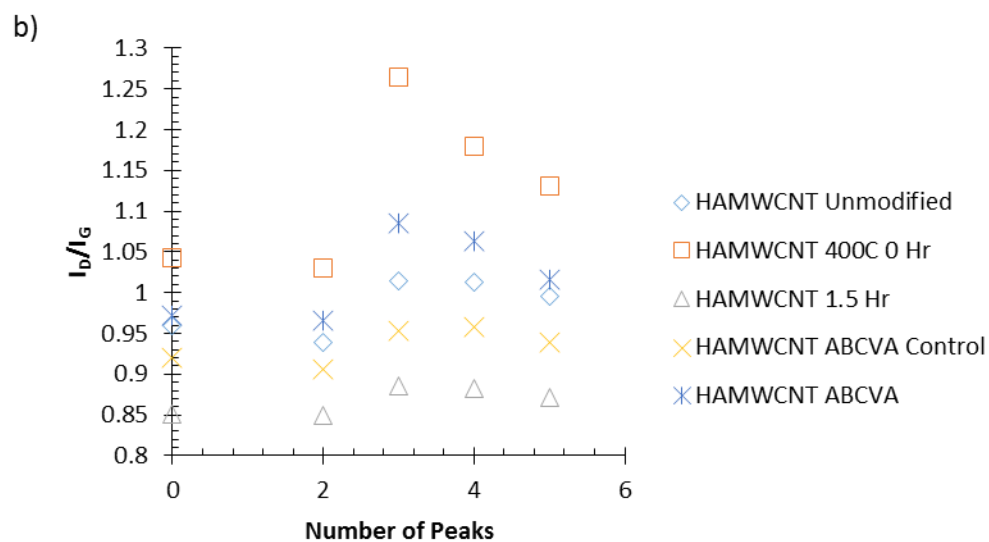
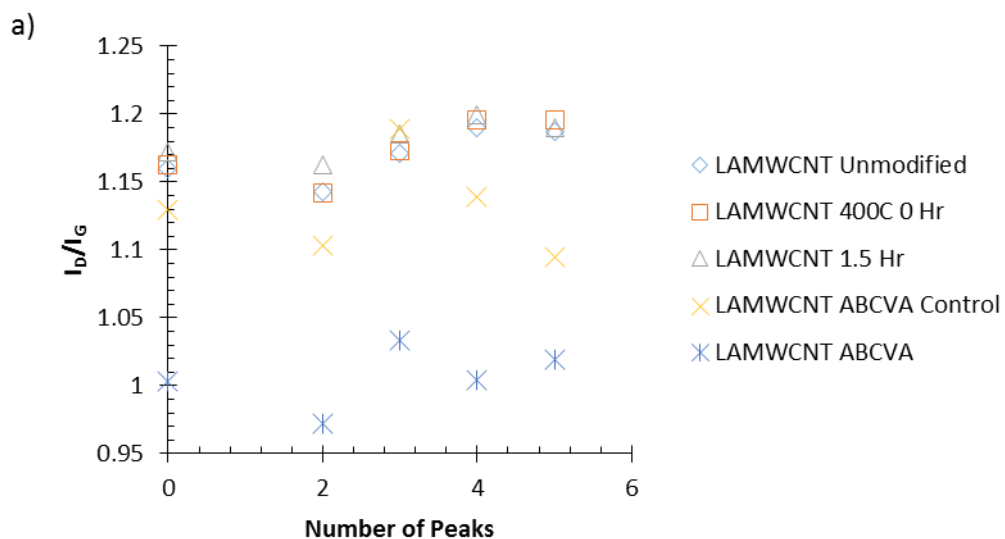


Figure 2.10 Pearson product moment correlation coefficients for area and intensity based calculations of the D<sup>7</sup>/G ratio as a function of employed deconvoluted peaks.

Note: Only the correlations that were statistically significant are shown in the figure.

To investigate the effects of employing various Raman spectrum deconvolution protocols on the reported values and MWCNT molecular structure interpretation, the D/G values were plotted as a function of the number of deconvoluted peaks. It was determined that employing the area or the intensity for the D/G ratio calculation each resulted in a different interpretation of the MWCNT molecular structure for a given treatment, however, this was observed for only the LAMWCNT and not HAMWCNT (Figures 2.11 a-d). This may be attributed to the lower confidence in the linear relationship of the area-based calculations compared to the intensity-based calculations for 3PD and 5PD (Figure 2.9). In the most extreme case, the LAMWCNT  $A_D/A_G$  values (Figure 2.11c) indicated that the ABCVA treatment increased the MWCNT crystallite size for all deconvolution types except 5PD; such an observation was unexpected as radical functionalization of MWCNT has been shown to increase molecular disorder and

therefore increase the D/G ratio.<sup>149</sup> However, an inversion in the molecular structure interpretation for the LAMWCNT ABCVA  $A_D/A_G$  value was determined increasing the number of peaks from four to five (i.e., LAMWCNT ABCVA > LAMWCNT ABCVA control), which was the expected observation.



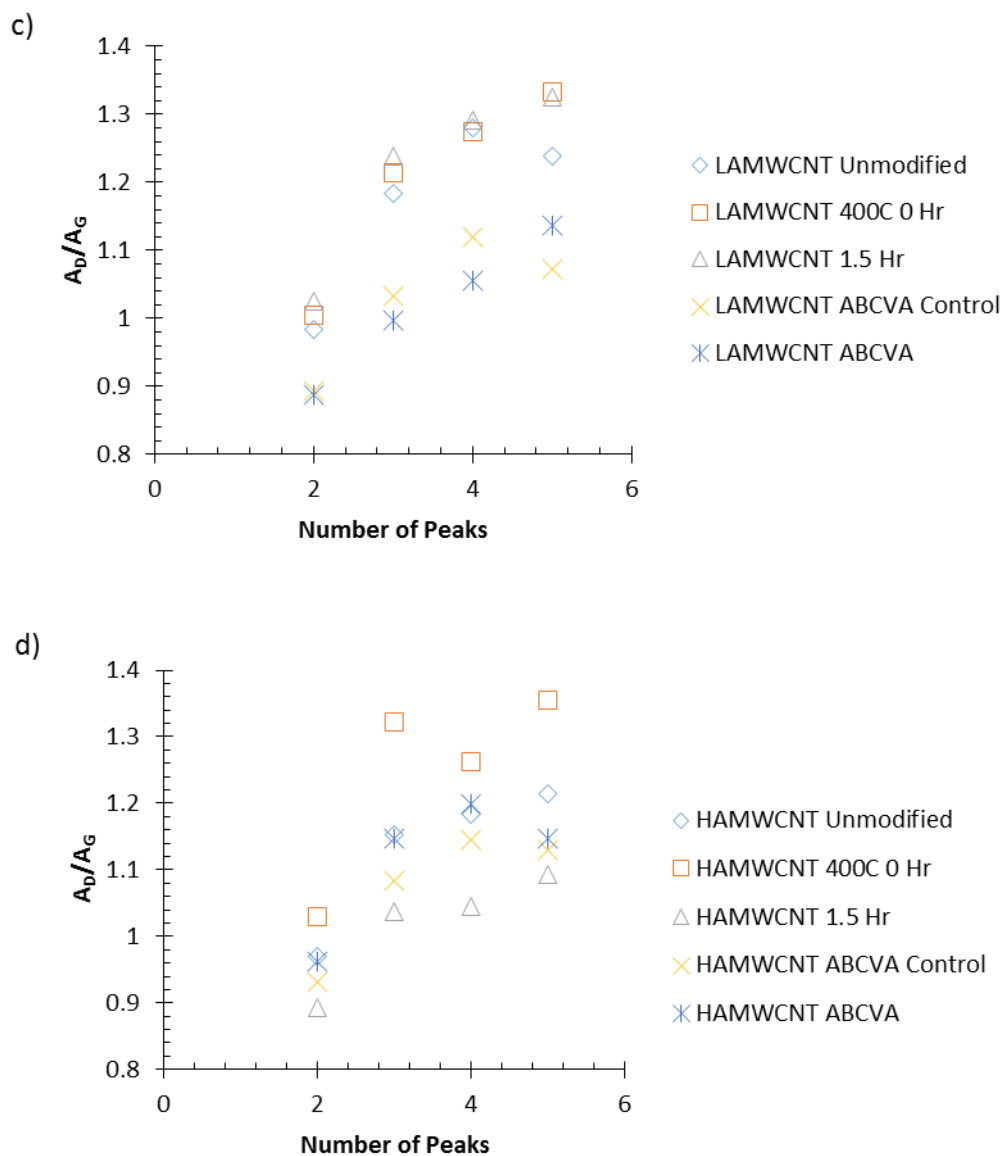
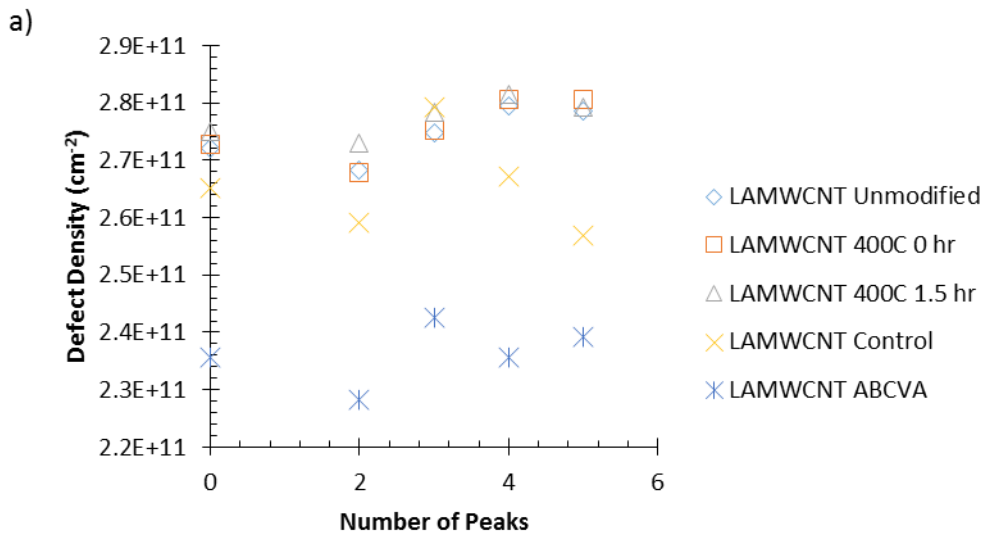


Figure 2.11 Peak intensity and area based D/G ratio calculations as a function of the number of deconvoluted peaks for first order Raman spectra.

Note: peak intensity for LAMWCNT (a) and HAMWCNT (b) and the peak area for LAMWCNT (c) and HAMWCNT (d).

Employing the intensity based  $I_D/I_G$  resulted in a drastically different interpretation, i.e., the  $I_D/I_G$  value of the LAMWCNT ABCVA sample was lower than both the unmodified and ABCVA control LAMWCNT samples for all deconvolution types, suggesting a higher degree of crystallinity. The  $I_D/I_G$  values indicated that the

LAMWCNT ABCVA control sample was more disordered than the unmodified sample employing a 3PD, but more ordered utilizing all other deconvolution protocols (Figure 2.11a). A similar inversion of molecular structure interpretation was observed employing  $A_D/A_G$  for the LAMWCNT ABCVA control and LAMWCNT ABCVA samples between 4PD and 5PD (Figure 2.11c). As the D/G ratio has been commonly substituted directly into the defect density calculation,<sup>76</sup> the differences observed with the D/G ratios were also noted in the estimated defect density for each MWCNT aspect ratio - treatment combination (Figure 2.12). However, inversion points were observed between different deconvolution protocols indicating that MWCNT molecular structure interpretation employing a different number of deconvoluted peaks can vary and is not equivalent for all MWCNT aspect ratios or treatments.



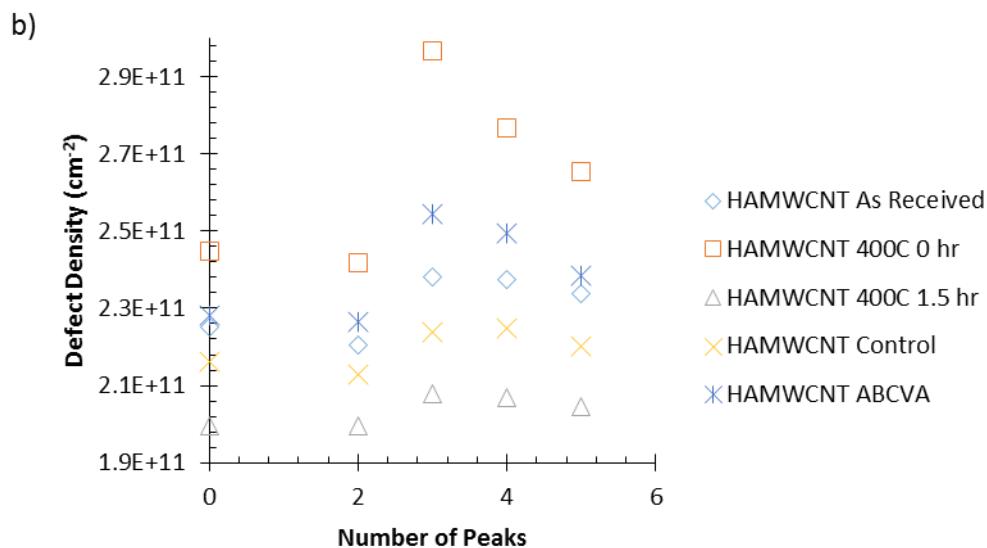


Figure 2.12 Calculated defect density as a function of the number of deconvoluted peaks.

Note: The defect density calculated according to Caçado and co-workers; for LAMWCNT (a) and HAMWCNT (b).<sup>76</sup>

MWCNT molecular structure interpretation via the D'/G ratio had similar observations as the D/G ratio, i.e., multiple inversion points of the molecular structure as a function of the number of deconvoluted peaks for a given protocol (Figure 2.13). Although the inversion points observed for the D'/G ratios were not identical to those observed for the D/G ratios, these two calculated spectral properties were determined to be statistically correlated ( $\alpha = 0.05$ ) for a specific deconvolution protocol and area/intensity based calculation, except for LAMWCNT 5PD (see Appendix A, Figures A.1 and A.2).

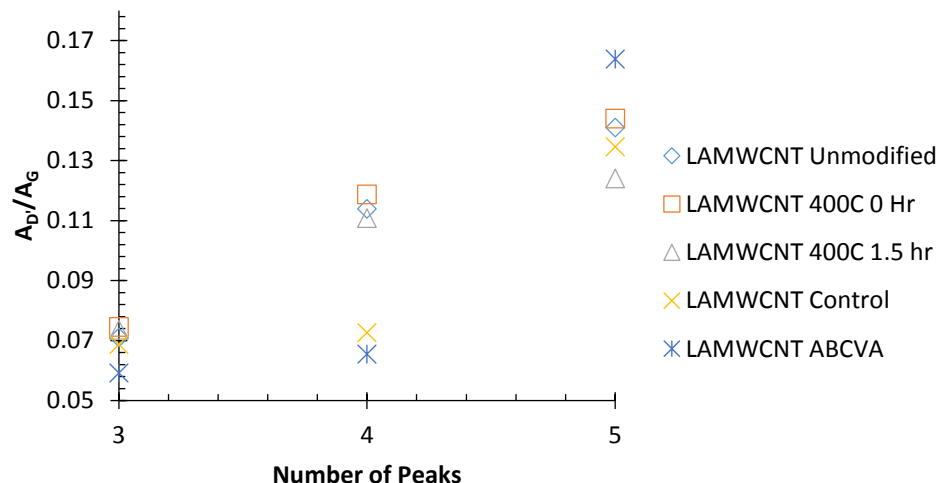


Figure 2.13 Area based D'/G values for LAMWCNT as a function of the number of deconvoluted peaks.

Note: other MWCNT-treatment combinations in Appendix A, Figures A.3-A.4.

From these investigations, it is clear that employing different deconvolution protocols singularly (i.e., number of peaks for deconvolution, peak area, peak intensity) for first order MWCNT Raman spectra altered the reported D/G and D'/G values. Furthermore, the results are potentially misleading for MWCNT molecular structure interpretations based upon these calculated values alone. Therefore, the next logical step of this investigation was to establish a deconvolution protocol most representative of MWCNT molecular structures by establishing statistical correlations with additional analytical techniques.

#### 2.4.2 Correlating MWCNT Raman Spectra, Thermal Degradation, and XPS

The primary purpose of this research was to establish a Raman spectral deconvolution protocol representative of the MWCNT molecular structure with high confidence. The rationale was that if Raman spectral properties generated from a specific deconvolution protocol of HAMWCNT and LAMWCNT correlated statistically with a

complementary technique utilized to investigate MWCNT molecular structure (e.g., TGA or XPS measurements), it would impart a high degree of confidence in that specific deconvolution protocol for investigating MWCNT molecular structure changes. Thus, in this investigation, Raman spectroscopy would correlate with TGA, TGA with XPS, and XPS with Raman spectroscopy to establish a more standardized Raman deconvolution protocol for MWCNT molecular structure interpretation. Further complications arise as Raman spectra can be generated from more than 20 graphene layers,<sup>146</sup> thus, most or all of the MWCNT walls can be probed by Raman spectroscopy depending on the number of walls.

As MWCNT oxidation properties have been demonstrated to be partially dependent on the properties of the outer wall, the OTD is expected to decrease with increasing D/G ratio due to increased disorder in the MWCNT molecular structure (which decreases the thermal stability).<sup>108, 150</sup> In general, spectral properties calculated with either the peak area or intensity for both MWCNT aspect ratios singularly did not statistically correlate with the OTD or TD temperatures for any deconvolution protocols employing  $\alpha = 0.05$  or  $\alpha = 0.10$  (Figure 2.14; Appendix A, Figures A.5-A.9 for other deconvolution protocols). This suggests that Raman spectroscopy and/or TGA cannot be employed singularly to universally monitor changes in the molecular structure of MWCNTs induced via chemical modification. However, it has been noted that the presence/intensity of the D band does not necessarily imply disorder in MWCNTs, and that OTD measurements may be confounded by burning/oxidation of contaminants or amorphous carbon.<sup>119</sup> Alternatively, the LO/G and LO/D' (4PD) intensity based calculations both statistically correlated with the TD for HAMWCNT and LAMWCNT

types, albeit at a low confidence level ( $\alpha = 0.20$ ). A positive PC suggests that the LO phonon is related to the degree of crystallinity because the ratio increases with the degradation temperature. Additionally, the  $I_{D'}/I_G$  ratio (4PD) of the LAMWCNT correlated with the OTD and TD properties ( $\alpha = 0.20$ ). A negative PC for this correlation signifies that the disorder based  $D'/G$  ratio increases as the degradation temperature decreases, as would be expected.

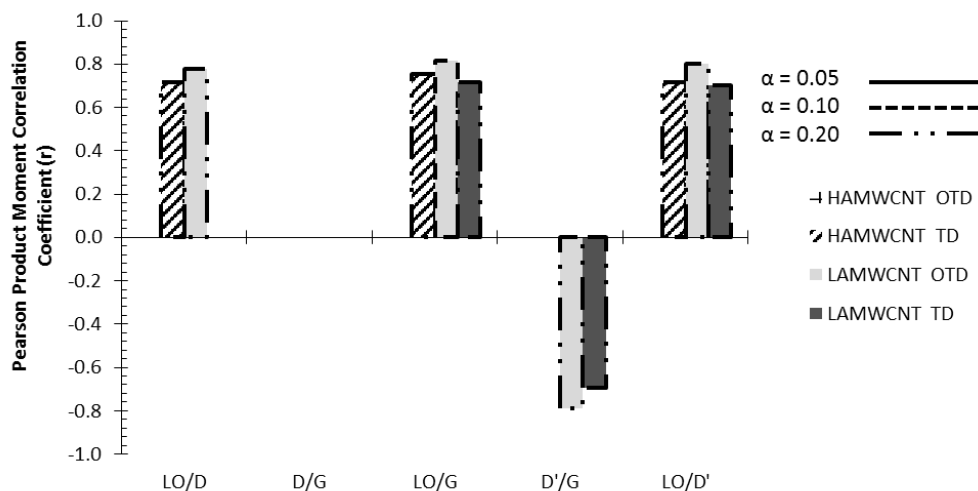


Figure 2.14 Pearson product moment correlation coefficient between Raman spectral properties and thermal degradation properties.

Note: calculated via peak intensity (four peak deconvolution).

The high resolution C 1s spectrum of each MWCNT aspect ratio - treatment combination was deconvoluted employing six peaks (Table 2.2 and Figure 2.15 for representative XPS C 1s deconvolution<sup>115, 136-140, 142</sup>). Statistical correlations at  $\alpha = 0.05$  determined singularly for LAMWCNT and HAMWCNT for various Raman spectral calculations and XPS indicated that a deeper investigation into each MWCNT type was required for determining MWCNT molecular structure information (Figure 2.16).

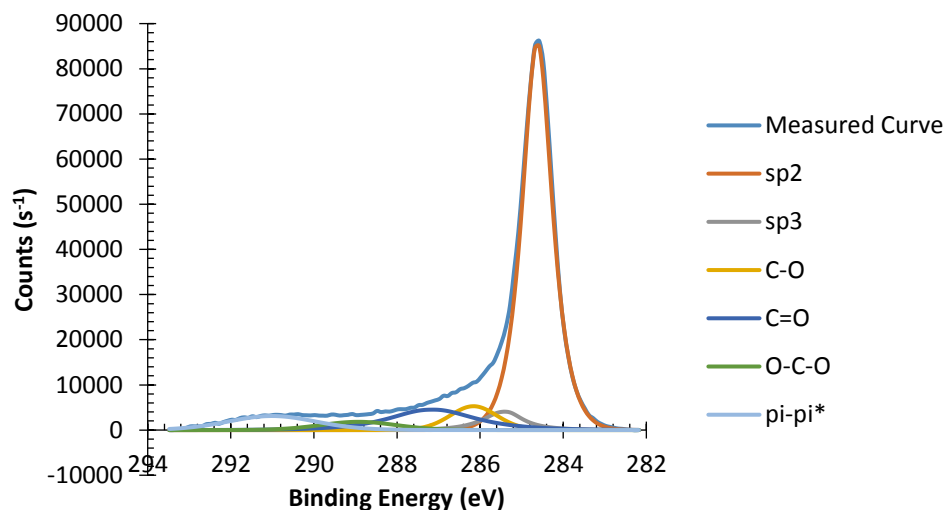


Figure 2.15 Representative deconvolution of MWCNT X-ray photoelectron spectra.

Note. Deconvolution protocol was determined by Dr. Steven Trigwell at NASA Kennedy Space Center.<sup>115,136-144</sup>

The  $I_D/I_G$  ratios for both MWCNT types calculated via spectrum intensity, 2PD, 3PD, and 4PD correlated with the C=O/sp<sup>2</sup> ratio XPS data ( $\alpha = 0.20$ , see Appendix A, Figures A.10-A.18 for other deconvolution protocols). Such a correlation would be expected as both the chemical treatments employed in this study increase the carbonyl content with increasing degree of functionalization (disorder of the MWCNT molecular structure). Additionally,  $A_{D'}/A_G$  (3PD and 5PD),  $I_{D'}/I_G$  (3PD),  $A_{LO}/A_D$  (5PD),  $A_{LO}/A_G$  (5PD),  $A_{LO}/A_{D'}$  (5PD),  $A_D/A_{D'}$  (5PD), and  $I_D/I_{D'}$  (5PD) statistically correlated with C=O/sp<sup>2</sup> for both MWCNT types.

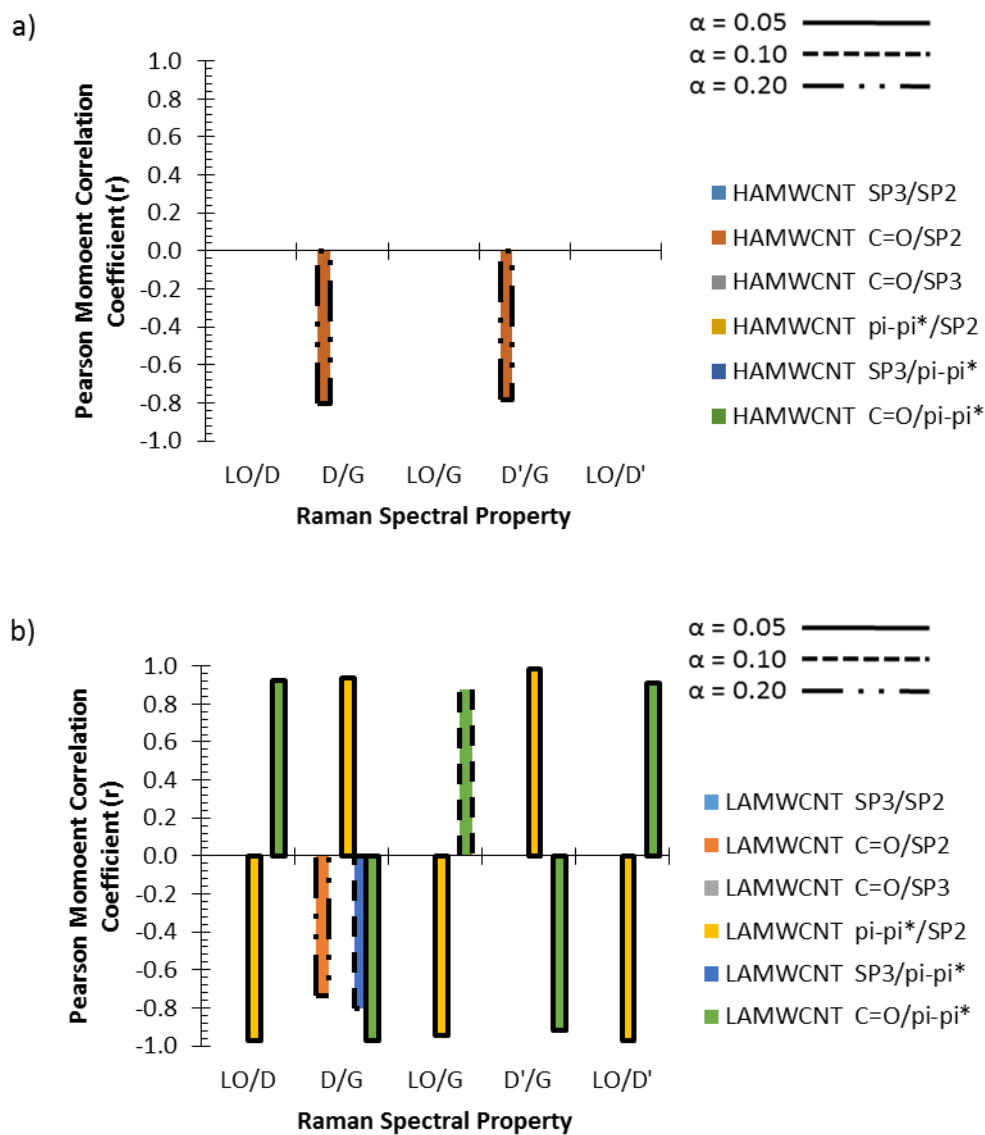


Figure 2.16 Pearson product moment correlation coefficient between Raman spectral properties and XPS.

Note: calculated via peak intensity (four peak deconvolution); for HAMWCNT (a) and LAMWCNT (b).

To establish the most relevant deconvolution protocol for Raman spectroscopy and determine the most accurate representation of the MWCNT molecular structure, all three analytical techniques should have strong statistical correlations. It was established above that employing a four peak deconvolution protocol for Raman spectra was most

representative of MWCNT molecular structure as the deconvolution protocol was the only protocol to yield statistical correlations with both XPS and TGA, singularly, for both MWCNT types (see Figure 2.16,  $\alpha = 0.20$ ). More specifically, statistical correlations between the OTD/TD and  $I_D/I_G$  (4PD),  $I_D/I_G$  (4PD) and  $\pi-\pi^*/sp^2$ , and OTD/TD and  $\pi-\pi^*/sp^2$  were observed for LAMWCNT. Although statistical correlations were determined between TGA and XPS, no statistical correlations were observed for a set of properties that corresponded to both MWCNT types in combination (Figure 2.17) indicating that universal interpretation of data from these instruments was not observed and directly interpreting these data singularly may provide misleading molecular structure information/interpretation.

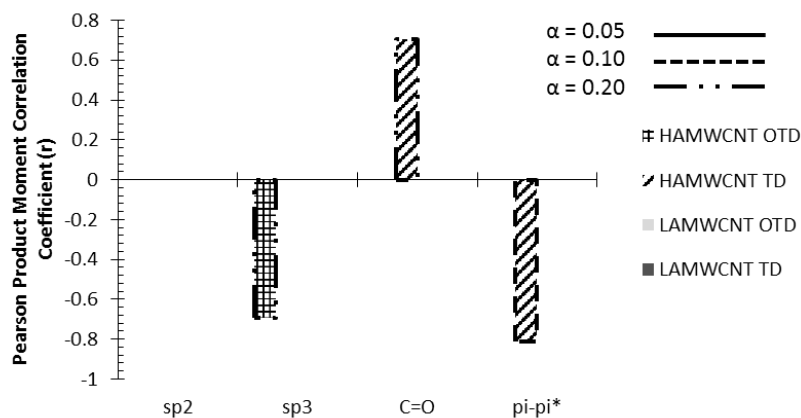


Figure 2.17 Pearson product moment correlation coefficient between X-ray photoelectron spectroscopy and thermal degradation properties.

## 2.5 Discussion

Raman spectroscopy has been the most common MWCNT spectroscopic method utilized to qualify, quantify, and correlate MWCNT purity and molecular changes. The goals of this Chapter were to simplify characterization and gain understanding reproducibly and directly by quantifying a variety of Raman spectral properties from

different deconvolution parameters. Regardless of the attempts here and methods developed, the results validated that the literature method and characterization protocols consistently are questionable and confirm that the simplified, i.e., oversimplified, approaches result in misleading data/understanding for structural feature changes in MWCNTs. It was noted that the D/G ratio calculations employing peak heights or area can vary dramatically from one deconvolution protocol to the next. This was surprising as the D/G ratio is very simplistically approached in literature as a valid and direct method to extensively track molecular changes in the MWCNT structure from annealing (decrease in D/G) or chemical modification (increase in D/G), and purported to relate directly to higher and lower molecular order, respectively. Thus, great care must be taken prior to directly substituting the D/G ratio into an empirical formula and subsequent molecular structure interpretation.

Generally, statistical correlations between Raman spectroscopy and TGA or XPS were not detected above a confidence level of 80% for both the MWCNT aspect ratios evaluated in this study, indicating that these techniques cannot be simply and universally employed to confirm changes in the molecular structure of MWCNTs. Furthermore, the  $I_D/I_G$  of the high aspect ratio MWCNT (4PD) statistically correlated with an XPS property that correlated with the degradation properties, even though the  $I_D/I_G$  ratio did not directly correlate with the degradation properties. Specifically, it was observed that employing various deconvolution protocols can have a dramatic effect on the interpretation of MWCNT molecular structure, indicating the importance of determining correlations with supplemental analytical techniques for employment of the proper deconvolution protocol. This may be attributed to the low statistical confidence in using

spectral properties generated from a given deconvolution protocol interchangeably.

However, a four peak deconvolution protocol statistically correlated ( $\alpha = 0.20$ ) with both TGA and XPS for both MWCNT aspect ratios providing higher confidence in employing a 4PD protocol for the first order Raman spectra.

The LAMWCNT type was determined to have better statistical correlations with complementary analytical techniques and at higher confidence levels compared to the HAMWCNT type, confirming the premise that Raman spectroscopy cannot be universally and simply employed for MWCNTs. The working hypothesis is that the varying length(s), number of layers, and defect types/concentrations result in such complexities for MWCNTs that Raman spectroscopy results are consistently unpredictable, and therefore are unreliable as a universally applied characterization tool to investigate changes in MWCNT molecular structure alone. Further characterization of a broader range of carbon nanomaterials, e.g., single wall carbon nanotubes, graphene sheets, and MWCNTs of various diameters and lengths, before and after modification is required to derive a standardized protocol for proper investigation of carbon nanomaterials via Raman spectroscopy.

## **2.6 Conclusions**

The results presented in this Chapter verified that the most common and simplified literature approach to quantify MWCNT structure and modifications to the structure are misleading when based solely upon the Raman D/G ratios. The D/G ratio did not reveal direct and/or consistent structural information even though these have been traditionally the primary characterization methods. The data presented herein verified the absence of consistent statistical correlations with TGA and XPS measurements for both

MWCNT aspect ratios. However, the results support a four peak deconvolution protocol that consistently provided the most reliable information regarding changes of the MWCNT molecular structure of the treatments employed in this study. Specifically, the  $I_D/I_G$  calculated from a four peak deconvolution protocol exhibited the most reliable MWCNT molecular structural detection as verified via statistical correlation with supplemental analytical techniques. Understanding the molecular basis for why the various methods result in such dramatic Raman ratio differences would provide a key insight and understanding of the source and meaning for compositional differences between MWCNTs from a variety of modifications, whether the modifications are thermal, chemical, or mechanical in origin.

## 2.7 References

35. Burghard, M., Electronic and Vibrational Properties of Chemically Modified Single-Wall Carbon Nanotubes. *Surface Science Reports* **2005**, *58* (1–4), 1-109.
45. Bose, S.; Khare, R. A.; Moldenaers, P., Assessing the Strengths and Weaknesses of Various Types of Pre-Treatments of Carbon Nanotubes on the Properties of Polymer/Carbon Nanotubes Composites: A Critical Review. *Polymer* **2010**, *51* (5), 975-993.
53. Grossiord, N.; Loos, J.; Regev, O.; Koning, C. E., Toolbox for Dispersing Carbon Nanotubes into Polymers to Get Conductive Nanocomposites. *Chemistry of Materials* **2006**, *18* (5), 1089-1099.
54. Leonard, F., *Physics of Carbon Nanotube Devices*. William Andrew: 2009.
60. Bonard, J.-M., Carbon Nanostructures by Hot Filament Chemical Vapor Deposition: Growth, Properties, Applications. *Thin Solid Films* **2006**, *501*, 8-14.
61. Hernadi, K.; Ljubović, E.; Seo, J. W.; Forró, L., Synthesis of Mwnt-Based Composite Materials with Inorganic Coating. *Acta Materialia* **2003**, *51* (5), 1447-1452.
62. Ryan, K. P.; Cadek, M.; Nicolosi, V.; Walker, S.; Ruether, M.; Fonseca, A.; Nagy, J. B.; Blau, W. J.; Coleman, J. N., Multiwalled Carbon Nanotube Nucleated Crystallization and Reinforcement in Poly (Vinyl Alcohol) Composites. *Synthetic Metals* **2006**, *156* (2-4), 332-335.
63. Kim, Y. A.; Kakegawa, H.; Fujisawa, K.; Shimamoto, D.; Muramatsu, H.; Kim, J. H.; Jung, Y. C.; Hayashi, T.; Endo, M.; Terrones, M.; Dresselhaus, M. S., Sensitive G-Band Raman Features for the Electrical Conductivity of Multi-Walled Carbon Nanotubes. *Journal Nanoscience Nanotechnology* **2010**, *10*, 3940-3944.
64. DiLeo, R. A.; Landi, B. J.; Raffaele, R. P., Purity Assessment of Multiwalled Carbon Nanotubes by Raman Spectroscopy. *Journal of Applied Physics* **2007**, *101* (6), 064307.
65. Dresselhaus, M. S.; Dresselhaus, G.; Saito, R.; Jorio, A., Raman Spectroscopy of Carbon Nanotubes. *Physics Reports* **2005**, *409* (2), 47-99.
66. Dresselhaus, M. S.; Jorio, A.; Saito, R., Characterizing Graphene, Graphite, and Carbon Nanotubes by Raman Spectroscopy. *Annual Review of Condensed Matter Physics* **2010**, *1* (1), 89-108.
67. Grady, B. P., *Carbon Nanotube-Polymer Composites Manufacture, Properties, and Applications*. Wiley: Hoboken, N.J., 2011; p 352.
68. Saito, R.; Dresselhaus, G.; Dresselhaus, M. S., *Physical Properties of Carbon Nanotubes*. Imperial College Press: London, 1998; p 259.
69. Singh, L. T.; Nanda, K. K., General Theories for the Electrical Transport Properties of Carbon Nanotubes. *Nanotechnology* **2011**, *22* (31), 315705.
70. Lehman, J. H.; Terrones, M.; Mansfield, E.; Hurst, K. E.; Meunier, V., Evaluating the Characteristics of Multiwall Carbon Nanotubes. *Carbon* **2011**, *49* (8), 2581-2602.
71. Dresselhaus, M. S.; Jorio, A.; Souza Filho, A. G.; Saito, R., Defect Characterization in Graphene and Carbon Nanotubes Using Raman Spectroscopy. *Philosophical Transactions of the Royal Society A: Mathematical, Physical and Engineering Sciences* **2010**, *368* (1932), 5355-5377.

72. Chakrapani, N.; Curran, S.; Wei, B.; Ajayan, P. M.; Carrillo, A.; Kane, R. S., Spectral Fingerprinting of Structural Defects in Plasma-Treated Carbon Nanotubes. *Journal of Materials Research* **2011**, *18* (10), 2515-2521.
73. Tuinstra, F.; Koenig, J. L., Raman Spectrum of Graphite. *The Journal of Chemical Physics* **1970**, *53* (3), 1126-1130.
74. Tuinstra, F.; Koenig, J. L., Characterization of Graphite Fiber Surfaces with Raman Spectroscopy. *Journal of Composite Materials* **1970**, *4*, 492-9.
75. Osswald, S.; Havel, M.; Gogotsi, Y., Monitoring Oxidation of Multiwalled Carbon Nanotubes by Raman Spectroscopy. *Journal of Raman Spectroscopy* **2007**, *38* (6), 728-736.
76. Cançado, L. G.; Takai, K.; Enoki, T.; Endo, M.; Kim, Y. A.; Mizusaki, H.; Jorio, A.; Coelho, L. N.; Magalhaes-Paniago, R.; Pimenta, M. A., General Equation for the Determination of the Crystallite Size  $L_{[Sub a]}$  of Nanographite by Raman Spectroscopy. *Applied Physics Letters* **2006**, *88* (16), 163106-3.
77. Singh, C.; Srivastava, S.; Ali, M. A.; Gupta, T. K.; Sumana, G.; Srivastava, A.; Mathur, R. B.; Malhotra, B. D., Carboxylated Multiwalled Carbon Nanotubes Based Biosensor for Aflatoxin Detection. *Sensors and Actuators B: Chemical* **2013**, *185* (0), 258-264.
78. Wang, Y.-H.; Chang, C.-M.; Liu, Y.-L., Benzoxazine-Functionalized Multi-Walled Carbon Nanotubes for Preparation of Electrically-Conductive Polybenzoxazines. *Polymer* **2012**, *53* (1), 106-112.
79. Chen, X.; Zhou, M.; Hou, Q.; Tu, X.; Wu, X., Active Poly(4-Chloromethyl Styrene)-Functionalized Multiwalled Carbon Nanotubes. *Macromolecular Chemistry and Physics* **2013**, *214* (16), 1829-1835.
80. Pelalak, R.; Baniadam, M.; Maghrebi, M., Controllable Purification, Cutting and Unzipping of Multi-Walled Carbon Nanotubes with a Microwave Method. *Applied Physics A* **2013**, *111* (3), 951-957.
81. Donato, M. G.; Messina, G.; Santangelo, S.; Galvagno, S.; Milone, C.; Pistone, A., Aid of Raman Spectroscopy in Diagnostics of Mwcnt Synthesised by Fe-Catalysed Cvd. *Journal of Physics: Conference Series* **2007**, *61*, 931-935.
82. Lefrant, S.; Buisson, J. P.; Schreiber, J.; Chauvet, O.; Baibarac, M.; Baltog, I., Raman Studies of Carbon Nanotubes and Polymer Nanotube Composites. *Molecular Crystals and Liquid Crystals* **2004**, *415* (1), 125-132.
83. Mkhabela, V. J.; Mishra, A. K.; Mbianda, X. Y., Thermal and Mechanical Properties of Phosphorylated Multiwalled Carbon Nanotube/Polyvinyl Chloride Composites. *Carbon* **2011**, *49* (2), 610-617.
84. Kar, P.; Choudhury, A., Carboxylic Acid Functionalized Multi-Walled Carbon Nanotube Doped Polyaniline for Chloroform Sensors. *Sensors and Actuators B: Chemical* **2013**, *183* (0), 25-33.
85. Pumera, M.; míd, B.; etislav; Veltruská, K.; ina, Influence of Nitric Acid Treatment of Carbon Nanotubes on Their Physico-Chemical Properties. *Journal of Nanoscience and Nanotechnology* **2009**, *9* (4), 2671-2676.
86. Wepasnick, K. A.; Smith, B. A.; Schrote, K. E.; Wilson, H. K.; Diegelmann, S. R.; Fairbrother, D. H., Surface and Structural Characterization of Multi-Walled Carbon Nanotubes Following Different Oxidative Treatments. *Carbon* **2011**, *49* (1), 24-36.

87. Bokova, S. N.; Obraztsova, E. D.; Grebenyukov, V. V.; Elumeeva, K. V.; Ishchenko, A. V.; Kuznetsov, V. L., Raman Diagnostics of Multi-Wall Carbon Nanotubes with a Small Wall Number. *physica status solidi (b)* **2010**, *247* (11-12), 2827-2830.
88. Awasthi, K.; Kumar, R.; Tiwari, R. S.; Srivastava, O. N., Large Scale Synthesis of Bundles of Aligned Carbon Nanotubes Using a Natural Precursor: Turpentine Oil. *Journal of Experimental Nanoscience* **2010**, *5* (6), 498-508.
89. Lachman, N.; Sui, X.; Bendikov, T.; Cohen, H.; Wagner, H. D., Electronic and Mechanical Degradation of Oxidized Cnts. *Carbon* **2012**, *50* (5), 1734-1739.
90. Ling, X.; Wei, Y.; Zou, L.; Xu, S., The Effect of Different Order of Purification Treatments on the Purity of Multiwalled Carbon Nanotubes. *Applied Surface Science* **2013**, *276* (0), 159-166.
91. Chang, C.-M.; Liu, Y.-L., Functionalization of Multi-Walled Carbon Nanotubes with Furan and Maleimide Compounds through Diels–Alder Cycloaddition. *Carbon* **2009**, *47* (13), 3041-3049.
92. Zhao, Z.; Yang, Z.; Hu, Y.; Li, J.; Fan, X., Multiple Functionalization of Multi-Walled Carbon Nanotubes with Carboxyl and Amino Groups. *Applied Surface Science* **2013**, *276* (0), 476-481.
93. Hussain, S.; Shah, K.; Islam, S. S., Investigation of Effects Produced by Chemical Functionalization in Single-Walled and Multi-Walled Carbon Nanotubes Using Raman Spectroscopy. *Materials Science-Poland* **2013**, *31* (2), 276-280.
94. Amiri, A.; Memarpoor-Yazdi, M.; Shanbedi, M.; Eshghi, H., Influence of Different Amino Acid Groups on the Free Radical Scavenging Capability of Multi Walled Carbon Nanotubes. *Journal of Biomedical Materials Research Part A* **2013**, *101A* (8), 2219-2228.
95. Ran, M.; Sun, W.; Liu, Y.; Chu, W.; Jiang, C., Functionalization of Multi-Walled Carbon Nanotubes Using Water-Assisted Chemical Vapor Deposition. *Journal of Solid State Chemistry* **2013**, *197* (0), 517-522.
96. Farbod, M.; Tadavani, S. K.; Kiasat, A., Surface Oxidation and Effect of Electric Field on Dispersion and Colloids Stability of Multiwalled Carbon Nanotubes. *Colloids and Surfaces A: Physicochemical and Engineering Aspects* **2011**, *384* (1–3), 685-690.
97. Luo, Z.; Cai, X.; Hong, R. Y.; Li, J. H.; Wei, D. G.; Luo, G. H.; Li, H. Z., Surface Modification of Multiwalled Carbon Nanotubes Via Gliding Arc Plasma for the Reinforcement of Polypropylene. *Journal of Applied Polymer Science* **2013**, *127* (6), 4756-4763.
98. Qian, W.; Liu, T.; Wei, F.; Yuan, H., Quantitative Raman Characterization of the Mixed Samples of the Single and Multi-Wall Carbon Nanotubes. *Carbon* **2003**, *41* (9), 1851-1854.
99. Vix-Guterl, C.; Couzi, M.; Dentzer, J.; Trinquocoste, M.; Delhaes, P., Surface Characterizations of Carbon Multiwall Nanotubes: Comparison between Surface Active Sites and Raman Spectroscopy. *The Journal of Physical Chemistry B* **2004**, *108* (50), 19361-19367.
100. Andrade, N.; Martinez, D.; Paula, A.; Silveira, J.; Alves, O.; Souza Filho, A., Temperature Effects on the Nitric Acid Oxidation of Industrial Grade Multiwalled Carbon Nanotubes. *Journal of Nanoparticle Research* **2013**, *15* (7), 1-11.

101. Delhaes, P.; Couzi, M.; Trinquecoste, M.; Dentzer, J.; Hamidou, H.; Vix-Guterl, C., A Comparison between Raman Spectroscopy and Surface Characterizations of Multiwall Carbon Nanotubes. *Carbon* **2006**, *44* (14), 3005-3013.
102. Yang, D.-Q.; Rochette, J.-F.; Sacher, E., Controlled Chemical Functionalization of Multiwalled Carbon Nanotubes by Kilolectronvolt Argon Ion Treatment and Air Exposure. *Langmuir* **2005**, *21* (18), 8539-8545.
103. Baitinger, E. M.; Vekesser, N. A.; Kovalev, I. N.; Ryabkov, Y. I.; Viktorov, V. V., Defect Structure of Multiwalled Carbon Nanotubes Studied by Raman Spectroscopy. *Inorganic Materials* **2011**, *47* (5), 471-474.
104. Schönfelder, R.; Avilés, F.; Bachmatiuk, A.; Cauch-Rodriguez, J. V.; Knupfer, M.; Büchner, B.; Rummeli, M. H., On the Merits of Raman Spectroscopy and Thermogravimetric Analysis to Assess Carbon Nanotube Structural Modifications. *Applied Physics A* **2012**, *106* (4), 843-852.
105. Chen, C.; Liang, B.; Ogino, A.; Wang, X.; Nagatsu, M., Oxygen Functionalization of Multiwall Carbon Nanotubes by Microwave-Excited Surface-Wave Plasma Treatment. *The Journal of Physical Chemistry C* **2009**, *113* (18), 7659-7665.
106. Santangelo, S.; Messina, G.; Faggio, G.; Lanza, M.; Pistone, A.; Milone, C., Calibration of Reaction Parameters for the Improvement of Thermal Stability and Crystalline Quality of Multi-Walled Carbon Nanotubes. *Journal of Materials Science* **2010**, *45* (3), 783-792.
107. Murphy, H.; Papakonstantinou, P.; Okpalugo, T. I. T., Raman Study of Multiwalled Carbon Nanotubes Functionalized with Oxygen Groups. *Journal of Vacuum Science & Technology B: Microelectronics and Nanometer Structures* **2006**, *24* (2), 715-720.
108. Santangelo, S.; Messina, G.; Faggio, G.; Lanza, M.; Milone, C., Evaluation of Crystalline Perfection Degree of Multi-Walled Carbon Nanotubes: Correlations between Thermal Kinetic Analysis and Micro-Raman Spectroscopy. *Journal of Raman Spectroscopy* **2011**, *42* (4), 593-602.
109. Judek, J.; Jastrzebski, C.; Malolepszy, A.; Mazurkiewicz, M.; Stobinski, L.; Zdrojek, M., Laser Induced Temperature Effects in Multi-Walled Carbon Nanotubes Probed by Raman Spectroscopy. *physica status solidi (a)* **2012**, *209* (2), 313-316.
110. Repalle, S.; Chen, J.; Drozd, V.; Choi, W., The Raman Spectroscopic Studies of Aligned Mwcnts Treated under High Pressure and High Temperature. *Journal of Physics and Chemistry of Solids* **2010**, *71* (8), 1150-1153.
111. Kumar, S.; Kaur, I.; Dharamvir, K.; Bharadwaj, L. M., Controlling the Density and Site of Attachment of Gold Nanoparticles onto the Surface of Carbon Nanotubes. *Journal of Colloid and Interface Science* **2012**, *369* (1), 23-27.
112. Gohil, S.; Ghosh, S., Surface Enhanced Raman Scattering from Multiwalled Carbon Nanotubes at Low Temperatures. *Applied Physics Letters* **2010**, *96* (14), 143108.
113. Soin, N.; Roy, S. S.; Ray, S. C.; McLaughlin, J. A., Excitation Energy Dependence of Raman Bands in Multiwalled Carbon Nanotubes. *Journal of Raman Spectroscopy* **2010**, *41* (10), 1227-1233.
114. de los Arcos, T.; Garnier, M. G.; Oelhafen, P.; Seo, J. W.; Domingo, C.; García-Ramos, J. V.; Sánchez-Cortés, S., In Situ Assessment of Carbon Nanotube Diameter Distribution with Photoelectron Spectroscopy. *Physical Review B* **2005**, *71* (20), 205416.

115. Datsyuk, V.; Kalyva, M.; Papagelis, K.; Parthenios, J.; Tasis, D.; Siokou, A.; Kallitsis, I.; Galiotis, C., Chemical Oxidation of Multiwalled Carbon Nanotubes. *Carbon* **2008**, *46* (6), 833-840.
116. Stobinski, L.; Lesiak, B.; Kövér, L.; Tóth, J.; Biniak, S.; Trykowski, G.; Judek, J., Multiwall Carbon Nanotubes Purification and Oxidation by Nitric Acid Studied by the Ftir and Electron Spectroscopy Methods. *Journal of Alloys and Compounds* **2010**, *501* (1), 77-84.
117. Tan, P.; An, L.; Liu, L.; Guo, Z.; Czerw, R.; Carroll, D. L.; Ajayan, P. M.; Zhang, N.; Guo, H., Probing the Phonon Dispersion Relations of Graphite from the Double-Resonance Process of Stokes and Anti-Stokes Raman Scatterings in Multiwalled Carbon Nanotubes. *Physical Review B* **2002**, *66* (24), 245410.
118. Lee, S.; Peng, J.-W.; Liu, C.-H., Probing Plasma-Induced Defect Formation and Oxidation in Carbon Nanotubes by Raman Dispersion Spectroscopy. *Carbon* **2009**, *47* (15), 3488-3497.
119. Rao, A. M.; Jorio, A.; Pimenta, M. A.; Dantas, M. S. S.; Saito, R.; Dresselhaus, G.; Dresselhaus, M. S., Polarized Raman Study of Aligned Multiwalled Carbon Nanotubes. *Physical Review Letters* **2000**, *84* (8), 1820-1823.
120. Pietraß, T.; Dewald, J. L.; Clewett, C. F. M.; Tierney, D.; Ellis, A. V.; Dias, S.; Alvarado, A.; Sandoval, L.; Tai, S.; Curran, S. A., Electron Spin Resonance and Raman Scattering Spectroscopy of Multi-Walled Carbon Nanotubes: A Function of Acid Treatment. *Journal of Nanoscience and Nanotechnology* **2006**, *6* (1), 135-140.
121. Behler, K.; Osswald, S.; Ye, H.; Dimovski, S.; Gogotsi, Y., Effect of Thermal Treatment on the Structure of Multi-Walled Carbon Nanotubes. *Journal of Nanoparticle Research* **2006**, *8* (5), 615-625.
122. Safibonab, B.; Reyhani, A.; Nozad Golikand, A.; Mortazavi, S. Z.; Mirershadi, S.; Ghoranneviss, M., Improving the Surface Properties of Multi-Walled Carbon Nanotubes after Irradiation with Gamma Rays. *Applied Surface Science* **2011**, *258* (2), 766-773.
123. Antunes, E. F.; Lobo, A. O.; Corat, E. J.; Trava-Airoldi, V. J.; Martin, A. A.; Veríssimo, C., Comparative Study of First- and Second-Order Raman Spectra of Mwcnt at Visible and Infrared Laser Excitation. *Carbon* **2006**, *44* (11), 2202-2211.
124. Zhao, X.; Ando, Y.; Qin, L.-C.; Kataura, H.; Maniwa, Y.; Saito, R., Multiple Splitting of G-Band Modes from Individual Multiwalled Carbon Nanotubes. *Applied Physics Letters* **2002**, *81* (14), 2550-2552.
125. Frielinghaus, R.; Goss, K.; Trellenkamp, S.; Houben, L.; Schneider, C. M.; Meyer, C., Comprehensive Characterization of an Individual Carbon Nanotube Transport Device. *Phys. Status Solidi B* **2011**, *248*, 2660-2663.
126. Yuan, S.; Zhang, Q.; You, Y.; Shen, Z.-X.; Shimamoto, D.; Endo, M., Correlation between in Situ Raman Scattering and Electrical Conductance for an Individual Double-Walled Carbon Nanotube. *Nano Letters* **2008**, *9* (1), 383-387.
127. Singh, D. K.; Iyer, P. K.; Giri, P. K., Diameter Dependence of Interwall Separation and Strain in Multiwalled Carbon Nanotubes Probed by X-Ray Diffraction and Raman Scattering Studies. *Diamond and Related Materials* **2010**, *19* (10), 1281-1288.

128. Nanot, S.; Millot, M.; Raquet, B.; Broto, J.-M.; Magrez, A.; Gonzalez, J., Doping Dependence of the G-Band Raman Spectra of an Individual Multiwall Carbon Nanotube. *Physica E: Low-dimensional Systems and Nanostructures* **2010**, *42* (9), 2466-2470.
129. Vollebregt, S.; Ishihara, R.; Tichelaar, F. D.; Hou, Y.; Beenakker, C. I. M., Influence of the Growth Temperature on the First and Second-Order Raman Band Ratios and Widths of Carbon Nanotubes and Fibers. *Carbon* **2012**, *50* (10), 3542-3554.
130. Jeet, K.; Jindal, V. K.; Bharadwaj, L. M.; Bhandari, R.; Dharamvir, K., Three-Stage Structural Modification of Carbon Nanotubes by Swift Heavy Ion Irradiation. *Nuclear Instruments and Methods in Physics Research Section B: Beam Interactions with Materials and Atoms* **2012**, *285* (0), 30-36.
131. Ritter, U.; Scharff, P.; Siegmund, C.; Dmytrenko, O. P.; Kulish, N. P.; Prylutsky, Y. I.; Belyi, N. M.; Gubanov, V. A.; Komarova, L. I.; Lizunova, S. V.; Poroshin, V. G.; Shlapatskaya, V. V.; Bernas, H., Radiation Damage to Multi-Walled Carbon Nanotubes and Their Raman Vibrational Modes. *Carbon* **2006**, *44* (13), 2694-2700.
132. Puech, P.; Anwar, A. W.; Flahaut, E.; Dunstan, D. J.; Bassil, A.; Bacsa, W., Raman G and D Band in Strongly Photoexcited Carbon Nanotubes. *Physical Review B* **2009**, *79* (8), 085418.
133. Piscanec, S.; Lazzeri, M.; Robertson, J.; Ferrari, A. C.; Mauri, F., Optical Phonons in Carbon Nanotubes: Kohn Anomalies, Peierls Distortions, and Dynamic Effects. *Physical Review B* **2007**, *75* (3), 035427.
134. Van der Heide, P., *X-Ray Photoelectron Spectroscopy: An Introduction to Principles and Practices*. John Wiley & Sons, Inc.: Hoboken, 2012; p 241.
135. Ballard, R. E., Empirical Mean Free Path Curves for Electron Scattering in Solids. *Journal of Electron Spectroscopy and Related Phenomena* **1982**, *25* (1), 75-78.
136. Pirlot, C.; Willems, I.; Fonseca, A.; Nagy, J. B.; Delhalle, J., Preparation and Characterization of Carbon Nanotube/Polyacrylonitrile Composites. *Advanced Engineering Materials* **2002**, *4* (3), 109-114.
137. Okpalugo, T. I. T.; Papakonstantinou, P.; Murphy, H.; McLaughlin, J.; Brown, N. M. D., High Resolution Xps Characterization of Chemical Functionalised Mwcnts and Swcnts. *Carbon* **2005**, *43* (1), 153-161.
138. Ago, H.; Kugler, T.; Cacialli, F.; Salaneck, W. R.; Shaffer, M. S. P.; Windle, A. H.; Friend, R. H., Work Functions and Surface Functional Groups of Multiwall Carbon Nanotubes. *The Journal of Physical Chemistry B* **1999**, *103* (38), 8116-8121.
139. Mattevi, C.; Eda, G.; Agnoli, S.; Miller, S.; Mkhoyan, K. A.; Celik, O.; Mastrogiovanni, D.; Granozzi, G.; Garfunkel, E.; Chhowalla, M., Evolution of Electrical, Chemical, and Structural Properties of Transparent and Conducting Chemically Derived Graphene Thin Films. *Advanced Functional Materials* **2009**, *19* (16), 2577-2583.
140. Li, M.; Boggs, M.; Beebe, T. P.; Huang, C. P., Oxidation of Single-Walled Carbon Nanotubes in Dilute Aqueous Solutions by Ozone as Affected by Ultrasound. *Carbon* **2008**, *46* (3), 466-475.
141. Wang, H.; Zhou, A.; Peng, F.; Yu, H.; Yang, J., Mechanism Study on Adsorption of Acidified Multiwalled Carbon Nanotubes to Pb(II). *Journal of Colloid and Interface Science* **2007**, *316* (2), 277-283.

142. Meng, L.-Y.; Park, S.-J., Preparation and Characterization of Reduced Graphene Nanosheets Via Pre-Exfoliation of Graphite Flakes. *Bulletin of the Korean Chemical Society* **2012**, *33* (1), 209-214.
143. Belin, T.; Epron, F., Characterization Methods of Carbon Nanotubes: A Review. *Materials Science and Engineering: B* **2005**, *119* (2), 105-118.
144. Moulder, J. F., *Handbook of X-Ray Photoelectron Spectroscopy*. Physical Electronics: Eden Praaire, 1992.
145. Fouquet, M.; Telg, H.; Maultzsch, J.; Wu, Y.; Chandra, B.; Hone, J.; Heinz, T. F.; Thomsen, C., Longitudinal Optical Phonons in Metallic and Semiconducting Carbon Nanotubes. *Physical Review Letters* **2009**, *102* (7), 075501.
146. Gupta, A.; Chen, G.; Joshi, P.; Tadigadapa, S.; Eklund, Raman Scattering from High-Frequency Phonons in Supported N-Graphene Layer Films. *Nano Letters* **2006**, *6* (12), 2667-2673.
147. Arepalli, S., Freiman, S., Hooker, S., Migler, D, Measurement Issues in Single-Wall Carbon Nanotubes. *NIST Recommended Practice Guide* **2008**.
148. Weathington, B. L.; Cunningham, C. J. L.; Pittenger, D. J., *Understanding Business Research*. John Wiley & Sons, Inc.: Hoboken, 2012; p 492.
149. D'Souza, F.; Kadish, K., *Handbook of Carbon Nano Materials: Synthesis and Supramolecular Systems*. World Scientific Publishing Co. Pte. Ltd.: Hackensack, 2011; Vol. 1.
150. Morishita, K.; Takarada, T., Gasification Behavior of Carbon Nanotubes. *Carbon* **1997**, *35* (7), 977-981.

CHAPTER III – A RAPID QUANTITATIVE PROTOCOL FOR MEASURING  
CARBON NANOTUBE DEGREE OF DISPERSION IN A WATERBORNE  
EPOXY-AMINE MATRIX MATERIAL

**3.1 Abstract**

The open literature makes it clear that accurate measurements of carbon nanotube dispersion quality is very complicated and the typical characterization is neither simple nor reliable. Most methods to quantify carbon nanotube dispersion reported in the literature required investigator chosen assumptions or software interpretations that were impractical at best and misleading at worst for facile application. In this Chapter, the use of visible light absorption-based method(s) will be proposed and validated for quantitatively discerning dispersibility differences of MWCNTs with three distinct surface chemistry modifications and four concentration levels blended with polymeric materials. Ultimately, the dispersion quality was quantified via the trendline slope of the thickness normalized absorbance values as a function of MWCNT concentration. Extremely poor dispersions were represented by statistically insignificant trendline slopes. The absorbance and blackness data revealed that hydroxyl surface modification increased MWCNT dispersibility by a factor of ~2.8 and ~2.6 compared to the unmodified MWCNT epoxy-amine polymer thin films, respectively. These results support and quantifiably validate that simple optical blackness values directly measured the degree of dispersion for MWCNTs in coatings applied to substrates and the data support that this is a simple and effective quality control metric.

### 3.2 Introduction

Carbon nanotubes (CNTs) are not commonly utilized in industrial applications despite their proven and potential performance property advantages. The basis for poor commercial integration is rooted in several main limitations, 1) CNTs are expensive, 2) effective dispersion is often time-consuming, and 3) the most common analytical techniques for discerning the degree of dispersion in polymers are destructive.<sup>67, 151-154</sup> It has been well demonstrated that complete exfoliation, high degrees of dispersion, and strong CNT-polymer interfacial interactions need to be attained in combination when fabricating systems to achieve maximum property gains.<sup>67, 153-156</sup> Thus, the ability to rapidly and reliably quantify dispersion states for a specific CNT surface treatment-polymer combination at different concentrations (e.g., Figure 3.1) would remove barriers for new materials utilization and performance attainment. To date, the most common quantitative determination of CNT dispersion in polymers often involves user-based software interpretation of optical or electron micrographs, critical limits imposed by the each distinct investigator, and the analysis may be limited by detector efficiency and resolution.<sup>157-161</sup>

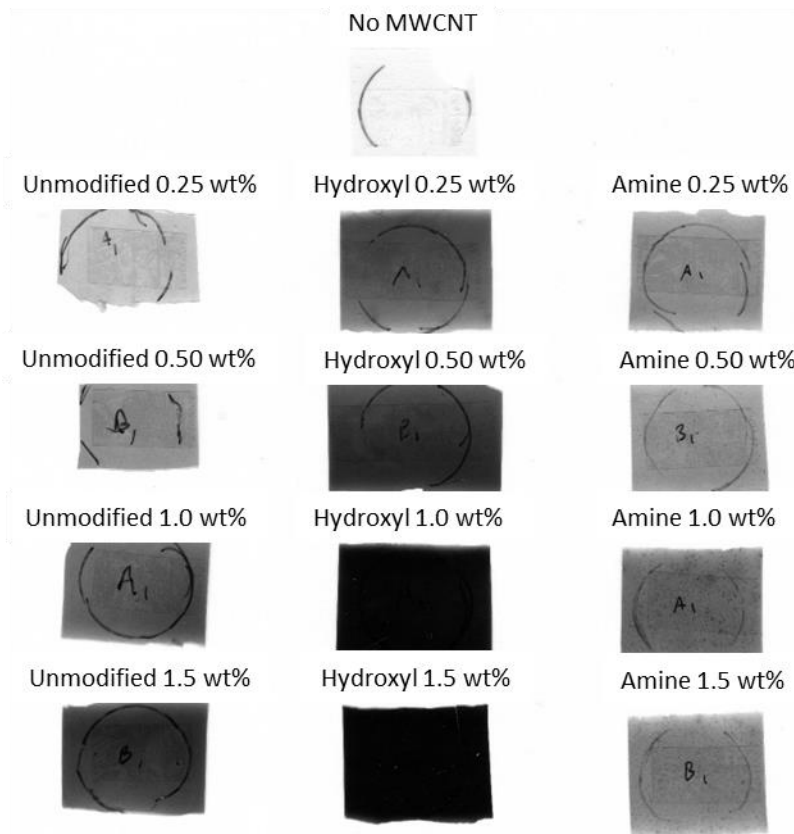


Figure 3.1 Representative optical images of waterborne epoxy-amine thin films comprised of different MWCNT surface chemistry-concentration combinations.

Note: the rectangles observable within each specimen is the double sided adhesive used to fix the sample to the backing and aid in observing the transparent nature of these 50 micron polymer films.

High magnification techniques for dispersion analysis, such as electron microscopy (EM; i.e., transmission electron microscopy<sup>47, 155, 160, 162-169</sup> and scanning electron microscopy<sup>154-155, 161-162, 169-174</sup>) and atomic force microscopy (AFM)<sup>155, 167, 169, 174-176</sup>, requires microtoming or cryo-fracturing samples which eliminates these techniques for rapid analysis. Additionally, EM and AFM techniques assume that the analyzed sample is an accurate representation of the bulk material.<sup>155, 169-170, 177</sup> Several literature optical microscopy protocols provide quantitative information about agglomerate size and CNT distribution (dispersion index, dispersion

parameter, clustering parameter); some of these parameters were demonstrated to correlate with composite performance characteristics.<sup>161, 173, 178-180</sup> However, these techniques may still be beyond practicality for facile use as a non-destructive quality control metric and additionally may be inadequate in highly exfoliated systems. Accordingly, the purpose of this study was to develop an economically viable protocol to investigate the dispersibility of a given MWCNT type/treatment - formulation combination. In Figure 3.1 are shown a variety of samples studied and the distinct visual differences from varying MWCNT surface modification and loading level.

Colorimetric properties have been widely used to quantify dispersion and deagglomeration of pigments such as carbon black.<sup>181-185</sup> Carbon black agglomeration is known to limit blackness/jetness properties of a coating due to reduced light-particle interactions (decreased surface area) compared to a highly dispersed pigment system (high surface area)<sup>181-184</sup>, i.e., decreasing particle size increases absorption and scattering efficiencies.<sup>181, 183</sup> Blackness values converge to a maximum when the particle size is smaller than approximately  $\frac{1}{3}$  the incident light wavelength ( $\sim 180$  nm for white light).<sup>183</sup> It was hypothesized that blackness/jetness measurements will be sufficiently sensitive to provide sub-micron quantitative measurements on the dispersion of MWCNTs bound to a non-transparent substrate.

Individual carbon nanotubes have been shown to be almost translucent as the amount of light absorbed is minimal due to nano-scale diameters.<sup>67</sup> CNTs absorb all wavelengths of ultraviolet, visible, and near infrared wavelengths to some degree, however, nanotubes with different chiralities have distinct absorption bands due to

excitation of discrete electronic transitions known as van Hove singularities (vHSs).<sup>35, 67</sup>

As a result, these transitions can be used to determine the chirality and diameter of small diameter single-wall carbon nanotubes through the Katura plot (Figure 3.2); however, the wavelength and intensity of the characteristic bands in these spectra require complete exfoliation as the transitions are quenched in bundled CNTs.<sup>65, 67</sup>

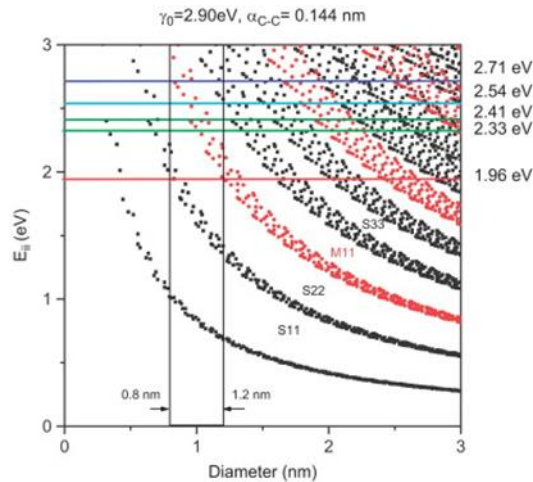


Figure 3.2 Katura plot exhibiting the effect of carbon nanotube diameter on the energy of electronic transitions in the electronic density of states.

Note: The transitions from top to bottom correspond to the ES<sup>11</sup>, ES<sup>22</sup>, EM<sup>11</sup>, ES<sup>33</sup>, ES<sup>44</sup>, and EM<sup>22</sup> transitions.<sup>35, 65</sup>

Increased light absorption has been reported for single wall carbon nanotubes (SWCNTs) and MWCNTs in aqueous and organic solvents upon improved dispersion and exfoliation.<sup>157, 166, 177, 186</sup> However, the use of visible light absorption properties to characterize SWCNT dispersion in a system requires that the selected wavelength not overlap with optically induced transitions (resonant energy absorption, Figure 3.2).<sup>67, 179, 187-188</sup> Light absorption in MWCNT filled polymers is expected to increase with decreasing agglomerate size (similar to carbon black) independent of full MWCNT exfoliation and MWCNT diameter. Increased light absorption has been

observed with increased MWCNT exfoliation in water<sup>166, 177, 182, 186</sup> and within a polymer matrix in the solid state,<sup>157</sup> increased visible light absorption and jetness are expected in solid polymers upon increasing MWCNT exfoliation.

The research in this Chapter resulted in a usable, simple and rapid method to reproducibly and quantifiably establish the difference between CNT dispersion states and dispersibility in clear waterborne epoxy-amine free films and the dispersibility of the same materials bound to coated metal substrates via ultraviolet-visible (UV-vis) spectroscopy and colorimetric (blackness) properties, respectively. Additionally, it is proposed that the use of blackness values can be utilized as a protocol for quality control in a variety of applications. The reasoning follows that if the colorimetric properties (blackness values) of an optically clear coating containing MWCNTs is related to the transmission optical absorption properties of the analogous free films, then its colorimetric properties can be utilized to investigate MWCNT dispersion states and subsequently employed as a rapid technique for quality control in industrial applications.

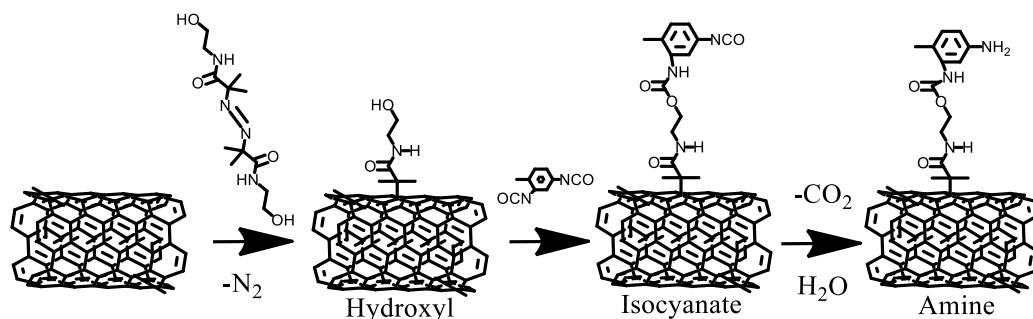
### **3.3 Experimental**

#### **3.3.1 Materials**

Multiwall carbon nanotubes (MWCNTs, 0.5-2  $\mu\text{m}$  length, 8-15 nm diameter, Cheap Tubes, Inc.) were modified as described below. 2,2'-Azobis[2-methyl-N-(2-hydroxyethyl) propionamide] (AMP), toluene diisocyanate (TDI), and tetrahydrofuran (THF, HPLC grade and 99.85% extra dry), were received from Fisher Scientific and used without modification and purification. Anquamine<sup>®</sup> 419 (60% solids as supplied) was donated by Air Products and diluted with deionized (DI) water to 25.25 wt% prior to use.

### 3.3.2 Surface Modification of MWCNTs

MWCNTs (150 mg) were weighed into a round bottom flask (RBF) followed by 30 mL of 1/1 v/v mixture of THF/DI water and 1.0 g AMP. The RBF was purged with nitrogen for 10 minutes before bath sonication for three hours at 50 °C. The resulting hydroxyl-functional MWCNTs were washed via four centrifugation/resuspension cycles with a 1/1 v/v THF/DI water blend to remove unreacted initiator, and then dried overnight at 50 °C. The hydroxyl-functional MWCNTs were dispersed in dry THF via tip sonication before dropwise addition to 10 mL 1/1 v/v TDI/dry THF blend. The mixture was maintained at 60 °C for 24 hours to yield isocyanate-functional MWCNTs that were washed via four cycles of centrifugation/resuspension with dry THF. The isocyanate-functional MWCNTs were tip sonicated for 10 minutes in dry THF and then added dropwise to 30 mL of a 30/70 blend of THF/DI water at 50 °C under continuous bath sonication for 90 minutes and then heated at 60 °C for 16 hours. The reaction product was washed via four centrifugation/resuspension cycles with a 30/70 blend of THF/DI water to yield amine-functional MWCNTs. The synthetic routes to obtain the desired surface functionality of each MWCNT type are shown in Scheme 3.1. Each MWCNT surface modification type will be referenced by its terminal functional group, i.e., unmodified (no modification), hydroxyl, and amine.



Scheme 3.1 Synthetic scheme for surface modification of MWCNTs.

### 3.3.3 Characterization of Functionalized MWCNTs

The MWCNT molecular structure of each functional type (unmodified, hydroxyl, and amine) were characterized via 10 Raman spectra collected with a Thermo Scientific DXR Raman microscope equipped with a 532 nm excitation laser through a 10x optical lens (spot size  $\sim 2 \mu\text{m}$ ). Each spectrum was baseline corrected and the spectral region between 1100 and 1800  $\text{cm}^{-1}$  was deconvoluted into four peaks using OMNIC 8.2 software as described in Chapter II. The mass of organic molecules attached to the MWCNTs was quantified via thermogravimetric analysis (TGA) in air at a heating rate of 5  $^{\circ}\text{C}/\text{minute}$  from room temperature to 800  $^{\circ}\text{C}$  in a TA Analysis Q500 TGA following NIST recommendations for SWCNT characterization (three thermograms per MWCNT surface modification type).<sup>147, 189</sup> All thermograms were normalized to the weight percent at 200  $^{\circ}\text{C}$  to account for residual solvent.<sup>75, 147</sup> The number of functional group equivalents was estimated by dividing the mass loss per gram MWCNT by the formula mass of the proposed structure of a given synthetic step (Scheme 3.1).

### **3.3.4 Waterborne Epoxy-Amine Thin Film Material Combination, Free Film Fabrication, and Coating Application**

An epoxy dispersion was produced in-house via the phase inversion technique. A known amount of diglycidyl ether of bisphenol-A (DGEBA)-based liquid epoxy and surfactant (14 wt% on DGEBA solids) were weighed into a dispersion chamber. The DGEBA and surfactant were mixed at 2,000 rpm at ambient temperature for five minutes. The agitation speed was raised to 3,000 rpm and DI water was added at 4 mL/minute into the DGEBA -surfactant blend. Agitation continued for one hour after complete water addition for homogenization the resulting dispersion. Epoxy equivalent weight (EEW), solids content, and particle size of the prepared epoxy dispersion were measured to be 365 g/equivalent, 58 wt%, and ~800 nm, respectively.

The appropriate amount of each MWCNT type (unmodified, hydroxyl, or amine) was added to the diluted Anquamine<sup>®</sup> 419 solution and bath sonicated at room temperature for 60 minutes. The corresponding amount of the epoxy dispersion (1:1 stoichiometric ratio) was added to the MWCNT/Anquamine<sup>®</sup> 419 suspension, vortex mixed for one minute, vertically mixed for 10 minutes, and then bath sonicated for 10 minutes prior to application. Free films and coatings of each material combination were generated via drawdown (eight mils wet) on polypropylene sheets and SAE 1008/1010 carbon steel with an average surface roughness < 20 microinches (QPanel) QD steel panels, respectively. All substrates were cleaned with an acetone soaked low lint wipe prior to coating application. Each system was cured at ambient conditions for seven days

prior to analysis. The dried film thicknesses were measured with a Positector 6000 coating thickness gauge and determined to be 45-50 microns.

### 3.3.5 MWCNT Dispersion Analysis

The MWCNT dispersion of each thin film material combination was investigated qualitatively via optical microscopy and scanning electron microscopy. Reflectance optical micrographs of the free films were collected with a Keyence VHX-600 digital optical microscope at 1000x magnification. Free films were cryo-fractured and the cross-sections sputter coated with ~ 5 nm of silver using an Emitech K550X sputter coater. The sputter coated cross-section of each thin film material combination was analyzed via field emission-scanning electron microscopy (SEM; Zeiss SigmaVP) with an acceleration voltage of 20 kV and a working distance of 2-4 mm.

The MWCNT dispersions were investigated quantitatively via calculation of the dispersion index from optical micrographs, UV-vis absorption spectroscopy, and calculation of the blackness/jetness values. The dispersion index ( $D$ ) was calculated employing Olympus Stream Essentials image analysis software and reflects the normalized agglomeration state within a system using Equation 3.1.<sup>160</sup>

$$D = \left(1 - f \frac{A_{CNT}/A_0}{\phi_{vol}}\right) \quad \text{Equation 3.1}$$

The area occupied by nanotube agglomerates ( $A_{CNT}$ ) and the total investigated area ( $A_0$ ) were obtained from image analysis. The parameter  $\phi_{vol}$  is the CNT volume fraction, and  $f$  is a factor related to the density of CNT agglomerates ( $0.25^{160}$ ). By this protocol, agglomerates with diameters smaller than 1  $\mu\text{m}$  are neglected, so a  $D$  value of 1

corresponds to a perfect microscale dispersion of CNT where all agglomerates are less than 1  $\mu\text{m}$ . A decreasing dispersion state is reflected in a decreasing  $D$  value.

Transmission UV-vis spectra were collected from free films of each coating type with a Tecan M1000 Infinite PRO plate reader in absorbance mode. Single wavelength absorbance measurements were collected (177 measurements, beam width  $\sim 1$  mm) of each free film type (three sets of measurements per thin film material combination) within 177  $\text{mm}^2$  area of each specimen at 500, 700, and 900 nm.

CIE  $L^*a^*b^*$  color space value sets and the corresponding XYZ coordinates were recorded with a BYK Spectro-Guide Sphere Gloss portable spectrophotometer for each thin film material combination applied to a steel substrate (three measurements per thin film material combination from individual panels for each measurement).<sup>183</sup> The XYZ color coordinates were used to calculate the jetness ( $M_c$ ), blackness ( $M_y$ ), and undertone ( $d_M$ ) of each coating system using Equations 3.2, 3.3, and 3.4, respectively.<sup>190</sup>

$$M_c = 100 \times \left[ \log \frac{X_n}{X} - \log \frac{Z_n}{Z} + \log \frac{Y_n}{Y} \right] \quad \text{Equation 3.2}$$

$$M_y = 100 \times \log \frac{Y_n}{Y} \quad \text{Equation 3.3}$$

$$d_M = M_c - M_y \quad \text{Equation 3.4}$$

where  $X_n = 94.811$ ,  $Y_n = 100.00$ , and  $Z_n = 107.304$

### 3.3.6 Statistical Analysis

Investigations for linear statistical correlations and the statistical significance of trendline slopes between data sets were performed by calculating the Pearson product-moment correlation coefficient and linear regression analysis, respectively, via Minitab 17 software and 95% confidence ( $\alpha = 0.05$ ).<sup>191</sup>

### 3.4 Results

The established basis of the intensity for D' characteristic band arises from the concentration of defects and strain of the MWCNT wall and not amorphous carbon,<sup>70, 72, 120</sup> therefore the D'/G ratio was employed to investigate changes in the molecular structure resulting from chemical modifications (Scheme 3.1). A statistical increase in the D'/G ratio was determined after the MWCNTs were treated with AMP indicating more disorder in the molecular structure after the chemical treatment suggesting successful incorporation of hydroxyl moieties via radical addition (Figure 3.3). The D'/G ratios of the amine and hydroxyl modified MWCNTs were determined to be statistically same, which was expected as the TDI addition to the hydroxyl functional group does not occur directly with the MWCNT surface thereby avoiding further damage the molecular structure (Scheme 3.1).

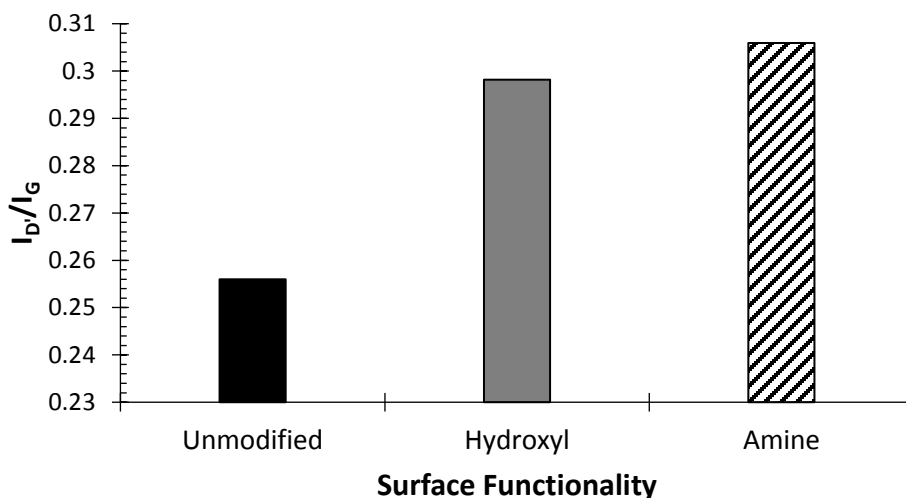


Figure 3.3 Average D'/G values calculated employing a four peak deconvolution protocol for unmodified MWCNTs, hydroxyl MWCNTs, and amine MWCNTs.

The functional equivalents of amines attached to the MWCNTs were quantified from the change in mass of organic moieties attached to the MWCNTs via thermogravimetric analysis. The attenuated total reflectance-Fourier transform infrared spectra did not reliably and discernibly exhibit the characteristic bands associated with functional groups of the proposed MWCNT surface chemistry employed in this study (Scheme 3.1) due to their low mass percent. However, successful 1:1 addition of TDI to the hydroxyl MWCNTs was inferred via the associated change in mass loss by TGA, i.e., the molar equivalent of the expected attached organic mass per gram MWCNT was determined to be statistically the same (Figure 3.4).

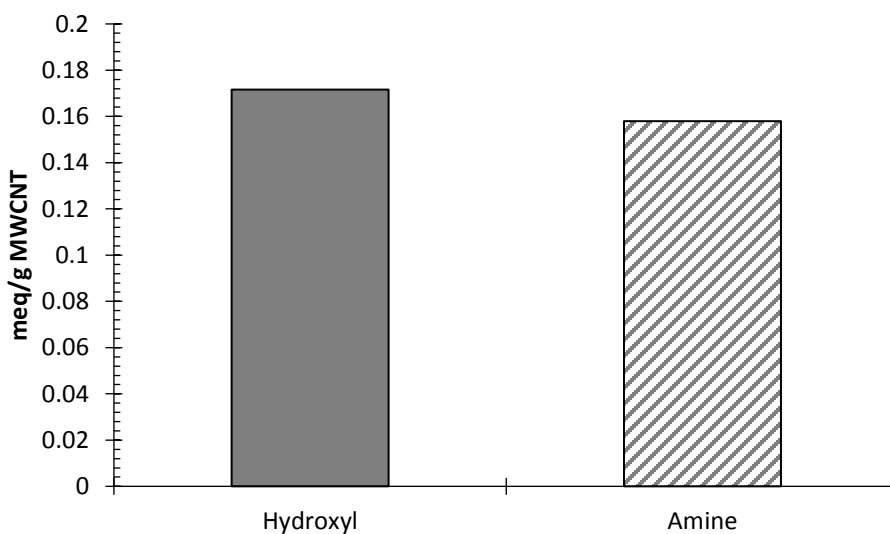


Figure 3.4 Average meq hydroxyl/g MWCNT and average meq amine/g MWCNT.

Note: These data suggests the successful 1:1 addition of TDI and subsequent decarboxylation to the hydroxyl MWCNTs.

The increased mass loss measured via TGA after TDI addition and subsequent decarboxylation corresponded well to the predicted mass loss according to Scheme 3.1. The lack of statistical change in the D'/G ratio for TDI addition and decarboxylation suggests that reaction did not occur at the MWCNT surface damaging the molecular

structure of the surface as proposed in Scheme 3.1. The increased molecular disorder of the MWCNTs determined via the increased D'/G ratio of the Raman spectra and the mass loss associated with oxygenated materials measured via TGA indicated successful radical modification of the MWCNTs.

### **3.4.2 MWCNT Dispersion in Epoxy-Amine Coatings**

All MWCNT/epoxy-amine thin film material combinations possessed agglomerates larger than one micron in diameter, independent of surface functionalization and concentration as determined via SEM and optical microscopy (Figures 3.5-3.8). Such agglomeration may be attributed to poor solvent wetting of the MWCNT surface during sonication and/or the inability to break the MWCNT intermolecular forces and inhibit reagglomeration.<sup>182</sup> SEM analysis suggested that the hydroxyl functionalized MWCNTs were better individualized and dispersed within the matrix compared to the unmodified and amine MWCNT types (Figure 3.5-3.8); this observation was confirmed quantitatively via visible light absorption and blackness/jetness values. The most extreme difference in dispersion states, and subsequently, visible light absorption occurred at 1.5 wt% MWCNT concentration where the relative frequency and size of MWCNT agglomerates was in the order: amine > unmodified > hydroxyl. Although optical and electron microscopy clearly discern differences in dispersion states for all three MWCNT types at 1.5 wt%, the ability to quantify dispersibility differences at lower concentrations was not as definitive (Figure 3.1).

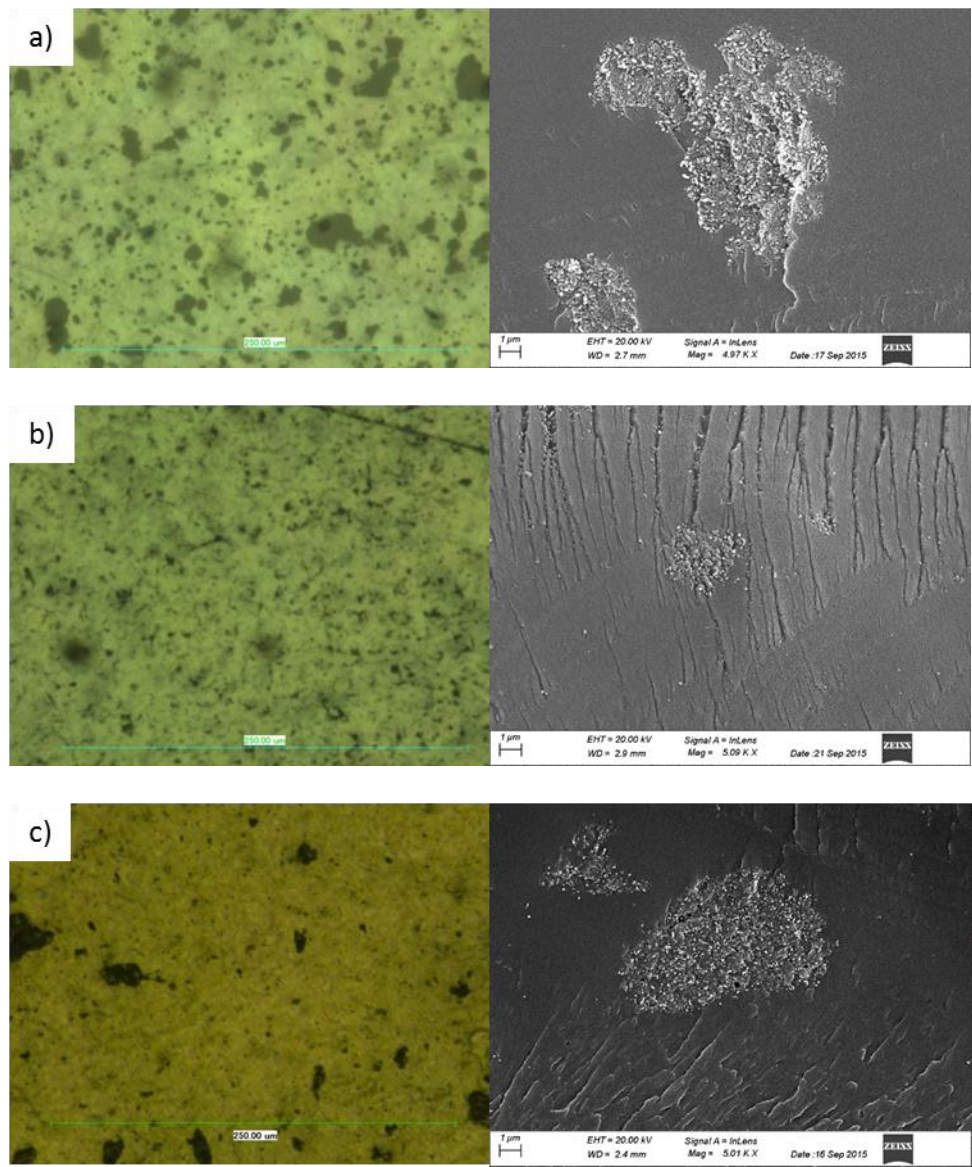


Figure 3.5 Optical (left) and scanning electron micrographs (right) of MWCNT/waterborne epoxy-amine thin films at a 0.25 wt% MWCNTs loading level.

Note: optical micrographs (left) were captured at 1000x magnification and scanning electron micrographs (right) were collected at 5000x magnification; unmodified MWCNT (a), hydroxyl MWCNT (b), and amine MWCNT (c) free films, respectively.

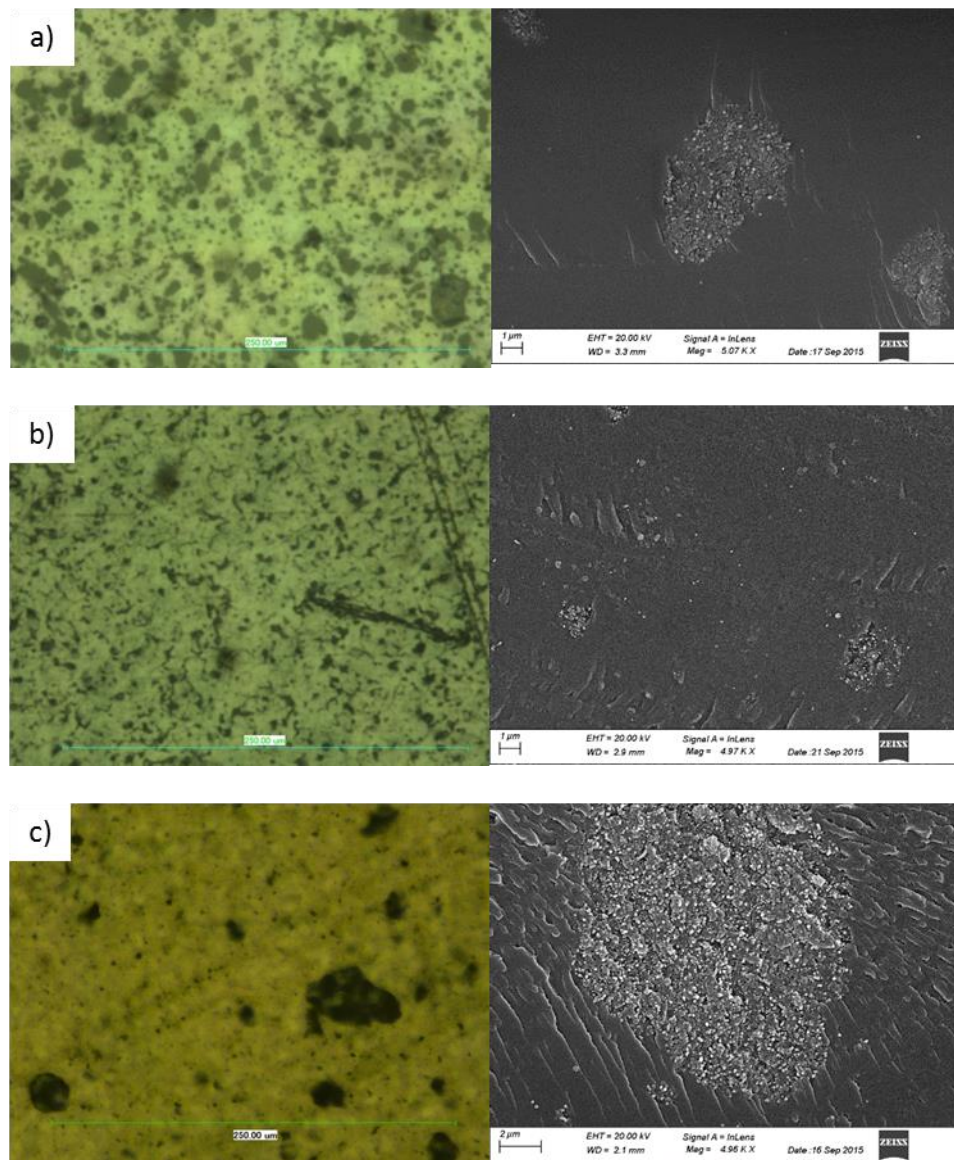


Figure 3.6 Optical (left) and scanning electron micrographs (right) of MWCNT/waterborne epoxy-amine thin films at a 0.50 wt% MWCNTs loading level.

Note: optical micrographs (left) were captured at 1000x magnification and scanning electron micrographs (right) were collected at 5000x magnification; unmodified MWCNT (a), hydroxyl MWCNT (b), and amine MWCNT (c) free films, respectively.

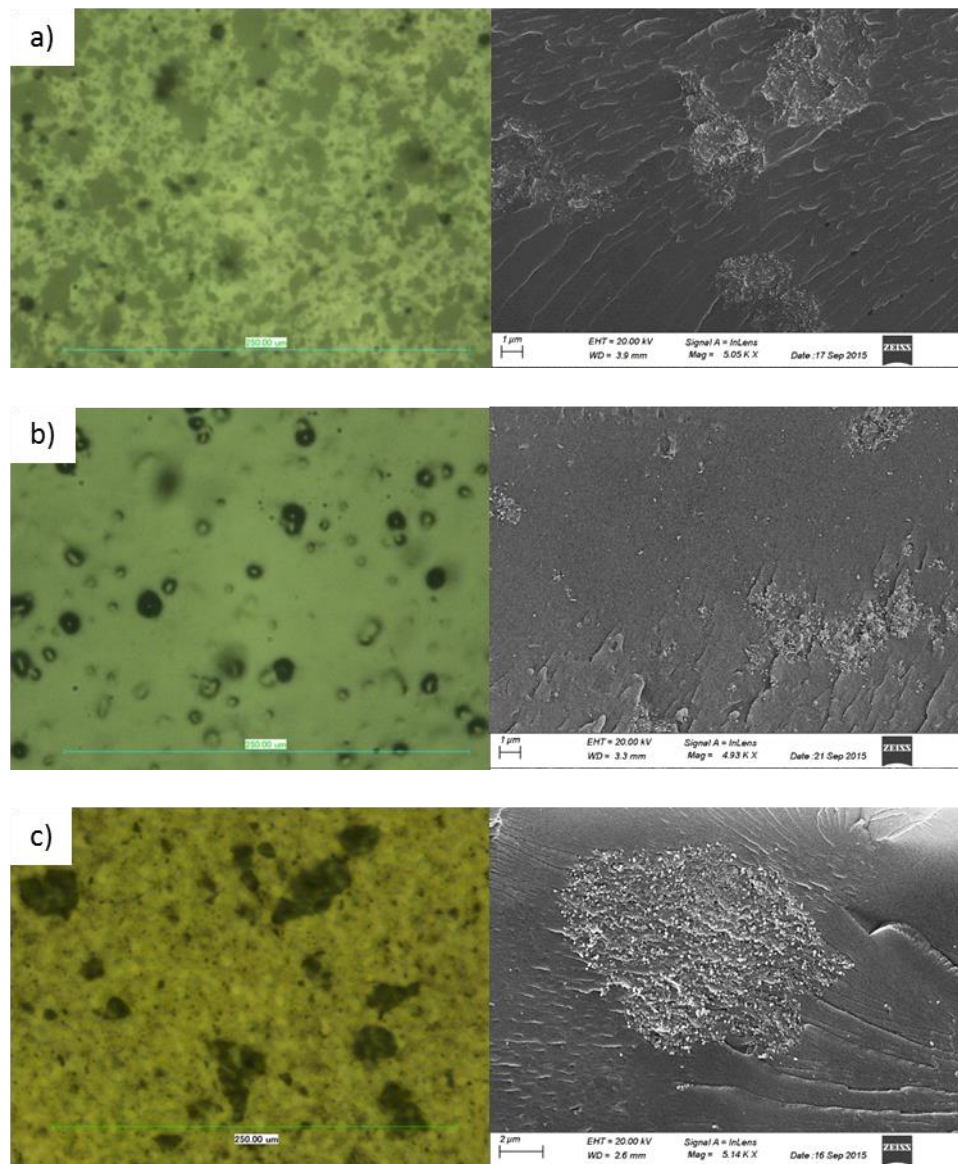


Figure 3.7 Optical (left) and scanning electron micrographs (right) of MWCNT/waterborne epoxy-amine thin films at a 1.0 wt% MWCNTs loading level.

Note: optical micrographs (left) were captured at 1000x magnification and scanning electron micrographs (right) were collected at 5000x magnification; unmodified MWCNT (a), hydroxyl MWCNT (b), and amine MWCNT (c) free films, respectively.

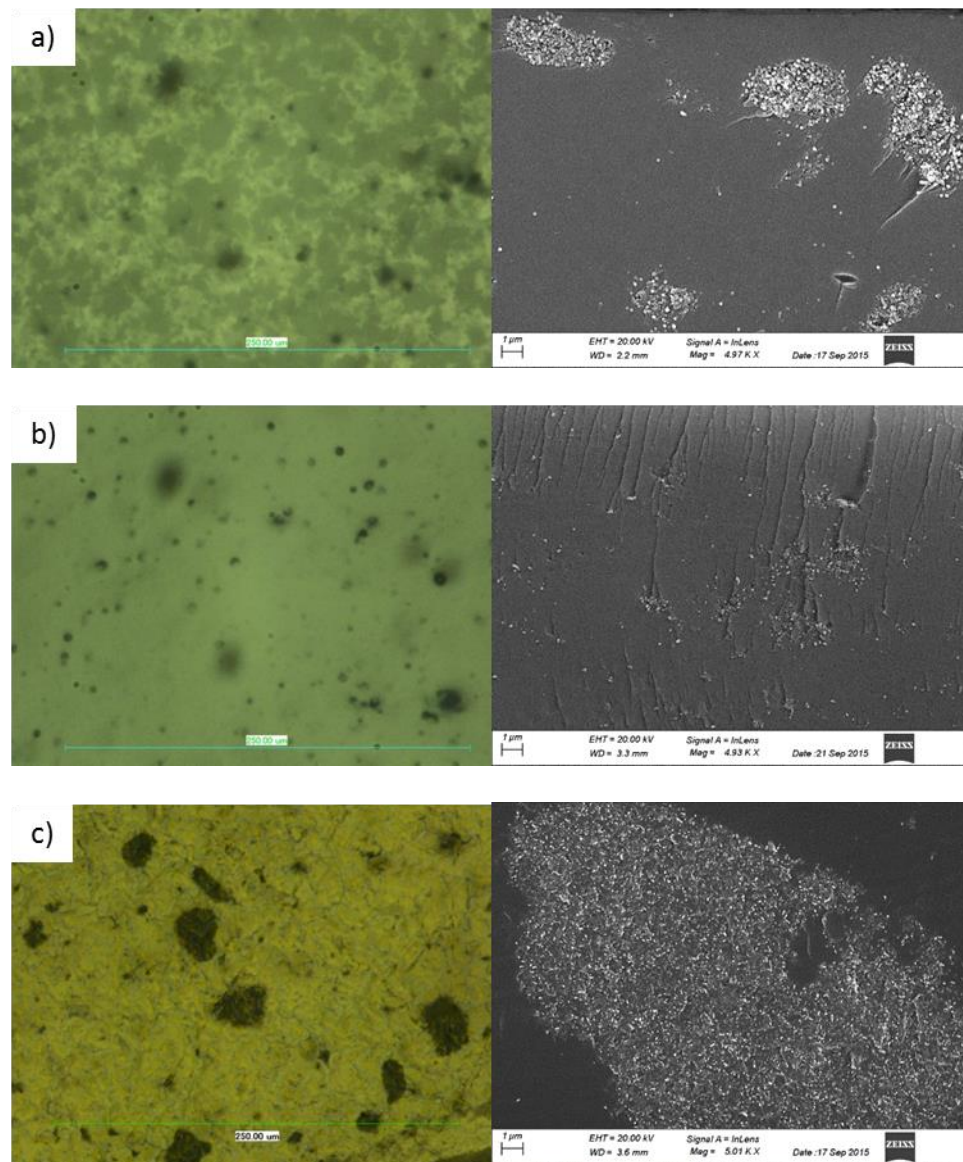


Figure 3.8 Optical (left) and scanning electron micrographs (right) of MWCNT/waterborne epoxy-amine thin films at a 1.5 wt% MWCNTs loading level.

Note: optical micrographs (left) were captured at 1000x magnification and scanning electron micrographs (right) were collected at 5000x magnification; unmodified MWCNT (a), hydroxyl MWCNT (b), and amine MWCNT (c) free films, respectively.

Image analysis has been widely employed in the literature as a quantitative method for investigating MWCNT dispersion in polymers.<sup>157-158, 160-161</sup> The proposed methods to quantify MWCNT dispersion were directly compared with those of other

authors in accepted literature protocols by calculating the dispersion index for each MWCNT treatment-material combination from the obtained optical micrographs (Figure 3.9). The dispersion index calculations indicated that the amine MWCNTs achieved a higher level of dispersion than the other two MWCNT surface treatments. However, these calculations clearly misrepresent the achieved level of dispersion of each MWCNT surface treatment as observed qualitatively via optical and electron microscopy.

If the dispersion index was capable of investigating MWCNT dispersibility of a given surface treatment in a polymer, the dispersion index value would be similar independent of MWCNT concentration as the calculation was normalized to the MWCNT volume fraction (Equation 3.1). Since the dispersion index values changed as a function of MWCNT concentration for all three surface modification types, this method alone cannot adequately describe nor quantify MWCNT dispersibility of the material combinations investigated here. The optical micrographs of the 1.0 and 1.5 wt% hydroxyl MWCNT thin films appeared as a nearly continuous phase and the image analysis software was unable to discern agglomerates from the continuous phase; thus, the analysis was inconclusive for these thin films and the values are not reported (Figure 3.9). These observations exemplify the limitations of the literature-based image analysis due to detector sensitivity and resolution. The contradiction between the dispersion index and the qualitative techniques necessitates that an alternative method be developed to quantify dispersion and the dispersibility of MWCNTs in thin films.

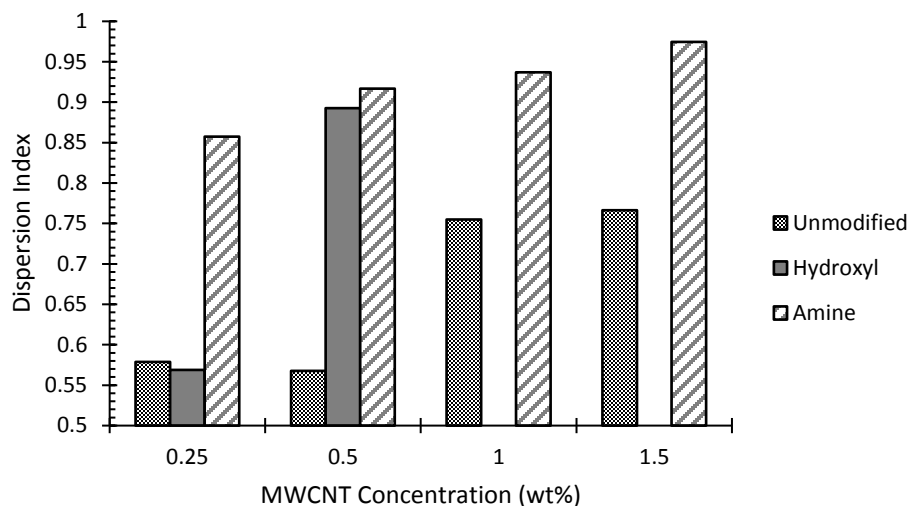
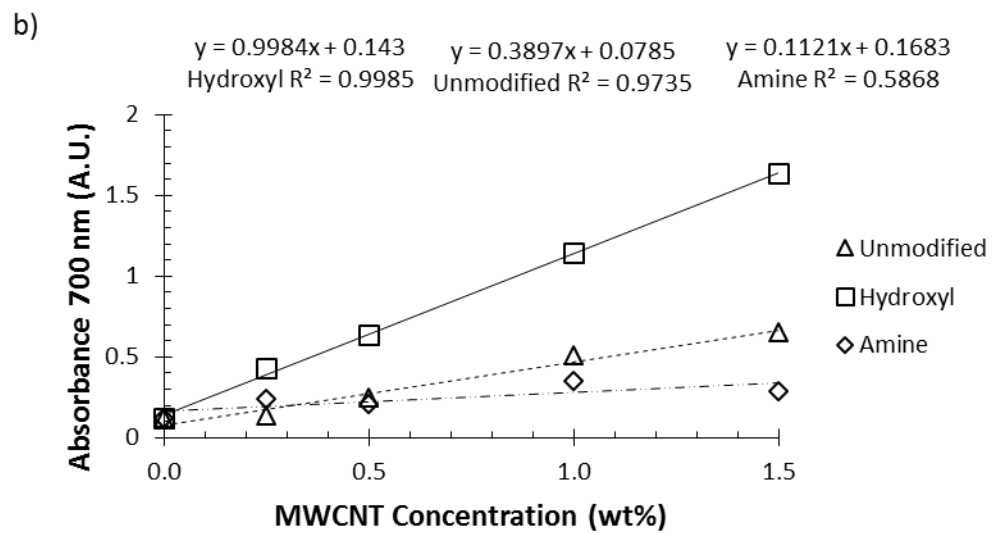
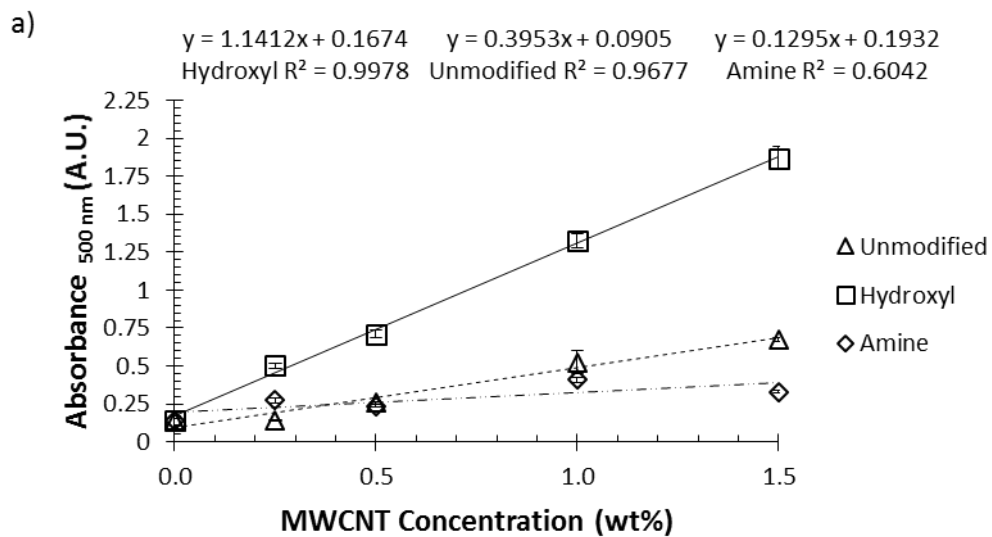


Figure 3.9 Calculated dispersion index as a function of MWCNT concentration by surface chemistry.

The calculated dispersion index was determined using a representative accepted literature protocol.<sup>11</sup> These calculated values are clearly not consistent with the optical images in Figure 3.5-3.8 and yet are derived from the same samples.

The linear absorbance trendline slopes measured at 500 nm, 700 nm, and 900 nm incident light as a function of MWCNT concentration suggests that coating absorbance properties followed Beer's law at these specific wavelengths (Figure 3.10). The trendline slopes of the  $A_{500 \text{ nm}}$  as a function of MWCNT concentration for the hydroxyl MWCNTs and unmodified MWCNTs were statistically relevant ( $r^2 > 0.96$  for all three wavelengths). Similar absorption properties were determined for the hydroxyl and unmodified MWCNTs at wavelengths of 700 and 900 nm (Figures 3.10b-c) and would be expected to be similar to other non-resonant absorbing wavelengths (Figure 3.11). However, the amine MWCNT sample possessed a statistically insignificant trendline slope at all three incident wavelengths indicating poor dispersibility under the conditions employed in this study which was verified via optical and scanning electron microscopy.



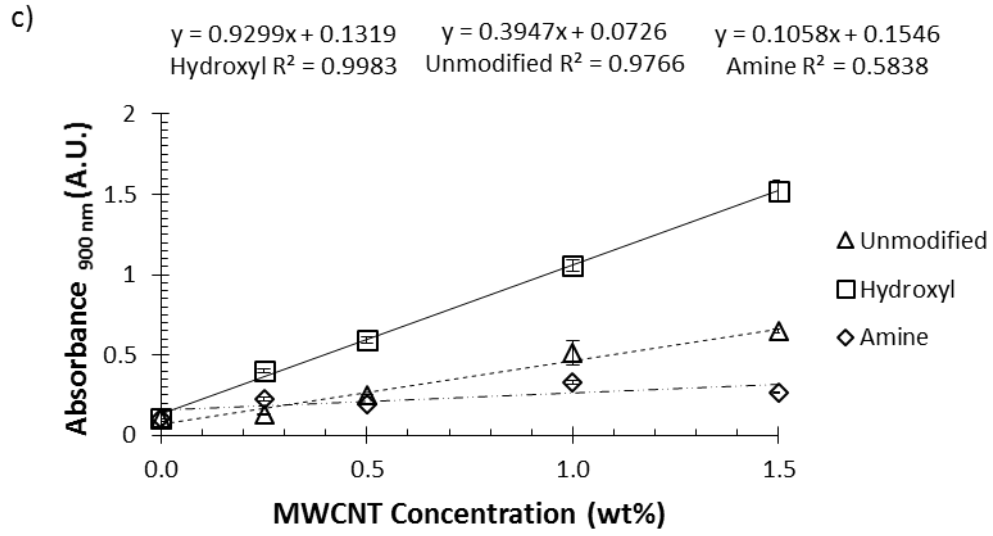
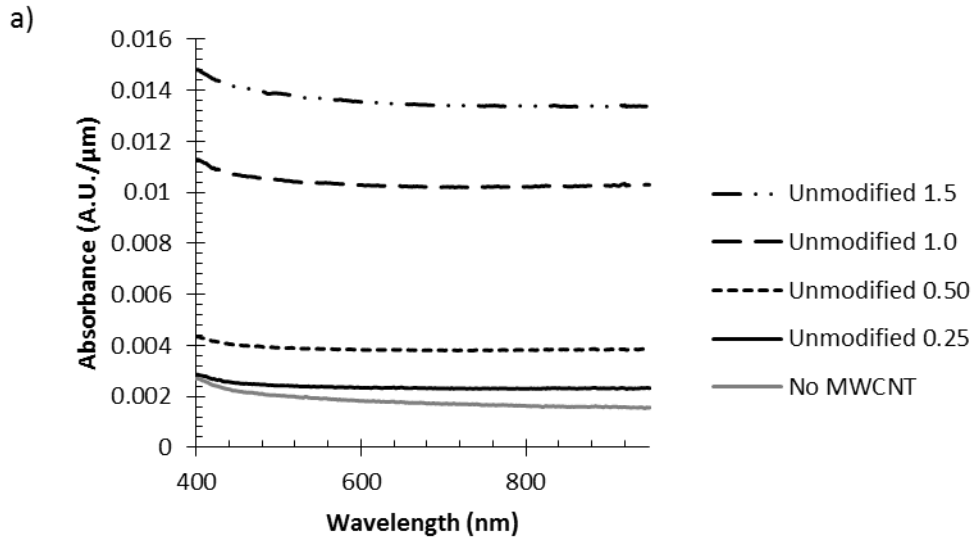


Figure 3.10 Absorbance of MWCNT/waterborne epoxy-amine thin films as a function of concentration by MWCNT treatment.

Note: absorbance at 500 nm (a), 700 nm (b), and 900 nm (c).



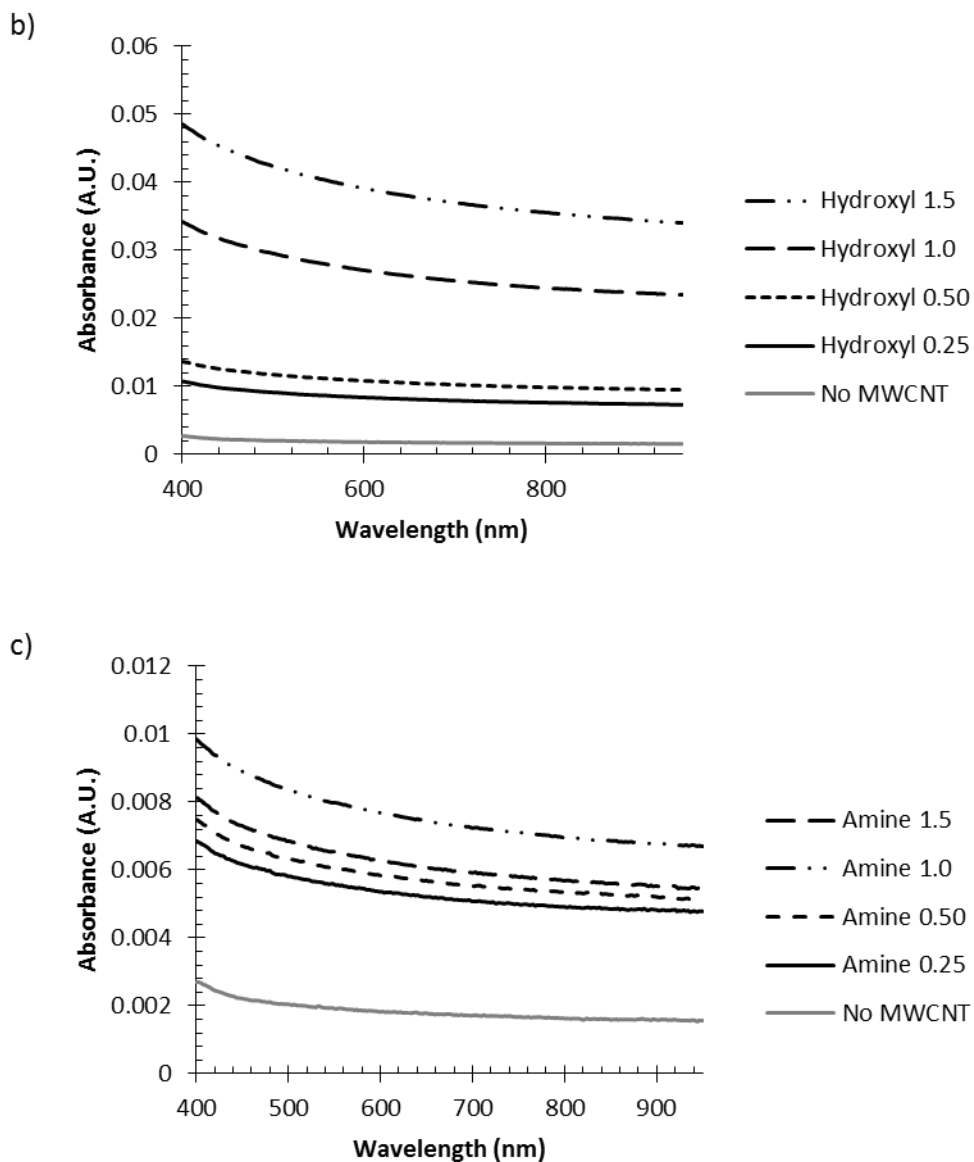


Figure 3.11 Representative visible light absorption spectra of MWCNT/waterborne epoxy-amine thin films.

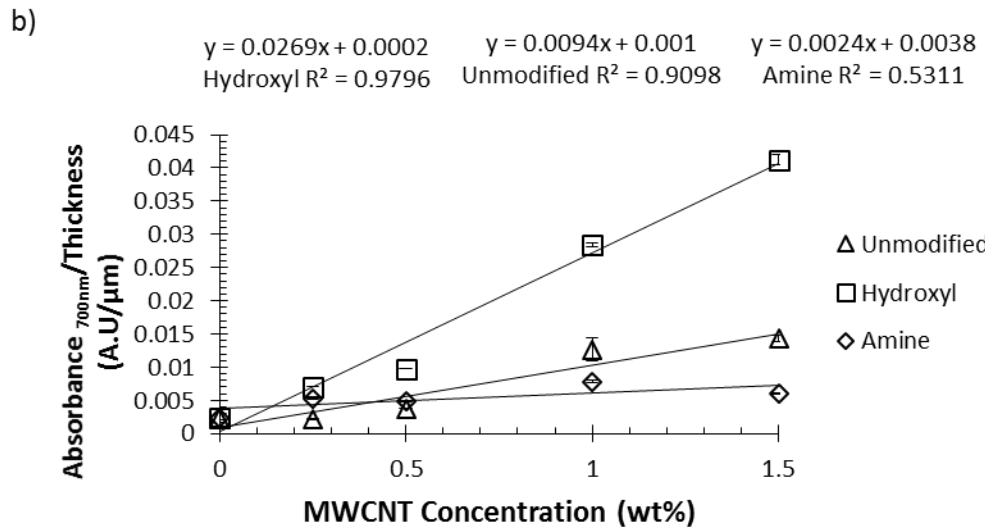
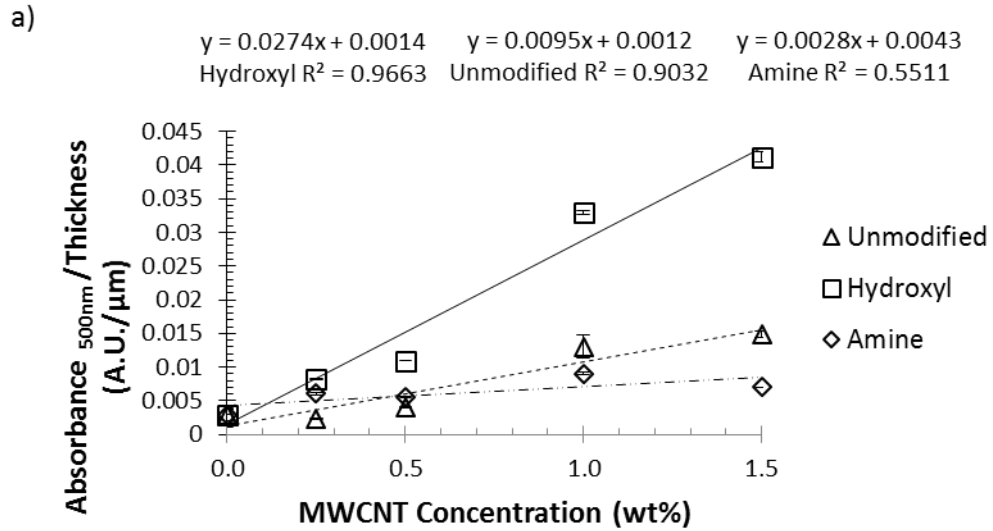
Note: unmodified MWCNTs (a), hydroxyl-functional MWCNTs (b), and amine-functional (c); the material combination without MWCNTs was included in each plot for comparison.

Since the absorbance properties of the unmodified and hydroxyl-functional MWCNTs appeared to follow Beer's law, the slope of the thickness (path length) normalized absorbance values as a function of MWCNT concentration will equal an

effective optical absorption coefficient (EOAC) (Figure 3.12). The EOAC, if statistically relevant, is expected to be related to the dispersibility of a given MWCNT type (diameter, length, surface functionality) paired with a coating system, and can provide a quantifiable metric for dispersibility investigations. As increasing absorbance properties is indicative of increased surface area, a larger EOAC value indicates increased MWCNT dispersion and exfoliation. The hydroxyl-functional MWCNT type possessed the highest EOAC and the best dispersion/exfoliation properties observed via optical microscopy and SEM (Figures 3.5-3.8). These data indicate that the hydroxyl-functional MWCNT disperse ~2.8 times better than the unmodified MWCNT ( $EOAC_{\text{hydroxyl}} = 2.74 \times 10^{-3}$ ;  $EOAC_{\text{unmodified}} = 0.95 \times 10^{-3}$ ) in the current material combination and processing conditions.

Although the trendline slope of the amine-functional MWCNTs was unable to provide a reliable quantitative number for the dispersion quality (statistically insignificant;  $p > 0.05$ ) this method still provided reliable *qualitative* identification the poor dispersibility (Figure 3.11). Very large agglomerates were observed in the amine-functional MWCNT sample type visually (Figure 3.1) as well as via optical microscopy and SEM at all MWCNT concentrations (Figures 3.5-3.8). It is important to note that some agglomerates were not considered in the CNT dispersion index as they were above the typical size cut-off.<sup>157-158</sup> It is further proposed that the use of UV-vis absorption properties can be utilized to compare dispersion states of a single MWCNT concentration. Although the data reveals a high confidence in UV-vis analysis for

quantitative MWCNT dispersion investigations, the technique is still limited by sample thickness, concentration, and whether it is bound to a non-transparent substrate.



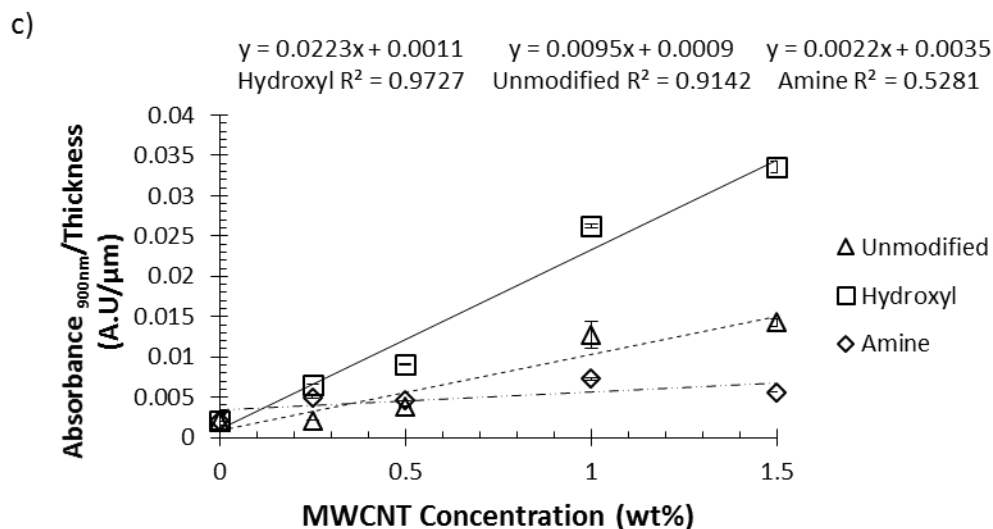
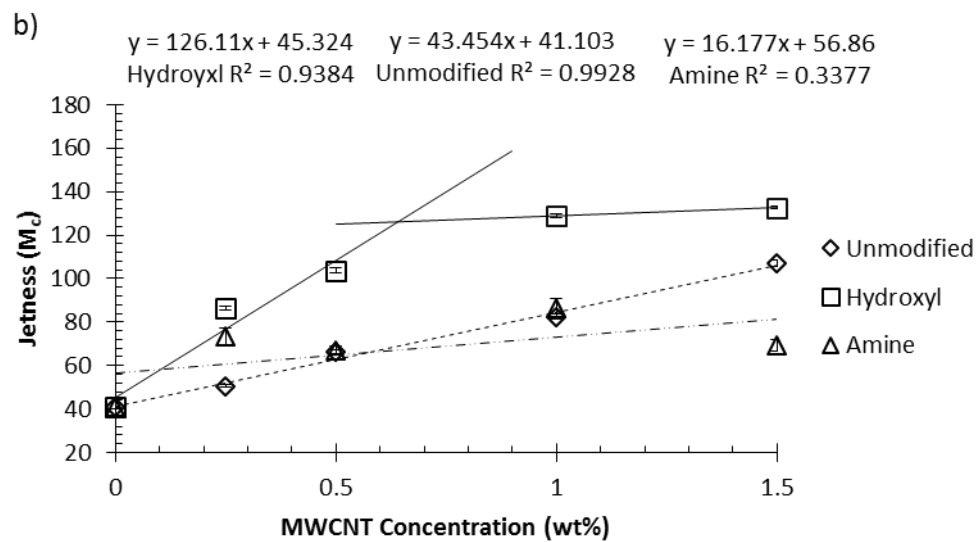
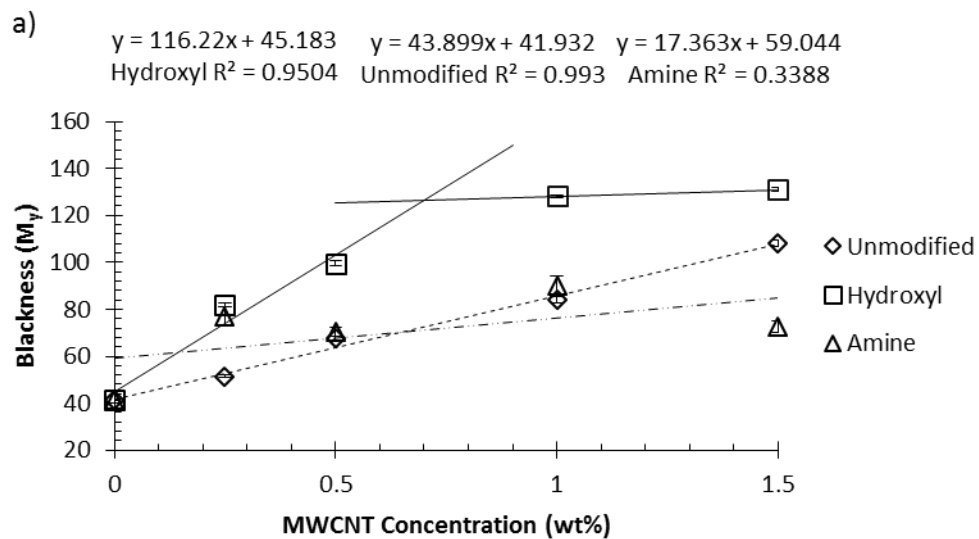


Figure 3.12 Thickness normalized absorbance of MWCNT/waterborne epoxy-amine thin films as a function of concentration by MWCNT treatment.

Note: absorbance at 500 nm (a), 700 nm (b), and 900 nm (c).

### 3.4.3 Free Film Absorbance and Blackness/Jetness of Steel Bound Coatings

The objective of this study was to develop/validate a method to monitor and quantify MWCNT dispersion in a coating bound to a non-transparent substrate. If color properties such as blackness or jetness of a MWCNT containing polymer coated substrate statistically correlates to the optical absorption properties of the corresponding free films, then blackness ( $M_y$ ) and jetness ( $M_c$ ) measurements can be utilized to quantify the dispersion level of MWCNTs in coating systems.



c)

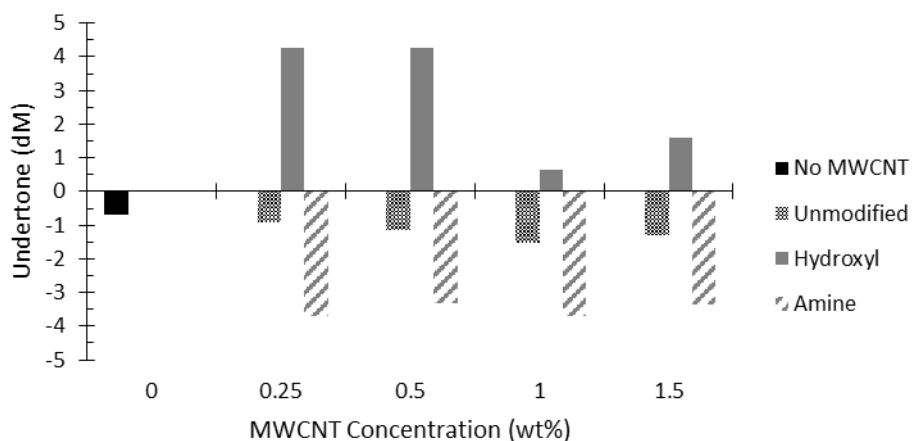


Figure 3.13 Blackness ( $M_y$ ) values (a), jetness ( $M_c$ ) values (b) and the undertone ( $d_M$ ) properties (c) of epoxy-amine thin films applied to steel substrates.

The blackness value of each coated steel panel increased linearly ( $p < 0.05$ ) as a function of MWCNT concentration for both the unmodified and hydroxyl-functional MWCNTs (Figure 3.13a) indicating that these properties can be employed to measure the MWCNT dispersibility in a polymer thin film applied to a steel substrate. However, a linear fit to the hydroxyl-functional MWCNT blackness data may oversimplify the relationship between blackness properties and the dispersion state at each concentration investigated. These data suggest that there may be a practical upper limit or a non-linear relationship for higher dispersion states at relatively higher concentrations. However, comparison of the trendline slope of the hydroxyl-functional MWCNT material combinations linear region to the unmodified MWCNT material combinations trendline indicated that the hydroxyl-functional MWCNTs dispersed  $\sim 2.6$  times better than the unmodified MWCNTs which is similar to what was calculated via the absorbance method ( $\sim 2.8$  times).

Throughout the open literature, the concentration of MWCNTs utilized in polymeric systems is commonly within the concentrations utilized in this study<sup>29-30, 163-165</sup> exhibiting the practical use of these methods. Similar trends were observed for the jetness values as a function of MWCNT concentration (Figure 3.13b) for each MWCNT surface chemistry. The trendline slope of the jetness and blackness values of the amine-functional MWCNT surface modification as a function of MWCNT concentration were not statistically relevant indicating their poor overall dispersibility as noted with the UV-vis measurements of the free films. The statistically relevant linear trendline of the blackness values as a function of concentration indicates that blackness value can be employed as a quality control metric for MWCNT dispersion of thin films bound to a non-transparent substrate. The differences between the blackness and jetness values was attributed to the color undertone characteristics (Figure 3.13c). For carbon black systems, decreased particle size has been associated with higher blackness values and brown undertones ( $d_M < 0$ )<sup>192</sup>; however, the smallest particle size for the MWCNT-surface chemistry combination (noted by SEM analysis) in this study resulted in the highest blackness values with a *blue* undertone (Figure 3.13c).

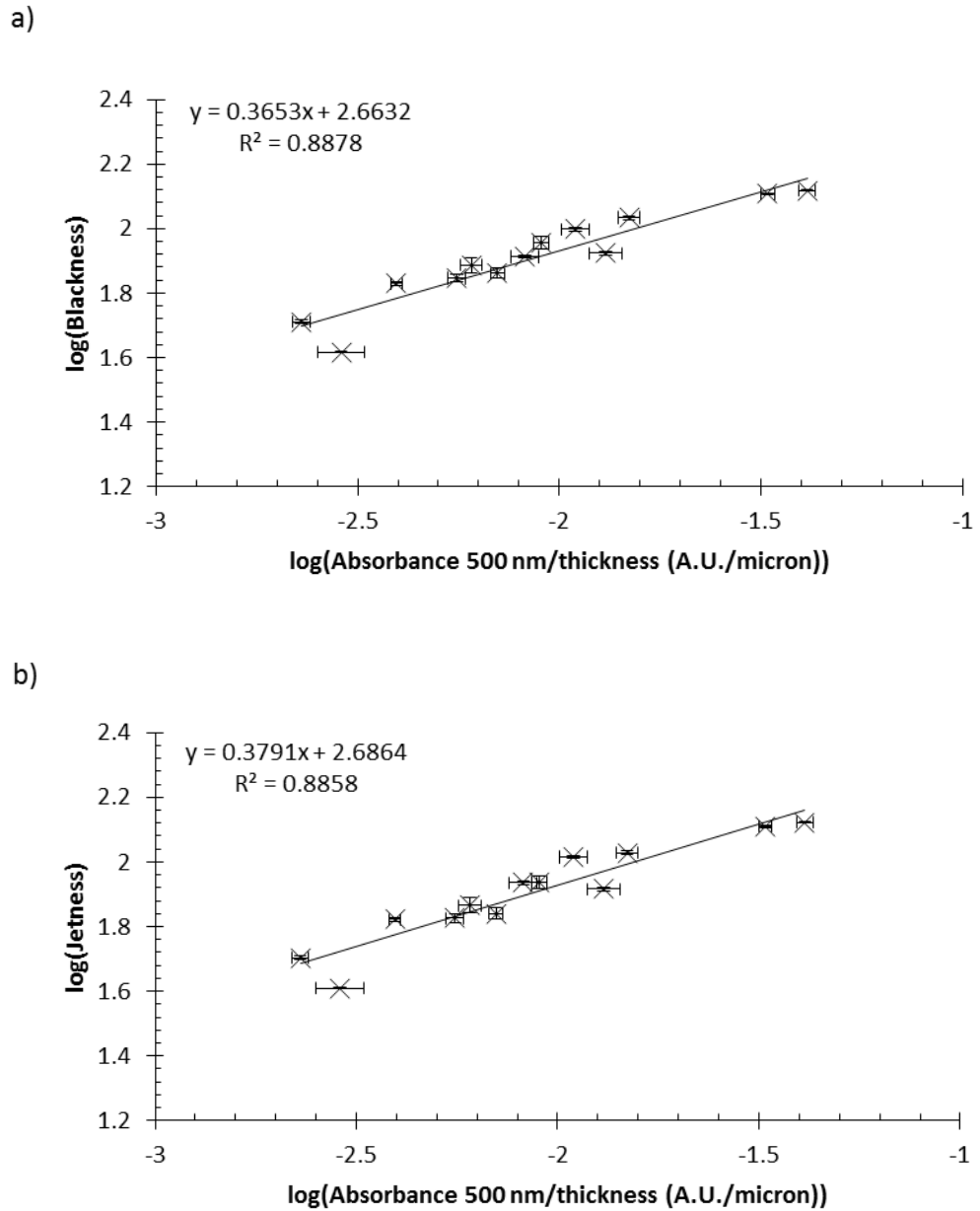


Figure 3.14 Blackness (a) and jetness (b) values of MWCNT waterborne epoxy-amine thin films as a function of the thickness normalized absorbance at 500 nm of the corresponding free film.

The blackness and jetness of the coated steel panel values increased linearly as a function of the thickness normalized absorbance value of the corresponding free film via a log-log relationship (Figure 3.14a-b;  $p < 0.05$ ); it should be noted that the data sets of

all MWCNT types were included in the regression analysis independent of surface modification and degree of agglomeration, i.e., all data sets were used to finalize the confirmation of detection and quantification. These trends were expected as increased dispersion realizes increased surface area of the light absorbing moiety and increases the visible light absorption and therefore, the blackness and jetness values.<sup>183</sup> The established statistical correlation between the absorbance and blackness properties reveals the potential for employing blackness properties as a quantitative metric of MWCNT dispersion in optically clear thin films (Figures 3.13 and 3.14). This provides an alternative method with relatively low cost equipment and high confidence to investigate CNT dispersion in coated substrates independent of investigator assumptions or additional measurements, and can be utilized as a quality control metric for in industrial applications.

### **3.5 Discussion**

The research results herein demonstrated that literature methods to quantify carbon nanotube dispersion may not accurately represent carbon nanotube dispersion states for all carbon nanotube polymeric materials, e.g., the standard literature method for calculation of the dispersion index from optical micrographs. Thus, the main objective of this research was to provide a rapid and facile non-destructive method to quantitatively discern multiwall carbon nanotube dispersion states in polymers and polymers bound to non-transparent substrates. Transmission absorption spectra of MWCNT epoxy-amine polymers indicated that increasing MWCNT degree of dispersion and exfoliation increases the visible light absorbance at all wavelengths (qualitatively verified via optical

and scanning electron microscopy). Similar trends of increasing visible light absorption with increasing exfoliation and dispersion have been observed in liquid systems for both SWCNTs<sup>172, 188</sup> and MWCNTs<sup>157, 166, 193-194</sup> for different carbon nanotube diameters, lengths, and manufacturers providing support that these methods can be broadly utilized. Furthermore, quantification of the absorbance slope at a specific wavelength (e.g.,  $A_{500\text{ nm}}$ ) as a function of concentration (effective optical absorption coefficient: EOAC) provided a quantifiable metric to compare the dispersibility of a specific MWCNT-dispersion protocol in the waterborne epoxy-amine thin films utilized herein. Although a statistically relevant slope of the absorbance as a function of MWCNT concentration was required for quantitative comparison between systems, a statistically insignificant slope was indicative of poor dispersibility.

The dispersibility of MWCNTs in a polymer bound to a non-transparent substrate was additionally represented by the trendline slope of the blackness values from colorimetric measurements as a function of MWCNT concentration similar to the visible absorption measurements. It should be noted that there appears to be a measurable saturation limit of increasing blackness values with increasing exfoliation and dispersion; this may be attributed to the convergence of blackness values to a maximum value as the particle size approaches  $\sim\frac{1}{3}$  the wavelength of incident light.<sup>183</sup> The concentration-dispersion state combination corresponding to the blackness value saturation may be dependent on both the MWCNT type and polymer matrix. However, the ratio of EOAC values of the hydroxyl-functional MWCNTs to the unmodified MWCNTs was similar in value for the both the visible absorption and colorimetric methods (when excluding the

values at saturation) further increasing confidence of using blackness properties to investigate MWCNT dispersion in polymers bound to non-transparent substrates. The established statistical correlation between the absorbance and blackness properties reveals the potential for employing blackness properties as a quantitative metric of MWCNT dispersion in optically clear coating formulations. This provides an alternative method with relatively low cost equipment and high confidence to investigate CNT dispersion in coated substrates independent of investigator assumptions or additional measurements, and can be utilized as a quality control metric for in industrial applications.

Literature examples of increased visible light absorption with increased CNT exfoliation and dispersion combined with the data reported in this Chapter suggests that the trends observed here between the visible absorption properties and the blackness properties will be applicable for other carbon nanotube/polymer systems. Furthermore, the MWCNT concentrations utilized in polymeric systems in the open literature are commonly within the concentration range utilized in this study<sup>29-30, 163-165</sup> exhibiting the practical use of the methods described herein. It is important to note that impurities such as carbon black will increase visible light absorption<sup>181</sup> and blackness values, thus, MWCNT purity should be taken into consideration before directly comparing results between systems with different carbon nanotube purities. However, the visible light absorption and blackness properties of a MWCNT-polymer system with the same MWCNT source is expected to be independent of the purity provided that any chemical modification steps do not remove the impurities. Indeed, other factors may influence the

absorbance properties, however, these factors (e.g., diameter, length, carbon black/catalyst impurities) are not accounted for in accepted literature protocols such as the dispersion index. The utilization of visible absorption measurements and blackness measurements described herein enables the rapid investigation of MWCNT dispersion over larger length-scales which increases the confidence of the measurement over the analysis of near micron and nanometer length-scales as with AFM and EM techniques.<sup>169</sup>

### **3.6 Conclusions**

The most common methods employed throughout CNT literature utilize image analysis techniques for quantifying CNT dispersion and these methods require each investigator specific and deliberately chosen assumptions and parameters or in-house derived algorithms, which increases the difficulty in directly comparing CNT dispersion states between systems and laboratories. Some literature protocols may not be available or practical for general use in all technical fields. Quantifying the trendline slope of the optical absorption/blackness properties as a function of concentration as shown herein revealed a quantitative metric for MWCNT dispersion and dispersibility in optically clear waterborne epoxy-amine free films. The data revealed that hydroxyl surface modification increased MWCNT dispersibility by ~2.8 and ~2.6 times in the waterborne epoxy-amine material combination utilized in this study by the UV absorption method and the blackness method, respectively. The agreement between the UV absorption method and the blackness method increases confidence in using either method for quantifying MWCNT dispersion. Additionally, a statistically relevant correlation between optical absorption properties of free films and measured blackness properties of the

corresponding coated substrate systems was established increasing confidence in the protocols established here. These trends were qualitatively validated via optical microscopy and scanning electron microscopy. Although the methods described herein required a minimum degree of dispersion for direct, quantitative comparisons of MWCNT dispersibility, extremely poor dispersibility was readily identified via statistically insignificant trendline slopes. The research reported here provides a rapid and economically viable protocol to investigate and quantify CNT degree of dispersion within polymer coated substrates that can be applied as a quality control metric. Furthermore, these protocols have potential to be used in applications such as extrusion, injection molding, and composites at various thicknesses and depending upon MWCNT material loading levels.

### 3.7 References

29. Deyab, M. A., Effect of Carbon Nano-Tubes on the Corrosion Resistance of Alkyd Coating Immersed in Sodium Chloride Solution. *Progress in Organic Coatings* **2015**, *85*, 146-150.
30. Jeon, H.; Park, J.; Shon, M., Corrosion Protection by Epoxy Coating Containing Multi-Walled Carbon Nanotubes. *Journal of Industrial and Engineering Chemistry* **2013**, *19* (3), 849-853.
35. Burghard, M., Electronic and Vibrational Properties of Chemically Modified Single-Wall Carbon Nanotubes. *Surface Science Reports* **2005**, *58* (1-4), 1-109.
47. Ma, P.-C.; Siddiqui, N. A.; Marom, G.; Kim, J.-K., Dispersion and Functionalization of Carbon Nanotubes for Polymer-Based Nanocomposites: A Review. *Composites Part A: Applied Science and Manufacturing* **2010**, *41* (10), 1345-1367.
65. Dresselhaus, M. S.; Dresselhaus, G.; Saito, R.; Jorio, A., Raman Spectroscopy of Carbon Nanotubes. *Physics Reports* **2005**, *409* (2), 47-99.
67. Grady, B. P., *Carbon Nanotube-Polymer Composites Manufacture, Properties, and Applications*. Wiley: Hoboken, N.J., 2011; p 352.
70. Lehman, J. H.; Terrones, M.; Mansfield, E.; Hurst, K. E.; Meunier, V., Evaluating the Characteristics of Multiwall Carbon Nanotubes. *Carbon* **2011**, *49* (8), 2581-2602.
72. Chakrapani, N.; Curran, S.; Wei, B.; Ajayan, P. M.; Carrillo, A.; Kane, R. S., Spectral Fingerprinting of Structural Defects in Plasma-Treated Carbon Nanotubes. *Journal of Materials Research* **2011**, *18* (10), 2515-2521.
75. Osswald, S.; Havel, M.; Gogotsi, Y., Monitoring Oxidation of Multiwalled Carbon Nanotubes by Raman Spectroscopy. *Journal of Raman Spectroscopy* **2007**, *38* (6), 728-736.
120. Pietraß, T.; Dewald, J. L.; Clewett, C. F. M.; Tierney, D.; Ellis, A. V.; Dias, S.; Alvarado, A.; Sandoval, L.; Tai, S.; Curran, S. A., Electron Spin Resonance and Raman Scattering Spectroscopy of Multi-Walled Carbon Nanotubes: A Function of Acid Treatment. *Journal of Nanoscience and Nanotechnology* **2006**, *6* (1), 135-140.
147. Arepalli, S., Freiman, S., Hooker, S., Migler, D, Measurement Issues in Single-Wall Carbon Nanotubes. *NIST Recommended Practice Guide* **2008**.
151. Liao, Y.-H.; Marietta-Tondin, O.; Liang, Z.; Zhang, C.; Wang, B., Investigation of the Dispersion Process of Swnts/Sc-15 Epoxy Resin Nanocomposites. *Materials Science and Engineering: A* **2004**, *385* (1-2), 175-181.
152. Grady, B. P., Effects of Carbon Nanotubes on Polymer Physics. *Journal of Polymer Science Part B: Polymer Physics* **2012**, *50* (9), 591-623.
153. Zhu, J.; Peng, H.; Rodriguez-Macias, F.; Margrave, J. L.; Khabashesku, V. N.; Imam, A. M.; Lozano, K.; Barrera, E. V., Reinforcing Epoxy Polymer Composites through Covalent Integration of Functionalized Nanotubes. *Advanced Functional Materials* **2004**, *14* (7), 643-648.
154. Coleman, J. N.; Khan, U.; Blau, W. J.; Gun'ko, Y. K., Small but Strong: A Review of the Mechanical Properties of Carbon Nanotube-Polymer Composites. *Carbon* **2006**, *44* (9), 1624-1652.

155. Pötschke, P.; Bhattacharyya, A. R.; Janke, A., Melt Mixing of Polycarbonate with Multiwalled Carbon Nanotubes: Microscopic Studies on the State of Dispersion. *European Polymer Journal* **2004**, *40* (1), 137-148.
156. Sandler, J.; Shaffer, M. S. P.; Prasse, T.; Bauhofer, W.; Schulte, K.; Windle, A. H., Development of a Dispersion Process for Carbon Nanotubes in an Epoxy Matrix and the Resulting Electrical Properties. *Polymer* **1999**, *40* (21), 5967-5971.
157. Combessis, A.; Mazel, C.; Maugin, M.; Flandin, L., Optical Density as a Probe of Carbon Nanotubes Dispersion in Polymers. *Journal of Applied Polymer Science* **2013**, *130* (3), 1778-1786.
158. Haslam, M. D.; Raeymaekers, B., A Composite Index to Quantify Dispersion of Carbon Nanotubes in Polymer-Based Composite Materials. *Composites Part B: Engineering* **2013**, *55* (0), 16-21.
159. Eckel, D. F.; Balogh, M. P.; Fasulo, P. D.; Rodgers, W. R., Assessing Organo-Clay Dispersion in Polymer Nanocomposites. *Journal of Applied Polymer Science* **2004**, *93* (3), 1110-1117.
160. Villmow, T.; Pötschke, P.; Pegel, S.; Häussler, L.; Kretzschmar, B., Influence of Twin-Screw Extrusion Conditions on the Dispersion of Multi-Walled Carbon Nanotubes in a Poly(Lactic Acid) Matrix. *Polymer* **2008**, *49* (16), 3500-3509.
161. Gao, Y.; Li, Z.; Lin, Z.; Zhu, L.; Tannenbaum, A.; Bouix, S.; Wong, C. P., Automated Dispersion and Orientation Analysis for Carbon Nanotube Reinforced Polymer Composites. *Nanotechnology* **2012**, *23* (43), 435706-435706.
162. *Polymer Nanotubes Nanocomposites Synthesis, Properties and Applications*. 2 ed.; Scrivener Publishing: Beverly, MA 2014; p 470.
163. Gojny, F. H.; Schulte, K., Functionalisation Effect on the Thermo-Mechanical Behaviour of Multi-Wall Carbon Nanotube/Epoxy-Composites. *Composites Science and Technology* **2004**, *64* (15), 2303-2308.
164. Koo, J.; Shin, K.; Seo, Y.-S.; Koga, T.; Park, S.; Satija, S.; Chen, X.; Yoon, K.; Hsiao, B. S.; Sokolov, J. C.; Rafailovich, M. H., Stabilizing Thin Film Polymer Bilayers against Dewetting Using Multiwalled Carbon Nanotubes. *Macromolecules* **2007**, *40* (26), 9510-9516.
165. Xu, X.; Thwe, M. M.; Shearwood, C.; Liao, K., Mechanical Properties and Interfacial Characteristics of Carbon-Nanotube-Reinforced Epoxy Thin Films. *Applied Physics Letters* **2002**, *81* (15), 2833-2835.
166. Yu, J.; Grossiord, N.; Koning, C. E.; Loos, J., Controlling the Dispersion of Multi-Wall Carbon Nanotubes in Aqueous Surfactant Solution. *Carbon* **2007**, *45*, 618-623.
167. Farrokhpay, S.; Morris, G. E.; Fornasiero, D.; Self, P., Titania Pigment Particles Dispersion in Water-Based Paint Films. *JCT Research* **2006**, *3* (4), 275-283.
168. Pazokifard, S.; Farrokhpay, S.; Mirabedini, M.; Esfandeh, M., Surface Treatment of TiO<sub>2</sub> Nanoparticles Via Sol-Gel Method: Effect of Silane Type on Hydrophobicity of the Nanoparticles. *Progress in Organic Coatings* **2015**, *87*, 36-44.
169. Farrokhpay, S., Application of Spectroscopy and Microscopy Techniques in Surface Coatings Evaluation: A Review. *Applied Spectroscopy Reviews* **2012**, *47* (3), 233-243.

170. Kovacs, J. Z.; Andresen, K.; Pauls, J. R.; Garcia, C. P.; Schossig, M.; Schulte, K.; Bauhofer, W., Analyzing the Quality of Carbon Nanotube Dispersions in Polymers Using Scanning Electron Microscopy. *Carbon* **2007**, *45* (6), 1279-1288.
171. Zhao, M.; Ming, B.; Kim, J.-W.; Gibbons, L. J.; Gu, X.; Nguyen, T.; Park, C.; Lillehei, P. T.; Villarrubia, J. S.; Vladar, A.; Liddle, J. A. *New Insights into Subsurface Imaging of Carbon Nanotubes in Polymer Composites Via Scanning Electron Microscopy*; National Institute of Standards and Technology: 2015.
172. Grossiord, N.; Loos, J.; Meuldijk, J.; Regev, O.; Miltner, H. E.; Van, M. B.; Koning, C. E. In *Conductive Carbon-Nanotube/Polymer Composites: Spectroscopic Monitoring of the Exfoliation Process in Water and the Crucial Role of Wetting*, Nano Science and Technology Institute: 2006; pp 222-225.
173. Ferreira, T.; Paiva, M.; Pontes, A., Dispersion of Carbon Nanotubes in Polyamide 6 for Microinjection Moulding. *Journal of Polymer Research* **2013**, *20* (11), 1-9.
174. Jurewicz, I.; Worajittiphon, P.; King, A. A.; Sellin, P. J.; Keddie, J. L.; Dalton, A. B., Locking Carbon Nanotubes in Confined Lattice Geometries--a Route to Low Percolation in Conducting Composites. *Journal Physical Chemistry B* **2011**, *115* (20), 6395-400.
175. Vandervorst, P.; Lei, C. H.; Lin, Y.; Dupont, O.; Dalton, A. B.; Sun, Y. P.; Keddie, J. L., The Fine Dispersion of Functionalized Carbon Nanotubes in Acrylic Latex Coatings. *Progress in Organic Coatings* **2006**, *57* (2), 91-97.
176. Curtzwiler, G.; Costanzo, P. J.; Fernando, R.; Danes, J. E.; Vorst, K., Thermal-Initiated Hydroxyethyl Methacrylate Functionalization of Multiwalled Carbon Nanotubes. *Journal of Applied Polymer Science* **2011**, *121* (2), 964-969.
177. Rastogi, R.; Kaushal, R.; Tripathi, S. K.; Sharma, A. L.; Kaur, I.; Bharadwaj, L. M., Comparative Study of Carbon Nanotube Dispersion Using Surfactants. *Journal of Colloid and Interface Science* **2008**, *328* (2), 421-428.
178. Bakshi, S. R.; Batista, R. G.; Agarwal, A., Quantification of Carbon Nanotube Distribution and Property Correlation in Nanocomposites. *Composites Part A: Applied Science and Manufacturing* **2009**, *40* (8), 1311-1318.
179. Kashiwagi, T.; Fagan, J.; Douglas, J. F.; Yamamoto, K.; Heckert, A. N.; Leigh, S. D.; Obrzut, J.; Du, F.; Lin-Gibson, S.; Mu, M.; Winey, K. I.; Haggemueller, R., Relationship between Dispersion Metric and Properties of Pmma/Swnt Nanocomposites. *Polymer* **2007**, *48* (16), 4855-4866.
180. Sul, I. H.; Youn, J. R.; Song, Y. S., Quantitative Dispersion Evaluation of Carbon Nanotubes Using a New Analysis Protocol. *Carbon* **2011**, *49* (4), 1473-1478.
181. Sharif Sh, M.; Golestani Fard, F.; Khatibi, E.; Sarpoolaky, H., Dispersion and Stability of Carbon Black Nanoparticles, Studied by Ultraviolet-Visible Spectroscopy. *Journal of the Taiwan Institute of Chemical Engineers* **2009**, *40* (5), 524-527.
182. Goldschmidt, A.; Streitberger, H.-J., *Basics of Coating Technology*. 2nd ed.; Vincentz Network: Hannover, 2007.
183. Koleske, J. V., *Paint and Coating Testing Manual*. 15th ed.; ASTM International: West Conshohocken, 2012.
184. Nsib, F.; Ayed, N.; Chevalier, Y., Selection of Dispersants for the Dispersion of Carbon Black in Organic Medium. *Progress in Organic Coatings* **2006**, *55* (4), 303-310.

185. Gordon Carbon Blackness [My], Jetness [Mc], Undertone [Dm] and Tint Strength [T]. <https://measuretruecolor.hunterlab.com/2015/06/02/carbon-blackness-my-jetness-mc-undertone-dm-and-tint-strength-t/> (accessed April 4).
186. Xia, H.; Qiu, G.; Wang, Q., Polymer/Carbon Nanotube Composite Emulsion Prepared through Ultrasonically Assisted in Situ Emulsion Polymerization. *J. Appl. Polym. Sci.* **2006**, *100* (Copyright (C) 2012 American Chemical Society (ACS). All Rights Reserved.), 3123-3130.
187. Grossiord, N.; Loos, J.; Meuldijk, J.; Regev, O.; Miltner, H. E.; Van Mele, B.; Koning, C. E., Conductive Carbon-Nanotube/Polymer Composites: Spectroscopic Monitoring of the Exfoliation Process in Water. *Composites Science and Technology* **2007**, *67* (5), 778-782.
188. Grossiord, N.; Regev, O.; Loos, J.; Meuldijk, J.; Koning, C. E., Time-Dependent Study of the Exfoliation Process of Carbon Nanotubes in Aqueous Dispersions by Using Uv-Visible Spectroscopy. *Analytical Chemistry* **2005**, *77*, 5135-5139.
189. Singh, P.; Campidelli, S.; Giordani, S.; Bonifazi, D.; Bianco, A.; Prato, M., Organic Functionalisation and Characterisation of Single-Walled Carbon Nanotubes. *Chemical Society Reviews* **2009**, *38* (8), 2214-2230.
190. Anonymous Carbon Blackness [My], Jetness [Mc], Undertone [Dm] and Tint Strength [T]. <http://measuretruecolor.hunterlab.com/2015/06/02/carbon-blackness-my-jetness-mc-undertone-dm-and-tint-strength-t/> (accessed February 1).
191. Ellison, S.; Barwick, V.; Trevor, F., *Practical Statistics for the Analytical Scientist: A Bench Guide*. 2nd ed.; The Royal Society of Chemistry: Cambridge, 2009.
192. Baxbaum, G.; Pfaff, G., *Industrial Inorganic Pigments*. 3rd ed.; Wiley-VCH Verlag GmbH & Co. KGaA: Weinheim, 2005.
193. Barzegar-Bafrooei, H.; Ebadzadeh, T.; Tazike, M., A Survey on Dispersion Mechanisms of Multi-Walled Carbon Nanotubes in an Aqueous Media by Uv-Vis, Raman Spectroscopy, Tga, and Ftir. *Journal of Dispersion Science and Technology* **2011**, *33* (7), 955-959.
194. Li, Q.; Church, J. S.; Kafi, A.; Naebe, M.; Fox, B. L., An Improved Understanding of the Dispersion of Multi-Walled Carbon Nanotubes in Non-Aqueous Solvents. *Journal of Nanoparticle Research* **2014**, *16* (7), 2513.

CHAPTER IV – COMPARISON OF THE ADDED VALUE FOR CORROSION  
PERFORMANCE OF CHEMICALLY MODIFIED MULTIWALL CARBON  
NANOTUBE EPOXY-AMINE COATING SYSTEMS ON STEEL SUBSTRATES

**4.1 Abstract**

Carbon nanotubes are well-known for their ability to improve critical performance characteristics of polymeric materials in applications such as protective coatings and structural composites. The research objective of this Chapter was to quantify and understand the influence of chemically modified multiwall carbon nanotubes (MWCNTs) (modified with hydroxyl, amine, or epoxy functionalities) on the corrosion performance of epoxy-amine thin films applied to steel substrates. Free films formulated with chemically modified MWCNTs were characterized via attenuated total reflectance-Fourier transform infrared spectroscopy, Raman spectroscopy, differential scanning calorimetry, dynamic vapor sorption analysis, scanning electron microscopy, and UV-vis spectroscopy. Coated steel substrates were challenged against ASTM B117 salt fog conditions (5% NaCl at 35 °C) and were characterized via optical imaging as a function of exposure time. At the end of the salt fog test cycle, the coatings were removed from the steel substrate and the substrate/coating interface of the coating investigated by scanning electron microscopy (SEM)-energy dispersive X-ray spectroscopy (EDS). Overall, MWCNTs improved the corrosion resistance potential of the coatings compared to the control (without MWCNTs) when evaluated with and without a macroscopic breach (scribe). Regardless of the chemical functionalities on each of the MWCNTs, all MWCNT containing coatings performed similarly during corrosion testing under the

conditions of this investigation. SEM-EDS analysis indicated a qualitative reduction in the number of corrosion products (iron oxides/hydroxides and iron chlorides) and NaCl at the coating/substrate interface of MWCNT possessing thin films compared to each example without MWCNTs. Interestingly, the water vapor diffusion properties for all thin films were independent of the presence or absence of MWCNTs. The data revealed that MWCNTs are capable of blocking, absorbing, or neutralizing corrosive species at the coating-substrate interface due to a redistribution of water hydrogen bonding and strong interactions between the permeating ions and various MWCNT structural features.

## **4.2 Introduction**

Adsorbed or covalently attached polymeric materials and small molecules facilitate increased dispersion and inhibit re-agglomeration of the CNTs due to steric repulsion and favorable CNT-solvent/matrix interactions.<sup>56</sup> Chemical modification of the CNT side wall and end caps have been demonstrated for enhanced dispersion and interaction with host media.<sup>36, 45, 55-57, 195-198</sup> The most reactive sites on CNTs are where bond strain is highest and are most susceptible to chemical attack, e.g., smaller diameter (higher curvature), defects, and the tube ends.<sup>67, 199</sup> Chemical modification has the intrinsic drawback of interrupting the  $\pi$ -conjugated framework which reduces the unique CNT properties making control over functionalization a necessity. Gojny and co-workers indicated that modification of ~ 1% of the carbon atoms on the CNT surface will significantly enhance the CNT-polymer interfacial shear strength without having detrimental impacts on CNT properties.<sup>55</sup> However, the reduction of these properties is

generally outweighed by increased exfoliation and dispersion, and consequently, final composite properties realized by CNT functionalization.<sup>45, 53</sup>

Chemical modification modifies the stacking properties of the CNTs which debundles nanotubes provided that the chemical species can intercalate between bundles or can be attached while exfoliated.<sup>45</sup> The two common methods of covalent functionalization involve oxidation in strong acid mixtures and free radical chemistry (Figure 4.1).<sup>45, 53, 67, 200</sup> Both methods interrupt the  $\pi$ -conjugated framework which reduces electrical conductivity, thermal conductivity, and mechanical properties of the CNT, thus, it is critical to control and monitor the degree of functionalization.<sup>45, 53</sup>

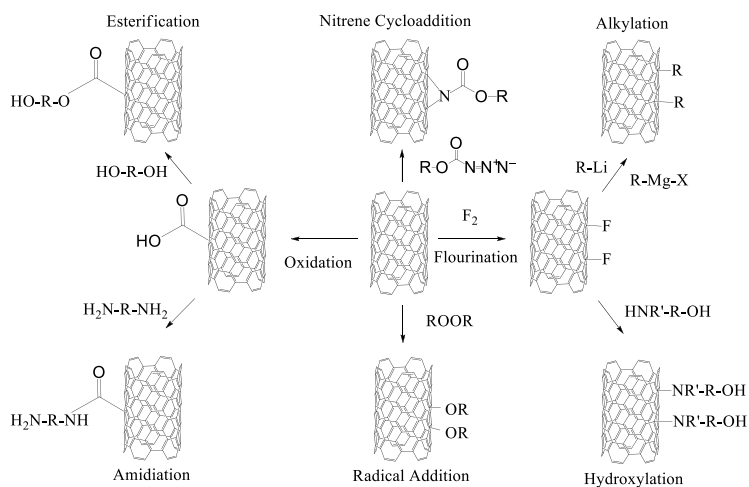


Figure 4.1 Synthetic approaches to functionalize the surface of carbon nanotubes.

Note: image adapted from Ma and co-workers and Cheng and co-workers.<sup>47, 59</sup>

## 4.2.2 Ultrasonication

Ultrasonication, or sonochemistry when chemical reactions occur, utilizes mechanical vibrations to induce ultrasonic waves in liquid media producing various physical and chemical effects.<sup>201-205</sup> Perhaps the most important physical effect of ultrasonication in liquid media containing nanoparticles is deagglomeration, exfoliation,

and dispersion.<sup>47, 201, 206</sup> Ultrasonication of liquids generates a series of compression and rarefaction cycles resulting in a phenomenon known as acoustic cavitation.<sup>201, 204</sup> A bubble is generated during the rarefaction phase due to the low pressure environment, which grows until it becomes unstable and collapses within a few microseconds.<sup>201-202, 205</sup> Acoustic cavitation produces localized hot spots up to 5000 K, 2000 atmospheres of pressure, and heating/cooling rates up to 10,000 K/s.<sup>201-202, 204-205</sup> Large shear and strain gradients generate high liquid mobility due to rapid streaming of solvent molecules around the cavitation bubble; the subsequent intense shock waves generated by the bubble collapse overcomes the strong van der Waals forces within CNT bundles resulting in CNT exfoliation and debundling.<sup>53, 202</sup>

The conditions generated during ultrasonication depend on the frequency, amplitude, and solvent vapor pressure (reduced vapor pressure in the bubble allows for a more energetic bubble collapse).<sup>202-204, 207</sup> When the cavitation bubble forms next to a surface, the bubble is asymmetrical and its collapse results in the formation of microjets traveling at speeds up to 500 m/s.<sup>201-203, 205</sup> However, microjets will only form when the surface size is several times larger than the resonance bubble size.<sup>202</sup> Thus, for ultrasonic frequencies of 20 kHz, microjets do not form near solid particles smaller than approximately 200 microns, thus, microjets only contribute to break apart agglomerates larger than 200 microns and the large shear gradients and shockwaves of collapsing cavitation bubbles exfoliate smaller the agglomerates.<sup>202, 205</sup> Although ultrasonication facilitates higher degrees of CNT exfoliation, the intense conditions can also cause tube rupture or damage.<sup>53, 202, 208</sup> Beneficially, the conditions generated by ultrasonication can

increase reaction rates at reduced bulk reaction temperatures.<sup>186, 201, 204, 207</sup> Generally, lower frequencies have been shown to generate more physical effects than chemical and the amount of chemical effects sharply increases with the ultrasonic frequency.<sup>203, 207</sup>

As described in more detail in Chapter I, the corrosion of steel substrates is thermodynamically favored in the presence of oxygen and conductive water.<sup>58</sup> It was hypothesized that increasing the tortuosity of corrosion inducing environmental contaminants via incorporation of MWCNTs, i.e., reducing the water solvated-ion concentration, and thus water conductivity, at the substrate/coating interface will reduce the corrosion rate of the substrate. Accordingly, if the surface functionality of multiwall carbon nanotubes and subsequent interactions with the polymer matrix are controlled, then the coating performance characteristics can be designed for increased corrosion rate control. The research objective of this Chapter was to quantify the effects and influence of chemically modified multiwall carbon nanotubes (MWCNTs) on the performance characteristics of corrosion control coatings. Free films of each material combination were characterized for their glass transition temperature ( $T_g$ ), secondary interactions via vibrational spectroscopic methods (Raman and FTIR spectroscopy), water vapor diffusivity, and corrosion resistance of coated steel substrates in a 5% NaCl salt fog environment (ASTM B117).

## **4.3 Experimental**

### **4.3.1 Materials**

Multiwall carbon nanotubes (MWCNT) were procured from Cheap tubes, Inc (diameter 8-15 nm; length 10-30  $\mu\text{m}$ ) and were used as-received (unmodified) and in

modified form as described below. HPLC grade tetrahydrofuran (THF), dry tetrahydrofuran (99.85%), parachlorobenzotrifluoride (PCBTF), hexanes, m-xylene (99% +), 2,2'-azobis[2-methyl-N-(2-hydroxyethyl) propionamide] (AMP), 4,4'-azobis(4-cyanovaleric acid) (ABCVA), toluene diisocyanate (TDI), and EPON<sup>®</sup> 1001F (Epoxy), EPON<sup>®</sup> 825, Polylink<sup>®</sup> 4200, Jeffamine<sup>®</sup> ED-600, and 2-methylpentamethylenediamine (MPMD) were used as received.

### **4.3.2 Chemical Modification of Multiwall Carbon Nanotubes**

#### **4.3.2.1 Radical Addition to MWCNT**

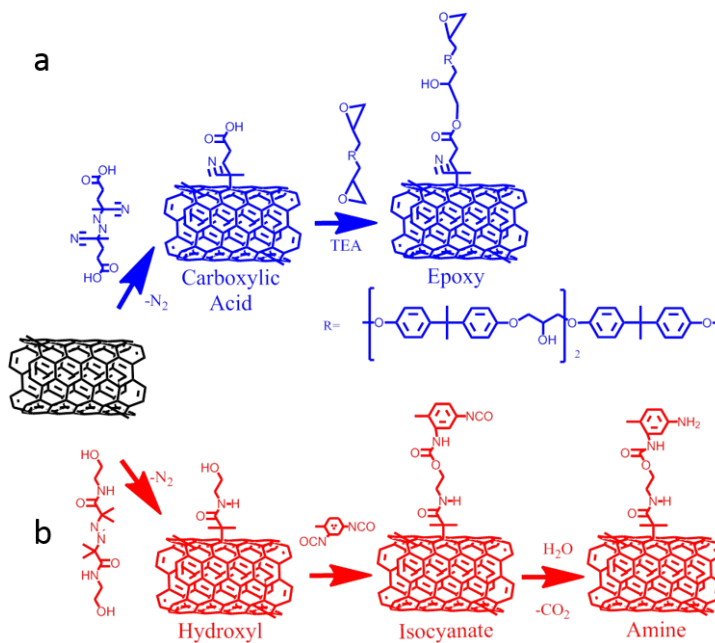
150 mg of unmodified MWCNTs and 30 mL of THF were added to a two neck round bottom flask (RBF) and probe sonicated (10 minutes, 15 W). The solution was cooled to ambient temperature and 1.0 g of ABCVA was added to the RBF, sealed with rubber septa, and purged with nitrogen for 10 minutes. The RBF was bath sonicated at 50 °C for 180 minutes to produce carboxylic acid functional MWCNTs (ABCVA MWCNTs) according to the pathway a in Scheme 4.1. The carboxylic acid MWCNTs were washed four times with THF via four centrifugation/suspension cycles. To produce hydroxyl functional MWCNTs (hydroxyl MWCNTs), the same procedure was employed substituting AMP as the radical source and a 70/30 v/v mixture of THF/DI H<sub>2</sub>O as the solvent (Scheme 4.1, pathway b).

#### **4.3.2.2 Subsequent Chemical Modification of ABCVA and AMP MWCNTs**

Carboxylic acid functional (ABCVA MWCNTs) were dispersed in THF via probe sonication (10 minutes, 15 W) and then added dropwise into a 1000 x equivalent excess EPON<sup>®</sup> 1001F dissolved in 30 mL THF. Triethylamine catalyst (15% by equivalent on

epoxide) was added to the blend and heated to 60 °C for 6 hours (Scheme 4.1, pathway a). The epoxy functionalized MWCNTs were purified via centrifugation/suspension four times in THF.

Hydroxyl functional MWCNTs were dispersed in dry THF via tip sonication (10 minutes, 15 W) and then added dropwise to 10 mL of a 1/1 v/v TDI/dry THF mixture in an RBF submerged in a bath sonicator set to 50 °C. The system was sealed with septa, bath sonicated for 90 minutes at 50 °C, and then heated to 60 °C for 24 hours with a heating mantle. The isocyanate functional MWCNTs were washed four times with dry THF via centrifugation. The functionalized MWCNTs were tip sonicated for (10 minutes, 6 W) in dry THF, added dropwise to a 30/70 mixture of THF/DI H<sub>2</sub>O at 50 °C under continuous bath sonication conditions for 90 minutes, and then heated at 60 °C for 16 hours (Scheme 4.1, pathway b). The product was washed four times via centrifugation/suspension cycles with a THF/DI H<sub>2</sub>O solution to yield amine functional MWCNTs.



Scheme 4.1 Synthetic scheme for chemical modification of MWCNTs to produce surface modified MWCNTs.

Note: pathway “a” was employed to synthesize epoxy functional MWCNTs and pathway “b” was employed to synthesize hydroxyl and amine MWCNTs.

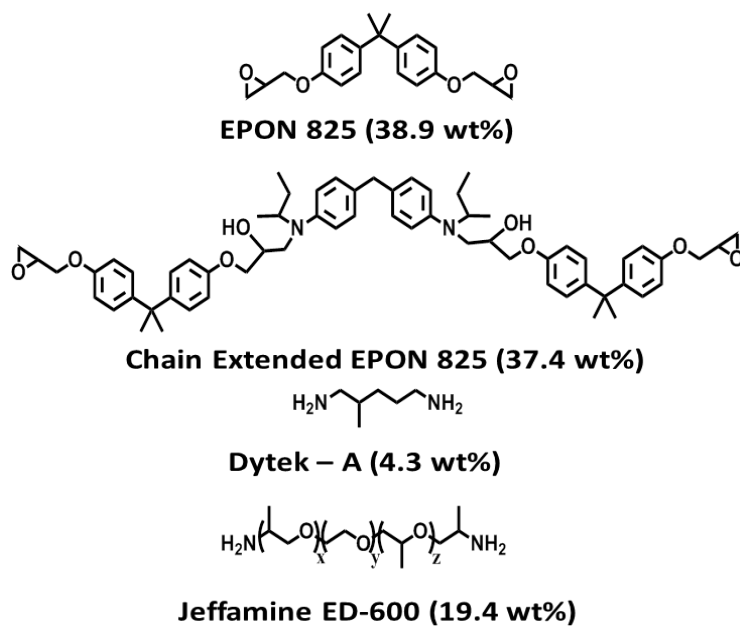
### 4.3.3 Characterization of MWCNT Functionalization

The unmodified MWCNT and modified MWCNTs were each characterized with ten Raman spectra collected with a Thermo Scientific DXR Raman microscope equipped with a 532 nm excitation laser through a 10x optical lens. The detector was set to auto-exposure to achieve a signal to noise ratio greater than 100. Each spectrum was baseline corrected and deconvoluted with four peaks (as noted in Chapter II) using OMNIC for Dispersive Raman 8.3 software and the  $D'/G$  ratio was utilized to investigate MWCNT molecular structure changes from chemical modifications.<sup>70, 72, 120</sup> The mass of organic molecules attached to the MWCNTs was quantified via thermogravimetric analysis (TGA) in air at a heating rate of 5 °C/minute from ambient temperature to 800 °C in a TA Instruments Q500 thermogravimetric analyzer.<sup>147</sup> The equivalents of each functional

group per gram MWCNT was calculated from the projected structure according to Scheme 4.1.<sup>189</sup>

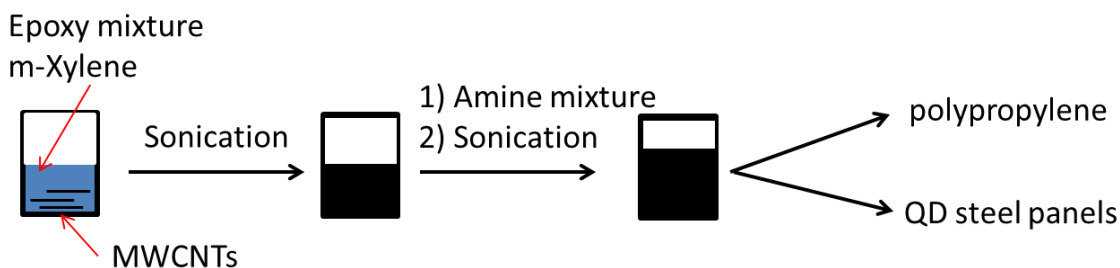
#### **4.3.4 Fabrication of Model Epoxy-Amine Coating and Free Films Containing Functionalized MWCNTs**

Epon 825<sup>®</sup> was chain extended with Polylink<sup>®</sup> 4200 to produce an “epoxy trimer” under a nitrogen atmosphere at 140 °C for five hours. Parachlorobenzotrifluoride was added after cooling to 70 °C to reduce the viscosity (78.5% solids). The appropriate amount and type of MWCNTs (0.50 wt% on polymer solids) was pulverized and placed in a scintillation vial followed by EPON<sup>®</sup> 825 (1.94 g), epoxy trimer (2.38 g), and m-xylene (8.6 g), tip sonicated for three minutes at ~ 10 W followed by bath sonication at ambient temperature for 30 minutes. Jeffamine<sup>®</sup> ED-600 (0.972 g) and 2-methylpentamethylenediamine (0.214 g) were mixed and added to the epoxy/MWCNT/m-xylene mixture and bath sonicated for an additional 30 minutes (Schemes 4.2 and 4.3). A control was prepared by repeating the material combination without MWCNTs.



Scheme 4.2 Epoxy-amine thin polymer film material combination and structures.

Each thin film material combination was spray applied at ~ 35 wt% solids either to acetone cleaned SAE 1008/1010 carbon steel with an average surface roughness < 20 microinches (QD steel panels; QPanel) for evaluation via ASTM B117 or acetone cleaned polypropylene sheets to obtain free films (Scheme 4.3). All coatings were conditioned at ambient temperature for one hour followed by heating in an oven at 60 °C/1 hour + 80 °C/1 hour.



Scheme 4.3 Fabrication scheme of multiwall carbon nanotube epoxy-amine free films and coated steel panels.

### 4.3.5 Coating Characterization

The glass transition temperature ( $T_g$ ) of each thin film material combination was measured via differential scanning calorimetry in a nitrogen atmosphere between -40 to 100 °C at a heating rate 10 °C/minute and cooling rate 5 °C/minute. Residual volatile content (mixture of solvent and ambient moisture) was investigated via thermogravimetric analysis (TGA) at a heating rate 10 °C/minute from ambient temperature to 700 °C in air; the residual volatile content after cure and storage in ambient condition was considered to be the mass loss at 200 °C.

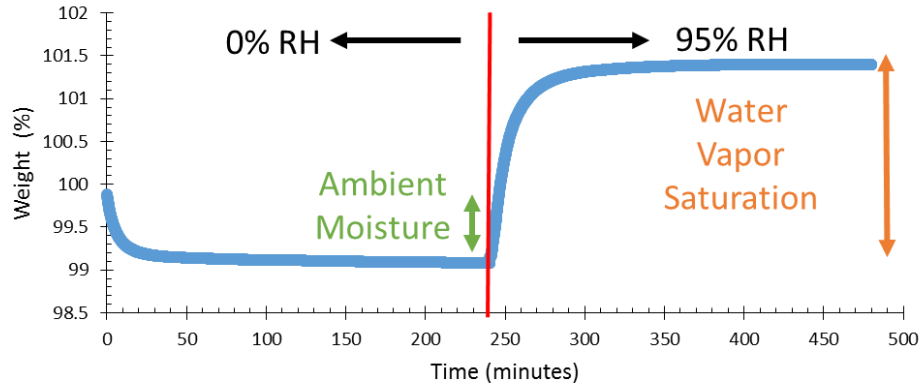
Raman spectroscopy and attenuated total reflectance-Fourier transform infrared (ATR-FTIR) spectroscopy were utilized to investigate the influence of functionalized and non-functionalized MWCNTs on the molecular interactions within the polymer network. Thus, the spectrum of the parent polymer material combination was subtracted from the corresponding spectrum of epoxy-amine coatings containing MWCNTs (Equation 4.1). Attenuated total reflectance-Fourier transform infrared (ATR-FTIR) spectra were collected on a diamond crystal with 32 scans and a resolution of 2  $\text{cm}^{-1}$  using a Smart iTR ATR stage attached to a Nicolet 6700 Fourier-transform infrared spectrometer. Each spectrum was baseline corrected and normalized to the maximum intensity at  $\sim 2865 \text{ cm}^{-1}$ .<sup>14, 16</sup> Raman spectra were collected with a Thermo Scientific DXR Raman microscope equipped with a 532 nm excitation laser through a 10x optical lens (spot size  $\sim 2 \mu\text{m}$ ). The detector was set to auto-exposure to achieve a signal to noise ratio greater than 100.

$$A(\nu)_{\text{subtracted spectrum}} = A(\nu)_{\text{MWCNT}} - A(\nu)_{\text{No MWCNT}} \quad \text{Equation 4.1}$$

Field emission scanning electron microscopy (FE-SEM) and ultraviolet visible spectroscopy were employed to investigate MWCNT dispersion as a function of chemical modification. Each coating type was fractured under cryogenic conditions then the cross section silver sputter coated with an Emitech K550X sputter coater. The silver sputter coated cross sections were scanned with a Zeiss Sigma-VP field emission scanning electron microscope (FE-SEM) operating at 20 kV electron acceleration voltage with a working distance of 2-5 mm. MWCNT dispersion of the free films was investigated quantitatively via transmission ultraviolet-visible absorption (UV-Vis) spectroscopy and quantifying the absorbance at 500 nm as noted in Chapter III.

Water vapor diffusivity, ambient moisture, and water vapor saturation at equilibrium were determined via dynamic vapor sorption analysis (Scheme 4.4).<sup>209</sup> Each specimen was desiccated in the instrument at 0% RH, 25 °C for 240 minutes followed by exposure to a 95% RH atmosphere at 25 °C for 240 minutes using a TA Instruments Q5000 Sorption Analyzer. The water vapor diffusivity was calculated following the procedure of Burnett and co-workers for values between  $0.1 < M_t/M_\infty < 0.4$  (Equation 4.2).<sup>209</sup>

$$\frac{M_t}{M_\infty} = \frac{4}{d} \sqrt{\frac{Dt}{\pi}} \quad \text{Equation 4.2}$$



Scheme 4.4 Protocol to determine ambient moisture content, water vapor diffusivity, and water vapor saturation by dynamic vapor sorption analysis.

#### 4.3.6 Corrosion Analysis

Corrosion rate analysis was carried out following ASTM B117 salt fog exposure conditions and employing corrosion area analysis at  $t = 2, 4, 22, 24, 48, 72, \& 192$  hours. Exposed samples were removed from the test chamber, rinsed with DI water, and blotted dry prior to analysis. The instantaneous percent corrosion area was determined as the area of visual corrosion divided by exposure area according to ASTM D610-08(2012);<sup>210</sup> the exposure area was defined by taping the edges of the panel with 3M 8992 polyester film tape (Figure 4.2). Images were captured via an Epson scanner to document corrosion progression, cathodic delamination, and whitening as a function of time. Images were converted into PDF files and Adobe Acrobat X Pro<sup>®</sup> was employed for quantitative area analysis.

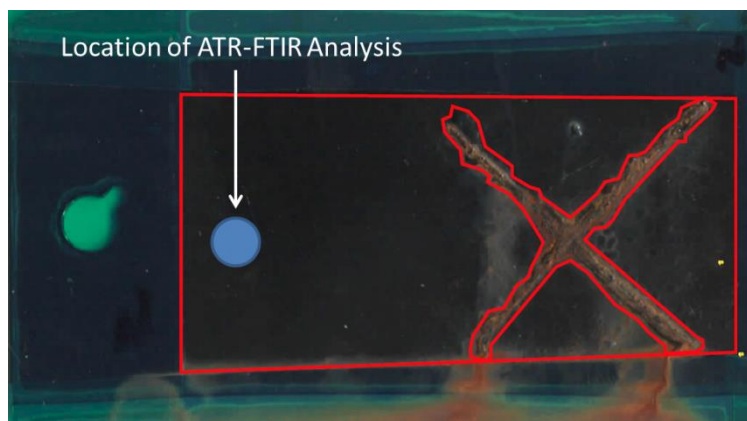


Figure 4.2 Representative panel for the semi-quantitative corrosion area determination and location of ATR-FTIR analyses.

#### 4.3.7 Water Hydrogen Bonding States

Attenuated total reflectance-Fourier transform infrared (ATR-FTIR) spectra were collected (Figure 4.2) at each time point to determine the water hydrogen bonding interactions at the coating/air interface. Each spectrum was collected on a diamond crystal in the same approximate X-Y spatial coordinates of the coating (near the scribe and away from the scribe) with 32 scans and a resolution of  $2\text{ cm}^{-1}$  using a Smart iTR ATR stage attached to a Nicolet 6700 Fourier-transform infrared spectrometer. Each spectrum was baseline corrected and normalized to the maximum intensity at  $\sim 2865\text{ cm}^{-1}$ .<sup>14, 16</sup> A desiccated (0% RH) free film specimen was considered the reference material for subtraction from the spectrum at time  $t$  and  $t=0$ , *ambient* (Equation 4.3). The O-H stretching  $\nu_{(\text{OH})}$  region of the subtracted ATR-FTIR spectrum was deconvoluted into five peaks corresponding to the Fermi overtone, free water ( $S_0$ ), and bound water states (singly-bound ( $S_1$ ) and multi-bound ( $S_2'$ ,  $S_2''$ )) utilizing a Gauss-Lorentz line shape via OMINC 8.3 software (Figure 4.3).<sup>15-16, 211</sup> The percent of each water state was calculated via quantification of the area of each deconvoluted peak. The peak area corresponding

to  $S_2'$  and  $S_2''$  were combined and was considered the total multi-bound water; the Fermi overtone peak was excluded from the total area prior to calculations.

$$A(\nu)_{\text{subtracted spectrum}} = A(\nu)_{\text{time=t}} - A(\nu)_{\text{t=0,desiccated}} \quad \text{Equation 4.3}$$

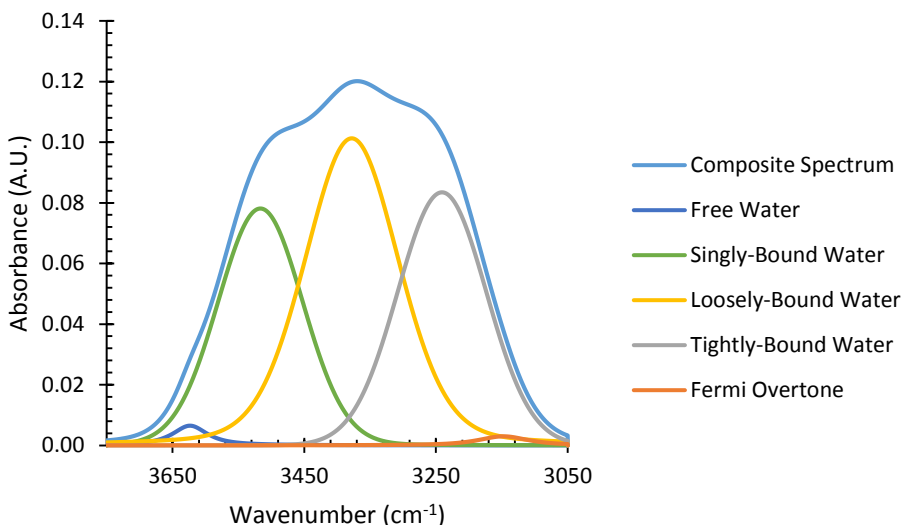
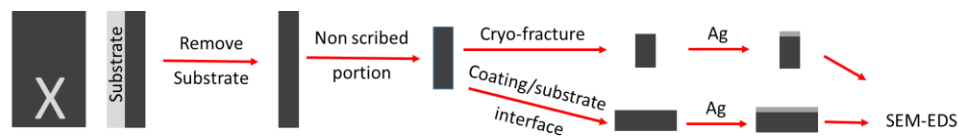


Figure 4.3 Representative deconvolution of the subtracted ATR-FTIR spectral hydroxyl region into various water interactions.

#### 4.3.8 Post-Exposure Analysis

Post-exposure analysis of the polymer thin film qualitatively investigated ion transport through the coating to the substrate. The thin film of each panel was removed from the substrate; a specimen away from the scribe (Scheme 4.5) was sectioned for analysis of the polymer thin film at the polymer/substrate interface and the cross section. A portion was removed from this specimen and cryo-fractured to expose the polymer cross section. Each specimen was sputter coated with silver as described in Section 4.3.5 and energy dispersive X-ray spectroscopy was used to qualitatively identify inorganic elements (e.g. Na, Fe, Cl) using a Zeiss Sigma-VP FE-SEM equipped with a Thermo Ultradry energy dispersive X-ray spectrometer.



Scheme 4.5 Protocol for post-exposure coating analysis after 168 hours of salt fog exposure.

#### 4.3.9 Statistical Analysis

A one-way ANOVA was employed at a 95% confidence level via MiniTab 17 software to investigate differences in mean property values and Tukey's post-hoc pairwise comparison was utilized to group means ( $n \geq 3$ ) that were statistically the same.<sup>191, 212</sup> The statistical significance of linear trendlines between data sets was accomplished via linear regression utilizing an  $\alpha=0.05$ .

### 4.4 Results

#### 4.4.1 MWCNT Characterization

Differences in detectable mass loss events between control and surface modified (hydroxyl, amine, epoxy) functionalized samples via thermogravimetric analysis provided indirect and yet consistent support for successful surface modification of the MWCNT surface chemistry. Thermogravimetric analysis was employed to determine the functional group equivalents per mass MWCNT and Raman spectroscopy was employed to investigate changes in MWCNT molecular structure for each synthetic step (Scheme 4.1). The equivalents per gram MWCNT were statistically the same through each synthetic pathway indicating that there was a 1:1 addition of the small molecules directly attached to the MWCNT surface via the radical addition. Assuming a diameter of 15 nm and a length of 10  $\mu\text{m}$ , it was calculated that the functional group density was

~ 0.15 mmol/gram. The mass percent of the AMP (hydroxyl) molecule was below the limit of detection for ATR-FTIR spectroscopy as expected from literature and past experience. Even though organic mass was detected via TGA, the D'/G ratio of the Raman spectra indicated that there was no detectable change in the molecular structure of the MWCNTs through either synthetic pathway in Scheme 4.1; this suggested that chemical functionalities were added to the MWCNTs without significant degradation to MWCNT intrinsic properties. The functional group density corresponded to changes of less than 0.01% of the total carbon on the surface of the MWCNT, which was the probable reason for non-statistical changes of the D'/G ratio (Figure 4.4).

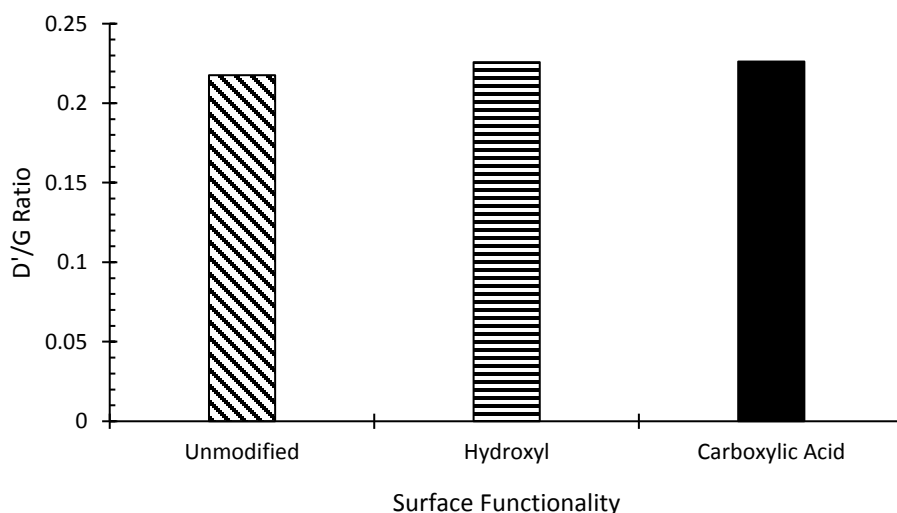


Figure 4.4 D'/G ratio of the unmodified and hydroxyl surface modified MWCNTs employing a four peak deconvolution protocol.

#### 4.4.2 Coating Microstructure and Carbon Nanotube Dispersion

Generally, the domain size and nodules of all epoxy-amine coatings was 30-50 nm in diameter similar to what has been observed in other epoxy-amine systems.<sup>213</sup> Investigation of the fractured surfaces suggested that the epoxy-amine matrix strongly

interacted with the carbon nanotube surface as nodules were observed on all surfaces of the MWCNTs types independent of chemical functionality.<sup>165</sup> Specifically, the diameters of MWCNTs protruding from the fracture surface were in the range of 80-120 nm which indicated that approximately one domain of the epoxy-amine matrix was strongly adsorbed to the MWCNT surface. This suggests that the interfacial shear stress between the matrix and the polymer was stronger than the cohesive strength of the matrix under cryogenic conditions.

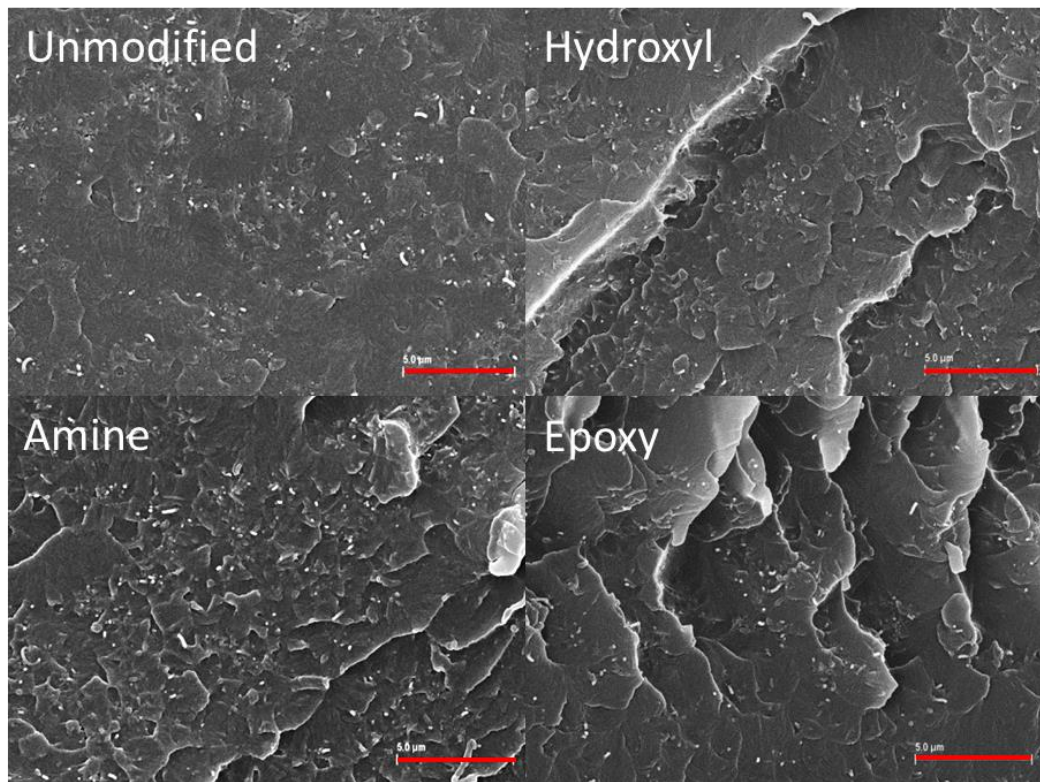


Figure 4.5 Scanning electron micrographs of epoxy-amine coatings containing MWCNTs displaying the degree of dispersion.

Note: the scale bar is five microns.

As observation of MWCNT dispersion in composites via SEM is a qualitative technique, quantitative investigations were conducted via UV-Vis spectroscopy.

Qualitative imaging via SEM at 5000 x magnification and an increase in visible light absorption at 500 nm (Figures 4.5 and 4.6, respectively) indicated improved MWCNT dispersion upon chemical modification; absorbance of chemically modified MWCNTs were in the order amine > epoxy > hydroxyl ~ unmodified. The differences in dispersion can be attributed to the complex balance of solvent/polymer wetting, MWCNT – solvent/polymer attraction, and MWCNT – MWCNT attraction/repulsion.

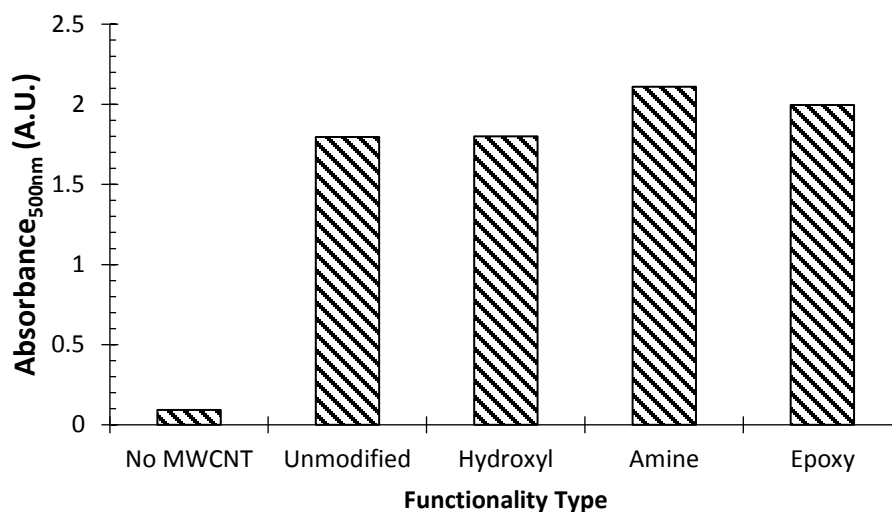


Figure 4.6 Absorbance values at 500 nm of epoxy-amine free films formulated with MWCNTs containing various functional groups.

#### 4.4.3 Polymer-MWCNT Interactions via Vibrational Spectroscopy

Spectroscopic peak frequency shifts of vibrational spectroscopy characterization techniques are well known to be induced by changes in secondary interactions and have been employed to investigate load transfer from polymer matrices to carbon nanotubes.<sup>154, 214</sup>

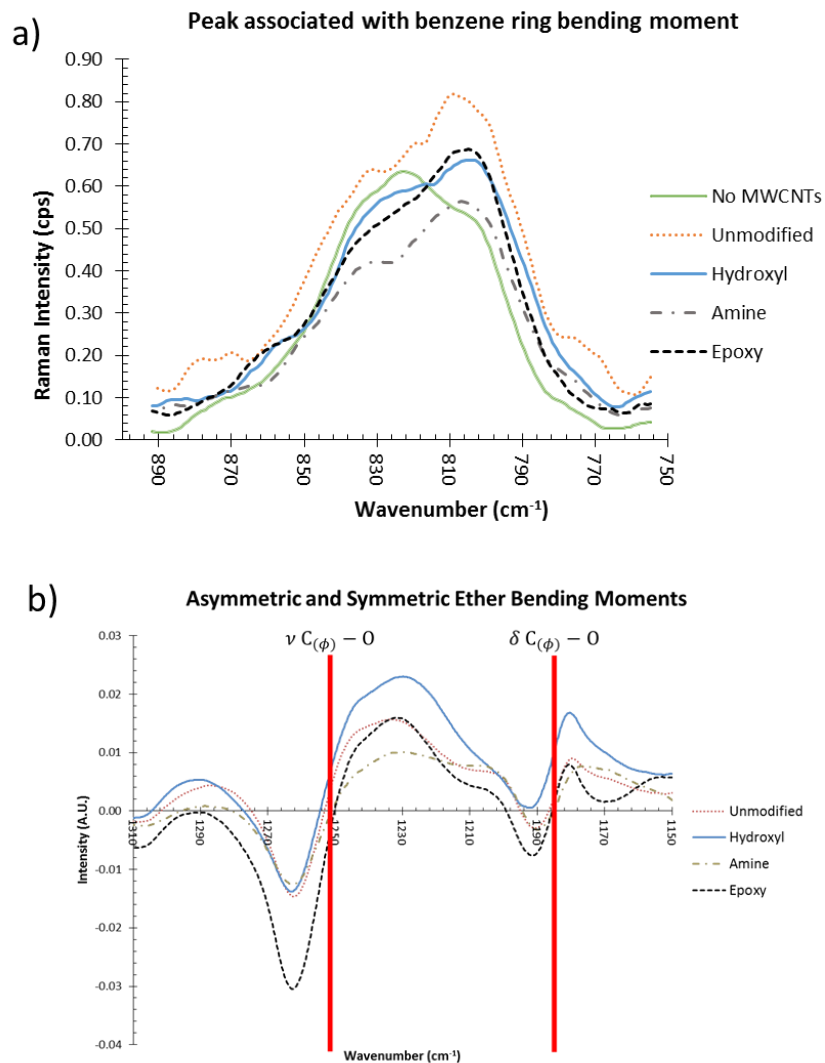


Figure 4.7 Representative Raman spectra associated with the out-of-plane bending moments of an asymmetric benzene ring (a) and ATR-FTIR subtraction spectra of the aromatic ether region (b).

Note: the No MWCNT spectrum was subtracted from the spectra of MWCNT epoxy-amine material combinations to generate the spectra of Figure 4.7b.

Raman spectroscopy suggested strong interactions between the benzene ring of EPON<sup>®</sup> 825 and/or the epoxy trimer and the multiwall carbon nanotube for all MWCNT surface chemistries as indicated by a peak shift to a lower wavenumber (redshift) at  $\sim 820 \text{ cm}^{-1}$ ; this peak is associated with the out of plane bending of an asymmetric

benzene ring (Figure 4.7a).<sup>215</sup> The redshift was attributed to an increased bond length from the strong  $\pi$ - $\pi$  interactions (pulling) between the MWCNT and the benzene ring. Additionally, a red shift of the characteristic peak associated with stretching of the C=C bonds within the benzene ring ( $\sim 1608\text{ cm}^{-1}$ ) and the deformation of the hydrogen attached to the benzene ring ( $\sim 1187\text{ cm}^{-1}$ ) were observed. Furthermore, redshifts in the ATR-FTIR spectra of the peaks associated with aromatic ethers (bending and stretching; Figure 4.7b), was observed increasing the confidence that strong interactions were realized between the aromatic constituents of the polymer and the sidewall of the MWCNTs and provides further evidence of the proposed secondary interactions. These observations provide an explanation to the lack of dependency on chemical modification of polymer adsorption to the MWCNTs.

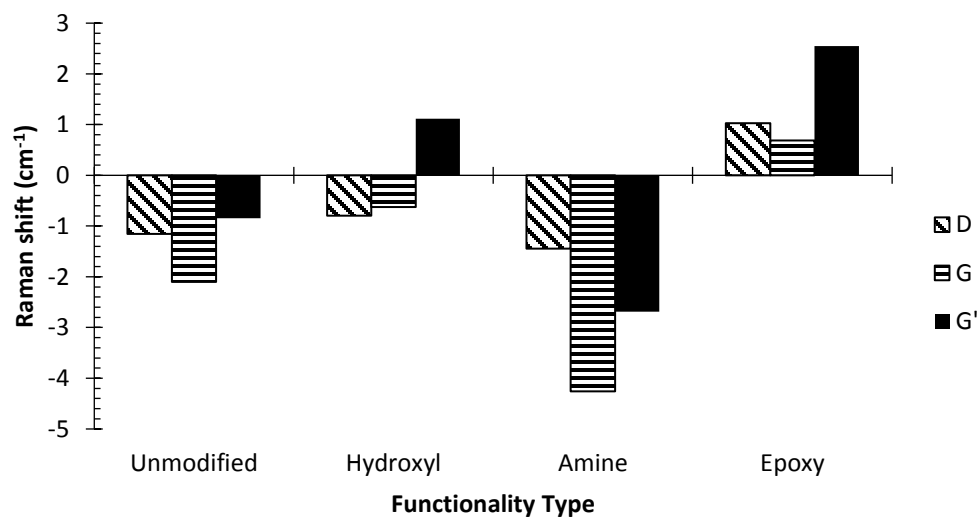


Figure 4.8 Change in Raman peak position of the D, G and G' bands due to incorporation of MWCNTs with different surface chemistries.

Note: a negative value indicates a blue shift and a positive value indicates a red shift as the spectrum of the No MWCNT material combination was subtracted from the spectra of the MWCNT epoxy-amine material combination.

Stress transfer to carbon nanotubes has been monitored in the literature via the change in the peak maximum of the G' band ( $\sim 2700 \text{ cm}^{-1}$ ).<sup>216-217</sup> The G' and D peak position of the functionalized MWCNTs statistically remained the same after MWCNT incorporation into the coating independent of chemical functionality (Figure 4.8); this indicated that the coating does not impart strain on the MWCNTs in the as-cured condition and the reduction of coating internal stress (Figure 4.9) was likely attributed to a different mechanism; e.g., the increased amount of interphase polymer present due to the presence of MWCNTs altering the global polymer structure or tube slippage between the outer and adjacent tube enabling for mobility during cure. The observed redshifts of these systems agreed qualitatively with the redshift of the out-of-plane bending moment asymmetric benzene ring observed  $\sim 820 \text{ cm}^{-1}$  of the polymer. It should be noted that the strong  $\pi$ - $\pi$  interactions identified via Raman and ATR-FTIR spectroscopies do not appear to greatly affect the polymer performance characteristics as chemical modification of the MWCNTs with various functional groups realized statistically different properties (e.g.,  $T_g$ ); this suggests changes in polymer properties measured here were a result of the polymer interacting with the functional groups bound to the MWCNT surface.

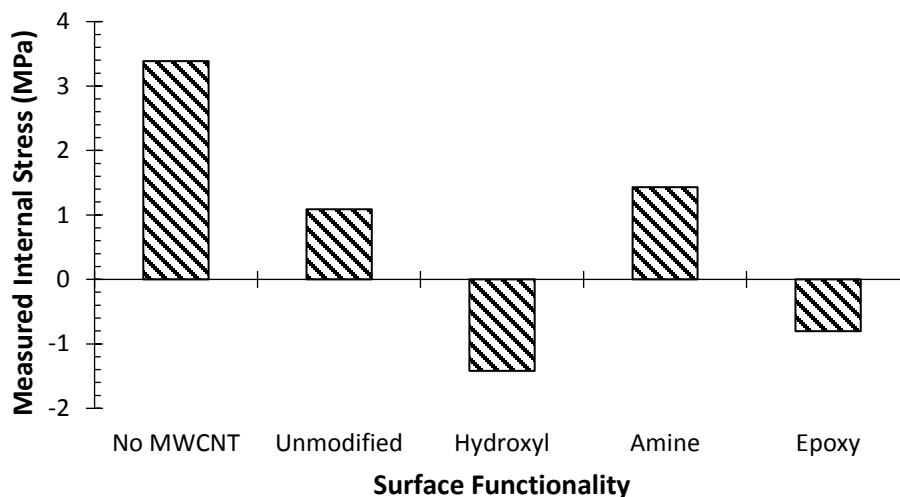


Figure 4.9 Internal stress measurements via the cantilever method.

#### 4.4.4 Coating Performance Characteristics

The low residual volatile content after cure (~ 1 wt% for all material combinations) indicated that changes in properties observed in this study were a result of interactions between the chemically modified MWCNTs and the polymer matrix, and not a result of varying levels of residual solvent/ambient moisture which is known to plasticize/alter polymer performance characteristics.<sup>218-220</sup> The glass transition temperature ( $T_g$ ) was determined via heat/cool/heat thermal cycling to erase the thermal history prior to analysis. The thin film containing amine functional MWCNTs possessed a higher  $T_g$  than the thin film without MWCNTs (Figure 4.10), which is a scarce observation in the literature as most systems are reported to either have no effect or a reduced  $T_g$ .<sup>67, 152</sup> The hydroxyl functional MWCNT thin film was determined to be statistically lower than all other thin films; the unmodified and epoxy MWCNT types did not statistically alter the glass transition temperature of the epoxy-amine material combination.

These data indicated that amine functionality provided additional interactions between the polymer and the MWCNT than what was detected via vibrational spectroscopic methods which hindered polymer movement, and thus increased the  $T_g$ . However, the hydroxyl functionality of MWCNTs decreased the  $T_g$  indicating that these MWCNTs may be acting as a solid lubricant enabling more facile chain movement at a lower temperature. The increased matrix chain mobility for the hydroxyl functional MWCNT system may be a result of two different phenomena: 1) unfavorable MWCNT-polymer interactions (which should result in poor dispersion) or 2) the hydroxyls attached to the MWCNTs have a strong interaction with the polymer backbone due to hydrogen bonding thus realizing a “correlation hole” where strongly adsorbed polymer cannot intercalate with the bulk polymer reducing the amount of thermal energy required for chain mobility.<sup>67</sup>

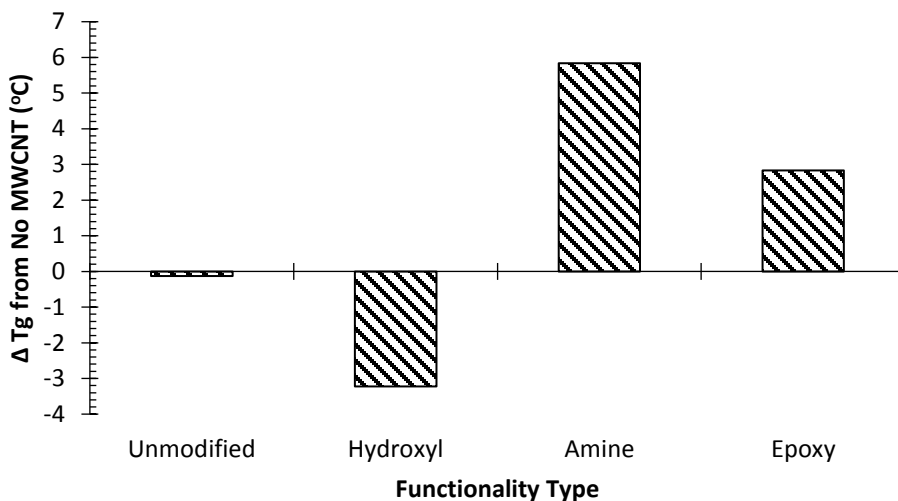


Figure 4.10 Difference in the  $T_g$  measured by DSC for crosslinked epoxy-amine thin films containing MWCNTs with different chemical functionalities.

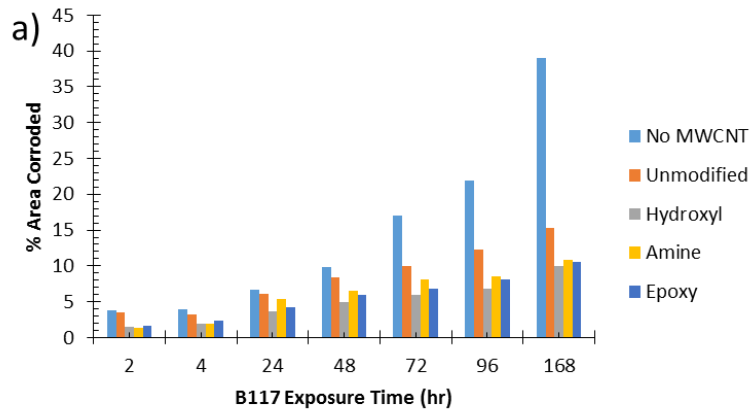
Regression analysis of  $M_t/M_\infty$  plotted as a function of  $t^{1/2}/d$  for the dynamic vapor sorption analysis determined statistically relevant slopes for all experiments ( $p < 0.001$ ;  $R^2 > 99.5\%$ ), thus the calculated slopes from the regression analyses were utilized to calculate the water vapor diffusion coefficient for each dry/wet cycle.<sup>209</sup> Generally, the water vapor diffusion coefficient did not change with incorporation of chemically modified MWCNTs which agrees with literature observations for MWCNT (0.50 wt%) epoxy-amine material combinations under full immersion conditions.<sup>40, 221</sup> Such an observation is counterintuitive as many studies predict increased permeant tortuosity with incorporation of high aspect ratio fillers.<sup>222-223</sup>

#### **4.4.5 Corrosion Performance of MWCNT Coatings on Steel Substrates**

The thin film without MWCNTs failed catastrophically after 168 hours of salt fog exposure (Figure 4.11 a-b) compared to thin films with MWCNTs which afforded a lower corrosion rate. It is acknowledged that 168 hours of salt fog exposure is insufficient for optimized corrosion control coatings and that further optimization and longer term performance is possible. However, the purpose of this Chapter was to compare the performance characteristics of thin films containing chemically modified MWCNTs to the experimental corrosion rate from intentionally created defects of the parent epoxy-amine matrix. Cursory investigations via ATR-FTIR indicated that the distribution of water interactions with the polymer was altered due to the presence of MWCNTs in the system.

It was hypothesized that the redistribution of water hydrogen bonding interactions by MWCNTs was mechanistically related to the differences in the corrosion rate as there

was no difference in water vapor diffusivity. Statistical analysis indicated that the corrosion performance was independent of chemical modification after 168 hours of B117 exposure, however, the non-significant difference up to this time point may change with increased exposure time; i.e., the chemically modified MWCNTs appeared to reduce the corrosion area compared to the systems with unmodified MWCNTs. Although increased water vapor barrier was not realized, the ion tortuosity hypothesis is supported by the reduced amount of corrosion near the scribe and non-scribed portion of the steel panel after the polymer thin films were removed (as determined via SEM - EDS). The corrosion performance of each system qualitatively agreed with the amount of inorganic moieties at the polymer/substrate interface of the polymer thin film away from the scribe determined via EDS (Figure 4.12). These cursory data support the hypotheses of increasing ion path tortuosity and redistributed water types within the matrix due to the presence of MWCNTs.



b)

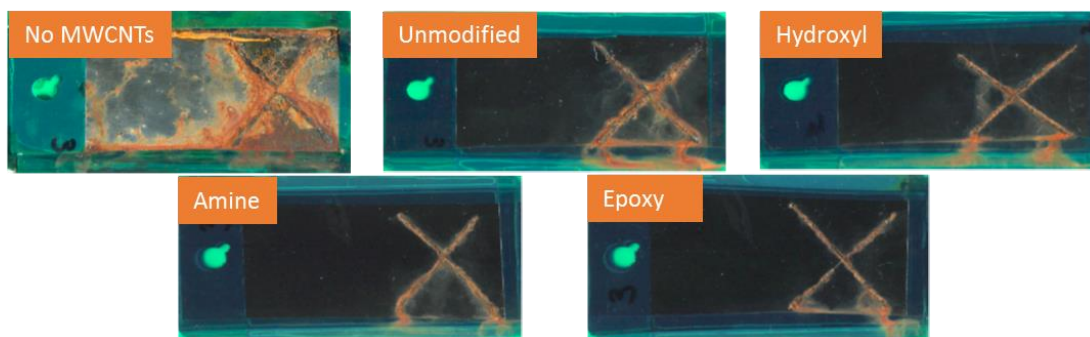


Figure 4.11 Percent corrosion area of epoxy-amine polymer thin films on steel substrates formulated with MWCNTs of various chemical functionalities as a function of salt fog accelerated corrosion exposure time (a) and representative panels after 168 hours of exposure (b).

SEM–EDS elemental mapping of the polymer thin film at the polymer/substrate interface detected probable corrosion product pairs [e.g., NaOH, Fe(OH)<sub>2</sub>, FeCl<sub>2</sub>] and corrosion inducing species (NaCl). Qualitatively, more inorganic species (Fe, Na, Cl) were detected at the polymer/substrate interface of the polymer thin film for the material combination without MWCNTs (white areas) along with several ruptured blisters containing relatively high amounts of iron and oxygen (Figure 4.12). The singular white spot in the amine - functional MWCNT material combination was comprised of the corrosion products iron, chlorine, and oxygen, but did not contain sodium. It was hypothesized that this anomaly is a result of a macroscopic defect in the polymer thin film that formed during application not visually detected in advance. It should be noted that most of the chlorine was located in close proximity to iron atoms rather than sodium atoms (which was also observed for the material combination without MWCNTs) consistent with anodic reactions of steel corrosion events.

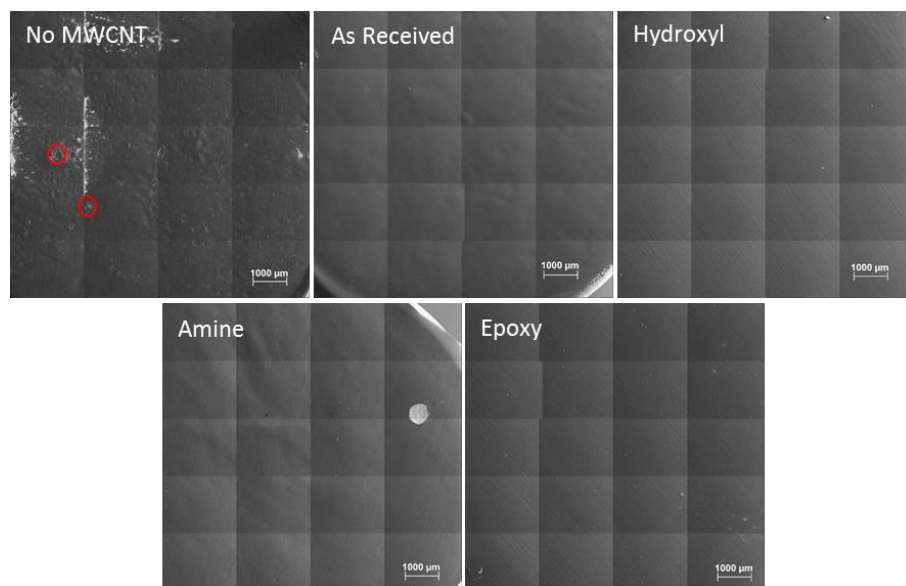


Figure 4.12 Scanning electron micrographs of the polymer at the polymer/substrate interface.

Note: the scale bar is 1000 microns.

Each polymer thin film material combination was removed from the substrate after accelerated corrosion conditioning and cryo-fractured for SEM-EDS analysis to qualitatively investigate ion diffusion through the polymer and the interaction between MWCNTs and permeating ions. The cross-sections of all polymer thin film material combinations contained corrosion products and NaCl within the matrix though to a lesser extent for thin films with chemically modified MWCNTs (Figure 4.13). These qualitative observations suggest that the MWCNTs influence/interact with the permeating ion, hindering their diffusion rate through the polymer. It will be demonstrated in the following Chapters that the reduced ion transport rates are related to the availability and ability for water molecules to contribute to the hydration shells of solvated ions altering ion transport potential.

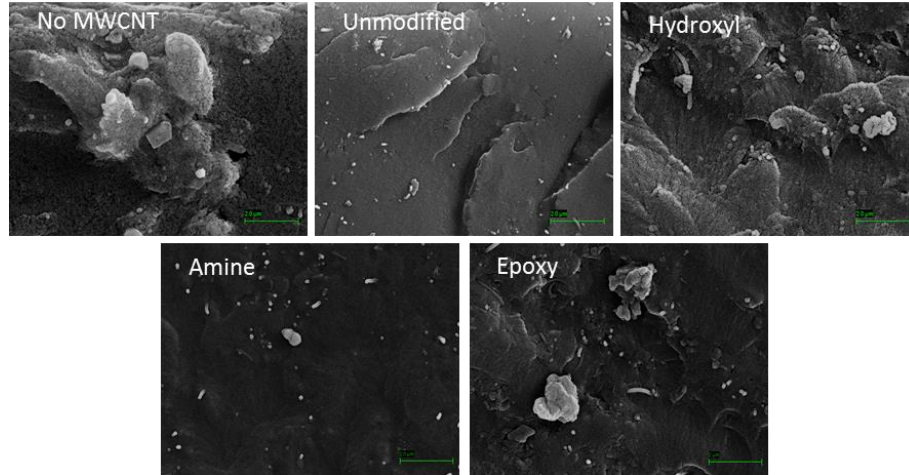


Figure 4.13 Scanning electron micrographs of the polymer cross-section after ASTM B117 salt fog exposure.

Note: the scale bar is 2 microns.

#### 4.4.6 Water Hydrogen Bonding Interactions

In an attempt to investigate the relationship between the water hydrogen bonding interactions after 168 hours of a 5% NaCl salt fog exposure and the corrosion area of a specific MWCNT/epoxy-amine material combination applied to a steel substrate, the free water, singly-bound water, and multi-bound water content of each material combination after 168 hours of exposure was compared to the corrosion area after 168 hours. Generally, most of the water was determined to be multi-bound within the coating (50-70%) and the free water to be lower than 10% with the remainder being comprised of singly-bound water (~30%) (Figure 4.14). The most notable difference in the water hydrogen bonding distribution was the reduction of the relative concentration of free water which was reduced from 7% to ~2% when MWCNT were incorporated into the thin films.

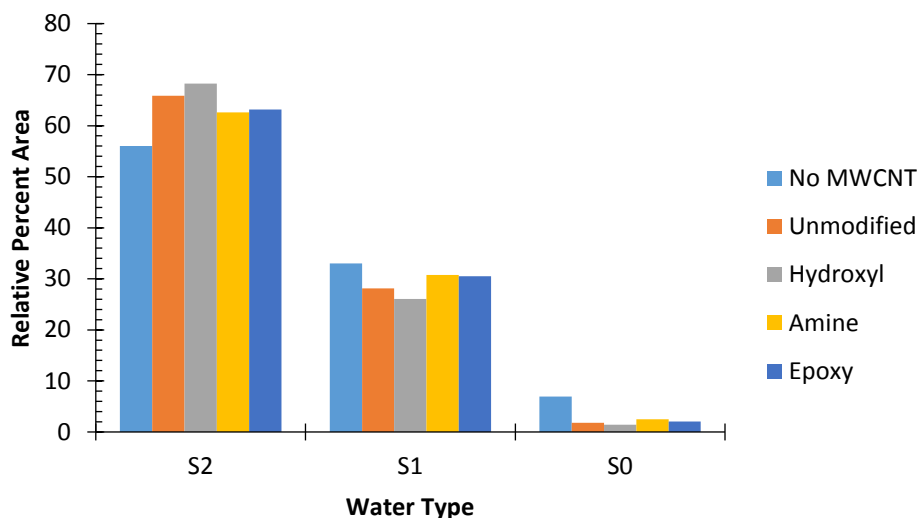


Figure 4.14 Water hydrogen bonding interactions at the air/polymer interface of epoxy-amine material combination after 168 hours of 5% NaCl fog exposure.

Both the free water ( $S_0$ ) and singly-bound ( $S_1$ ) water were determined to scale proportionally with the corrosion area suggesting that these water types both contributed to increasing the corrosion area (Figure 4.15), although the singly-bound water possessed a relatively low coefficient of determination ( $R^2 = 0.4051$ ). Multi-bound ( $S_2$ ), on the other hand, was determined to be inversely proportionate to the corrosion area suggesting that increasing the amount of multi-bound water in the matrix reduced the corrosion area as function of time. These data suggested that 1) MWCNTs reduces the amount of free water within the epoxy-amine matrix exposed to a 5% NaCl salt fog environment and 2) the reduction of free water due to MWCNTs reduces the corrosion area as a function of time more so than a direct physical tortuosity phenomenon.

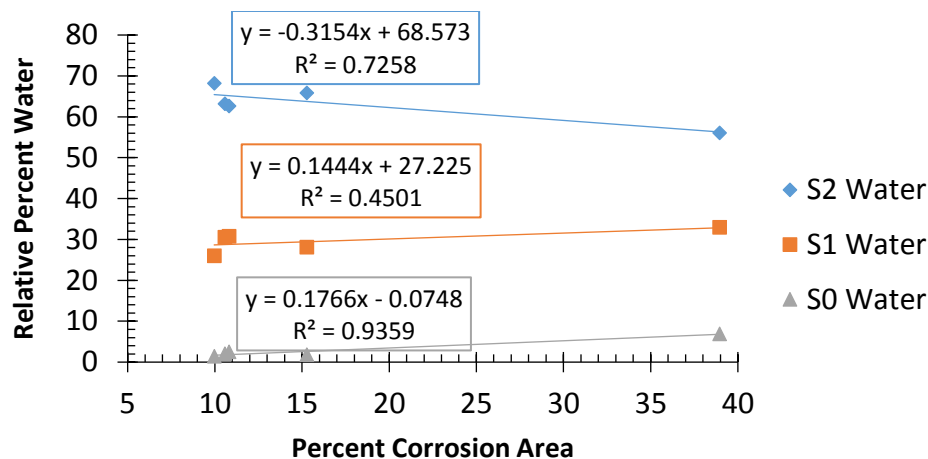


Figure 4.15 Relationship between the corrosion area and water hydrogen bonding interactions at the polymer/air interface after 168 hours of salt fog exposure.

#### 4.5 Discussion

Analysis of the thin film material combinations via attenuated total reflectance-Fourier transform infrared spectroscopy identified a redshift of the aromatic ethers which suggested an additional level of interaction within the polymer induced by the presence of multiwall carbon nanotubes, which was independent of the proposed surface chemistry. This is further supported by the presence of a redshift of the asymmetric benzene ring noted via Raman spectroscopy. Although the altered interactions were detected and were independent of surface chemistry, differences in the glass transition temperature were observed and attributed to the surface interactions. ATR-FTIR further identified that the presence of MWCNTs increased the number of hydrogen bonding interactions of water molecules for which the basis of increased hydrogen bonding in the presence of MWCNTs has been calculated in several literature examples.<sup>224-227</sup>

The data presented in this Chapter supports the concept that incorporating MWCNTs into an epoxy-amine polymer material combination reduces the measured

corrosion area after 168 hours of a 5% NaCl salt fog exposure at 35 °C (ASTM B117), and that the addition of MWCNTs increases the amount of time required for corrosion inducing ions to reach the substrate and along the polymer/substrate interface. It was hypothesized that the corrosion performance of MWCNT epoxy-amine material blends is directly related to the ability of MWCNTs to manage water hydrogen bonding interactions and the subsequent availability for water molecules to contribute to ion hydrations shells thereby reducing ion transport and the corrosion rate concurrently. The connection between MWCNTs, water hydrogen bonding interactions, and corrosion control properties is the subject of Chapters V and VI.

#### **4.6 Conclusions**

The main objective of this Chapter was to investigate and quantify the effects of chemical modification of MWCNTs on the anticorrosion performance of model epoxy-amine thin polymer films applied to steel substrates. Various functional groups were realized on the MWCNT surface at a functional group density of ~ 0.15 mmol/gram, specifically, primary hydroxyl, primary amine, and epoxy functionalities. Generally, adding functional groups increased dispersion as determined via scanning electron microscopy and ultraviolet visible spectroscopy. The aromatic constituents of the polymer interacted with the MWCNT sidewall, specifically, redshifts of the bending moment of an asymmetric benzene ring (EPON<sup>®</sup> 825 and chain extended EPON<sup>®</sup> 825) and the aromatic ethers were observed via Raman and ATR-FTIR spectroscopy, respectively. The water vapor diffusivity, determined via dynamic vapor sorption, was independent of incorporation of the MWCNTs and chemical modification. However,

statistically relevant shifts in the glass transition temperature were determined with the hydroxyl functional MWCNTs and the amine functional MWCNTs, i.e., a 3 °C decrease and 6 °C increase, respectively, indicating that functional groups attached to MWCNTs influences polymer dynamics even at a low concentration loading of 0.50 wt%.

Accelerated corrosion testing (ASTM B117) of experimental and control polymer thin film material combinations indicated that incorporation of MWCNTs reduced the corrosion rate of steel panels. Furthermore, epoxy-amine material combinations containing chemically modified MWCNTs afforded the best corrosion resistance, but were indistinguishable after 168 hours of salt fog exposure. The improved corrosion protection is attributed to reduced ion permeation through the coating to the substrate and was validated by SEM - EDS spectroscopy. These data indicated that increased tortuosity was not achieved in the current material combinations which necessitated that the original hypothesis be revised. Specifically, these data support the concept that the increased corrosion performance of the MWCNT epoxy-amine material blends is directly related to the ability of MWCNTs to manage water hydrogen bonding interactions and the subsequent availability for water molecules to contribute to ion hydrations shells thereby reducing ion transport and the corrosion rate concurrently.

## 4.7 References

14. Morsch, S.; Lyon, S.; Greensmith, P.; Smith, S. D.; Gibbon, S. R., Water Transport in an Epoxy–Phenolic Coating. *Progress in Organic Coatings* **2015**, *78*, 293-299.
15. Cotugno, S.; Larobina, D.; Mensitieri, G.; Musto, P.; Ragosta, G., A Novel Spectroscopic Approach to Investigate Transport Processes in Polymers: The Case of Water–Epoxy System. *Polymer* **2001**, *42* (15), 6431-6438.
16. Musto, P.; Ragosta, G.; Mascia, L., Vibrational Spectroscopy Evidence for the Dual Nature of Water Sorbed into Epoxy Resins. *Chemistry of Materials* **2000**, *12* (5), 1331-1341.
36. Chou, T.-W.; Gao, L.; Thostenson, E. T.; Zhang, Z.; Byun, J.-H., An Assessment of the Science and Technology of Carbon Nanotube-Based Fibers and Composites. *Composites Science and Technology* **2010**, *70* (1), 1-19.
40. Starkova, O.; Buschhorn, S. T.; Mannov, E.; Schulte, K.; Aniskevich, A., Water Transport in Epoxy/Mwcnt Composites. *European Polymer Journal* **2013**, *49* (8), 2138-2148.
45. Bose, S.; Khare, R. A.; Moldenaers, P., Assessing the Strengths and Weaknesses of Various Types of Pre-Treatments of Carbon Nanotubes on the Properties of Polymer/Carbon Nanotubes Composites: A Critical Review. *Polymer* **2010**, *51* (5), 975-993.
47. Ma, P.-C.; Siddiqui, N. A.; Marom, G.; Kim, J.-K., Dispersion and Functionalization of Carbon Nanotubes for Polymer-Based Nanocomposites: A Review. *Composites Part A: Applied Science and Manufacturing* **2010**, *41* (10), 1345-1367.
53. Grossiord, N.; Loos, J.; Regev, O.; Koning, C. E., Toolbox for Dispersing Carbon Nanotubes into Polymers to Get Conductive Nanocomposites. *Chemistry of Materials* **2006**, *18* (5), 1089-1099.
55. Gojny, F. H.; Nastalczyk, J.; Roslaniec, Z.; Schulte, K., Surface Modified Multi-Walled Carbon Nanotubes in Cnt/Epoxy-Composites. *Chemical Physics Letters* **2003**, *370* (5–6), 820-824.
56. Butt, H.-J.; Graf, K.; Kappl, M., *Physics and Chemistry of Interfaces*. John Wiley and Sons Inc: New York, NY, 2006.
57. Morrison, I.; Ross, S., *Colloidal Dispersion: Suspension, Emulsion, and Foams*. Wiley and Sons Inc: New York, NY, 2002.
58. Fontana, M., *Corrosion Engineering*. 3 ed.; McGraw-Hill, Inc: Singapore, 1986.
59. Cheng, H. K. F.; Basu, T.; Sahoo, N. G.; Li, L.; Chan, S. H., Current Advances in the Carbon Nanotube/Thermotropic Main-Chain Liquid Crystalline Polymer Nanocomposites and Their Blends. *Polymers* **2012**, *4* (2), 889-912.
67. Grady, B. P., *Carbon Nanotube-Polymer Composites Manufacture, Properties, and Applications*. Wiley: Hoboken, N.J., 2011; p 352.
70. Lehman, J. H.; Terrones, M.; Mansfield, E.; Hurst, K. E.; Meunier, V., Evaluating the Characteristics of Multiwall Carbon Nanotubes. *Carbon* **2011**, *49* (8), 2581-2602.

72. Chakrapani, N.; Curran, S.; Wei, B.; Ajayan, P. M.; Carrillo, A.; Kane, R. S., Spectral Fingerprinting of Structural Defects in Plasma-Treated Carbon Nanotubes. *Journal of Materials Research* **2011**, *18* (10), 2515-2521.
120. Pietraß, T.; Dewald, J. L.; Clewett, C. F. M.; Tierney, D.; Ellis, A. V.; Dias, S.; Alvarado, A.; Sandoval, L.; Tai, S.; Curran, S. A., Electron Spin Resonance and Raman Scattering Spectroscopy of Multi-Walled Carbon Nanotubes: A Function of Acid Treatment. *Journal of Nanoscience and Nanotechnology* **2006**, *6* (1), 135-140.
147. Arepalli, S., Freiman, S., Hooker, S., Migler, D, Measurement Issues in Single-Wall Carbon Nanotubes. *NIST Recommended Practice Guide* **2008**.
152. Grady, B. P., Effects of Carbon Nanotubes on Polymer Physics. *Journal of Polymer Science Part B: Polymer Physics* **2012**, *50* (9), 591-623.
154. Coleman, J. N.; Khan, U.; Blau, W. J.; Gun'ko, Y. K., Small but Strong: A Review of the Mechanical Properties of Carbon Nanotube–Polymer Composites. *Carbon* **2006**, *44* (9), 1624-1652.
165. Xu, X.; Thwe, M. M.; Shearwood, C.; Liao, K., Mechanical Properties and Interfacial Characteristics of Carbon-Nanotube-Reinforced Epoxy Thin Films. *Applied Physics Letters* **2002**, *81* (15), 2833-2835.
186. Xia, H.; Qiu, G.; Wang, Q., Polymer/Carbon Nanotube Composite Emulsion Prepared through Ultrasonically Assisted in Situ Emulsion Polymerization. *J. Appl. Polym. Sci.* **2006**, *100* (Copyright (C) 2012 American Chemical Society (ACS). All Rights Reserved.), 3123-3130.
189. Singh, P.; Campidelli, S.; Giordani, S.; Bonifazi, D.; Bianco, A.; Prato, M., Organic Functionalisation and Characterisation of Single-Walled Carbon Nanotubes. *Chemical Society Reviews* **2009**, *38* (8), 2214-2230.
191. Ellison, S.; Barwick, V.; Trevor, F., *Practical Statistics for the Analytical Scientist: A Bench Guide*. 2nd ed.; The Royal Society of Chemistry: Cambridge, 2009.
195. Ganguli, S., Effect of Loading and Surface Modification of Mwcnts on the Fracture Behavior of Epoxy Nanocomposites. *Journal of Reinforced Plastics and Composites* **2005**, *25* (2), 175-188.
196. Yaping, Z.; Aibo, Z.; Qinghua, C.; Jiaoxia, Z.; Rongchang, N., Functionalized Effect on Carbon Nanotube/Epoxy Nano-Composites. *Materials Science and Engineering: A* **2006**, *435–436* (0), 145-149.
197. Granier, A.; Nguyen, T.; Steffens, K. L.; Lee, H.-J.; Shapiro, A.; Martin, J. W. In *A Novel Method to Covalently Functionalize Carbon Nanotubes with Isocyanate for Polyurethane Nanocomposite Coatings*, International Coatings Expo: Clean-Lean-Green: Innovative Solutions for the Global Coatings Community, Toronto, ON, Canada, Federation of Societies for Coatings Technology: Toronto, ON, Canada, 2007; pp 41/1-41/21.
198. Xiong, J.; Zhou, D.; Zheng, Z.; Yang, X.; Wang, X., Fabrication and Distribution Characteristics of Polyurethane/Single-Walled Carbon Nanotube Composite with Anisotropic Structure. *Polymer* **2006**, *47* (6), 1763-1766.
199. Itkis, M. E.; Perea, D. E.; Jung, R.; Niyogi, S.; Haddon, R. C., Comparison of Analytical Techniques for Purity Evaluation of Single-Walled Carbon Nanotubes. *Journal of the American Chemical Society* **2005**, *127* (10), 3439-3448.

200. Peng, Z.; Feng, C.; Luo, Y.; Yi, Z.; Kong, L., Structure and Properties of Self-Assembled Natural Rubber/Multi-Walled Carbon Nanotube Composites. *Journal of Wuhan University of Technology--Materials Science Edition* **2011**, 26 (5), 807-811.
201. Cobley, A., Ultrasound Sonochemistry – a More Sustainable Approach to Surface Modification? *Surface Engineering* **2013**, 25 (8), 559-564.
202. Suslick, K. S.; Price, G. J., Applications of Ultrasound to Materials Chemistry. *Annual Review of Materials Science* **1999**, 29 (1), 295-326.
203. Mason, T. J.; Cobley, A. J.; Graves, J. E.; Morgan, D., New Evidence for the Inverse Dependence of Mechanical and Chemical Effects on the Frequency of Ultrasound. *Ultrason Sonochem* **2011**, 18 (Copyright (C) 2012 U.S. National Library of Medicine.), 226-30.
204. Xia, H.; Wang, Q.; Liao, Y.; Xu, X.; Baxter, S. M.; Slone, R. V.; Wu, S.; Swift, G.; Westmoreland, D. G., Polymerization Rate and Mechanism of Ultrasonically Initiated Emulsion Polymerization of N-Butyl Acrylate. *Ultrasonics Sonochemistry* **2002**, 9 (3), 151-158.
205. Doktycz, S. J.; Suslick, K. S., Interparticle Collisions Driven by Ultrasound. *Science (Washington, D. C.)* **1990**, 247, 1067-9.
206. Cobley, A.; Mason, T. J.; Paniwnyk, L.; Saez, V. In *Aspects of Ultrasound and Materials Science*, CRC Press: 2012; pp 41-73.
207. Petrier, C.; Jeunet, A.; Luche, J. L.; Reverdy, G., Unexpected Frequency Effects on the Rate of Oxidative Processes Induced by Ultrasound. *Journal of the American Chemical Society* **1992**, 114 (8), 3148-3150.
208. Gojny, F. H.; Wichmann, M. H. G.; Köpke, U.; Fiedler, B.; Schulte, K., Carbon Nanotube-Reinforced Epoxy-Composites: Enhanced Stiffness and Fracture Toughness at Low Nanotube Content. *Composites Science and Technology* **2004**, 64 (15), 2363-2371.
209. Burnett, D. J.; Garcia, A. R.; Thielmann, F., Measuring Moisture Sorption and Diffusion Kinetics on Proton Exchange Membranes Using a Gravimetric Vapor Sorption Apparatus. *Journal of Power Sources* **2006**, 160 (1), 426-430.
210. International, A., Standard Practice for Evaluating Degree of Rusting on Painted Steel Surfaces. In *ASTM D610-08(2012)* West Conshohocken, 2012.
211. Franks, F., *The Physics and Physical Chemistry of Water*. Springer: London, 1972; Vol. 1, p 596.
212. Mullins, E., *Statistics for the Quality Control Chemistry Laboratory*. The Royal Society of Chemistry: Cambridge, 2003.
213. Foster, S. F.; Hoff, E. A.; Curtzwiler, G. W.; Williams, E. B.; Davis, K. B.; Patton, D. L.; Rawlins, J. W., Chemorheology Investigation of a Glassy Epoxy Thermoset on Tensile Plastic Flow and Fracture Morphology. *Journal of Polymer Science Part B: Polymer Physics* **2015**, n/a-n/a.
214. Schadler, L. S.; Giannaris, S. C.; Ajayan, P. M., Load Transfer in Carbon Nanotube Epoxy Composites. *Applied Physics Letters* **1998**, 73 (26), 3842-3844.
215. Dusek, K., *Epoxy Resins and Composites II*. Springer-Verlag: New York, 1986.
216. Ni, Z. H.; Yu, T.; Lu, Y. H.; Wang, Y. Y.; Feng, Y. P.; Shen, Z. X., Uniaxial Strain on Graphene: Raman Spectroscopy Study and Band-Gap Opening. *ACS Nano* **2008**, 2 (11), 2301-2305.

217. Eitan, A.; Fisher, F. T.; Andrews, R.; Brinson, L. C.; Schadler, L. S., Reinforcement Mechanisms in Mwcnt-Filled Polycarbonate. *Composites Science and Technology* **2006**, *66* (9), 1162-1173.
218. Hiemenz, P.; Lodge, T., Glass Transition. In *Polymer Chemistry*, 2 ed.; Taylor and Francis Group: Boca Raton, FL, 2007.
219. Curtzwiler, G.; Early, M.; Gottschalk, D.; Konecki, C.; Peterson, R.; Wand, S.; Rawlins, J. W., The World of Surface Coatings Is Centered around the Glass Transition Temperature but Which One? Part 2. *JCT CoatingsTech* **2014**, *11*, 40-51.
220. Curtzwiler, G.; Early, M.; Gottschalk, D.; Konecki, C.; Peterson, R.; Wand, S.; Rawlins, J. W., The World of Surface Coatings Is Centered around the Glass Transition Temperature but Which One? Part I. *JCT CoatingsTech* **2014**, *11*, 28-38.
221. Prolongo, S. G.; Gude, M. R.; Urena, A., Water Uptake of Epoxy Composites Reinforced with Carbon Nanofillers. *Composites, Part A* **2012**, *43*, 2169-2175.
222. Choudalakis, G.; Gotsis, A. D., Free Volume and Mass Transport in Polymer Nanocomposites. *Current Opinion in Colloid & Interface Science* **2012**, *17* (3), 132-140.
223. Silva, J.; Ribeiro, S.; Lanceros-Mendez, S.; Simões, R., The Influence of Matrix Mediated Hopping Conductivity, Filler Concentration, Aspect Ratio and Orientation on the Electrical Response of Carbon Nanotube/Polymer Nanocomposites. *Composites Science and Technology* **2011**, *71* (5), 643-646.
224. Politano, A.; Chiarello, G., The Nature of Free O-H Stretching in Water Adsorbed on Carbon Nanosystems. *The Journal of Chemical Physics* **2013**, *139* (6), 064704.
225. Thomas, J. A.; McGaughey, A. J. H., Density, Distribution, and Orientation of Water Molecules inside and Outside Carbon Nanotubes. *The Journal of Chemical Physics* **2008**, *128* (8), 084715.
226. Martí, J.; Gordillo, M. C., Structure and Dynamics of Liquid Water Adsorbed on the External Walls of Carbon Nanotubes. *The Journal of Chemical Physics* **2003**, *119* (23), 12540-12546.
227. Gordillo, M. C.; Martí, J., Water on the Outside of Carbon Nanotube Bundles. *Physical Review B* **2003**, *67* (20), 205425.

CHAPTER V – MEASUREABLE AND INFLUENTIAL PARAMETERS THAT  
INFLUENCE CORROSION PERFORMANCE DIFFERENCES BETWEEN  
MULTIWALL CARBON NANOTUBE COATING MATERIAL COMBINATIONS  
AND MODEL PARENT MATERIAL COMBINATIONS DERIVED  
FROM EPOXY-AMINE MATRIX MATERIALS

**5.1 Abstract**

Protective coatings are often erroneously thought of as perfect environmental barriers for metal substrates, however, a host of corrosion inducing environmental contaminants permeate through defect-free coatings. The research objective was to quantify and understand the influential effects and relationships between low concentration levels of multiwall carbon nanotubes (MWCNT) dispersed into epoxy-amine matrix materials and the different water hydrogen bonding states on corrosion rates of steel substrates. It was hypothesized that when water directly hydrogen bonds with polymer, substrate, and/or MWCNTS, the localized water's capacity to transfer environmental contaminants through the polymer, i.e., to and from the substrate, diminishes and therefore the corrosion rate concurrently. The absolute pre-exposure water content was measured and the ratio of *in situ* **free** versus **bound water** hydrogen bonding interactions was monitored at the polymer/air interface using ATR-FTIR spectroscopy in a 5% NaCl fog environment in an attempt to correlate these differences with experimental corrosion rates from intentionally created defect locations. **Free** water content was reduced from ~20% to lower than 1% of the total water concentration when 1.0 wt% MWCNTs was dispersed into the parent polymer network. Concurrently, the

**bound** water content was measured to shift from ~2% to greater than 80% with the same MWCNT concentration. MWCNT bound water resulted in 25% less corrosion for the same steel substrates albeit the measured water vapor diffusivity was the same for each epoxy-amine material combination evaluated. Interestingly, the measured pre-exposure bound water content was predictive of which material would corrode slowest and fastest from an intentionally created defect, i.e., the ratio of starting water states seems to be mechanistically related to the corrosion process and the values have potential to predict corrosion rates for a variety of samples evaluated.

## **5.2 Introduction**

In the context of corrosion control coating systems, water, ion, and oxygen transport, accumulation and relative concentration are each of great concern as they collectively participate in the corrosion of steel.<sup>58</sup> From the results of Chapter IV, it was hypothesized the corrosion performance of MWCNT epoxy-amine material blends is directly related to the ability of the combined materials, and more specifically, the MWCNTs to manage water, i.e., the free versus bound water states; specifically, the potential of each water molecule in a specific hydrogen bonding state to contribute to ion hydration shells and readily transport corrosion inducing environmental contaminants and corrosion products to and from the substrate directly influences the corrosion rate.

Several authors have identified and provided the basis of highly structured water adsorbed to the surface of CNTs via molecular simulations.<sup>22, 224-227</sup> Recently, Farimani and Aluro identified the existence of multiple phases of water near the inside of a (20,20) carbon nanotube surface, i.e., vapor, ice-like, and bulk water at distances of < 0.3 nm,

0.3 – 0.4 nm, and > 0.4 nm from the surface, respectively.<sup>22</sup> Martí and Gordillo calculated the vibrational spectra of water adsorbed to a CNT surface which identified multi-bound water characteristic bands similar to that observed in polymer matrices.<sup>226</sup> Furthermore, Thomas and co-workers calculated an increased water density 0.3 nm from the outside of the CNT surface compared to bulk water independent of carbon nanotube diameter.<sup>225</sup> This was attributed to an energetically favorable region where the oxygen of a water molecule is attracted to the center of the aromatic six membered ring of the CNT surface.<sup>225</sup> The restricted movement of the O-H vibrational modes of water molecules in a local energy minimum gives rise to the characteristic band associated with multi-bound water in vibrational spectra. These data suggest that incorporating carbon nanotubes into polymers will drive conditions towards increased concentrations of bound water, i.e., singly and multi-bound water in polymer networks as demonstrated in Chapter IV, and provides the basis for those observations.

The distribution of water hydrogen bonding interactions (i.e. free and bound water) within a polymer can have a significant impact on the instantaneous material properties;<sup>14-18</sup> for some polymers this effect is broadly detected, more subtly than the overall bulk water absorption properties of polymers.<sup>16</sup> Water hydrogen bonding interactions within polymers have been identified via nuclear magnetic resonance, near-infrared spectroscopy, dielectric spectroscopy, and mid-infrared spectroscopy.<sup>14, 16, 18-20</sup> Common for mid-infrared analysis, the spectrum of a desiccated sample is subtracted from the collected spectrum after exposure (deionized water, NaCl solution, salt fog) and the hydroxyl region  $\nu_{(\text{OH})}$  deconvoluted into the various water hydrogen bonding

interactions associated with the number of hydrogen bonds with the polymer. Bound water is further classified as multi-bound ( $S_2'$  and  $S_2''$ ) and singly-bound ( $S_1$ ) states most often identified in infrared spectra via characteristic bands centered at  $\sim 3265\text{ cm}^{-1}$ ,  $\sim 3420\text{ cm}^{-1}$ ,  $\sim 3555\text{ cm}^{-1}$ , respectively. Free ( $S_0$ ) water is representative of the hydroxyl group of a water molecule that is not hydrogen bound to other water molecules nor directly with the polymer matrix; the characteristic band of free water is centered at  $\sim 3610\text{ cm}^{-1}$ .<sup>15-16</sup>

Previous data indicated that epoxy-amine material combinations containing MWCNTs reduced corrosion inducing conditions at the substrate from intentionally created defects.<sup>41</sup> In this Chapter, the research objective was to quantify and understand the influential effects and relationships between various, low concentration levels of multiwall carbon nanotubes (MWCNT) dispersed into epoxy-amine matrix materials and the different water hydrogen bonding states on corrosion rates of steel substrates. This research addressed a critical gap in knowledge in the open literature recently noted by Lyon and co-workers: specifically, what is the nature of water within a coating (free or bound) and how does the distribution of water hydrogen bonding states in spatial and temporal domains affect the overall corrosion performance from system to system or within the same system versus time and environmental conditions.<sup>228</sup>

The research results in this Chapter supports the concept that MWCNTs alter ion transport characteristics, specifically by occupying water via hydrogen bonding interactions thereby reducing its potential to form ion hydration shells and the subsequent ability to facilitate ion transport to and from the substrate. To validate this concept and

increase the depth of understanding of the effects of water hydrogen bonding states within coatings on corrosion performance, the corrosion rates of steel substrates coated with MWCNT epoxy-amine material combinations (three different concentrations of MWCNTs with two different MWCNT surface chemistries) with intentionally created defect sites were quantified and compared to the distribution of water hydrogen bonding states, free versus bound, within the coating.

### **5.3 Experimental**

#### **5.3.1 Materials and Methods**

Chapter IV established that the type of surface modification did not greatly affect the corrosion performance of the epoxy-amine thin film material combinations, thus, only the unmodified and hydroxyl modified multiwall carbon nanotubes were utilized for the investigation in this Chapter; the detailed synthesis of the hydroxyl MWCNTs can be found in section 4.3.2. A detailed description of all other materials, procedures, and characterizations can be found in Chapter IV, section 4.3; below is a brief description.

#### **5.3.2 Characterization of MWCNT Functionalization**

Both the unmodified MWCNT and hydroxyl group functionalized MWCNTs were characterized with Raman spectroscopy and the D'/G ratio was utilized to investigate MWCNT molecular structure changes from chemical modifications.<sup>70, 72, 120</sup> The functional group equivalents per gram MWCNT attached to the MWCNTs was quantified via thermogravimetric analysis.<sup>147</sup>

### **5.3.3 Model Epoxy-Amine Steel Bound and Free Films Containing MWCNTs**

The appropriate combination of MWCNT and concentration (unmodified MWCNTs, hydroxyl MWCNTs; 0.50, 0.75, and 1.0 wt% on coating solids) was dispersed in the epoxy mixture then mixed with the amines as in Section 4.3.2. Each thin film material combination was spray applied either to SAE 1008/1010 carbon steel for corrosion evaluation via ASTM B117 or polypropylene substrates to obtain free films (Scheme 4.3). All substrates were cleaned with an acetone soaked low lint wipe followed by a hexanes soaked low lint wipe prior to coating application. All coatings were cured according to the procedure in Section 4.3.2 (dried film thickness 25-30  $\mu\text{m}$ ).

### **5.3.4 Coating Characterization**

Multiwall carbon nanotube dispersion, the glass transition of each thin film, and water vapor diffusivity properties were investigated in a similar manner as in Section 4.3.5.

### **5.3.5 Corrosion Analysis**

Four coated steel panels per material combination were scribed with a Vision Express engraver equipped with a 120 degree diamond drag spindle at 100 mm/s in an X pattern with equal arms of 15.5 mm in length in the lower portion of the panel (Figure 5.1). Each scribed panel was subjected to accelerated corrosion conditions (5% NaCl salt fog spray, 35 °C) according to ASTM B117,<sup>229</sup> removed at time,  $t$ , ( $t = 24, 48, 72, 96,$  and 168 hours) rinsed with deionized water, then blotted dry with a low lint wipe. Images of each panel were captured at time  $t$  via an Epson scanner and Adobe Acrobat X Pro<sup>®</sup> was

subsequently used to quantify the corrosion area of each panel as a function of time (Figure 5.1) according to ASTM D610-08(2012).<sup>210</sup>

The scribed area was subtracted from the measured corrosion area to quantify the corrosion progress. The dominant corrosion mechanism visually appeared to be cathodic delamination (verified via post exposure analysis); thus, determining the square root of the corrosion area yields the average corrosion distance due to cathodic delamination. Following the interpretation of Leng and co-workers, the average corrosion distance was plotted as a function of the square root of time (Equation 5.1) and the corrosion rate was defined as the slope,  $A$ ; where  $\bar{x}$  is the average measured corrosion distance due to cathodic delamination and  $t$  is the time in hours.<sup>7</sup>

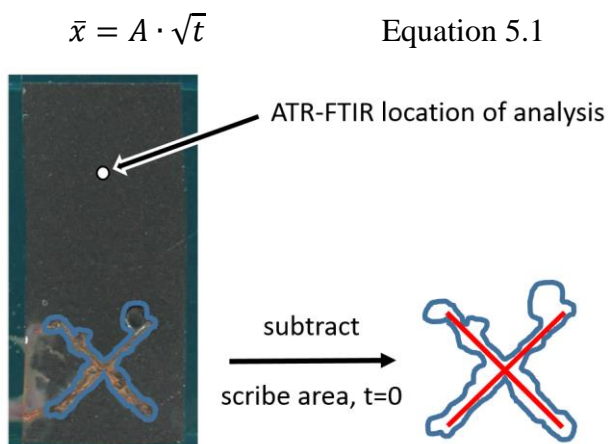


Figure 5.1 Determination of the cathodic corrosion area by quantitative image analysis.

### 5.3.6 Water Hydrogen Bonding Interactions

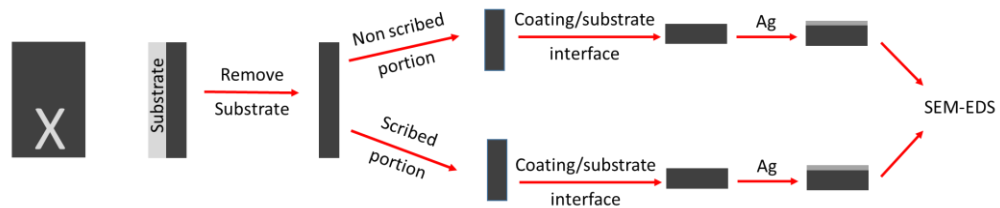
Attenuated total reflectance-Fourier transform infrared (ATR-FTIR) spectra were collected (Figure 5.1) at each time point to determine the water hydrogen bonding interactions at the polymer/air interface in a similar manner as in Section 4.3.7. Each spectrum was collected on a diamond crystal in the same X-Y spatial coordinates. Each

spectrum was baseline corrected and normalized to the maximum intensity at  $\sim 2865 \text{ cm}^{-1}$ .<sup>14, 16</sup> A desiccated (0% RH) free film specimen was considered the reference material for subtraction from the spectrum at time  $t$  and  $t=0$ , *ambient* (Equation 5.2). Spectral corrections, normalizations, subtractions, deconvolutions, and water state distributions were completed and determined as in Section 4.3.7.

$$A(\nu)_{\text{subtracted spectrum}} = A(\nu)_{\text{time}=t} - A(\nu)_{t=0, \text{desiccated}} \quad \text{Equation 5.2}$$

### 5.3.7 Post-Exposure Analysis

Post-exposure analysis of the coating qualitatively investigated ion transport through the coating to the substrate and along the substrate near the scribe (cathodic delamination). The coating of each panel was removed from the substrate; a specimen away from the scribe and near the scribe (Scheme 5.1) was sectioned for analysis of the coating at the coating/substrate interface. Each specimen was sputter coated with silver as described above and energy dispersive X-ray spectroscopy was used to qualitatively identify inorganic elements (e.g., Na, Fe, Cl) using a Zeiss Sigma-VP FE-SEM equipped with a Thermo Ultradry energy dispersive X-ray spectrometer.



Scheme 5.1 Protocol for post-exposure coating analysis after 168 hours of salt fog exposure.

### 5.3.8 Statistical Analysis

A one-way ANOVA was employed at a 95% confidence level via MiniTab 17 software to investigate differences in mean property values, and Tukey's post-hoc

pairwise comparison was utilized to group means ( $n \geq 3$ ) that are statistically the same.<sup>191, 212</sup> The statistical significance of linear trendline slopes between data sets was accomplished via linear regression utilizing an  $\alpha=0.05$ . Monotonic non-linear relationships were investigated via Spearman's coefficient, rho, utilizing an  $\alpha = 0.05$ .<sup>230</sup>

## 5.4 Results

### 5.4.1 MWCNT Characterization

Details of the hydroxyl surface modification can be found in section 4.4.1. Briefly, the hydroxyl functional group density was calculated to be  $\sim 0.15$  mmol/MWCNT g on the surface corresponding to less than 0.01% change for the total carbon atoms on the MWCNT *surface*. Even though organic mass was detected via TGA, there were no measured changes in the D'/G ratio of the Raman spectra indicating that the MWCNT molecular structure was not detectably changed by the radical-based hydroxyl functionalization treatment (Figure 5.2).

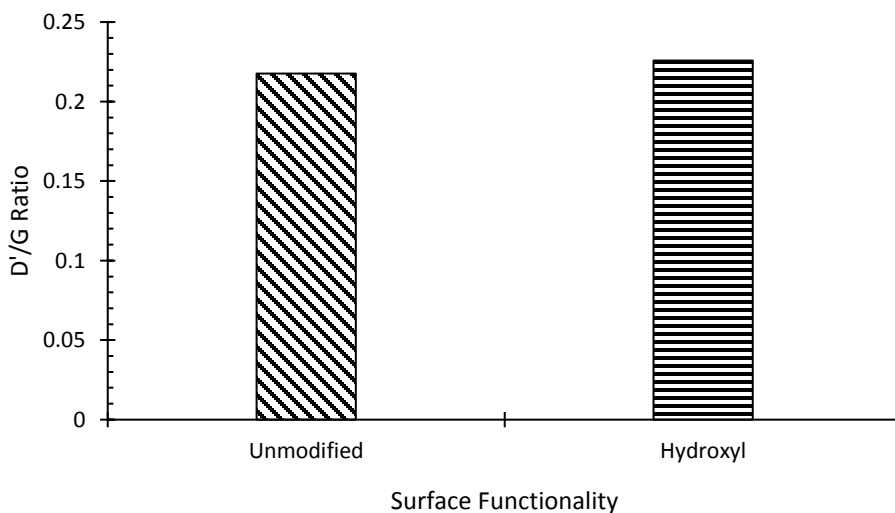


Figure 5.2 D'/G ratio of the unmodified and hydroxyl surface modified MWCNTs employing a four peak deconvolution protocol.

#### **5.4.2 Carbon Nanotube Dispersion of Free Films and Their Properties**

The domain size and nodules of all epoxy-amine coatings was 30-50 nm in diameter, which is similar to what has been reported in other epoxy-amine systems and in Chapter IV.<sup>213</sup> Investigation of the fracture surfaces indicates that the epoxy-amine matrix strongly interacted with the MWCNT surface as nodules were observed on all MWCNT surfaces independent of surface functionality.<sup>165</sup> Specifically, the diameters of MWCNTs protruding from the fracture surface were in the range of 80-120 nm, which indicated that approximately one domain nodule of the epoxy-amine matrix was strongly adsorbed to the MWCNT surface. Furthermore, this suggests that the interfacial shear stress between the MWCNT and the polymer was stronger than the cohesive strength of the matrix under cryogenic conditions. SEM investigation of cross-sections revealed that MWCNTs protruded from the surface in the micrographs of all MWCNT/epoxy-amine material combinations indicating shear alignment parallel to the substrate due to spray application (the substrate would be orientated at the top of each micrograph). A high degree of exfoliation and nano-scale dispersion was achieved in all MWCNT/epoxy-amine material combination. No agglomerates/flocs were observed independent of surface chemistry or concentration (Figure 5.3). With thorough sample area study, there is high confidence that each SEM micrograph is representative of the bulk dispersion properties as multiple micrographs were collected at various magnifications for each thin film material combination and sample.

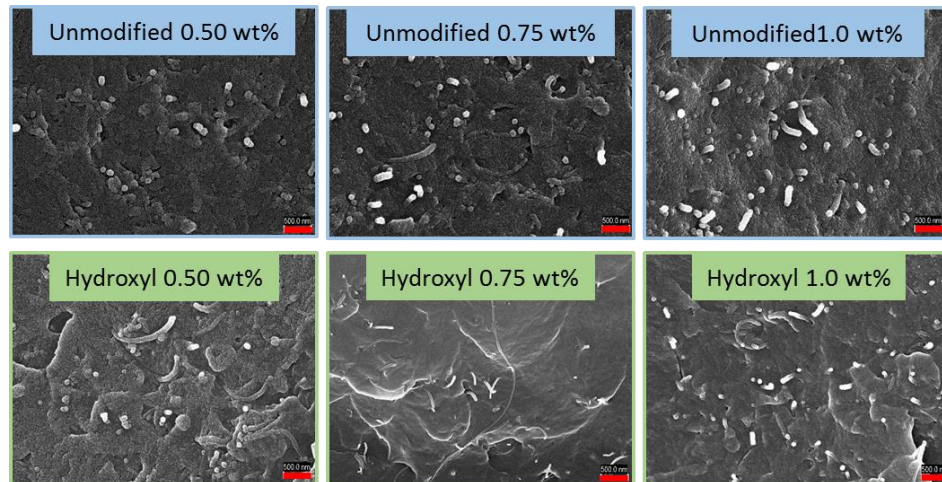
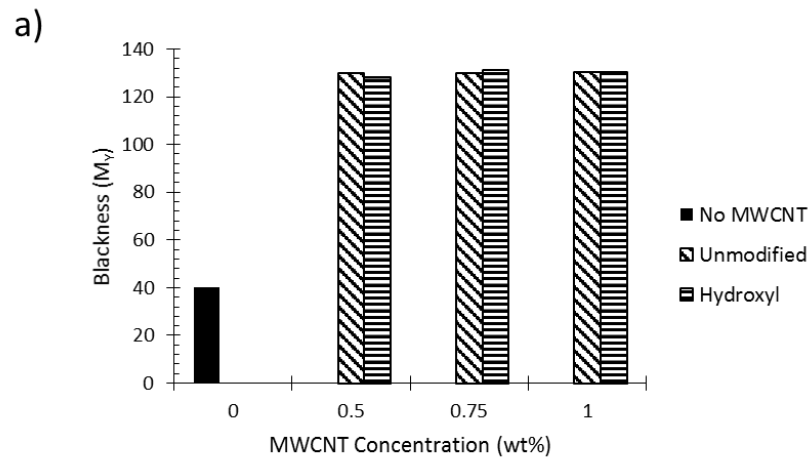


Figure 5.3 Scanning electron micrographs of epoxy-amine coatings containing MWCNTs (~20kx magnification). Scale bar for each micrograph is 500 nm.



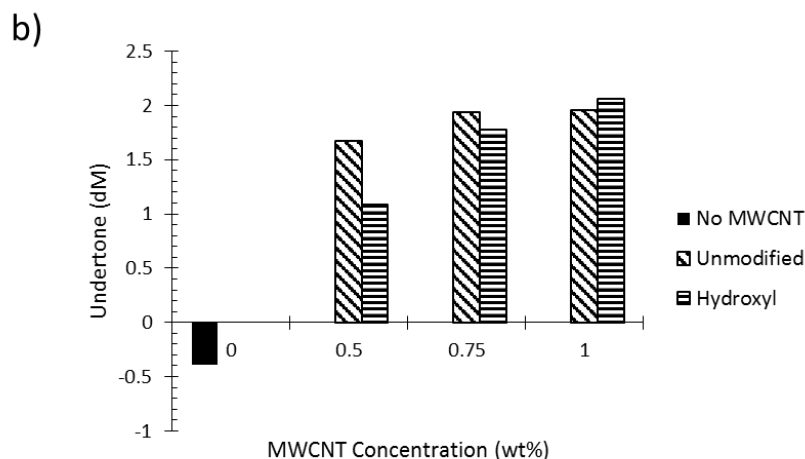


Figure 5.4 Blackness (a) and undertone (b) properties for epoxy-amine material combinations containing various nano-carbon allotropes at concentrations of 0.50, 0.75, and 1.0 wt%.

Generally, MWCNT agglomerates were not observed at any of the concentration – surface functionality combinations as determined by SEM of the cross sections. The blackness properties of each thin film material combination was used to determine the particle dispersion more quantitatively. Generally, utilizing blackness measurements from white light sources can probe particle sizes of approximately 180 nm, where values converge to a maximum.<sup>183</sup> Thus, increased blackness values at a given concentration for a specific particle-thin film material combination is indicative of higher dispersion quality. Additionally, increasing concentration of the particle should also increase the blackness properties, which was not observed for either of the MWCNT/epoxy-amine material combinations (Figure 5.4). However, the magnitude of the blue undertone was determined to increase with MWCNT concentration. For tint/full shade systems, increasing blue undertone is associated with smaller particle sizes due to increased absorption and scattering events; the increased blue undertone suggests the presence of a

higher concentration of small particles increasing the absorption/scattering events of the incident light.

The difference between the ambient temperature and the glass transition temperature ( $T_g$ ) dictates the simple polymer physical state, i.e., liquid, rubber, glass,<sup>219-220</sup> and what mechanism(s) become dominant for small molecule permeation.<sup>222</sup> Each of the coating materials reported herein exhibited a dry glass transition temperature ranging between 29 and 40 °C. Although significant differences of the measured  $T_g$  were determined between material combinations (Figure 5.5), each thin film type in this research was tested with a  $T_g$  value below or near the test conditions of the salt fog chamber (35 °C for ASTM B117) indicating that the mechanism of small molecule permeants is expected to be dominated by a rubbery polymer segmented mobility over tortuosity, as shown by Starkova and co-workers.<sup>40, 222</sup> Even though the free films are generally in the glassy state (as measured in the dry state) at the temperature of the water vapor sorption analysis (25 °C; 15 °C below  $T_g$  for the largest difference), the permeation mechanism of water vapor was not expected to greatly differ at 35 °C (ASTM B117).<sup>40, 231</sup>

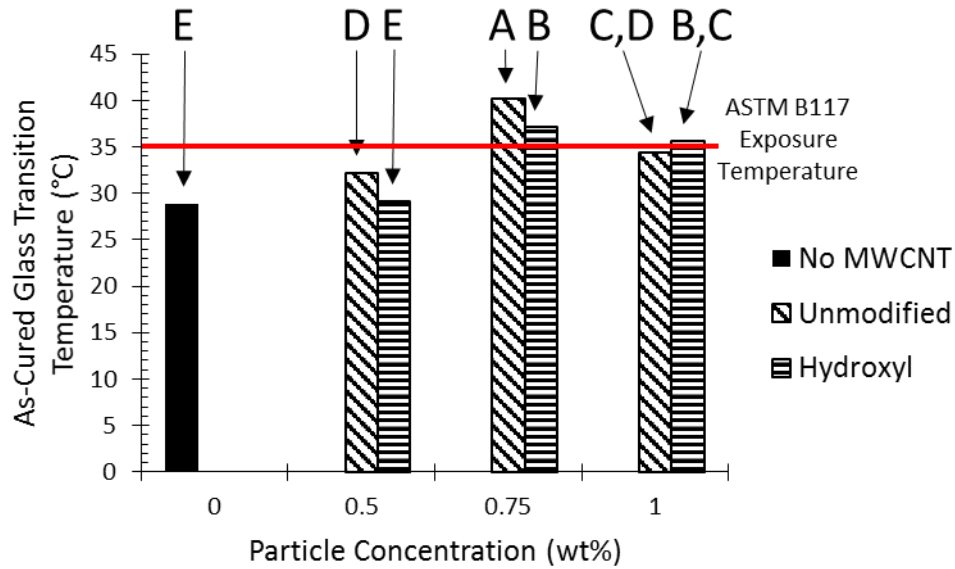
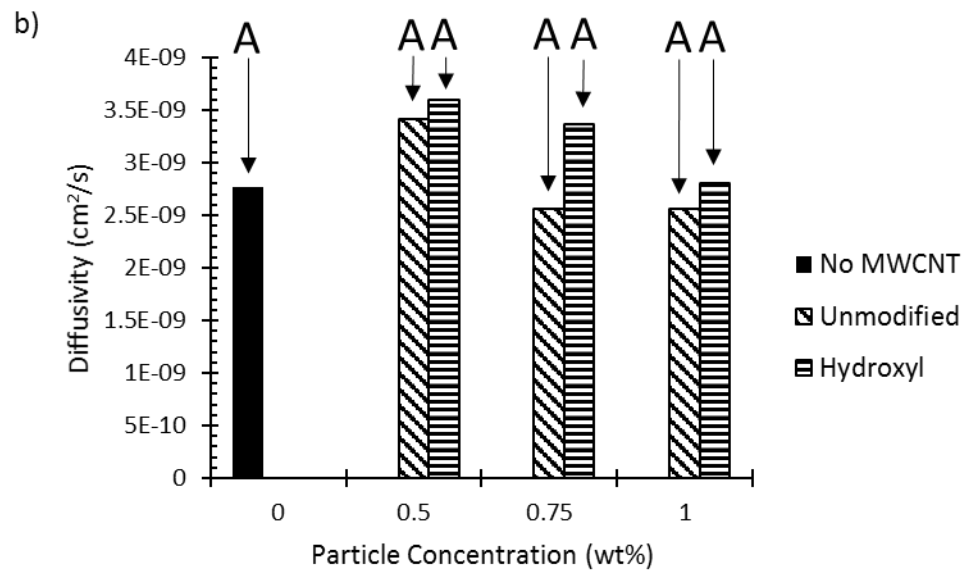
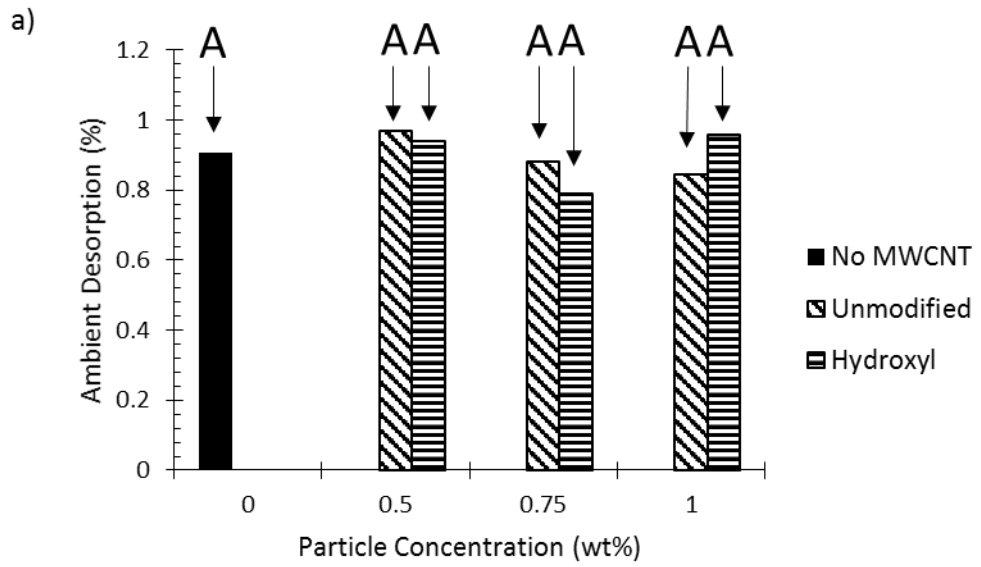


Figure 5.5 The glass transition temperature of MWCNT/epoxy-amine material combinations with various concentrations of multiwall carbon nanotubes.

Note: Means with different letters are statistically different.

Although the current work utilized water vapor instead of direct immersion as in Starkova and co-workers<sup>40, 231</sup>, the results were consistent in that there were no significant differences in water vapor diffusivity as a function of MWCNT concentration or surface modification (Figure 5.6b). Furthermore, there was no significant difference in the mass loss in the desiccation cycle (likely comprised of a mixture of ambient moisture and residual solvent, if any) or the water vapor saturation mass at equilibrium in a 95% RH atmosphere (Figures 5.6a and 5.6c, respectively). These data suggest that differences in corrosion performance for the material combinations here will be attributed to a mechanism other than directly attributable to any increased barrier properties to water or water saturation content differences during testing either within or between thin film material combinations.



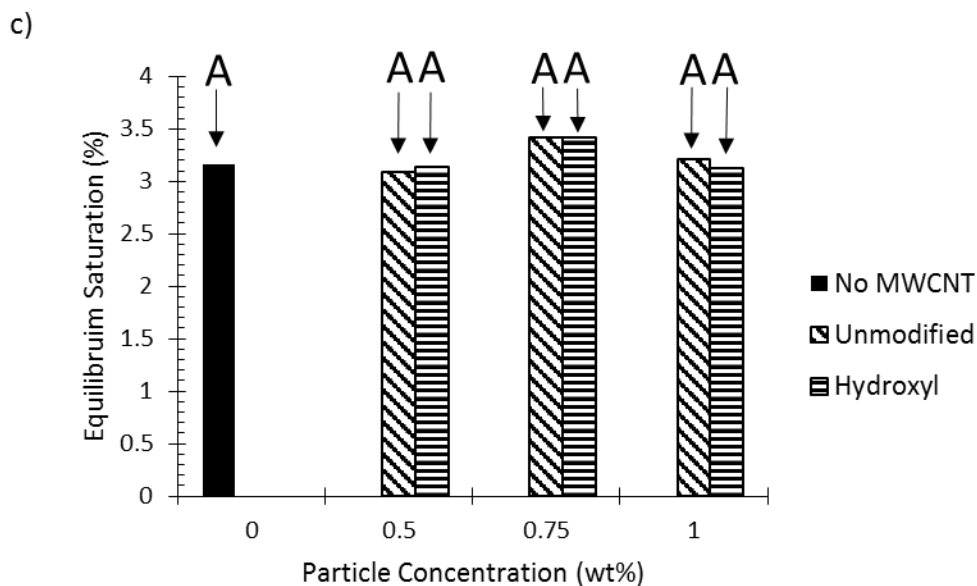


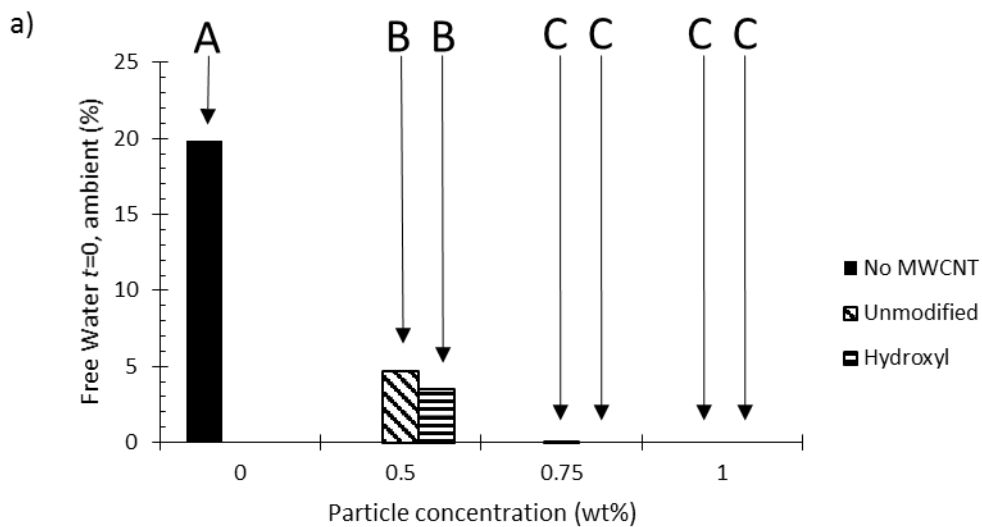
Figure 5.6 Measured water vapor sorption properties for epoxy-amine free films containing multiwall carbon nanotubes.

Note: Means with different letters are statistically different. Ambient water vapor concentration (a), water vapor diffusivity (b), and water vapor saturation at equilibrium (c).

### 5.4.3 Influence of MWCNTs on Water Type Distributions at Ambient Conditions

Ionic species require a hydration shell for solvation and diffusion through aqueous media and polymers.<sup>23, 26</sup> It was proposed that occupying hydrogen bonding sites of water molecules with any entity, including fillers within a polymer matrix, will increase the bound residence time of a water molecule at any given location and also decrease the likeliness and efficiency of a water molecule to participate in forming ion hydration shells and allowing facile ion diffusion through a polymer. The relative concentration of water hydrogen bonding interactions at the polymer/air interface ( $\sim 0.50$  micron depth of penetration at  $\sim 3400$   $\text{cm}^{-1}$ ) was determined via ATR-FTIR. ATR-FTIR was chosen for analysis as it was a non-destructive technique and for the ability to collect measurements at the same X-Y coordinates each time for a given specimen to reduce the local variation

effect of local variations in molecular structure and the variability in its influence on the collected ATR-FTIR spectrum. Although differences in water hydrogen bonding states are presented as definitive and discrete environments, it is important to note the rapid and dynamic nature of water hydrogen bonding within polymeric materials (on the order of picoseconds)<sup>22</sup>; thus, the data are representative of the average hydrogen bonding states over the experimental time scale which is much longer than the time scale required for redistribution of hydrogen bonding interactions of water within the polymer.



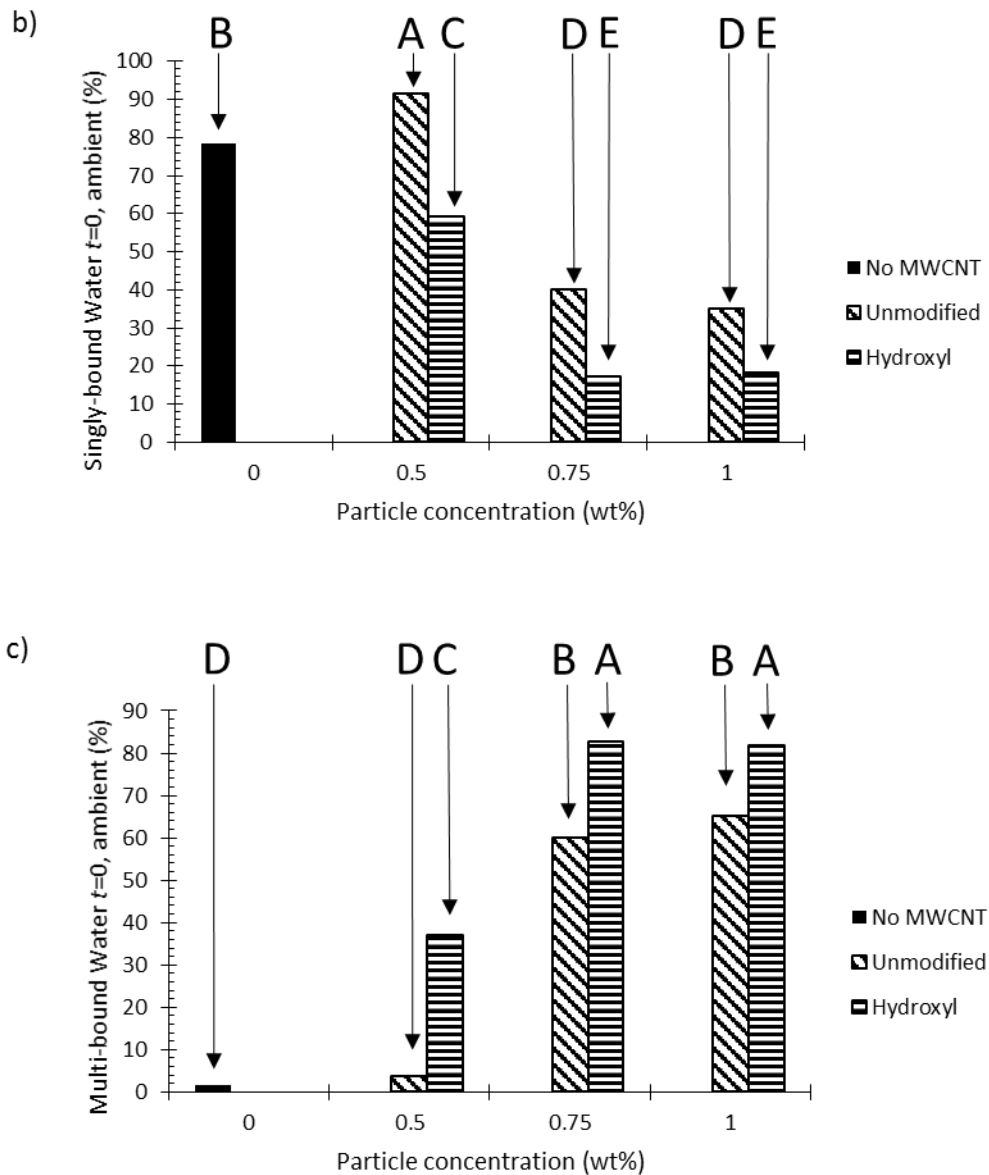


Figure 5.7 Relative concentration of water vapor hydrogen bonding interactions within MWCNT/epoxy-amine thin films at  $t=0$  hr, ambient.

Note: Means with different letters are statistically different. Free (a), singly-bound (b), and multi-bound (c) water hydrogen bonding interactions.

Generally, the material combination without MWCNTs contained 15 – 20% more free ( $S_0$ ) water than the MWCNT/epoxy-amine material combinations (unmodified and

hydroxyl MWCNTs) for all concentrations at ambient conditions (Figure 5.7a). The measured free water was found to be independent of the surface chemistry at each concentration and all four MWCNT material combinations above a 0.50 wt% loading level. At 0.75 and 1.0 wt% MWCNT concentrations, the free water content was statistically the same (0 – 0.05%; Figure 5.7a). Increasing the unmodified MWCNT concentration from 0.50 to 0.75 and 1.0 wt% decreased the singly-bound ( $S_1$ ) water content from ~90% to 40% and 35% (statistically the same; Figure 5.7b), respectively. The hydroxyl MWCNT thin films had lower amounts of singly-bound water compared to the unmodified MWCNT thin films at all concentrations; furthermore, the singly-bound ( $S_1$ ) water content for the 0.75 wt% and 1.0 wt% hydroxyl MWCNT thin films was statistically the same at 17% and 18%, respectively. Unmodified MWCNTs increased the amount of multi-bound ( $S_2$ ) water from ~2% water for the parent polymer thin film material combination without MWCNTs to 60% and 65% for the 0.75 wt% and 1.0 wt%, respectively. However, the hydroxyl MWCNTs created conditions within the coating that further increased the amount of multi-bound water to 37%, 82 %, and 81% for the 0.50 wt%, 0.75 wt%, and 1.0 wt%, respectively (Figure 5.7c). Similar to the singly-bound water, the multi-bound water was independent of concentration for the unmodified and hydroxyl MWCNT thin films, singularly, for the 0.75 and 1.0 wt% concentrations.

Differences in water hydrogen bonding states can be directly attributed to the increased available MWCNT surface area as a function of concentration that increases the frequency of water-MWCNT interactions; molecular simulations provided the basis of highly structured bound water adsorbed to the surface of CNTs.<sup>224-227</sup> These studies

support the hypothesis that MWCNTs contribute to the increased amount of bound water and decreased free water within the epoxy-amine coatings. However, the hydroxyl surface chemistry of the hydroxyl MWCNTs increased the relative amount of multi-bound/singly-bound water compared to the unmodified MWCNT at each concentration which suggests that the presence of the hydroxyl functional groups on the MWCNT surface realizes increased multi-bound ( $S_2$ ) water.

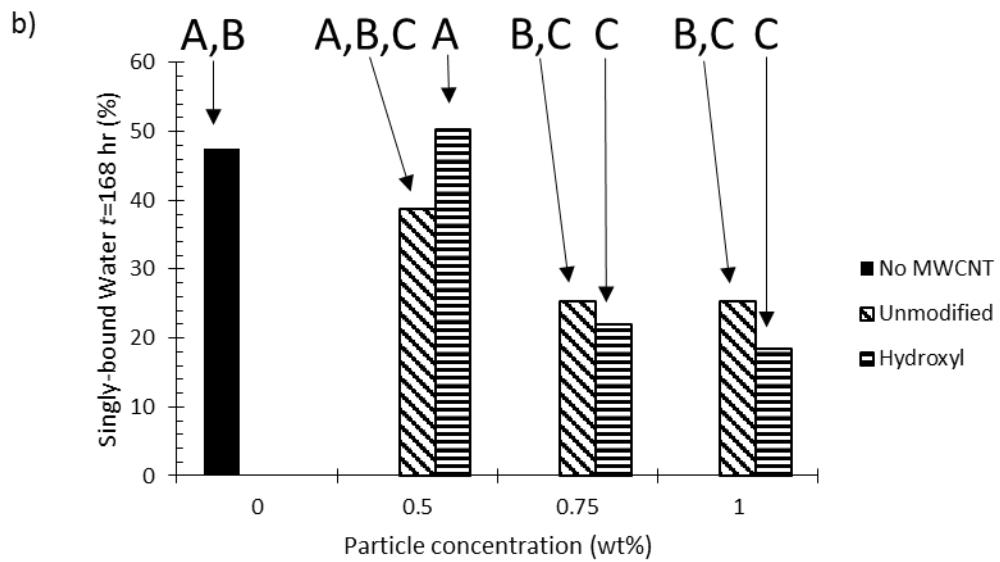
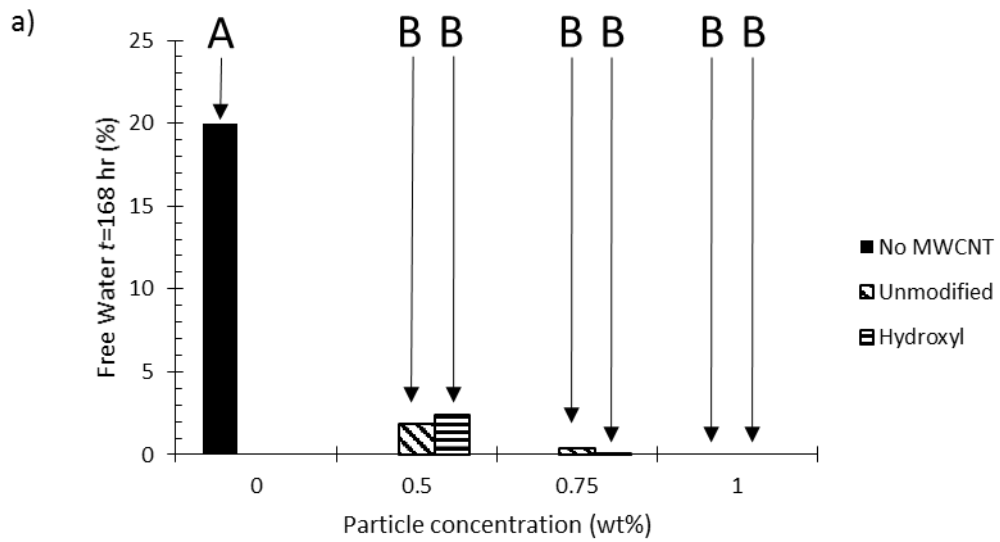
#### **5.4.4 Influence of MWCNTs on the Water Hydrogen Bonding Interactions**

##### **Distribution after 168 Hours of Salt Fog Exposure**

The smallest changes in water hydrogen bonding interactions due to salt fog exposure was observed using a MWCNT loading level of 1.0 wt%, and statistically did not change for the 1.0 wt% hydroxyl MWCNT thin film. There were no statistical changes in the amount of free water between  $t=0$ , *ambient* and  $t=168$  hours for all thin film material combinations, except for the unmodified MWCNT/epoxy-amine material combination loaded at 0.5 wt%, which a reduced amount of free water was determined after exposure from 4.7% to 2.4%. This indicated that changes in the water hydrogen bonding state due to salt fog exposure occurred between singly-bound ( $S_1$ ) and multi-bound ( $S_2$ ) water, which was inversely and equally proportionate. For all unmodified MWCNT/epoxy-amine material combinations, the amount of singly-bound water after 168 hours of salt fog was statistically lower than the  $t=0$ , *ambient* (38%, 25%, and 25% for 0.50, 0.75 and 1.0 wt%, respectively). However, the amount of singly-bound water for the hydroxyl MWCNT thin films remained statistically the same except for the 0.75 wt% loading level which had a higher amount (+4.7%) of  $S_1$  water. The material combination

without MWCNTs possessed lower amounts of singly-bound water (~48%) at  $t=168$  hours compared to  $t=0$ , ambient (~78%).

The free water content ( $S_0$ ) for all MWCNT/epoxy-amine material combinations at  $t=168$  hours of salt fog exposure were statistically the same (0.0-2.4 %) independent of surface chemistry and concentration (Figure 5.8a). Thin film material combinations containing 0.75 and 1.0 wt% MWCNTs (independent of surface chemistry) were determined to have statistically the same amount of both singly-bound and multi-bound water types, which indicates that increasing the concentration above 0.75 wt% was only minimally more effective at influencing water management in a salt fog environment similar to what was determined at ambient conditions. The parent material combination, without MWCNTs, contained statistically lower amounts of multi-bound water (~30%) than all thin film material combinations except the hydroxyl MWCNT thin film at 0.50 wt% (Figure 5.8c). Based on the hypothesis that multi-bound water possesses a lower potential to contribute to ion hydration shells, it is surmised that thin film material combinations with the lowest amount of free water and the highest amount of multi-bound water will realize the lowest overall uniform corrosion rate.



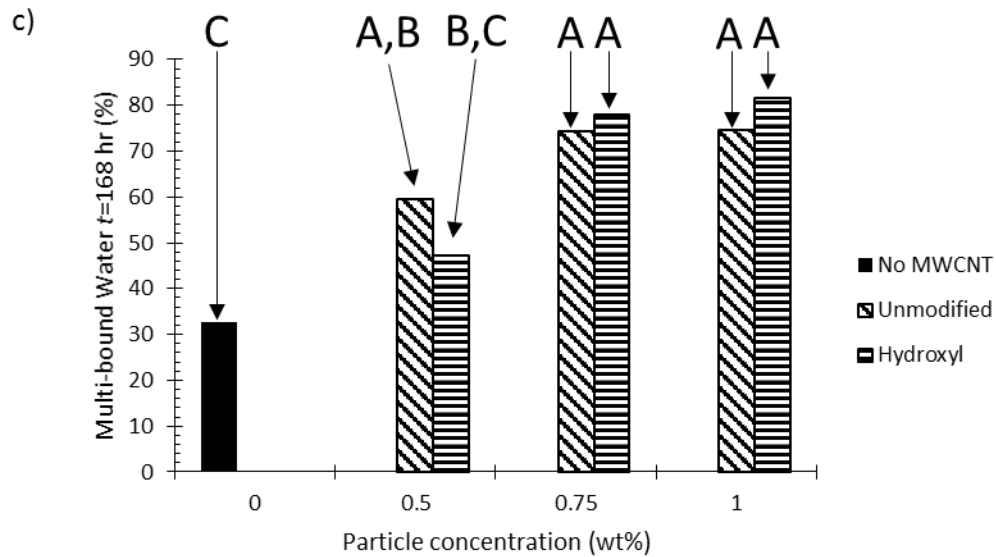


Figure 5.8 Relative concentration of water hydrogen bonding interactions within MWCNT/epoxy-amine material combinations after 168 hours of salt fog exposure.

Note: Means with different letters are statistically different. Free (a), singly-bound (b), and multi-bound (c) water hydrogen bonding interactions.

#### 5.4.5 Influence of MWCNTs on the Corrosion Performance of Epoxy-Amine Thin Films on Steel Substrates

To verify the assumption of a cathodic delamination mechanism, the coatings were removed from the substrate and the polymer/substrate interface of the coating analyzed via energy dispersive X-ray spectroscopy (EDS). Simplistically, the cathodic delamination process occurs as oxygen is reduced at the surface of the steel substrate producing hydroxyl moieties and a local net negative charge (the cathode). To balance the negative charge, water-solvated sodium ions from a macroscopic defect (the scribe) migrate along the polymer/substrate interface; the rate of this process is directly influenced by the physicochemical properties of the interface.<sup>232</sup> Metal dissolution at the anode produces iron chloride and subsequently iron oxide (rust).<sup>7</sup> Elemental mapping

analysis of the polymer thin film at the polymer/substrate interface near the scribe for each panel (Figure 5.9) indicated a relatively higher concentration of iron and chloride at the edge of the scribe and a higher concentration of sodium away from the scribe consistent with a cathodic delamination mechanism.

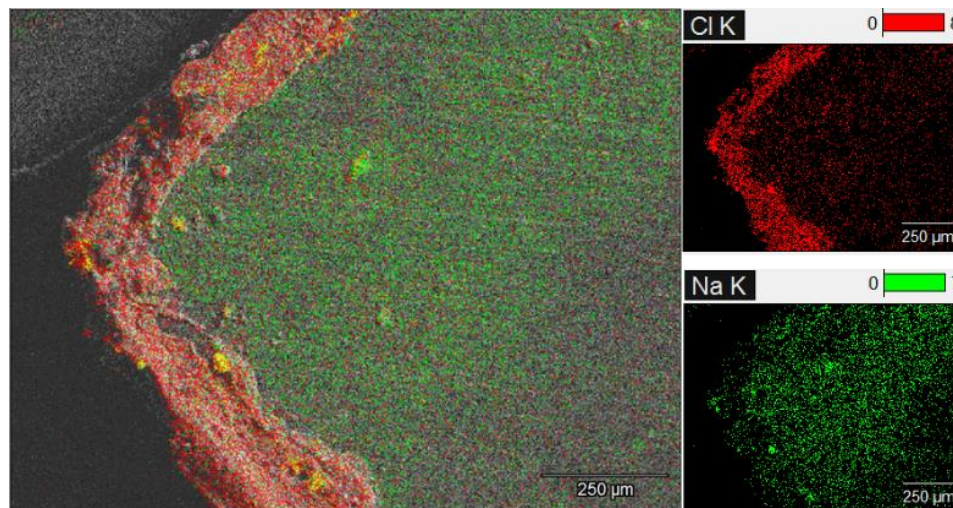


Figure 5.9 Representative scanning electron micrograph and energy dispersive X-ray elemental map of the polymer/substrate interface of the coating after 168 hours of salt fog exposure.

It is acknowledged that other corrosion mechanisms may take place in addition to cathodic delamination at the polymer/substrate interface and that quantifying only the corrosion attributed to cathodic delamination in a salt fog environment may not be representative of long-term corrosion performance in any given environment. Furthermore, it is recognized that 168 hours of salt fog exposure is insufficient for optimized corrosion control coatings and increased corrosion resistance is possible with fully formulated coatings. However, this work was designed to further investigate the mechanism(s) of corrosion protection of MWCNT/epoxy-amine thin film material combinations, noted in Chapter IV, at the onset of major but early corrosion events.

The corrosion rate for each thin film material combination (Figure 5.10a) was calculated according to Equation 5.1 (each corrosion-time combination data point was generated from the average of four panels); regression analysis indicated that the trendline slope for each thin film material combination was statistically relevant ( $p < 0.01$ ) suggesting a diffusion controlled corrosion process.<sup>7</sup> The MWCNT/epoxy-amine thin films containing 0.75 and 1.0 wt% concentrations had the lowest corrosion rates ( $\sim 42 \mu\text{m/hr}^{1/2}$ ) which corresponded to the thin films with the lowest free/multi-bound water ratio (Figures 5.7 and 5.8). The corrosion performance of each MWCNT/epoxy-amine thin film material combination was independent of the surface chemistry at each concentration which was consistent with the results from Chapter IV.<sup>41</sup> This may be attributed to the high degree of MWCNT exfoliation and dispersion throughout the coating resulting in the similar ability for MWCNTs to manage water hydrogen bonding interactions within the coating, and, specifically at the polymer/substrate interface.

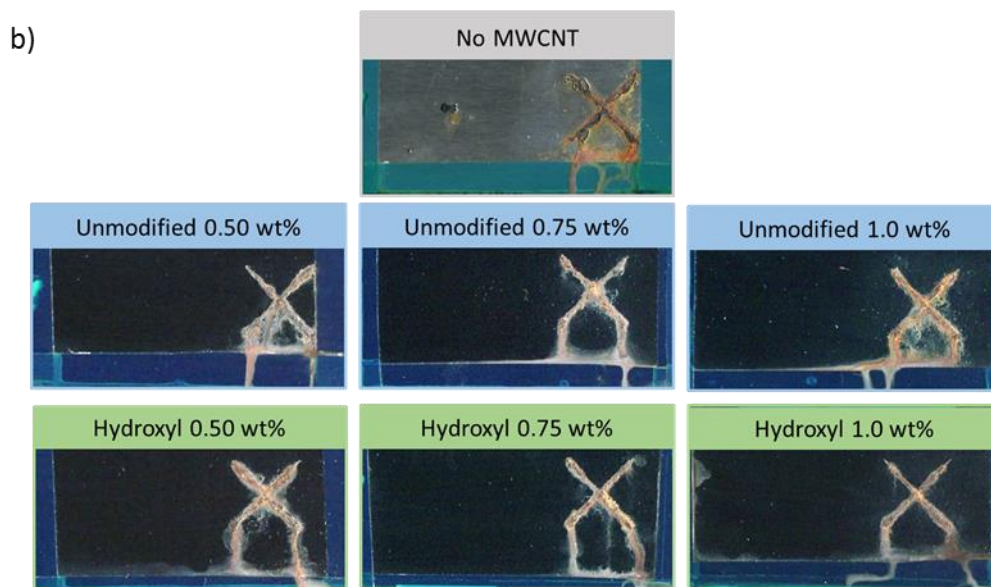
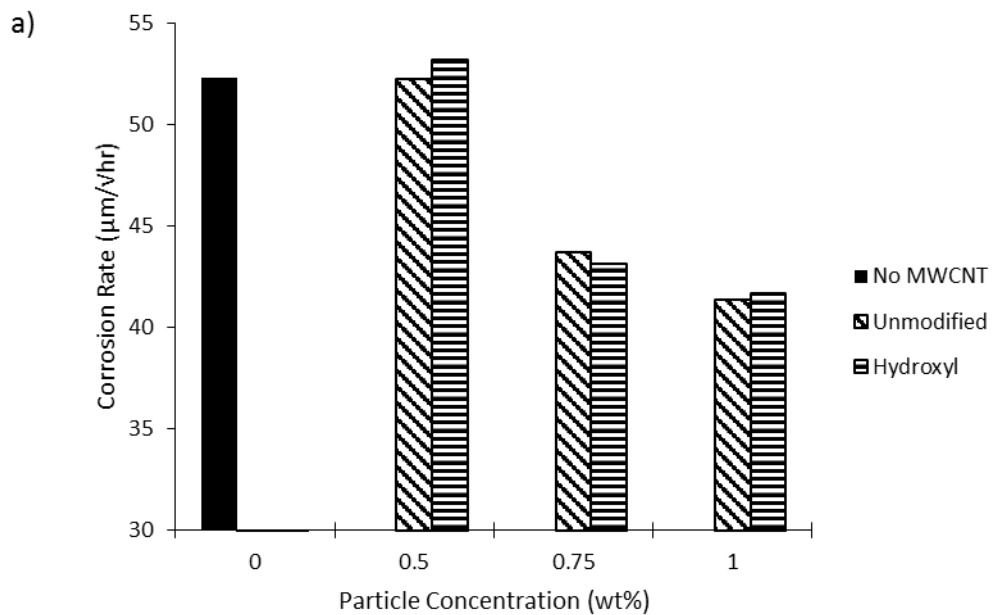


Figure 5.10 Corrosion rate for epoxy-amine coatings on steel substrates formulated without/with multiwall carbon nanotubes (a) and representative panels after 168 hours of salt fog exposure (b).

#### **5.4.6 Post-Exposure Analysis of Coated Panels Subjected to Accelerated Corrosion Conditions**

Although the dominant corrosion mechanism was cathodic delamination, a qualitative understanding of ion permeation through a coating without a macroscopic breach is of great interest for non-damaged, defect-free coatings. EDS elemental mapping of the polymer at the polymer/substrate interface identified elemental pairs consistent with corrosion events [e.g., NaOH, Fe(OH)<sub>2</sub>, FeCl<sub>2</sub>] and corrosion inducing species (NaCl). Qualitatively, more inorganic species (Fe, Na, Cl) were detected at the polymer/substrate interface for the thin film without MWCNTs and with MWCNTs at 0.50 wt% than those containing MWCNTs at 0.75 wt% and 1.0 wt% concurring with the quantitative corrosion measurements (Figure 5.10a-b) and water distributions (Figures 5.7 and 5.8). It should be noted that the micrographs shown (Figure 5.11) were purposely selected to show the worst-case scenario as corrosion products and sodium chloride crystals were difficult to detect in the MWCNT thin films containing loading levels of 0.75 and 1.0 wt%. These qualitative observations combined with the quantitative results above validates the hypothesis that thin film material combinations with higher amounts of multi-bound water relative to free water reduces ion transport through the coating. This is further supported by the non-significant changes in water vapor diffusivity and equilibrium water saturation levels for all material combinations (Figure 5.6).

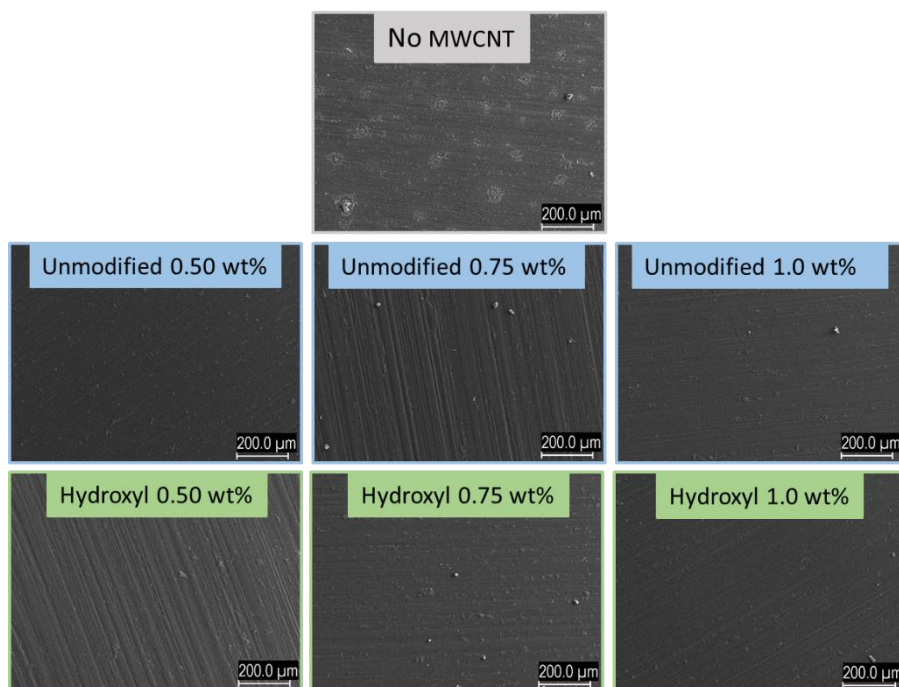


Figure 5.11 Representative scanning electron micrographs of the coating at the polymer/substrate interface away from the scribe after 168 hours of salt fog exposure.

#### 5.4.7 Influence of Water Hydrogen Bonding on Corrosion Performance of MWCNT/Epoxy-Amine Thin Films

To develop a more direct relationship between water the hydrogen bonding interaction distribution and the corrosion performance, the corrosion rate was plotted as a function of each water type at  $t=168$  hours of salt fog exposure (Figure 5.12). The free water content was determined not to correlate linearly with the corrosion rate after 168 hours of salt fog exposure ( $p = 0.192$ ); however, a monotonic increase in corrosion with increasing free water was established ( $p = 0.001$ ). The positive trendline slope of the corrosion rate as a function of singly-bound water suggests that the presence of singly-bound water contributes to increased corrosion rates. Conversely, there was an inverse

relationship between multi-bound water and the corrosion rate indicating that multi-bound water reduces corrosion rates.

All three water states strongly correlated with the corrosion rate after 168 hours of salt fog exposure when only the MWCNT containing thin films were considered ( $p \leq 0.005$ ,  $r^2 > 0.88$ ; Figure 5.12). The positive trendline slope of the free water for the MWCNT thin film material combinations was 11.8 times the value of the singly-bound water suggesting that free water contributes 11.8 times more to the corrosion rate than singly-bound water for the systems evaluated here. These data indicated that formulating coatings that controls/reduces free water reduces the corrosion rate and provides strong evidence that monitoring and managing water hydrogen bonding interactions drastically influences the corrosion performance of epoxy-amine coatings on steel substrates. Furthermore, the quantification and understanding of the difference between temporal and spatial single water molecule residence times for a given water hydrogen bonding state will provide great insight into the structure-property relationships required to hinder ion transport through a polymer matrix to the substrate for increased corrosion control and a deeper understanding of the interplay between protective coatings, substrates, and the environment.

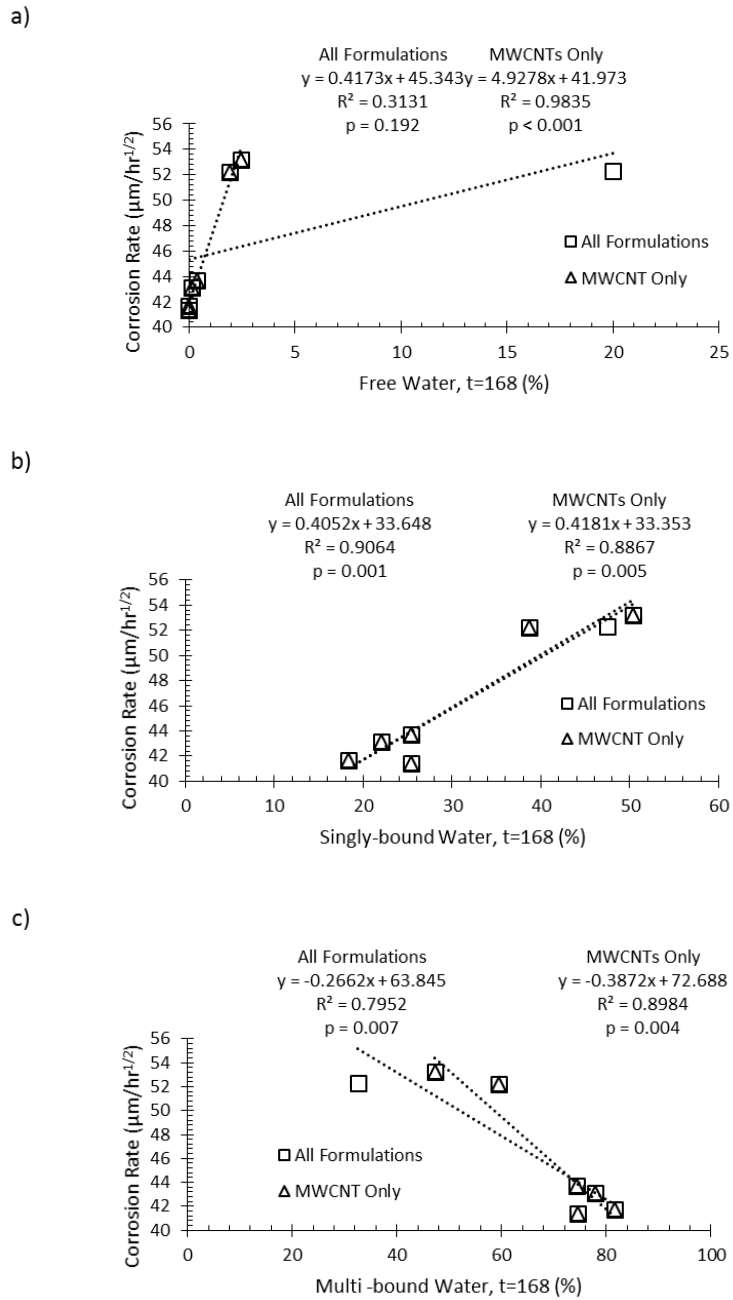


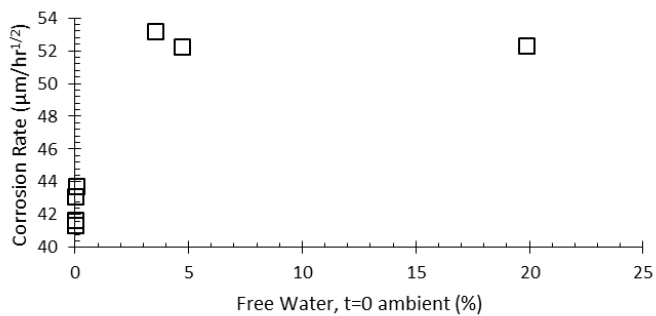
Figure 5.12 Experimental corrosion rate as a function of the relative water hydrogen bonding concentration of after 168 hours of salt fog exposure including all material combinations and including only the MWCNT material combinations.

Note: free water (a), singly-bound water (b), and multi-bound water (c) water hydrogen bonding interactions.

The ability to predict the experimental corrosion rate of new coating formulations *prior* to accelerated corrosion analysis would greatly increase testing/screening

formulation evaluations and throughput. The relative concentration of each water hydrogen bonding state for each thin film material combination at  $t=0$ , *ambient* pre-exposure was compared to the experimental corrosion rate measured up to 168 hours of salt fog exposure (Figure 5.13). Strong statistical correlations were determined for the relative concentration of singly-bound water ( $p = 0.008$ ) and multi-bound water ( $p = 0.008$ ) within the coating surface at *ambient* conditions with the experimental corrosion rate. The free ( $S_0$ ) water at  $t=0$ , *ambient* was determined to have a monotonic relationship with the corrosion rate ( $p = 0.015$ ). The data herein reveals that quantifying water hydrogen bonding states before exposure and how systems manage water hydrogen bonding interactions during and after environmental exposure is critical to understanding each system's potential for corrosion control. It is surmised that the incorporation of MWCNTs into thin film material combinations for corrosion rate reduction is applicable to other substrates in which ionic species initiate, propagate, and/or accelerate corrosion events. Additionally, determination of the relative concentration of water hydrogen bonding interactions within a coating as a function of real world exposure may provide insight into more accurate life-time modeling, maintenance schedules, and provide a protocol for real-time “damage” assessment.

a)



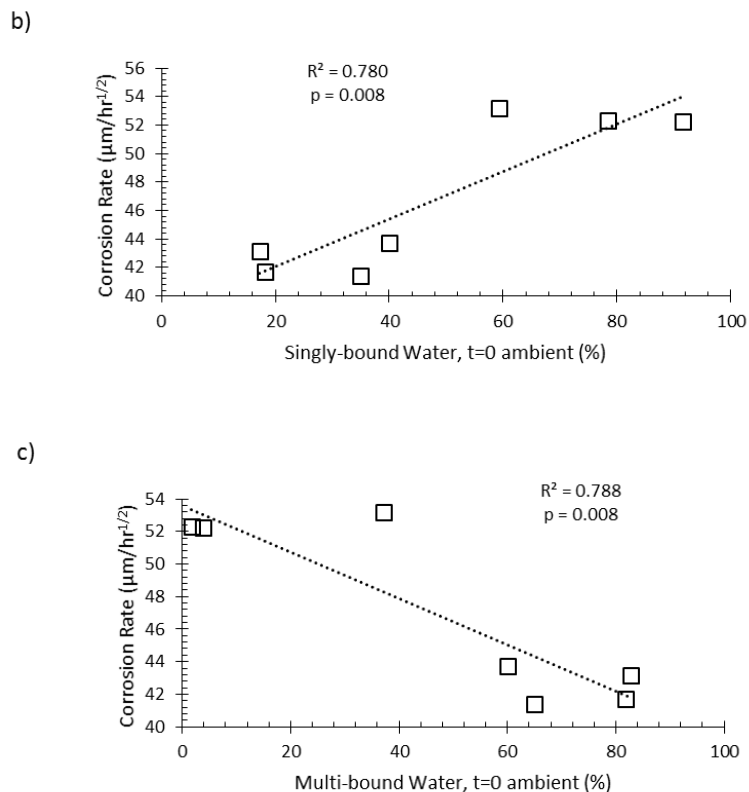


Figure 5.13 Corrosion rate of epoxy-amine coating thin films as a function of the relative water hydrogen bonding concentration of at ambient conditions before exposure.

Note: free water (a), singly-bound water (b), and multi-bound water (c) water hydrogen bonding interactions.

## 5.5 Discussion

It was hypothesized that higher relative concentrations of multi-bound water with longer hydrogen bonding lifetimes, and singly-bound water albeit to a lesser extent, reduces the concentration, availability and/or the time of availability for a given water molecule to contribute to the solvated ion hydration shell in comparison with free water thereby hindering ion permeation through the coating or metal/ion solvation at the coating/substrate interface. Farimani and Aluro calculated that the hydrogen bond lifetime near the surface of a carbon nanotube in the ice-like structure is 18.96 ps and is 13.4 ps for bulk water; additionally, the rotational diffusion of water decreases from 3.4

rad<sup>2</sup>/ps to 1.32 rad<sup>2</sup>/ps.<sup>22</sup> These data support that in addition to the increased amount of bound water with MWCNTs in the coating as demonstrated, the system also increases the residence time of the water in the bound states. Consistently, free water has been shown to be sufficiently mobile to correctly orient for facile ion hydration shell development and thereby accommodate increased mobility for ion diffusion.<sup>27</sup> It is expected that the requirement of hydration shells for ion permeation through a coating is similar for ion migration along the polymer/substrate interface consistent with the cathodic delamination mechanism. Indeed, the size of the cation hydration shell has been shown to have significant influence on the ion migration rate and subsequently the cathodic delamination rate.<sup>7</sup> Thus, reducing the availability of water to participate in the formation and retention of ion hydration shells at the polymer/substrate interface would, as these results have exhibited, inhibit the migration of cations along the polymer/substrate interface and reduce the cathodic delamination rate, concurrently.

Adhesion is generally a requirement for coatings to protect a substrate; indeed, the possible change in adhesion properties of coatings from the incorporation of MWCNTs during exposure due to the reduction of available water that interrupts the secondary interactions at the polymer/substrate interface cannot be overlooked. Although Wielant and co-workers noted a gradual decrease in the delamination rate with an increase in adhesion strength between a polyurethane and steel substrates with various pretreatments,<sup>232</sup> Lyon and co-workers pointed out that while adhesion is necessary, adhesion alone does not singularly dictate good corrosion performance.<sup>228</sup> It was shown in several varied examples by Marsh and co-workers that substrate pre-treatment-coating

formulation combinations can be prepared with good adhesion and poor corrosion performance (e.g., silane pre-treatment) and conversely, systems can exhibit poor adhesion and good corrosion performance (phosphated steel).<sup>233</sup> Additionally, Harun and co-workers have shown that while increased wet adhesion was observed for both epoxy and amine functional silane treatments on steel substrates, only the epoxy functional silane reduced the cathodic delamination rate.<sup>234</sup> These studies indicate that adhesion singularly cannot predict the corrosion performance of a given coating formulation.

The results presented here indicated that the corrosion rate correlated well with the distribution of water hydrogen bonding states. However, other mechanisms cannot be discounted that contribute to the overall corrosion performance of coating formulations containing MWCNTs as many critical polymer performance characteristics are increased simultaneously by incorporating MWCNTs (e.g., modulus, adhesion, glass transition temperature).<sup>10, 13, 29, 33, 38-39, 235</sup> These coating performance characteristics in a salt fog/full immersion environment may be influenced by the relative concentration of water hydrogen bonding interactions as it has been noted that the overall water absorption may not be a reliable predictor of the instantaneous polymer properties.<sup>15-16</sup> Thus, the mechanistic interplay between the water hydrogen bonding interactions at the coating/substrate interface, and within the polymer, and critical properties that affect the cathodic delamination rate (e.g., coating adhesion, ion transport/solvation, and facilitation/management of radical based interface degradation reactions) have the potential to increase coating performance properties if tuned to address the both adhesion and water hydrogen bonding. The mechanistic interdependence of adhesion and water

hydrogen bonding states at the coating substrate/interface for control of cathodic delamination needs to be understood to characterize the dominate influence of each complex singular event and interaction parameters between events/processes and distinct mechanisms. What is not understood is whether the adhesion controls the water hydrogen bonding distribution at the substrate interface or if the water hydrogen bonding distribution dominates the coating adhesion performance in the presence of water at the substrate interface and in potentially different ways from material to material type and combination.

The data reported herein provides empirical support to the concept that MWCNTs alter the temporal and spatial distribution of hydrogen bonding states within polymers. Furthermore, the fundamental understanding of how water hydrogen bonding interactions directly alter ion diffusion and corrosion rates are reported. The differences in the corrosion rates were attributed to the distribution of water hydrogen bonding interactions within the coating; the redistribution of water interactions within the coating is attributed to: 1) direct interactions of the water with MWCNT surfaces, and 2) the high aspect ratio of MWCNTs that spans potential hydrogen bonding sites of the polymer to increase the number of available hydrogen bonding sites for a single water molecule.<sup>19</sup> Both aspects finds literature support for reduced ion transport through the film with similar water saturation levels and salt content, i.e., an increased concentration of multi-bound water drives conditions toward poor ion hydration shell development at the polymer/substrate interface to prevent the migration of water-solvated ions along the polymer/substrate in the same time under the same conditions.<sup>23-24, 27-28</sup>

## 5.6 Conclusions

The main research objectives of this Chapter were to observe and quantify the influence of multiwall carbon nanotubes (unmodified MWCNTs and hydroxyl modified MWCNTs) on the corrosion performance differences between model epoxy-amine polymer thin film applied to steel substrates and to gain understanding of the mechanistic basis that influences corrosion performance. Short-term but accelerated corrosion testing (ASTM B117) of MWCNT/epoxy-amine thin film material combinations with three MWCNT concentrations indicated that MWCNTs influence the free versus bound water distribution of water hydrogen bonding interactions which subsequently reduced the corrosion rate by ~25% in a salt fog environment. Furthermore, the corrosion rate up to 168 hours of salt fog exposure correlated well with the measured concentration of each singly-bound and multi-bound water within each thin film material combination prior to exposure; further supporting data were found qualitatively by observing the relationship between increased multi-bound water (regardless of bound nature) and the reduced sodium, chlorine, and iron concentration measured at the polymer/substrate interface. It is proposed that the reduction of the experimental corrosion rate of MWCNT/epoxy-amine material combinations investigated here occurs when MWCNTs aid to redistribute and manage the water hydrogen bonding states such that the multi-bound water concentration and retention times increase and free water concentration and timing for availability decreases which in turn directly influences ion transport capability of system and the rate of ion driven corrosion processes.

## 5.7 References

7. Leng, A.; Streckel, H.; Stratmann, M., The Delamination of Polymeric Coatings from Steel. Part 2: First Stage of Delamination, Effect of Type and Concentration of Cations on Delamination, Chemical Analysis of the Interface. *Corrosion Science* **1998**, *41* (3), 579-597.
10. Pruna, A., Advances in Carbon Nanotube Technology for Corrosion Applications. In *Handbook of Polymer Nanocomposites. Processing, Performance and Application: Volume B: Carbon Nanotube Based Polymer Composites*, Kar, K. K.; Pandey, K. J.; Rana, S., Eds. Springer Berlin Heidelberg: Berlin, Heidelberg, 2015; pp 335-359.
13. Anonymous, Chromate Primer Alternative Uses Carbon Nanotubes Modified with Corrosion Inhibitors. *Materials Performance* 1 April 2016, 2016.
14. Morsch, S.; Lyon, S.; Greensmith, P.; Smith, S. D.; Gibbon, S. R., Water Transport in an Epoxy-Phenolic Coating. *Progress in Organic Coatings* **2015**, *78*, 293-299.
15. Cotugno, S.; Larobina, D.; Mensitieri, G.; Musto, P.; Ragosta, G., A Novel Spectroscopic Approach to Investigate Transport Processes in Polymers: The Case of Water-Epoxy System. *Polymer* **2001**, *42* (15), 6431-6438.
16. Musto, P.; Ragosta, G.; Mascia, L., Vibrational Spectroscopy Evidence for the Dual Nature of Water Sorbed into Epoxy Resins. *Chemistry of Materials* **2000**, *12* (5), 1331-1341.
17. Soles, C. L.; Yee, A. F., A Discussion of the Molecular Mechanisms of Moisture Transport in Epoxy Resins. *Journal of Polymer Science Part B: Polymer Physics* **2000**, *38* (5), 792-802.
18. Mijović, J.; Zhang, H., Local Dynamics and Molecular Origin of Polymer Network-Water Interactions as Studied by Broadband Dielectric Relaxation Spectroscopy, Ftir, and Molecular Simulations. *Macromolecules* **2003**, *36* (4), 1279-1288.
19. Takeshita, Y.; Becker, E.; Sakata, S.; Miwa, T.; Sawada, T., States of Water Absorbed in Water-Borne Urethane/Epoxy Coatings. *Polymer* **2014**, *55* (10), 2505-2513.
20. Lee, D. K.; Saito, T.; Benesi, A. J.; Hickner, M. A.; Allcock, H. R., Characterization of Water in Proton-Conducting Membranes by Deuterium Nmr T1 Relaxation. *The Journal of Physical Chemistry B* **2011**, *115* (5), 776-783.
22. Barati Farimani, A.; Aluru, N. R., Existence of Multiple Phases of Water at Nanotube Interfaces. *The Journal of Physical Chemistry C* **2016**, *120* (41), 23763-23771.
23. Geise, G. M.; Paul, D. R.; Freeman, B. D., Fundamental Water and Salt Transport Properties of Polymeric Materials. *Progress in Polymer Science* **2014**, *39* (1), 1-42.
24. Dias, C. R.; Rosa, M. J.; de Pinho, M. N., Structure of Water in Asymmetric Cellulose Ester Membranes — and Atr-Ftir Study. *Journal of Membrane Science* **1998**, *138* (2), 259-267.
26. Kropman, M. F.; Bakker, H. J., Dynamics of Water Molecules in Aqueous Solvation Shells. *Science* **2001**, *291* (5511), 2118-2120.
27. Gao, X.; Zhao, T.; Li, Z., Effects of Ions on the Diffusion Coefficient of Water in Carbon Nanotubes. *Journal of Applied Physics* **2014**, *116* (5), 054311.

28. Murphy, D.; de Pinho, M. N., An Atr-Ftir Study of Water in Cellulose Acetate Membranes Prepared by Phase Inversion. *Journal of Membrane Science* **1995**, *106* (3), 245-257.
29. Deyab, M. A., Effect of Carbon Nano-Tubes on the Corrosion Resistance of Alkyd Coating Immersed in Sodium Chloride Solution. *Progress in Organic Coatings* **2015**, *85*, 146-150.
33. Gergely, A.; Pászti, Z.; Hakkel, O.; Drotár, E.; Mihály, J.; Kálmán, E., Corrosion Protection of Cold-Rolled Steel with Alkyd Paint Coatings Compositated with Submicron-Structure Types Polypyrrole-Modified Nano-Size Alumina and Carbon Nanotubes. *Materials Science and Engineering: B* **2012**, *177* (18), 1571-1582.
38. Gergely, A.; Pászti, Z.; Mihály, J.; Drotár, E.; Török, T., Galvanic Function of Zinc-Rich Coatings Facilitated by Percolating Structure of the Carbon Nanotubes. Part II: Protection Properties and Mechanism of the Hybrid Coatings. *Progress in Organic Coatings* **2014**, *77* (2), 412-424.
39. Khun, N. W.; Frankel, G. S., Cathodic Delamination of Polyurethane/Multiwalled Carbon Nanotube Composite Coatings from Steel Substrates. *Progress in Organic Coatings* **2016**, *99*, 55-60.
40. Starkova, O.; Buschhorn, S. T.; Mannov, E.; Schulte, K.; Aniskevich, A., Water Transport in Epoxy/Mwcnt Composites. *European Polymer Journal* **2013**, *49* (8), 2138-2148.
41. Curtzwiler, G. W.; Williams, E. B.; Konecki, C. M.; Wand, S. W.; Rawlins, J. W., Comparison of the Added Value for Corrosion Performance of Chemically Modified Multiwall Carbon Nanotube Epoxy-Amine Coating Systems on Steel Substrates. In *The Waterborne Symposium*, New Orleans, LA, 2016.
58. Fontana, M., *Corrosion Engineering*. 3 ed.; McGraw-Hill, Inc: Singapore, 1986.
70. Lehman, J. H.; Terrones, M.; Mansfield, E.; Hurst, K. E.; Meunier, V., Evaluating the Characteristics of Multiwall Carbon Nanotubes. *Carbon* **2011**, *49* (8), 2581-2602.
72. Chakrapani, N.; Curran, S.; Wei, B.; Ajayan, P. M.; Carrillo, A.; Kane, R. S., Spectral Fingerprinting of Structural Defects in Plasma-Treated Carbon Nanotubes. *Journal of Materials Research* **2011**, *18* (10), 2515-2521.
120. Pietraß, T.; Dewald, J. L.; Clewett, C. F. M.; Tierney, D.; Ellis, A. V.; Dias, S.; Alvarado, A.; Sandoval, L.; Tai, S.; Curran, S. A., Electron Spin Resonance and Raman Scattering Spectroscopy of Multi-Walled Carbon Nanotubes: A Function of Acid Treatment. *Journal of Nanoscience and Nanotechnology* **2006**, *6* (1), 135-140.
147. Arepalli, S.; Freiman, S.; Hooker, S.; Migler, D., Measurement Issues in Single-Wall Carbon Nanotubes. *NIST Recommended Practice Guide* **2008**.
165. Xu, X.; Thwe, M. M.; Shearwood, C.; Liao, K., Mechanical Properties and Interfacial Characteristics of Carbon-Nanotube-Reinforced Epoxy Thin Films. *Applied Physics Letters* **2002**, *81* (15), 2833-2835.
183. Koleske, J. V., *Paint and Coating Testing Manual*. 15th ed.; ASTM International: West Conshohocken, 2012.
191. Ellison, S.; Barwick, V.; Trevor, F., *Practical Statistics for the Analytical Scientist: A Bench Guide*. 2nd ed.; The Royal Society of Chemistry: Cambridge, 2009.

210. International, A., Standard Practice for Evaluating Degree of Rusting on Painted Steel Surfaces. In *ASTM D610-08(2012)* West Conshohocken, 2012.
212. Mullins, E., *Statistics for the Quality Control Chemistry Laboratory*. The Royal Society of Chemistry: Cambridge, 2003.
213. Foster, S. F.; Hoff, E. A.; Curtzwiler, G. W.; Williams, E. B.; Davis, K. B.; Patton, D. L.; Rawlins, J. W., Chemorheology Investigation of a Glassy Epoxy Thermoset on Tensile Plastic Flow and Fracture Morphology. *Journal of Polymer Science Part B: Polymer Physics* **2015**, n/a-n/a.
219. Curtzwiler, G.; Early, M.; Gottschalk, D.; Konecki, C.; Peterson, R.; Wand, S.; Rawlins, J. W., The World of Surface Coatings Is Centered around the Glass Transition Temperature but Which One? Part 2. *JCT CoatingsTech* **2014**, *11*, 40-51.
220. Curtzwiler, G.; Early, M.; Gottschalk, D.; Konecki, C.; Peterson, R.; Wand, S.; Rawlins, J. W., The World of Surface Coatings Is Centered around the Glass Transition Temperature but Which One? Part I. *JCT CoatingsTech* **2014**, *11*, 28-38.
222. Choudalakis, G.; Gotsis, A. D., Free Volume and Mass Transport in Polymer Nanocomposites. *Current Opinion in Colloid & Interface Science* **2012**, *17* (3), 132-140.
224. Politano, A.; Chiarello, G., The Nature of Free O-H Stretching in Water Adsorbed on Carbon Nanosystems. *The Journal of Chemical Physics* **2013**, *139* (6), 064704.
225. Thomas, J. A.; McGaughey, A. J. H., Density, Distribution, and Orientation of Water Molecules inside and Outside Carbon Nanotubes. *The Journal of Chemical Physics* **2008**, *128* (8), 084715.
226. Martí, J.; Gordillo, M. C., Structure and Dynamics of Liquid Water Adsorbed on the External Walls of Carbon Nanotubes. *The Journal of Chemical Physics* **2003**, *119* (23), 12540-12546.
227. Gordillo, M. C.; Martí, J., Water on the Outside of Carbon Nanotube Bundles. *Physical Review B* **2003**, *67* (20), 205425.
228. Lyon, S. B.; Bingham, R.; Mills, D. J., Advances in Corrosion Protection by Organic Coatings: What We Know and What We Would Like to Know. *Progress in Organic Coatings* **2017**, *102*, 2-7.
229. Standard Practice for Operating Salt Spray (Fog) Apparatus. In *ASTM B117 - 11*, ASTM International: West Conshohocken, 2011.
230. Schneider, A.; Hommel, G.; Blettner, M., Linear Regression Analysis: Part 14 of a Series on Evaluation of Scientific Publications. *Deutsches Arzteblatt International* **2010**, *107* (44), 776-82.
231. Starkova, O.; Chandrasekaran, S.; Prado, L. A. S. A.; Tölle, F.; Mülhaupt, R.; Schulte, K., Hydrothermally Resistant Thermally Reduced Graphene Oxide and Multi-Wall Carbon Nanotube Based Epoxy Nanocomposites. *Polymer Degradation and Stability* **2013**, *98* (2), 519-526.
232. Wielant, J.; Posner, R.; Hausbrand, R.; Grundmeier, G.; Terryn, H., Cathodic Delamination of Polyurethane Films on Oxide Covered Steel – Combined Adhesion and Interface Electrochemical Studies. *Corrosion Science* **2009**, *51* (8), 1664-1670.
233. Marsh, J.; Scantlebury, J. D.; Lyon, S. B., The Effect of Surface/Primer Treatments on the Performance of Alkyd Coated Steel. *Corrosion Science* **2001**, *43* (5), 829-852.

234. Harun, M. K.; Marsh, J.; Lyon, S. B., The Effect of Surface Modification on the Cathodic Disbondment Rate of Epoxy and Alkyd Coatings. *Progress in Organic Coatings* **2005**, *54* (4), 317-321.
235. Khun, N. W.; Troconis, B. C. R.; Frankel, G. S., Effects of Carbon Nanotube Content on Adhesion Strength and Wear and Corrosion Resistance of Epoxy Composite Coatings on Aa2024-T3. *Progress in Organic Coatings* **2014**, *77* (1), 72-80.

CHAPTER VI – PREDICTION OF EPOXY-AMINE CORROSION PERFORMANCE  
ON STEEL IN A SALT FOG ENVIRONMENT USING PRE-EXPOSURE  
MEASUREMENTS AND STEPWISE REGRESSION ANALYSIS

**6.1 Abstract**

Determining the anticorrosive properties of new and modified coating formulations is a time intensive and expensive process that commonly requires thousands of hours in an accelerated corrosion environment or years of exposure in real world conditions before a final evaluation and decision can be made. It is therefore desirable to develop methods capable of predicting the corrosion performance of new or modified coating formulations from ambient performance characteristics. Chapter V demonstrated that quantifying water hydrogen bonding interactions within multiwall carbon nanotube epoxy-amine thin film material combinations at ambient conditions had predictive capabilities of the experimental corrosion rate in a 5% NaCl salt fog environment. The research objective of this Chapter is to improve the understanding of how water hydrogen bonding interactions at ambient conditions affects the corrosion rate and its applicability to predict experimental corrosion rates in a salt fog environment. Nano-carbon allotropes (carbon black, multiwall carbon nanotubes, and graphene) were incorporated at various, low filler volume fractions into a parent epoxy-amine material combination applied to steel substrates to alter the water hydrogen bonding interactions. The corrosion rates were quantified measuring the area growth from intentionally created defects and compared to the relative concentration of water hydrogen bonding states. It was validated that the corrosion rate of the current thin film material combinations was directly related to the

relative distribution of water hydrogen bonding interactions at the polymer/air interface before, during and after environmental exposure. Furthermore, a stepwise multivariable regression approach was used to develop a simple, first order equation capable of predicting ~91% of the variation in the experimental corrosion rates in a salt fog environment from ambient performance characteristics.

## **6.2 Introduction**

NACE international estimated that ~2.5 trillion USD was spent globally in 2013 due to asset maintenance and loss.<sup>2</sup> Corrosion of steel substrates occurs spontaneously in the presence of oxygen, water, and conductive species, thus, the proper management of these conditions will increase the service lifetime of a given substrate.<sup>5</sup> Corrosion testing under real-world conditions and even accelerated conditions is time consuming and expensive and may be impractical for all research funding cycles. For example, the military specification for epoxy-amine coating formulations requires that the substrate bound coating must not show blistering, lifting of the coating, or substrate pitting after 2000 hours in a 5% NaCl salt spray conditions at 35 °C (ASTM B117).<sup>229, 236</sup> Therefore, evaluation of pre-exposure performance characteristics of coating formulations to predict the corrosion performance would enable rapid screening of new and modified coating formulations. Preferably, the ability to use pre-exposure laboratory measurements to predict the experimental corrosion rates in accelerated corrosion conditions (e.g., ASTM B117, GM 14872, prohesion) or real world corrosion rates would save significant time and capital for coating formulators. Although assets such as vehicles and aircraft may be exposed to a wide variety of environments, each with varying degrees of severity and

often unpredictable time scales, facility assets and civil infrastructure maintain a more constant and predictable exposure profile that can be modeled with high confidence.

As noted in detail in Chapter I, the corrosion of steel substrates occurs spontaneously and generally inevitably, in the presence and accumulation of oxygen, water, and conductive electrolyte species.<sup>5-6</sup> The corrosion rate of steel substrates is significantly accelerated due to coating defects or possesses macroscopic breaches from in-service abuse as environmental contaminants have direct access to the substrate; thus, much attention has been paid to the development of technologies that inhibit the corrosion events of coated substrates with macroscopic breaches.<sup>5-6, 8-9</sup> In the case of coated substrates with intentionally created defects, as is common for most corrosion performance investigations, a higher concentration of iron and chlorine is spatially observed in the scribed area (anode) and a higher concentration of sodium is away from the scribe (cathode).

The distribution of water hydrogen bonding interactions (i.e., whether it is free or bound to the polymer) within a polymer can have a significant impact on the instantaneous material properties.<sup>14-18, 21</sup> Although the distribution of water states is typically described as definitive and discrete states, it is important to note the rapid and dynamic nature of water molecule hydrogen bonding possess hydrogen bonding lifetimes (on the order of picoseconds)<sup>22</sup> orders of magnitude much shorter than the length scales of most experimental investigations. Water hydrogen bond interactions is described more in detail in Chapter I, briefly, water is classified discretely by the number of hydrogen bonds with the polymer matrix or another water molecule: e.g., free water,

singly-bound water, and multi-bound water.<sup>15-16</sup> Li and co-workers further classified multi-bound water into loosely-bound and tightly-bound water.<sup>21</sup> Loosely-bound water was considered as water that hydrogen bonds to weak polar groups such as tertiary amines or sulfone groups or hydrogen bonds to highly polar, but sterically hindered groups.<sup>21</sup> Comparatively, tightly hydrogen bound water is strongly bound to hydroxyl groups whether it be another water molecule or the polymer network.<sup>21</sup> Free water does not directly hydrogen bond with the polymer matrix nor another water molecule.<sup>15-16</sup>

Results in Chapter V indicated that the corrosion rate of MWCNT/epoxy-amine coatings on steel substrates consistently correlated well with the distribution of water hydrogen bonding interactions within the coating at pre-exposure ambient conditions. The research objective of this Chapter is to further investigate the influence of water hydrogen bonding interactions on the experimental corrosion rates and validate the potential for utilizing ambient, pre-exposure measurements to predict the corrosion rate of epoxy-amine coating material combinations. Nano-carbon allotropes (carbon black, MWCNTs, and graphene) were utilized to alter the water hydrogen bonding interactions of epoxy-amine thin film material combinations at ambient pre-exposure conditions and subsequently the corrosion rate of steel substrate bound polymer coatings with intentionally created defects in a 5% NaCl salt fog environment. A stepwise multivariable regression analysis approach was used to determine the best set of predictor variables and produce an equation to predict the experimental corrosion rate of epoxy-amine thin film material combinations from intentionally created defects. This work directly expands on

the results of Chapter V regarding the distribution of water interactions within a polymer and its influence on the corrosion performance in accelerated corrosion conditions.

## **6.3 Experimental**

### **6.3.1 Materials and Methods**

Chapter IV established that the type of surface modification did not greatly affect the corrosion performance of the epoxy-amine thin film material combination, thus, only the unmodified and hydroxyl modified multiwall carbon nanotubes were utilized for this investigation in this Chapter; the detailed synthesis of the hydroxyl MWCNTs can be found in section 4.3.2. A detailed description of all other materials, procedures, and characterizations can be found in Chapter IV, section 4.3; below is a brief description.

### **6.3.2 Characterization of MWCNT Functionalization**

Both the unmodified MWCNT and hydroxyl group functionalized MWCNTs were characterized with Raman spectroscopy and the D<sup>'</sup>/G ratio was utilized to investigate MWCNT molecular structure changes from chemical modifications as noted in Chapter II.<sup>70, 72, 120</sup> The functional group equivalents per gram MWCNT attached to the MWCNTs was quantified via thermogravimetric analysis.<sup>147</sup>

### **6.3.3 Fabrication of Model Epoxy-Amine Steel Bound Polymer Thin Film and Free Films Containing Nano-Carbon Allotropes**

The appropriate combination of particle and concentration (unmodified MWCNTs, hydroxyl MWCNTs, graphene, carbon black; 0.50, 0.75, and 1.0 wt% on coating solids) was dispersed in the epoxy mixture then mixed with the amine as in Section 4.3.2. Each thin film material combination was spray applied either to SAE

1008/1010 carbon steel for corrosion evaluation via ASTM B117 or polypropylene substrates to obtain free films (Scheme 4.3). All substrates were cleaned with an acetone soaked low lint wipe followed by a hexanes soaked low lint wipe prior to coating application. All coatings were cured according to the procedure in Section 4.3.2 (dried film thickness 25-30  $\mu\text{m}$ ).

#### **6.3.4 Coating Characterization**

Particle dispersion, the glass transition temperature, and water vapor diffusivity properties of each thin film material combination were investigated in a similar manner as in Section 4.3.5.

#### **6.3.5 Corrosion Analysis**

Four coated steel panels per thin film material combination were scribed with a Vision Express engraver equipped with a 120 degree diamond drag spindle at 100 mm/s in an X pattern with equal arms of 15.5 mm in length in the lower portion of the panel (Figure 6.1). Each scribed panel was subjected to accelerated corrosion conditions (5% NaCl salt fog spray, 35 °C) according to ASTM B117.<sup>229</sup> Data collection and corrosion quantification as a function of time was completed as described in Section 5.3.5. The dominant corrosion mechanism of all thin films visually appeared to be cathodic delamination as in Chapter V; thus, determining the square root of the corrosion area yields the average corrosion distance due to cathodic delamination. Following the interpretation of Leng and co-workers, the average corrosion distance was plotted as a function of the square root of time (Equation 6.2) and the corrosion rate was defined as

the slope,  $A$ ; where  $\bar{x}$  is the average measured corrosion distance due to cathodic delamination and  $t$  is the time in hours.<sup>7</sup>

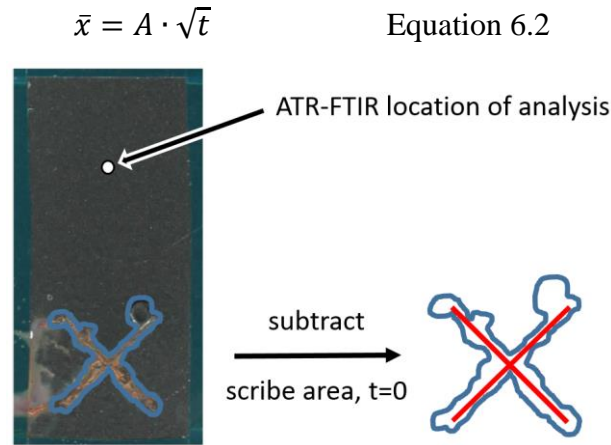


Figure 6.1 Determination of the cathodic corrosion area by quantitative image analysis.

### 6.3.6 Water Hydrogen Bonding Interactions

Attenuated total reflectance-Fourier transform infrared (ATR-FTIR) spectra were collected (Figure 6.1) at each time point to determine the water hydrogen bonding interactions at the polymer/air interface as in Section 5.3.6. A desiccated (0% RH) free film specimen for each corresponding thin film material combination was considered the reference material for subtraction from the spectrum at time  $t$  and  $t=0$ , *ambient* (Equation 6.3). The O-H stretching  $\nu_{(\text{OH})}$  region of the subtracted ATR-FTIR spectrum was deconvoluted into five peaks corresponding to multi-bound ( $S_2'$  and  $S_2''$ ), singly-bound ( $S_1$ ), and free (non-hydrogen bonded;  $S_0$ ) water types centered at  $\sim 3265 \text{ cm}^{-1}$ ,  $\sim 3420 \text{ cm}^{-1}$ ,  $\sim 3555 \text{ cm}^{-1}$ ,  $\sim 3610 \text{ cm}^{-1}$ , respectively, and the Fermi overtone utilizing a Gauss-Lorentz line shape via OMINC 8.3 software (Figure 4.3).<sup>15-16, 211</sup> The percent of each water hydrogen bonding interaction was calculated via quantification of the area of

each deconvoluted peak. The Fermi peak was excluded from the total area prior to calculations.

$$A(v)_{\text{subtracted spectrum}} = A(v)_{\text{time}=t} - A(v)_{\text{t}=0, \text{desiccated}} \quad \text{Equation 6.3}$$

### 6.3.7 Post-Exposure Analysis

Post-exposure corrosion analysis of the coating was performed to verify the cathodic delamination mechanism to justify the interpretation of the corrosion data quantitatively as noted in Section 6.3.5. The coating of each panel was removed from the substrate and a specimen near the scribe (Scheme 5.1) was sectioned for analysis of the polymer at the polymer/substrate interface as in Section 5.3.7. Each specimen was sputter coated with silver and energy dispersive X-ray spectroscopy was used to qualitatively identify inorganic elements (e.g. Na, Fe, Cl).

### 6.3.8 Statistical Analysis

A one-way ANOVA was utilized at a 95% confidence level via MiniTab 17 software to investigate differences in mean property values and Tukey's post-hoc pairwise comparison grouped means ( $n \geq 3$ ) that were statistically the same.<sup>191, 212</sup> The statistical significance of linear trendlines between data sets was accomplished via linear univariable regression analysis utilizing ( $\alpha = 0.05$ ). Stepwise multivariable regression analysis was used to generate predictive equations for the experimental corrosion rate of coated steel substrates with intentionally created defects in a 5% NaCl salt fog environment at 35 °C (ASTM B117). Stepwise multivariable regression analysis utilized an  $\alpha < 0.15$  to select each potential parameter to enter/exit the equation for each iteration. The stepwise selection of terms into a multivariable regression equation enters a single

independent variable (a single pre-exposure single measurement as noted above) that best describes the dependent variable (the corrosion rate) one iteration at a time. Each iteration performs a backwards check to remove all statistically irrelevant variables.<sup>230</sup> First, second, and third order interactions were allowed within the software to generate three different regression equations in the general form of Equations 6.4-6.6.<sup>237</sup>

$$y = \alpha + \beta_1 X_1 + \beta_2 X_2 + \beta_3 X_3 \dots \quad \text{Equation 6.4}$$

$$y = \alpha + \beta_1 X_1 + \beta_2 X_2 + \beta_3 X_3 + \beta_4 X_1^2 + \beta_5 X_2^2 + \beta_6 X_3^2 + \beta_7 X_1 X_2 + \beta_8 X_2 X_3 + \beta_9 X_1 X_3 \dots$$

Equation 6.5

$$y = \alpha + \beta_1 X_1 + \beta_2 X_2 + \beta_3 X_3 + \beta_4 X_1^2 + \beta_5 X_2^2 + \beta_6 X_3^2 + \beta_7 X_1 X_2 + \beta_8 X_2 X_3 + \beta_9 X_1 X_3 + \beta_{10} X_1^3 + \beta_{11} X_2^3 + \beta_{12} X_3^3 + \beta_{13} X_1^2 X_2 + \beta_{14} X_1 X_2^2 + \beta_{15} X_1^2 X_3 + \beta_{16} X_1 X_3^2 + \beta_{17} X_2^2 X_3 + \beta_{18} X_2 X_3^2 + \beta_{19} X_1 X_2 X_3 \dots \quad \text{Equation 6.6}$$

## 6.4 Results and Discussion

Generally, the MWCNTs are protruding from the surface indicating shear alignment parallel to the substrate; the substrate would be protruding from the page at the top of each image (Figure 6.2). Multiple voids were observed in the carbon black and graphene thin films at all concentrations; high degrees of agglomeration and flocculation was also observed for these systems. However, the MWCNT/epoxy-amine material combinations achieved a very high degree of exfoliation and nano-scale dispersion; in fact, no agglomerates/flocs were observed in any of the MWCNT/epoxy-amine material combinations independent of surface chemistry or concentration.

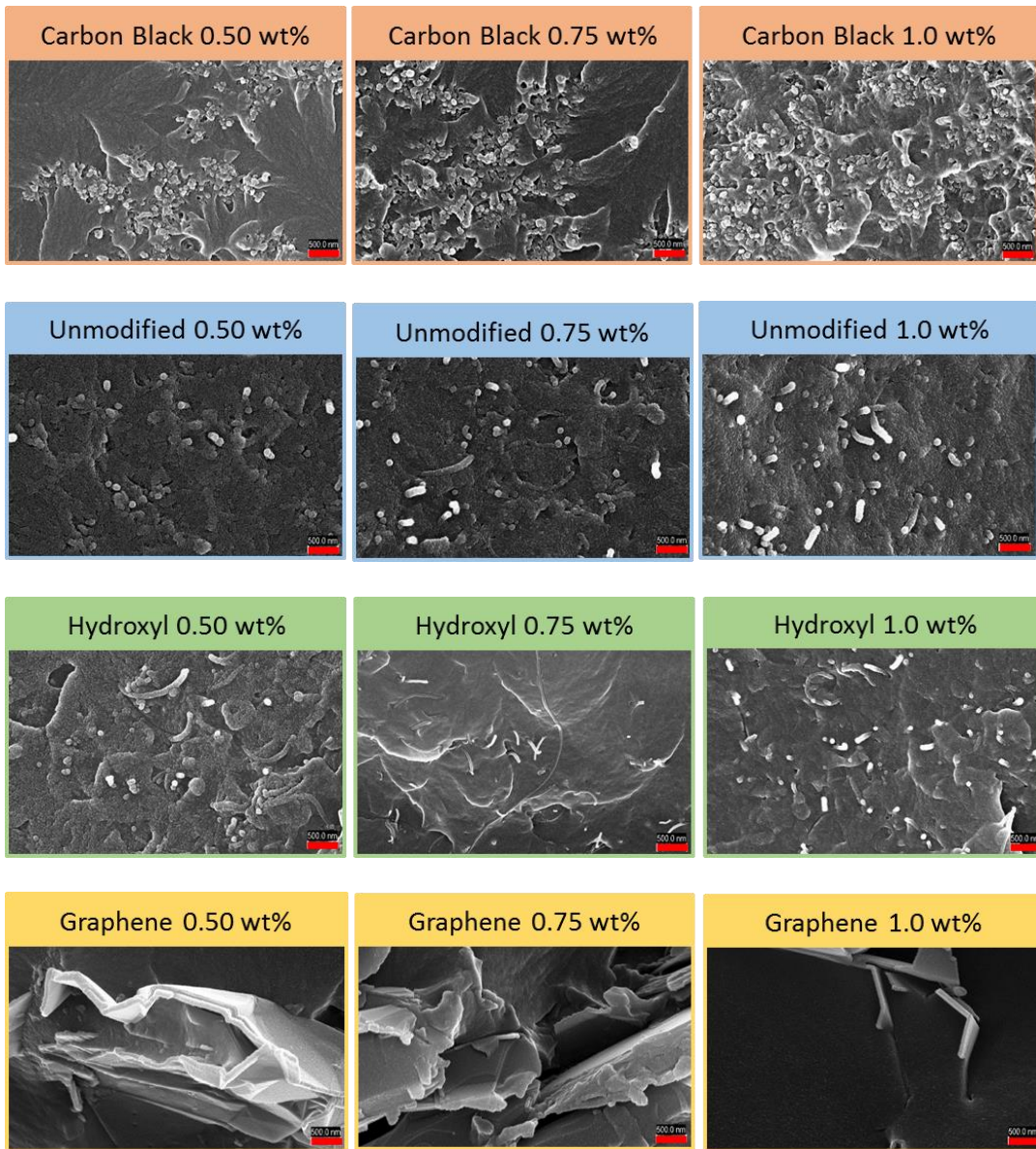


Figure 6.2 Scanning electron micrographs of epoxy-amine coatings containing MWCNTs (~20kx magnification).

Note: Scale bar is 500 nm.

## 6.4.2 Potential Predictor Input Parameters for Stepwise Multivariable Regression

### Analysis

#### 6.4.2.1 Glass Transition Temperature

The experimental/ambient temperature relative to the glass transition temperature ( $T_g$ ) of a polymer system has significant influence on the polymer's physical state and the various performance characteristics.<sup>219-220</sup> Similar to what was reported in Chapter V, incorporation of nano-carbon allotropes did not greatly affect the dry  $T_g$  (i.e., pre-exposure  $T_g$ ) of the parent polymer network at the loading concentrations utilized (Figure 6.3). Seemingly critical to this investigation is the small difference (maximum  $\sim 6$  °C) between the measured glass transition temperature and the exposure temperature of the salt fog environment (35 °C, ASTM B117)<sup>229</sup> as the simple physical state of the polymer directly influences the dominant small molecule permeation mechanism.<sup>222</sup> Although there was small difference between the exposure temperature and the  $T_g$  of each thin film type, statistical differences were determined and the  $T_g$  was included as a potential predictor of the corrosion rate.

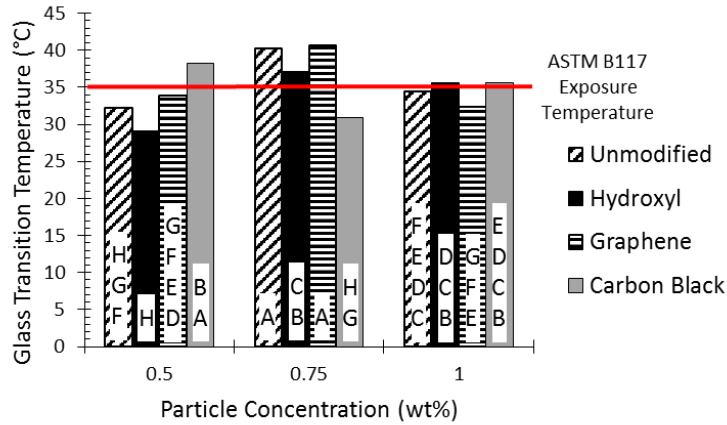


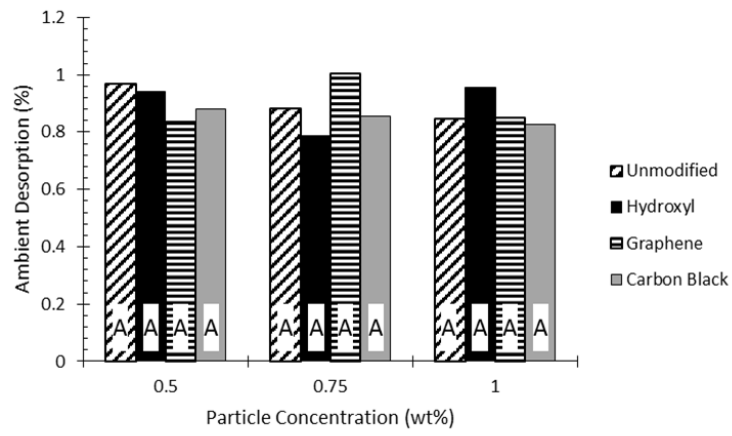
Figure 6.3 Glass transition temperature of epoxy-amine coating thin films containing various nano-carbon allotropes and concentrations.

Note: Means with different letters are statistically different.

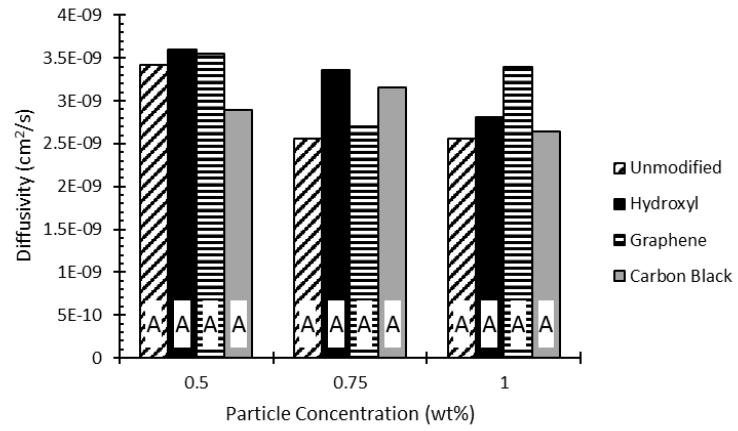
#### 6.4.2.2 Water Vapor Desorption, Diffusivity, and Equilibrium Saturation

Although the polymer free films start in the glassy state at the temperature of the water vapor sorption experiments (25 °C), the water vapor permeation properties are not be expected to greatly differ at 35 °C as in ASTM B117; Starkova and co-workers demonstrated the diminishing effect of tortuosity due to incorporation of MWCNTs on water diffusion when the exposure temperature was increased to 30 °C below the glass transition temperature of the polymer.<sup>40</sup> No significant differences were determined in the water vapor diffusivity for any of the thin film material combinations investigated here (Figure 6.4), nor in the mass loss in the desiccation cycle and the water vapor saturation at equilibrium after exposure to a 95% RH environment (Figure 6.4a-c). As a result, these parameters were excluded from the set of potential predictors for consideration by the stepwise regression algorithm.

a)



b)



c)

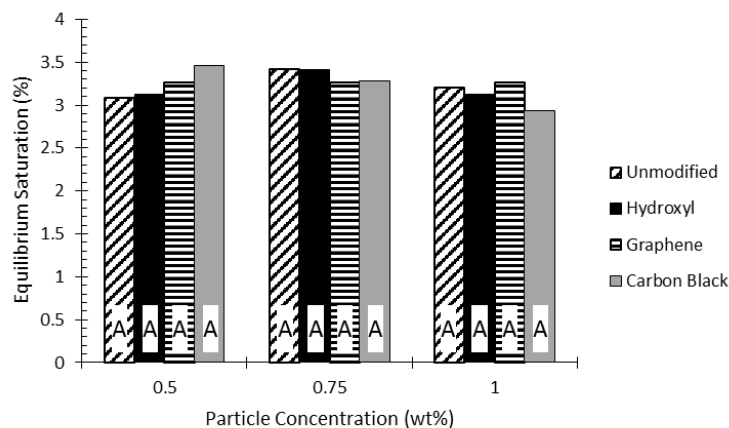


Figure 6.4 Ambient water concentration (a), water vapor diffusivity (b), and water vapor saturation at equilibrium (c) for epoxy-amine free films containing various nano carbon allotropes.

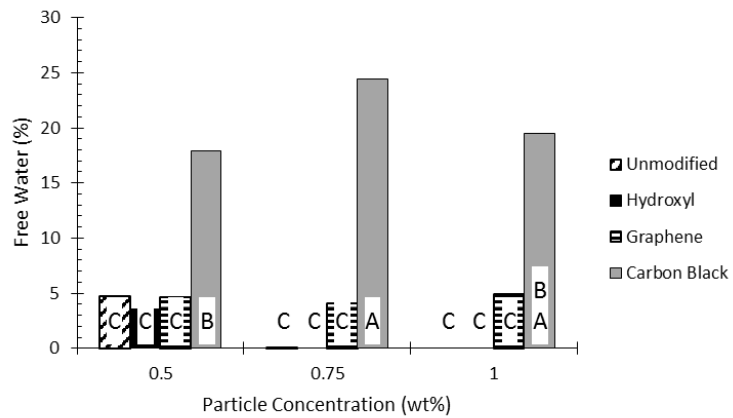
Note: Means with different letters are statistically different.

#### 6.4.2.3 Water Hydrogen Bonding Interactions at $t=0$ , *ambient*

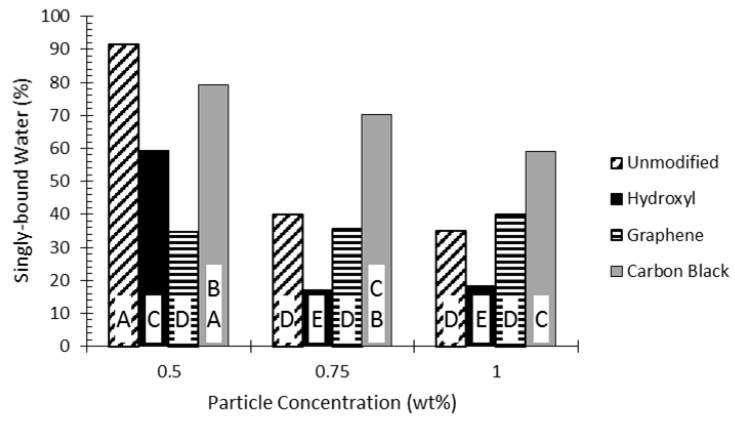
Generally, the carbon black thin films contained more free water than all thin film containing MWCNTs (unmodified and hydroxyl surface functionalities) and graphene for all concentrations. As the concentration of MWCNTs increased in the thin film material combination from 0.50 wt%, the amount of free water ( $S_0$ ) decreased to zero for the hydroxyl surface functionality at 0.75 wt% and nearly zero ( $< 0.10\%$ ) for the unmodified MWCNT type. Surprisingly, the free water and singly-bound water content at  $t=0$ , *ambient* for the graphene thin films was independent of concentration; these observations may be attributed to the relatively poor dispersion achieved under the conditions employed (Figure 6.2). Interestingly, the free water content of all thin film material combinations, except carbon black, were statistically the same independent of concentration (Figure 6.5); this may in part be attributed to the amount of variation in the

0.50 wt% hydroxyl MWCNT thin film type. For both MWCNT surface functionalities similar trends were observed in the relative amount of singly-bound ( $S_1$ ) water as with the free water, i.e., the 0.75 and 1.0 wt% concentrations possessed similar values and were lower than the 0.50 wt% loading level; however, the hydroxyl MWCNT possessed statistically lower amounts of singly-bound water compared to the unmodified MWCNT. The carbon black thin films possessed decreasing amounts of singly-bound water with increasing particle concentration, albeit, at a much lower rate than the MWCNT thin films.

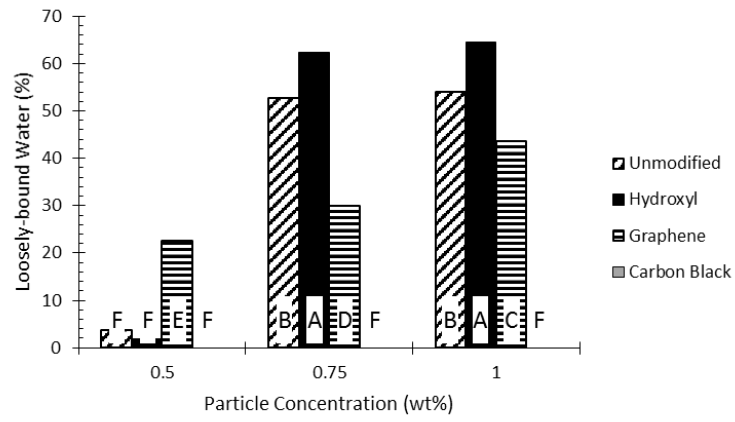
a)



b)



c)



d)

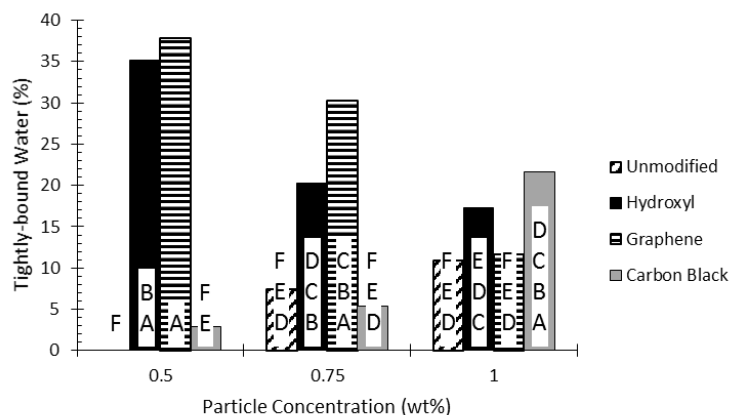


Figure 6.5 Relative concentration of water hydrogen bonding interactions within epoxy-amine material combinations at  $t=0$  Hr, ambient.

Note: Means with different letters are statistically different. free (a), singly-bound (b), loosely-bound (c), and tightly-bound (d) water hydrogen bonding interactions.

The graphene thin films possessed gradually increasing loosely-bound water ( $S_2'$ ) with concentration (23%, 30%, and 44% for the 0.50, 0.75, and 1.0 wt%, respectively). The loosely-bound water content was statistically the same for each particle type at loading levels of 0.75 and 1.0 wt% except for the graphene material combinations. The hydroxyl surface functionality afforded higher values than the unmodified MWCNT thin films. The  $S_2'$  content of the unmodified and hydroxyl modified MWCNTs were statistically the same as the carbon black thin films at a loading level of 0.50 wt% which had values between zero and four percent. The tightly-bound ( $S_2''$ ) water content of the carbon black thin film at 1.0 wt% was higher than the 0.50 wt%, but statistically the same as the 0.75 wt% loading level. Both the hydroxyl MWCNT and graphene material combinations were statistically the same for all concentrations. For each the graphene and hydroxyl material combinations, singularly, containing a 1.0 wt% loading level, the  $S_2''$

water state was lower in concentration than both the 0.75 and 0.50 wt% thin films (which were statistically the same). The tightly-bound water content of the 1.0 wt% hydroxyl MWCNT thin film was lower than the 0.50 wt% but the same as the 0.75 wt% loading level. The tightly-bound water of all material combinations containing a 1.0 wt% particle loading level were statistically the same independent of the particle type. Graphene possessed the highest amount of S<sub>2</sub>'' water content at 0.75 wt% and all other thin film material combinations were statistically the same. Graphene and hydroxyl at 0.50 wt% were the highest amount of tightly-bound water and were statistically the same; conversely, the unmodified MWCNT and carbon black at 0.50 wt% were the lowest and the same.

#### **6.4.3 Corrosion Rate**

Free water, and singly-bound water to a lesser extent, increases the potential of a water molecule to contribute to the hydration shell of solvated ions thereby increasing ion permeation through the coating due to the lower mobility.<sup>16</sup> Conversely, multi-bound water does not have sufficient mobility to change orientation to complete the hydration shell of ions to facilitate transport.<sup>26-27</sup> It is recognized that 168 hours of salt fog exposure is insufficient for optimized corrosion control coatings as U.S. military specifications requires 2000 hours of 5% NaCl fog exposure to qualify for use.<sup>236</sup> However, this work was designed to validate the observations that water hydrogen bonding within polymers influences the corrosion rate and utilization of pre-exposure measurements to predict the corrosion rate in a salt fog environment.

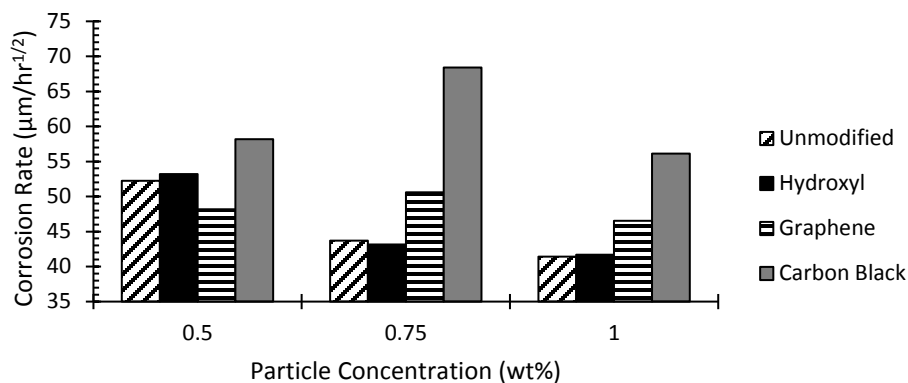
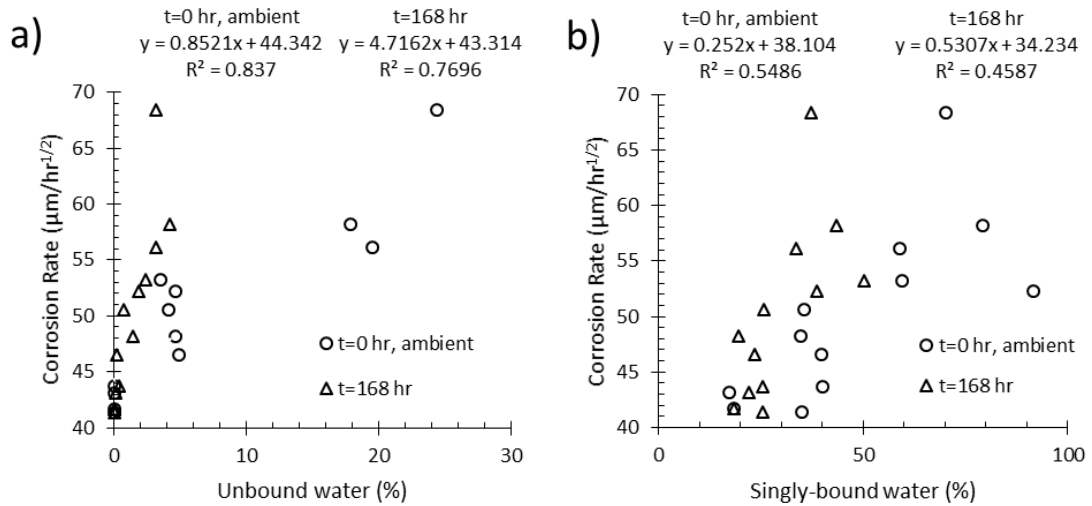


Figure 6.6 Average corrosion rate for epoxy-amine coatings on steel substrates formulated with various nano-carbon allotropes.

The corrosion rate (Figure 6.6) was calculated according to Equation 6.2 from the average of four measurements per time point; regression analysis indicated that the trendline slope for each material combination was statistically relevant ( $p < 0.01$ ) suggesting an ion diffusion controlled process consistent with a cathodic delamination mechanism.<sup>7</sup> All thin films containing carbon black corroded faster (5 – 18  $\mu\text{m/hr}^{1/2}$  more than the corrosion rate of the closest material combination) than all other particle types at each loading level concentration (Figure 6.6). Surprisingly, the corrosion rate of the graphene thin films was not greatly affected by increasing the concentration of the particle, similar to what was observed for the relative concentration of free and singly-bound water at  $t=0$ , *ambient*. In contrast, the corrosion rate for both the unmodified and hydroxyl modified MWCNT thin films decreased when the concentration increased from 0.50 wt% to 0.75 wt% ( $\sim 42 \mu\text{m/hr}^{1/2}$ ), but did not further decrease when the concentration was increased to 1.0 wt%.

Although the relationships between the water hydrogen bonding interactions at  $t=168 \text{ hours}$  were not considered as a predictor of the corrosion rate, an in-depth

understand of the mechanistic influence of water hydrogen bonding on the corrosion rate will enable the development of polymer coating formulations that can properly manage corrosion inducing conditions at the polymer/substrate interface. Consistent the results in Chapter V, there was a direct relationship between the free and singly-bound water content with the measured corrosion rate. Surprisingly, only the loosely-bound water type was determined to correlate well with the corrosion rate, but, the corrosion rate was determined to correlate well with the corrosion rate, but, the corrosion rate was independent of the tightly-bound water content. The slope of the corrosion rate as a function of the free water content was  $\sim 9$  times higher than the slope of the corrosion rate as a function of singly-bound water suggesting that free water contributes to increasing the corrosion rate nine times more than singly-bound water.



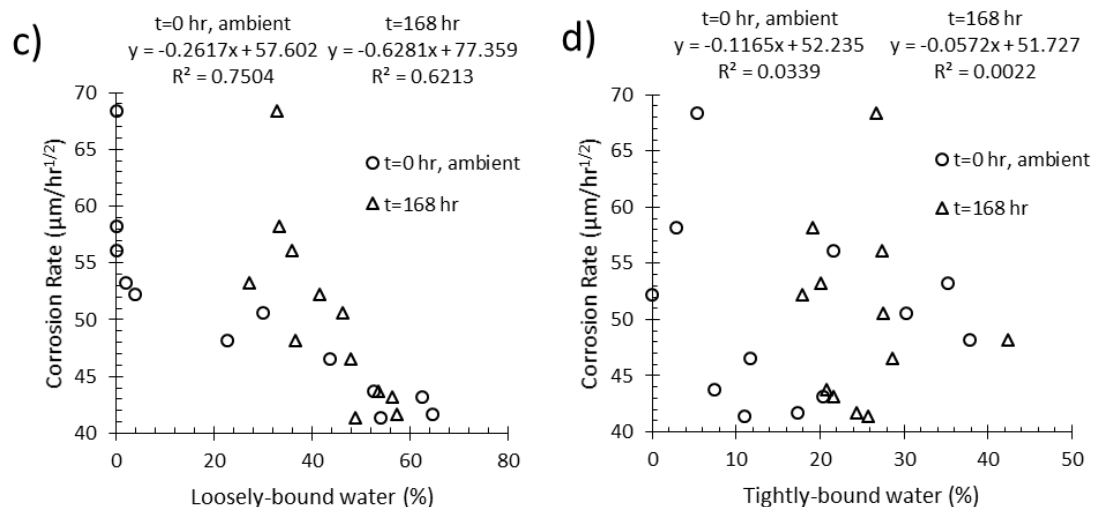


Figure 6.7 Experimental corrosion rate of epoxy-amine material combinations compared to the relative concentration of water hydrogen bonding interactions.

Note: free water (a), singly-bound water (b), loosely-bound water (c), and tightly-bound water (d) hydrogen bonding interactions

As it was established that the water distribution within a coating system influences the corrosion performance of the thin films investigated here, the ability to predict corrosion rates of a thin film material combination *prior* to empirical testing would greatly increase the screening throughput and potentially save capital and time for creating new and modified coating formulations. In an attempt to corroborate the results of Chapter V that water hydrogen bonding interactions at  $t=0$ , *ambient* can predict the experimental corrosion rate from intentionally created defects, the relative concentration of each water type for each thin film material combination at  $t=0$  *hr, ambient* was compared to the corrosion rate measured up to 168 hours of 5% salt fog exposure at 35 °C.

Similar to Chapter V, the amount of free water was determined to correlate well with the corrosion rate at  $t=0$ , *ambient* ( $p < 0.001$ ). These results further validate the

concept that free water has a high potential to contribute to ion hydration shells thereby facilitating ion transport to and from the substrate as well as along the polymer/substrate interface. The singly-bound water, singularly, possessed a positive trendline slope ( $p = 0.006$ ) and was lower in value than the free water by a factor of 3.4. However, the loosely-bound water was found to be inversely proportionate to the corrosion rate ( $p < 0.001$ ) indicating that increasing the hydrogen bonding of water molecules decreases the corrosion rate consistent with Chapter V. Surprisingly, the tightly-bound water did not greatly influence the corrosion rate directly. Although the free water and the loosely-bound water, singularly, can potentially be utilized to predict the experimental corrosion rate, using a stepwise multivariable regression approach enables the generation and identification of more robust equations with higher confidence. The observations noted in this Chapter additionally demonstrate the lack of dependence of the particle filler shape and aspect ratio on the corrosion rate for these thin film material combinations and emphasizes the importance of water hydrogen bonding interactions with respect to the corrosion rate. Furthermore, the directly proportionate relationship between the amount of free water and the corrosion rate is consistent with the results in Chapter V.

#### **6.4.4 Stepwise Multivariable Regression Analysis**

Multiple predictive equations were generated utilizing a different number of parameter order and interactions (Equations 6.4-6.6) in an attempt to create an equation with the highest level of confidence of predicting the experimental corrosion rate with the lowest number of input parameters and measurements.<sup>237</sup> It should be noted that the water vapor content at  $t=0$ , *ambient*, water vapor diffusivity, and the water vapor saturation at

equilibrium values were excluded as a potential predictor of the corrosion rate as these values were determined to not statistically vary between thin films for the investigated material combinations (Figure 6.4). The stepwise multivariable regression analysis indicated that the best predictors of the experimental corrosion rate using only first order terms included the free ( $S_0$ ) and loosely-bound water ( $S_2'$ ); specifically, the analysis generated Equation 6.7, with statistical p values of < 0.001, 0.023, and 0.003 for the regression equation,  $S_2'$ , and  $S_0$  variables, respectively. The negative coefficient of the  $S_2'$  term and positive coefficient of the  $S_0$  term suggests that loosely bound water ( $S_2'$ ) contributes to reducing the corrosion rate and free water ( $S_0$ ) contributes to increasing the corrosion rate (Figure 6.8). These results are consistent with the trends between the corrosion rate and the different water hydrogen bonding states, noted above.

$$\text{Corrosion rate } \frac{\mu\text{m}}{\sqrt{\text{hr}}} = 49.83 - 0.1244 S_2' + 0.565 S_0 \quad \text{Equation 6.7 First Order}$$

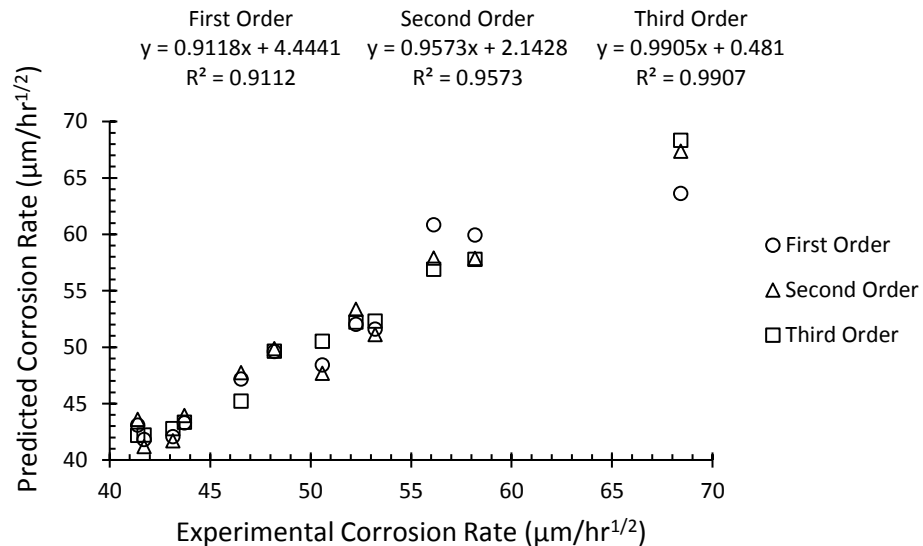


Figure 6.8 Experimental corrosion rate compared to the predicted corrosion rate from pre-exposure measurements.

Allowing interactions between the input variables has the potential to increase the fit of the resulting equation and the experimental data,<sup>237</sup> hence, variable input interactions were enabled and increased the order iteratively to include up to third order terms (Equations 6.8 and 6.9). Indeed, increasing the order and interaction between variables increased the coefficient of determination from 0.91 for first order variables to 0.95 and 0.99 for the second and third order variables, respectively (Figure 6.8).

$$\text{Corrosion rate } \frac{\mu\text{m}}{\sqrt{\text{hr}}} = 49.39 - 0.001973 (S'_2)^2 + 0.00785 (S_1 \times S_0) - 0.0461 (S_0 \times (T_g - 35)) \quad \text{Equation 6.8 Second Order}$$

$$\text{Corrosion rate } \frac{\mu\text{m}}{\sqrt{\text{hr}}} = 51.706 - 0.001668 (S'_2)^2 + 0.004843 (S_1 \times S_0) - 0.000061 (S'_2 \times S_1 \times T_g) - 0.00744 ((T_g - 35) \times (S_0)^2) + 0.00313 (S_0 \times T_g \times (T_g - 35)) \quad \text{Equation 6.9 Third Order}$$

#### 6.4.5 Discussion

In Chapter V, it was demonstrated that the influence of water hydrogen bonding interactions on the corrosion rate of epoxy-amine material combinations filled with low concentration levels of multiwall carbon nanotubes bound to steel substrates and their potential to predict the experimental corrosion rate from intentionally created defects. The objectives of the current research were to increase the understanding of how water hydrogen bonding interactions influence the corrosion rate of coated steel substrates from intentionally created defects and to develop an equation that can reliably and reproducibly predict the experimental corrosion rate from pre-exposure laboratory experiments.

The stepwise multivariable regression approach produced equations capable of explaining 91%, 95%, and 99% of the variation of the experimental corrosion rate for first, second, and third order variable interactions, respectively, from pre-exposure measurements. Although these equations provide high confidence of predicting the experimental corrosion rate, it is important to note, however, that these equations are applicable only for the thin film material combinations and conditions investigated here. The distribution of water hydrogen bonding interactions within a coating formulation that is shown to lower the corrosion rate from reduced ion mobility at the coating/substrate interface may also reduce the transport water-solvated ions of sparingly water-soluble pigments that passivate anodic reactions and/or repolarize the cathode.<sup>8</sup> As a result, to account for the variation of corrosion inhibiting mechanisms and efficiencies of different corrosion inhibiting pigments (e.g, strontium chromate, zinc phosphate, praseodymium) in fully formulated coating systems, a term must be added to the equation to predict the corrosion rate with high accuracy. Elucidation of the mechanistic interplay of water hydrogen bonding on the delivery of these corrosion inhibiting species to the corrosion reactions is critical to generating a term accurate of predicting the realized efficiency for inclusion into predictive equations. Other factors such as thickness, pigment volume concentration, polymer chemistry type, crosslink density, and other additives will additionally influence the overall corrosion performance.

Some limited literature examples have exhibited the ability to model and predict corrosion rates of reinforced concrete structures, but the prediction of coated metal substrates has yet to be reported.<sup>238-242</sup> In most cases, electrochemical impedance

spectroscopy (EIS) techniques were used to measure or estimate the corrosion current ( $i_{cor}$ ) and model the potential corrosion rate as a function of time in a given environment.<sup>239-240, 242</sup> It is known that ion, water, and oxygen permeation properties of concrete influence the reinforcing steel corrosion rate, and these parameters are consistent with the considerations for organic polymer coatings applied to metallic substrates. Yalçyn and co-workers combined these parameters into a single constant representative of the concrete properties, however, there were no direct measurements of concrete properties singularly that investigated mechanistically the understanding required to enable the development of new or modified formulations with increased performance.<sup>239</sup> Suleiman developed a predictive model of non-coated mild steel in a 0.5M sulfuric acid solution in the absence and presence of plant extracts corrosion inhibitor at multiple extract concentrations and temperatures.<sup>241</sup> The predicted corrosion rates were determined to be close to the experimental corrosion rates as demonstrated here for coated substrates.

In the thin film material combinations in this Chapter, quantification of the water distribution at pre-exposure  $t=0$ , *ambient* conditions can seemingly account for ~91% of the variation of the experimental corrosion rate independent of particle shape or concentration. As cathodic delamination is an ion diffusion limited corrosion mechanism, the distribution of water hydrogen bonding interactions directly influences the rate of ion diffusion along the polymer/substrate interface. These results provide direct evidence of how water hydrogen bonding within a polymer influences ion transport. Indeed, increasing the variable interaction order from one to two introduced the terms

representative of the difference between the exposure temperature and the glass transition temperature. Further increasing the interaction order from two to three introduced the glass transition temperature into the equation. The regression equations generated from the stepwise selection of terms emphasize the importance of the water hydrogen bonding within the coating with respect to the cathodic delamination.

Critically, the results validate the influence and importance of water hydrogen bonding interactions on the corrosion rate of the epoxy-amine coated steel substrates investigated here: specifically, free water and singly-bound water contribute to towards increasing the corrosion rate and loosely-bound water reduces the corrosion rate. Surprisingly, tightly-bound water did not greatly influence of the corrosion rate of these thin film material combinations. The influence of water hydrogen bonding on the corrosion rate was attributed to the variation in the ability of a given water molecule in each hydrogen bonding state to contribute to the formation of an ion hydration shell due to the ability to reorient in the appropriate spatial and temporal location to complete/contribute to an ion hydration shell.<sup>22, 26</sup> Leng and co-workers measured the formal diffusion coefficient (Equation 6.2) for Na<sup>+</sup> along the coating/substrate interface to be ~2 orders of magnitude lower than in bulk electrolyte solution,<sup>7</sup> thus, ion diffusion is expected to occur in a swollen, gel like polymer layer which will be greatly influenced by the water hydrogen bonding distribution of the swollen polymer. These data and the current work support the concept that water hydrogen bonding interactions mechanistically influences corrosion inducing environments at the coating/substrate interface of epoxy-amine coatings on steel substrates.

## 6.5 Conclusions

This research presented in this Chapter validated the dependence of the water hydrogen bond distribution, i.e., water hydrogen bonding interactions with the polymer, fillers, and substrate on the corrosion rate of epoxy-amine coated steel substrates. Nano-carbon allotropes (carbon black, unmodified MWCNTs, hydroxyl MWCNTs, graphene) were utilized to alter the management of water hydrogen bonds within an epoxy-amine matrix and attempt to develop an equation to predict the corrosion rate of epoxy-amine thin film material combinations. Accelerated corrosion testing (ASTM B117) of epoxy-amine thin films with various amounts and types of nano-carbon allotropes indicated that the relative concentration of free water and loosely-bound water correlated well with the corrosion rate independent of particle morphology and concentration. The established correlations were qualitatively validated via the reduction of sodium, chlorine, and iron both at the polymer/substrate interface with decreasing relative concentration of free water. Stepwise multivariable regression analysis identified an equation that can predict ~91% of the variation of experimental corrosion rates utilizing only the relative concentration of free and loosely-bound water in the coating measured *before* exposure to accelerated corrosion conditions. It was validated that the corrosion rate due to cathodic delamination was mechanistically related to the distribution of water hydrogen bonding states within the coating which directly alters the potential of ion transport through the coating.

## 6.6 References

2. Koch, G.; Varney, J.; Thompson, N.; Moghissi, O.; Gould, M.; Payer, J. *International Measures of Prevention, Application, and Economics of Corrosion Technologies Study*; NACE International: Houston, 2016.
5. Revie, W. R., *Uhlig's Corrosion Handbook*. 3rd ed.; John Wiley & Sons, Inc.: Hoboken, 2011; p 1253.
6. Sørensen, P. A.; Kiil, S.; Dam-Johansen, K.; Weinell, C. E., Anticorrosive Coatings: A Review. *Journal of Coatings Technology and Research* **2009**, *6* (2), 135-176.
7. Leng, A.; Streckel, H.; Stratmann, M., The Delamination of Polymeric Coatings from Steel. Part 2: First Stage of Delamination, Effect of Type and Concentration of Cations on Delamination, Chemical Analysis of the Interface. *Corrosion Science* **1998**, *41* (3), 579-597.
8. Sander, J.; Kirmaier, L.; Manea, M.; Shchukin, D.; Skorb, E., *Anticorrosive Coatings: Fundamentals and New Concepts*. Vincentz Network GmbH & Co.: Hannover, 2010.
9. *Protective Organic Coatings*. ASM International: Materials Park, OH, 2015; Vol. 5B.
14. Morsch, S.; Lyon, S.; Greensmith, P.; Smith, S. D.; Gibbon, S. R., Water Transport in an Epoxy–Phenolic Coating. *Progress in Organic Coatings* **2015**, *78*, 293-299.
15. Cotugno, S.; Larobina, D.; Mensitieri, G.; Musto, P.; Ragosta, G., A Novel Spectroscopic Approach to Investigate Transport Processes in Polymers: The Case of Water–Epoxy System. *Polymer* **2001**, *42* (15), 6431-6438.
16. Musto, P.; Ragosta, G.; Mascia, L., Vibrational Spectroscopy Evidence for the Dual Nature of Water Sorbed into Epoxy Resins. *Chemistry of Materials* **2000**, *12* (5), 1331-1341.
17. Soles, C. L.; Yee, A. F., A Discussion of the Molecular Mechanisms of Moisture Transport in Epoxy Resins. *Journal of Polymer Science Part B: Polymer Physics* **2000**, *38* (5), 792-802.
18. Mijović, J.; Zhang, H., Local Dynamics and Molecular Origin of Polymer Network–Water Interactions as Studied by Broadband Dielectric Relaxation Spectroscopy, Ftir, and Molecular Simulations. *Macromolecules* **2003**, *36* (4), 1279-1288.
21. Li, L.; Yu, Y.; Su, H.; Zhan, G.; Li, S.; Wu, P., The Diffusion Mechanism of Water Transport in Amine-Cured Epoxy Networks. *Applied Spectroscopy* **2010**, *64* (4), 458-466.
22. Barati Farimani, A.; Aluru, N. R., Existence of Multiple Phases of Water at Nanotube Interfaces. *The Journal of Physical Chemistry C* **2016**, *120* (41), 23763-23771.
26. Kropman, M. F.; Bakker, H. J., Dynamics of Water Molecules in Aqueous Solvation Shells. *Science* **2001**, *291* (5511), 2118-2120.
27. Gao, X.; Zhao, T.; Li, Z., Effects of Ions on the Diffusion Coefficient of Water in Carbon Nanotubes. *Journal of Applied Physics* **2014**, *116* (5), 054311.

40. Starkova, O.; Buschhorn, S. T.; Mannov, E.; Schulte, K.; Aniskevich, A., Water Transport in Epoxy/Mwcnt Composites. *European Polymer Journal* **2013**, *49* (8), 2138-2148.
70. Lehman, J. H.; Terrones, M.; Mansfield, E.; Hurst, K. E.; Meunier, V., Evaluating the Characteristics of Multiwall Carbon Nanotubes. *Carbon* **2011**, *49* (8), 2581-2602.
72. Chakrapani, N.; Curran, S.; Wei, B.; Ajayan, P. M.; Carrillo, A.; Kane, R. S., Spectral Fingerprinting of Structural Defects in Plasma-Treated Carbon Nanotubes. *Journal of Materials Research* **2011**, *18* (10), 2515-2521.
120. Pietraß, T.; Dewald, J. L.; Clewett, C. F. M.; Tierney, D.; Ellis, A. V.; Dias, S.; Alvarado, A.; Sandoval, L.; Tai, S.; Curran, S. A., Electron Spin Resonance and Raman Scattering Spectroscopy of Multi-Walled Carbon Nanotubes: A Function of Acid Treatment. *Journal of Nanoscience and Nanotechnology* **2006**, *6* (1), 135-140.
147. Arepalli, S.; Freiman, S.; Hooker, S.; Migler, D., Measurement Issues in Single-Wall Carbon Nanotubes. *NIST Recommended Practice Guide* **2008**.
191. Ellison, S.; Barwick, V.; Trevor, F., *Practical Statistics for the Analytical Scientist: A Bench Guide*. 2nd ed.; The Royal Society of Chemistry: Cambridge, 2009.
211. Franks, F., *The Physics and Physical Chemistry of Water*. Springer: London, 1972; Vol. 1, p 596.
212. Mullins, E., *Statistics for the Quality Control Chemistry Laboratory*. The Royal Society of Chemistry: Cambridge, 2003.
219. Curtzwiler, G.; Early, M.; Gottschalk, D.; Konecki, C.; Peterson, R.; Wand, S.; Rawlins, J. W., The World of Surface Coatings Is Centered around the Glass Transition Temperature but Which One? Part 2. *JCT CoatingsTech* **2014**, *11*, 40-51.
220. Curtzwiler, G.; Early, M.; Gottschalk, D.; Konecki, C.; Peterson, R.; Wand, S.; Rawlins, J. W., The World of Surface Coatings Is Centered around the Glass Transition Temperature but Which One? Part I. *JCT CoatingsTech* **2014**, *11*, 28-38.
222. Choudalakis, G.; Gotsis, A. D., Free Volume and Mass Transport in Polymer Nanocomposites. *Current Opinion in Colloid & Interface Science* **2012**, *17* (3), 132-140.
229. Standard Practice for Operating Salt Spray (Fog) Apparatus. In *ASTM B117 - 11*, ASTM International: West Conshohocken, 2011.
230. Schneider, A.; Hommel, G.; Blettner, M., Linear Regression Analysis: Part 14 of a Series on Evaluation of Scientific Publications. *Deutsches Arzteblatt International* **2010**, *107* (44), 776-82.
236. Mil-Prf-23377j, Performance Specification: Primer Coatings: Epoxy, High-Solids. Defense, D. o., Ed. 2005.
237. Yan, X.; Su, X. G., *Linear Regression Analysis: Theory and Computing*. World Scientific Publishing: Hackensack, NJ, 2009; p 349.
238. Siamphukdee, K.; Collins, F.; Zou, R., Sensitivity Analysis of Corrosion Rate Prediction Models Utilized for Reinforced Concrete Affected by Chloride. *Journal of Materials Engineering and Performance* **2013**, *22* (6), 1530-1540.
239. Yalçyn, H.; Ergun, M., The Prediction of Corrosion Rates of Reinforcing Steels in Concrete. *Cement and Concrete Research* **1996**, *26* (10), 1593-1599.

240. Otieno, M.; Beushausen, H.; Alexander, M., Prediction of Corrosion Rate in Reinforced Concrete Structures – a Critical Review and Preliminary Results. *Materials and Corrosion* **2012**, 63 (9), 777-790.
241. Suleiman, I. Y.; Oloche, O. B.; Yaro, S. A., The Development of a Mathematical Model for the Prediction of Corrosion Rate Behaviour for Mild Steel in 0.5% Sulphuric Acid. *ISRN Corrosion* **2013**, 2013, 9.
242. Otieno, M.; Beushausen, H.; Alexander, M., Prediction of Corrosion Rate in Rc Structures - a Critical Review. In *Modelling of Corroding Concrete Structures: Proceedings of the Joint Fib-Rilem Workshop Held in Madrid, Spain, 22–23 November 2010*, Andrade, C.; Mancini, G., Eds. Springer Netherlands: Dordrecht, 2011; pp 15-37.

## CHAPTER VII – DISSERTATION SUMMARY AND FUTURE OUTLOOK

The overall goal of this work was to provide the fundamental understanding of multiwall carbon nanotube (MWCNTs) polymer thin films required to practically utilize MWCNTs for corrosion control applications when applied to metallic substrates. The initial hypothesis was that incorporating high aspect ratio carbon nanotubes will decrease the rate of delivery of environmental contaminants that can induce corrosion to the substrate by increasing the tortuosity, and thereby reducing the corrosion rate concurrently. However, preliminary investigations indicated that increased water vapor barrier was not realized after incorporation of MWCNTs into the parent epoxy-amine material combination at loading level concentrations up to 1.0 wt%, yet, diminished corrosion rates were still observed. These observations necessitated that the original main hypothesis be revised: **the corrosion performance of MWCNT/epoxy-amine material blends is directly related to the ability of the combined materials, and more specifically the MWCNTs, to manage water, i.e., the distribution of water hydrogen bonding states within substrate bound polymer thin films (i.e., free versus bound water states); specifically, the potential of each water molecule in a specific hydrogen bonding state to contribute to ion hydration shells and readily transport corrosion inducing environmental contaminants and corrosion products to and from the substrate directly influences the corrosion rate.** The refined hypothesis was supported by both preliminary experimental evidence and literature precedence.

Literature investigations and experimental observations identified critical and key gaps in understanding that was directly addressed by this work. Specifically:

In Chapter II, it was determined that the various deconvolution protocols utilized for the Raman spectra of MWCNTs described in the literature are not universal nor equivalent and that random selection of deconvolution parameters may present misleading molecular structure interpretation. Thus, a more standardized protocol for utilizing Raman spectroscopy to investigate changes in the molecular structure of MWCNTs was developed by correlating Raman spectral properties with thermogravimetric analysis and X-ray photoelectron spectroscopy.

In Chapter III, it was determined that current literature protocols for quantifying carbon nanotube dispersion (e.g., the dispersion index) were not capable nor reliable for all MWCNT-polymer systems and generally cannot be used for polymers bound to a non-transparent substrate. A protocol was developed using traditionally measured blackness and jetness properties to quantify the dispersion states of MWCNTs in thin polymer films bound to non-transparent substrates independent of subjective parameter input.

In Chapter IV, it was established that the surface modification of multiwall carbon nanotubes did not greatly affect the corrosion rate from intentionally created defects of MWCNT/epoxy-amine thin film material combinations bound to steel substrates at a loading level of 0.50 wt%. However, a reduced corrosion rate was semi-quantitatively determined at the same loading level (0.50 wt%) when compared to the non-filled parent epoxy-amine material combination. Furthermore, a correlation was established between the free water concentration and the corrosion area at 168 hours of salt fog exposure for all epoxy-amine thin film material combinations. The redistribution of water hydrogen bonding states due to MWCNTs was hypothesized to be mechanistically related to the

observed decreased corrosion rates. These observations invoked the question: if the distribution of water hydrogen bonding interactions due to MWCNTs influences the experimental rate, can the distribution of water hydrogen bonding states be further altered to increase the corrosion rate control by increasing the MWCNT concentration?

In Chapter V, the MWCNT concentration was increased and the experimental corrosion rate was observed to decrease further when the concentration of MWCNTs was increased from 0.50 wt% to 0.75 wt%; surprisingly, increasing the concentration from 0.75 wt% to 1.0 wt% did not further decrease the corrosion rate. It was noticed that the insignificant change in the corrosion rate between the 0.75 wt% and the 1.0 wt% MWCNT/epoxy-amine thin films also existed for the water distribution content. The correlation between water hydrogen bonding states and the corrosion rate was validated quantitatively for a larger number of epoxy-amine thin film material combinations with different water hydrogen bonding distributions. Beneficially, the pre-exposure water hydrogen bonding states were determined to correlate well with the experimental corrosion rates, for all MWCNT concentrations which identified the potential of using pre-exposure measurements to predict the experimental corrosion rates. These observations supported the concept that altering/managing the water hydrogen bonding distribution of within thin polymer films coated over metallic substrates has a direct influence on the corrosion performance in a salt fog environment and warranted a more in-depth investigation, which was the subject of Chapter VI. It is surmised that these findings are applicable to other metallic substrates where water-solvation is required for the transport of corrosion inducing species to and from the substrate. The relationship

between free and bound water states and the corrosion rate appears to be first established here and further investigation and exploration is required to validate that these observations are universal for other coating formulations with different parent polymer systems and applied to various metallic substrates.

In Chapter VI, a stepwise multivariable regression approach was used to develop an equation capable of predicting the experimental corrosion rates of the epoxy-amine thin film material combinations bound to steel substrates used here with high confidence from pre-exposure laboratory measurements. The number of observations was increased from the investigation in Chapter V utilizing carbon black and graphene particles at three different concentrations in an attempt to alter the pre-exposure water hydrogen bonding interactions to develop a more accurate predictive equation. The stepwise selection of terms for the predictive equation identified the importance of determining and quantifying the distribution of water hydrogen bonding interactions of polymeric coatings for corrosion control applications. A simple first order predictive equation was generated capable of explaining ~91% of the variation in the experimental corrosion rate, of the epoxy-amine thin film material combinations utilized here with pre-exposure water hydrogen bonding measurements.

This work further identified the capability to produce equations capable of predicting experimental corrosion rates from pre-exposure laboratory measurements which could be a valuable tool to investigate changes in the parent polymer material combination. However, the equation developed here is likely only applicable to variations of the parent polymer material combination used in this work as many critical variables

were intentionally held constant, e.g., thickness, scribe length, parent material combination. For a predictive equation to be useful for fully formulated coating systems with corrosion inhibiting pigments on a specific metallic substrate, a more complex equation is required. Other critical parameters such as, the scribe profile, concentration and efficiency of the corrosion inhibitor, coating thickness, severity factor of the local environment, and the mechanism of corrosion protection must be considered and entered into the equation to become more universal for other coating systems and formulations. Furthermore, the development of such an equation enables damage assessment of an already in-service coating system as a function of a given set of parameters and time.

Many authors have shown the potential for carbon nanotubes to contribute to decreasing the corrosion rates metallic substrates and have measured various properties commonly associated with decreased corrosion rates, yet to date, there have been no reports of understanding why incorporation of carbon nanotubes altered certain properties on the molecular level. Indeed, this work contributes to that understanding and provides the basis for further work to elucidate fully the mechanisms of increased corrosion rate control of carbon nanotube-based polymeric coatings. Critical to the advancement of corrosion science and developing a deeper understanding of the mechanistic interplay between the corrosion rate of coated metal substrates and the applied polymeric coating is the systematic investigation of the influence of water hydrogen bonding states on adhesion, modulus, solvation and transport of corrosion inhibiting pigments, and metal dissolution of the substrate.

“I’m smart enough to know that I’m dumb.”— Richard Feynman

### A.1 Raman Spectral Properties

#### A.1.1 Relationship between D/G and D'/G Raman Spectral Calculations.

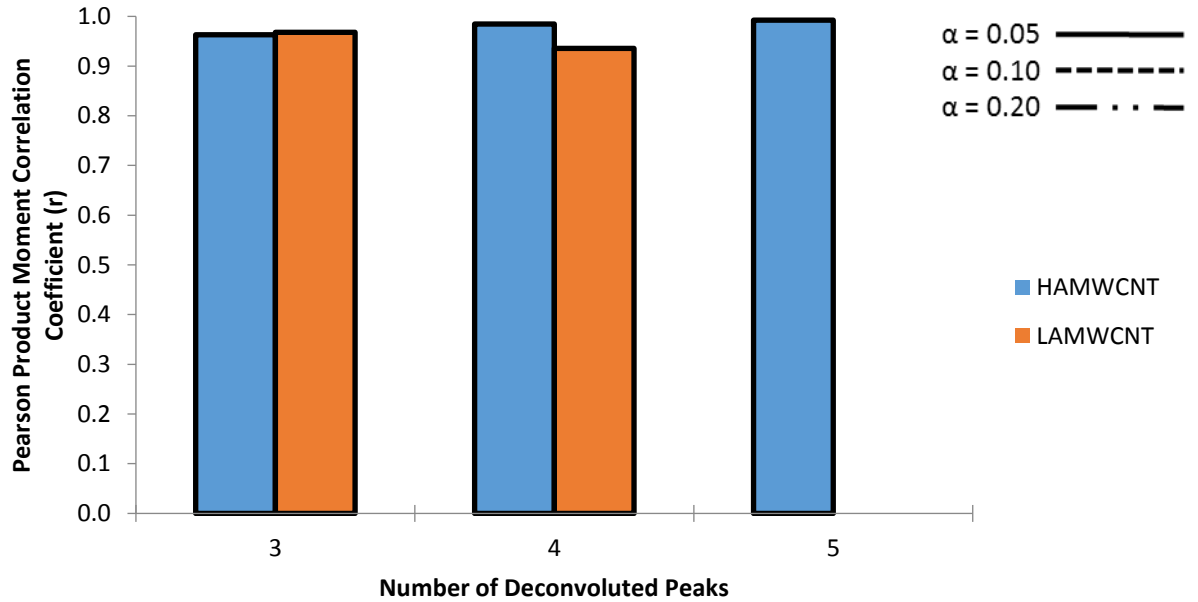


Figure A.1 Pearson product moment correlation coefficient as a probe of the relationship between the intensity based D/G and D'/G calculations for HAMWCNT and LAMWCNT types.

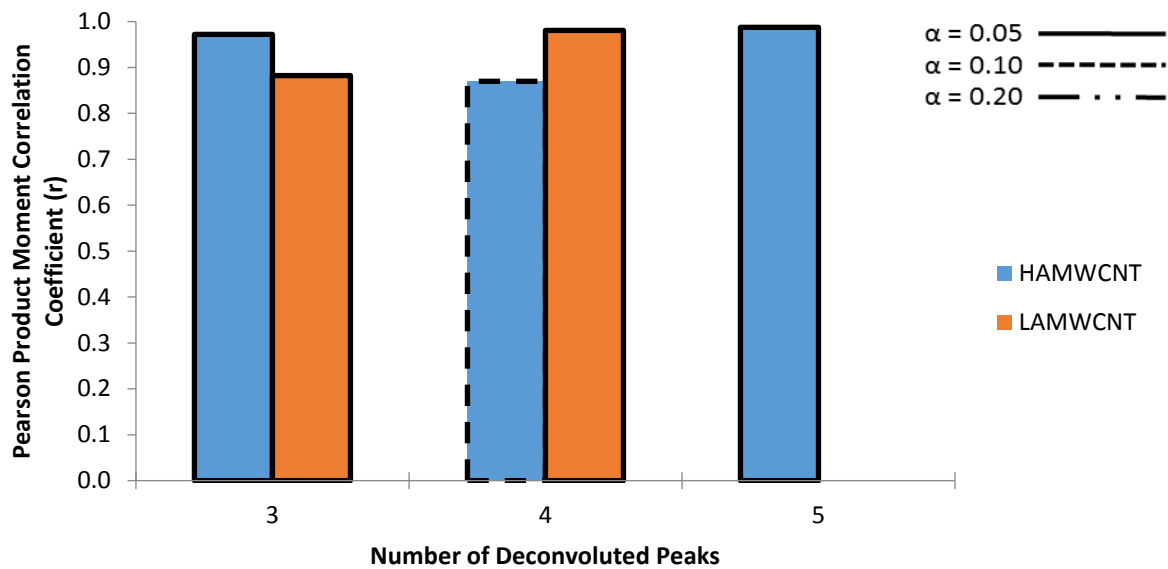


Figure A.2 Pearson product moment correlation coefficient as a probe of the relationship between the area based D/G and D'/G calculations for HAMWCNT and LAMWCNT types.

### A.1.2 D'/G Ratios

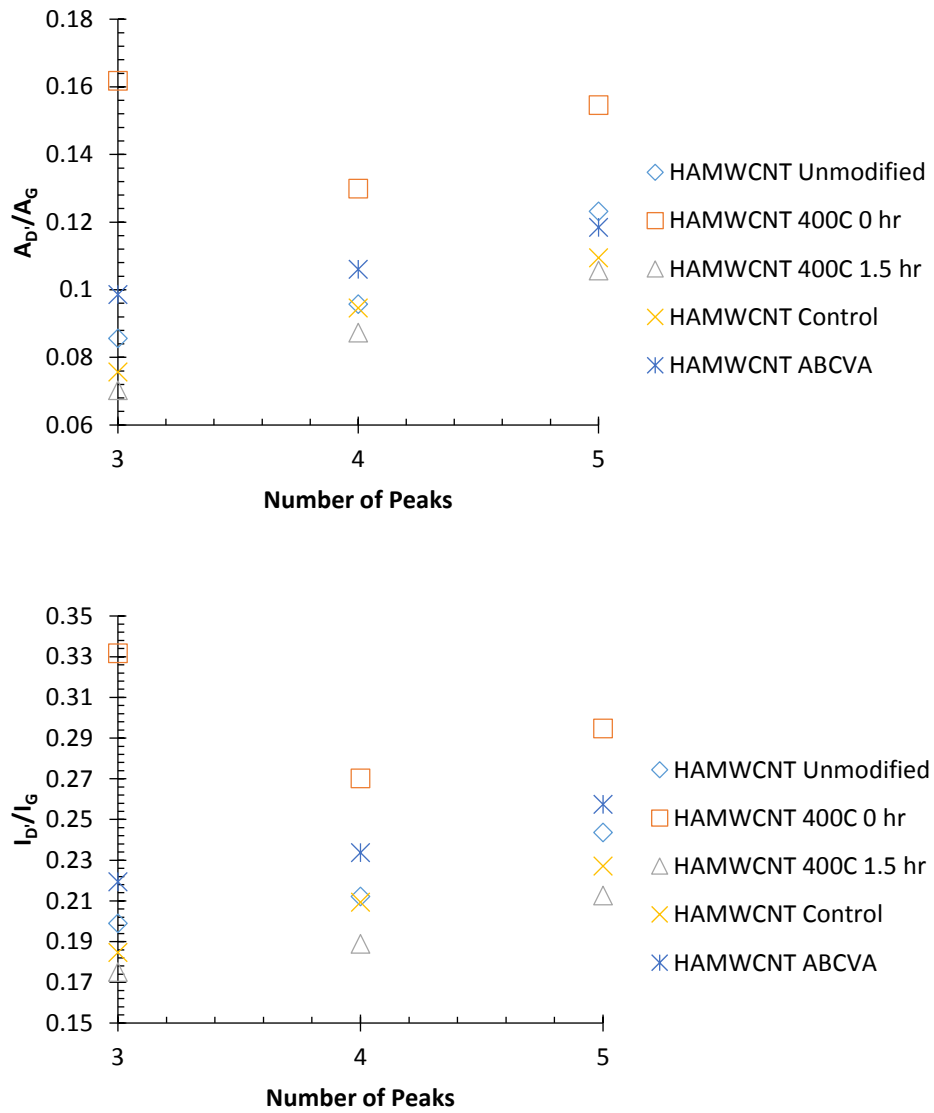


Figure A.3 Area and intensity based D'/G ratios as a function of the number of deconvoluted peaks for HAMWCNT.

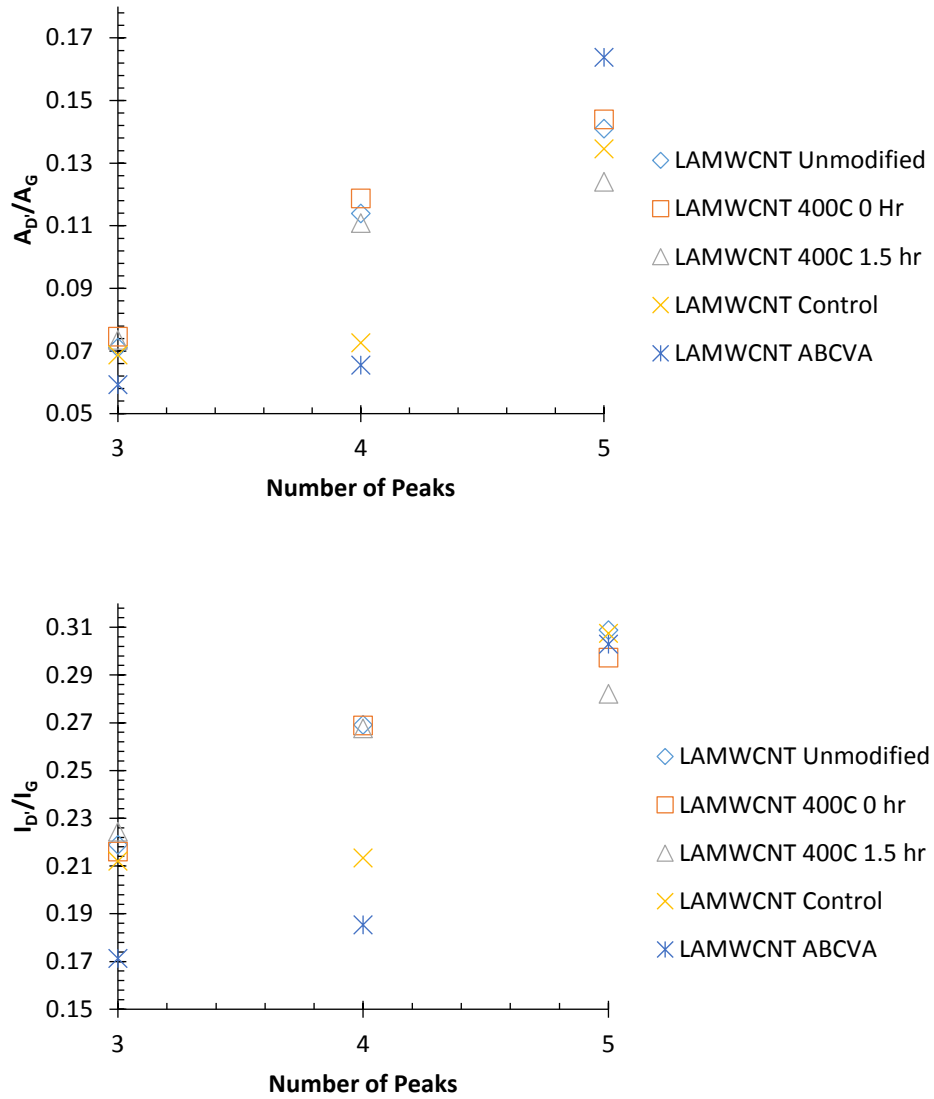


Figure A.4 Area and intensity based D'/G ratios as a function of the number of deconvoluted peaks for LAMWCNT.

## A.2 Correlation of thermogravimetric analysis with Raman spectral properties.

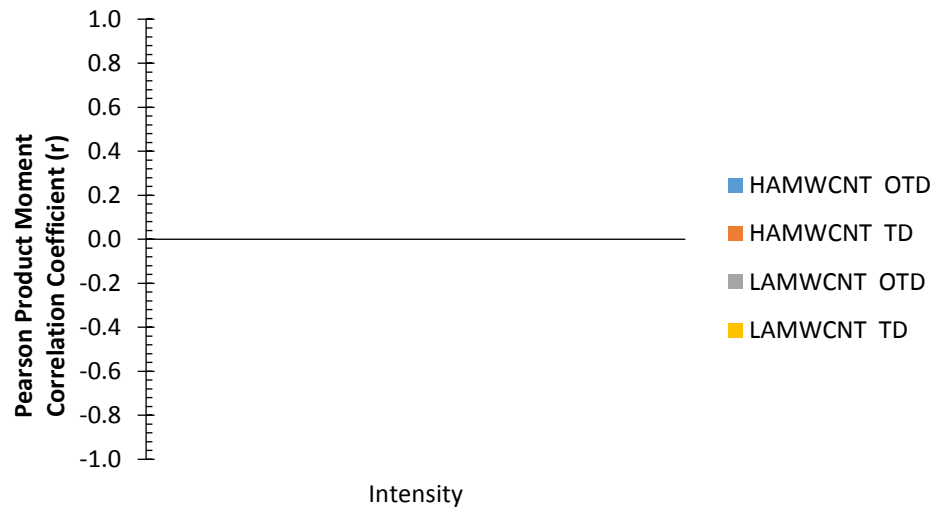


Figure A.5 Pearson product moment correlation coefficient between spectrum intensity based calculations and thermal degradation properties for HAMWCNT and LAMWCNT types.

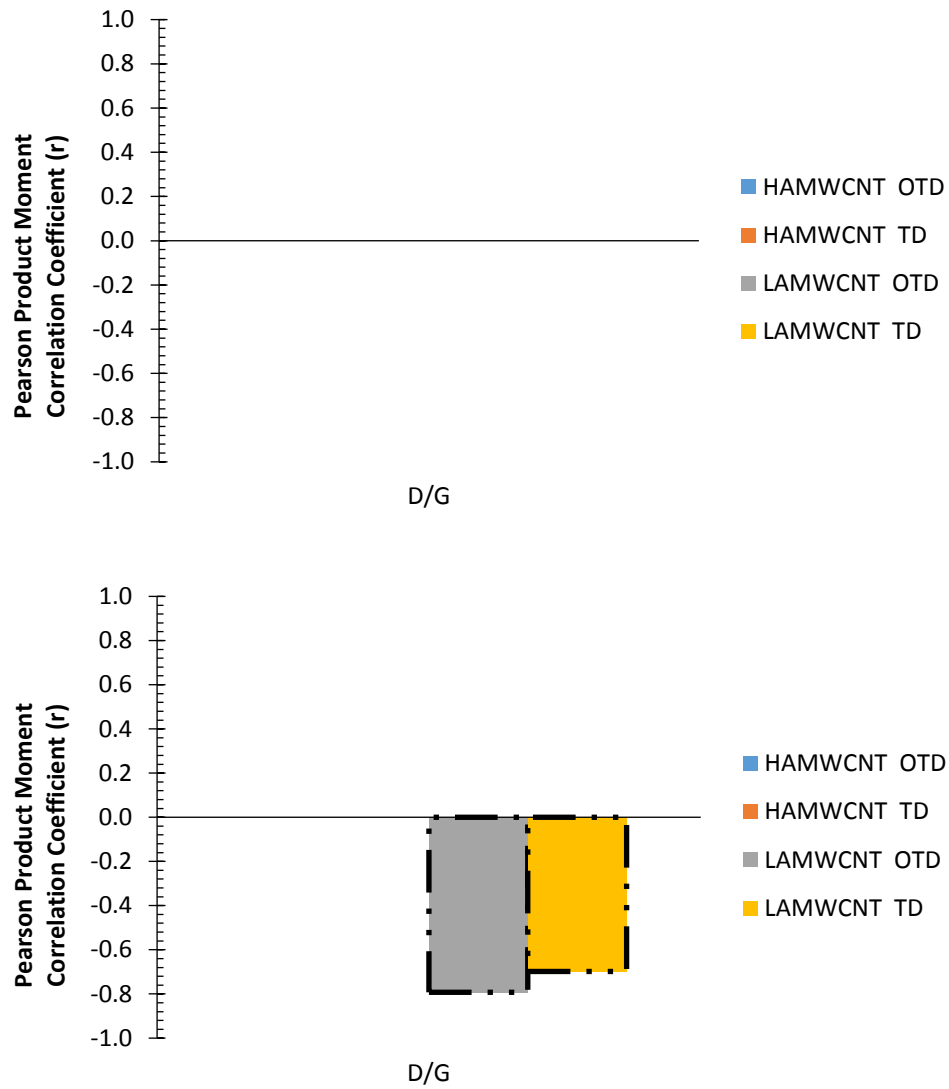


Figure A.6 Pearson product moment correlation coefficient between the intensity/area based calculations from a two peak deconvolution and thermal degradation properties for HAMWCNT and LAMWCNT types.

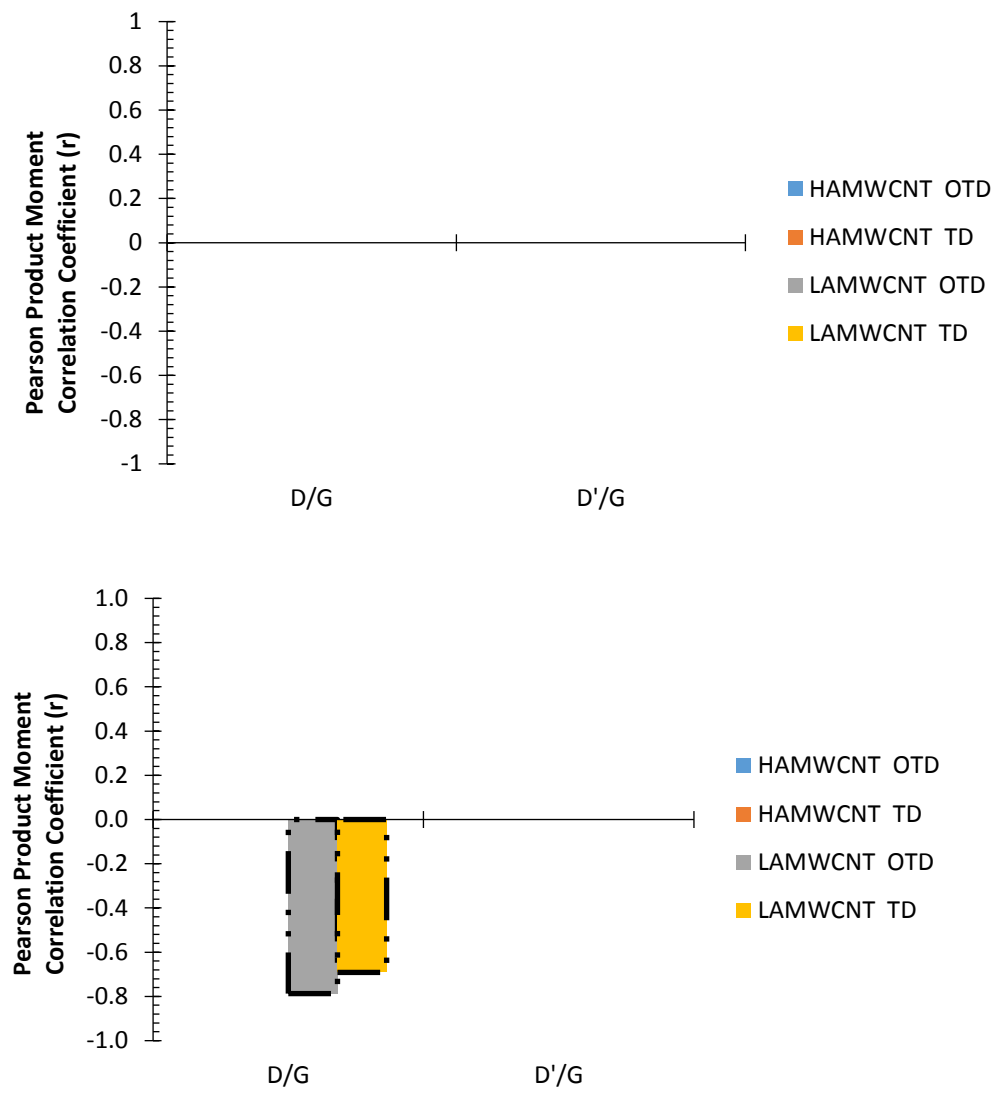


Figure A.7 Pearson product moment correlation coefficient between the intensity/area based calculations from a three peak deconvolution and thermal degradation properties for HAMWCNT and LAMWCNT types.

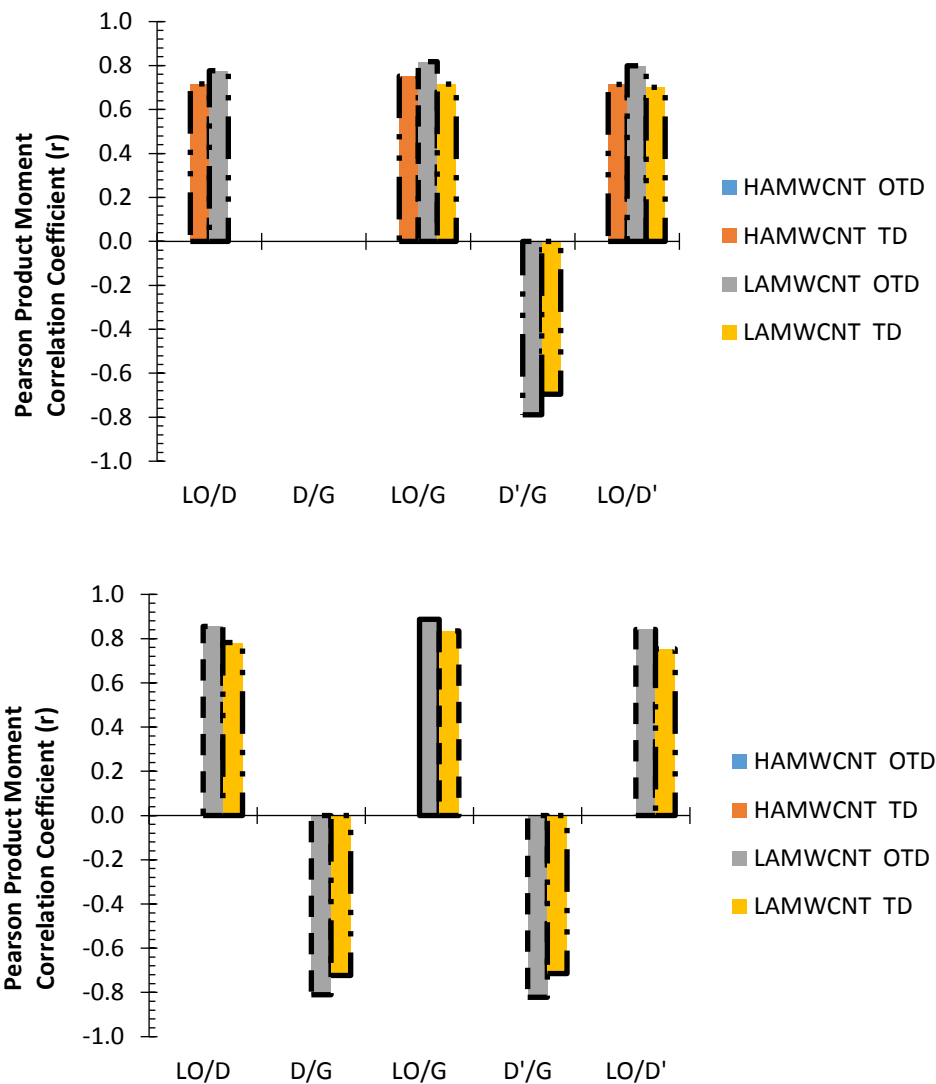


Figure A.8 Pearson product moment correlation coefficient between the intensity based calculations from a four peak deconvolution and thermal degradation properties for HAMWCNT and LAMWCNT types.

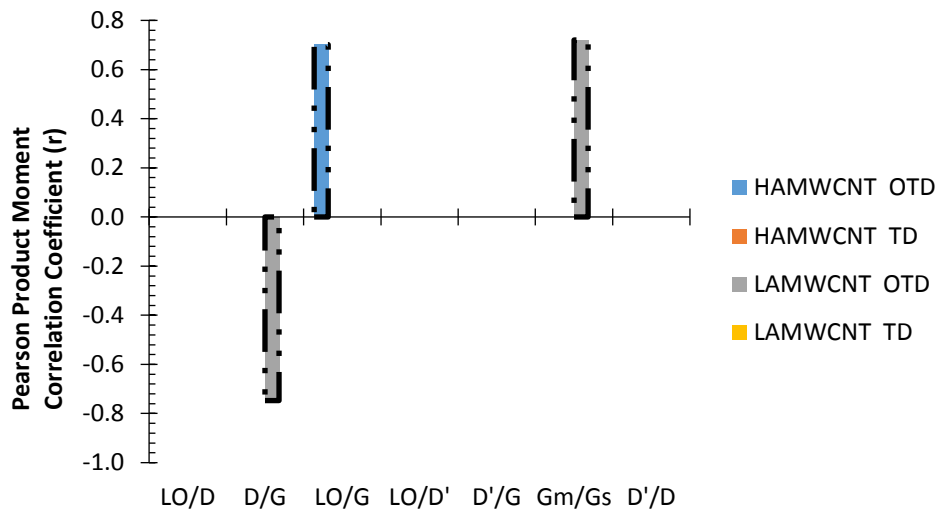
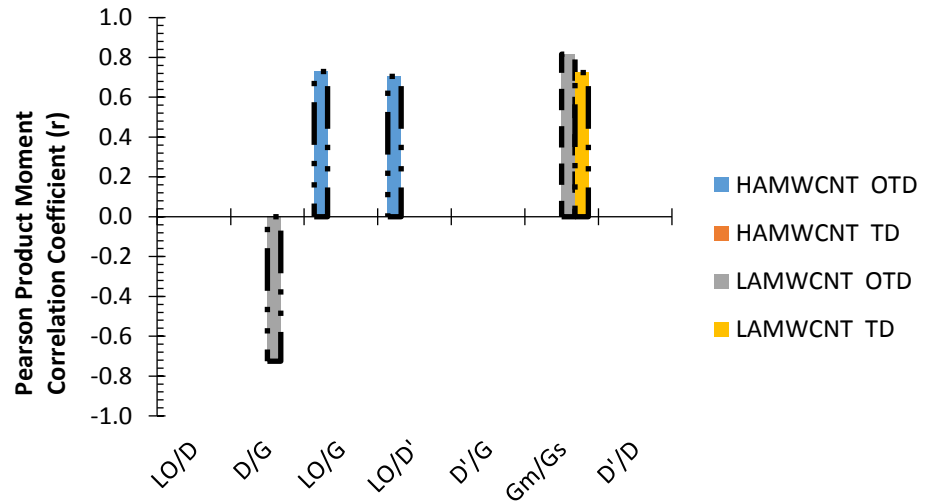


Figure A.9 Pearson product moment correlation coefficient between the area based calculations from a five peak deconvolution and thermal degradation properties for HAMWCNT and LAMWCNT types.

### A.3 Correlation between X-ray photoelectron spectroscopy and Raman spectral properties.

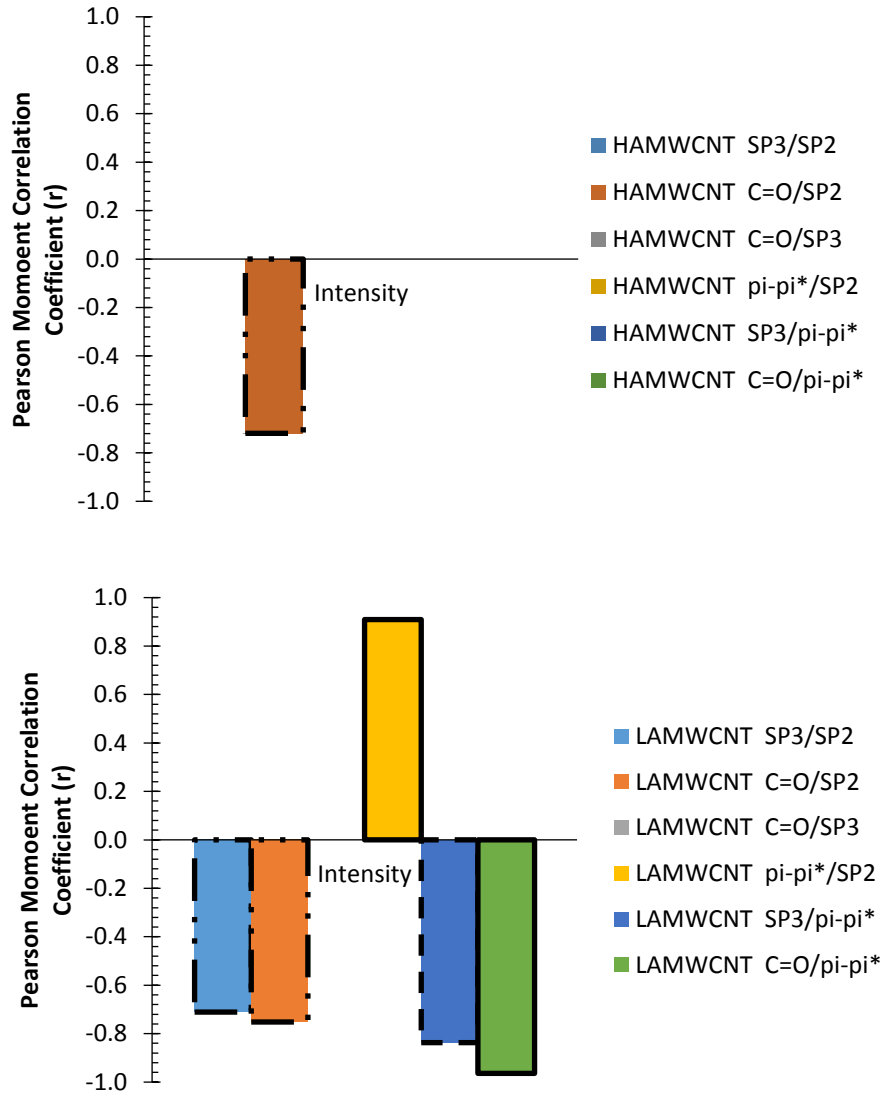


Figure A.10 Pearson product moment correlation coefficient for the spectrum intensity based calculations and XPS calculations for HAMWCNT and LAMWCNT types.

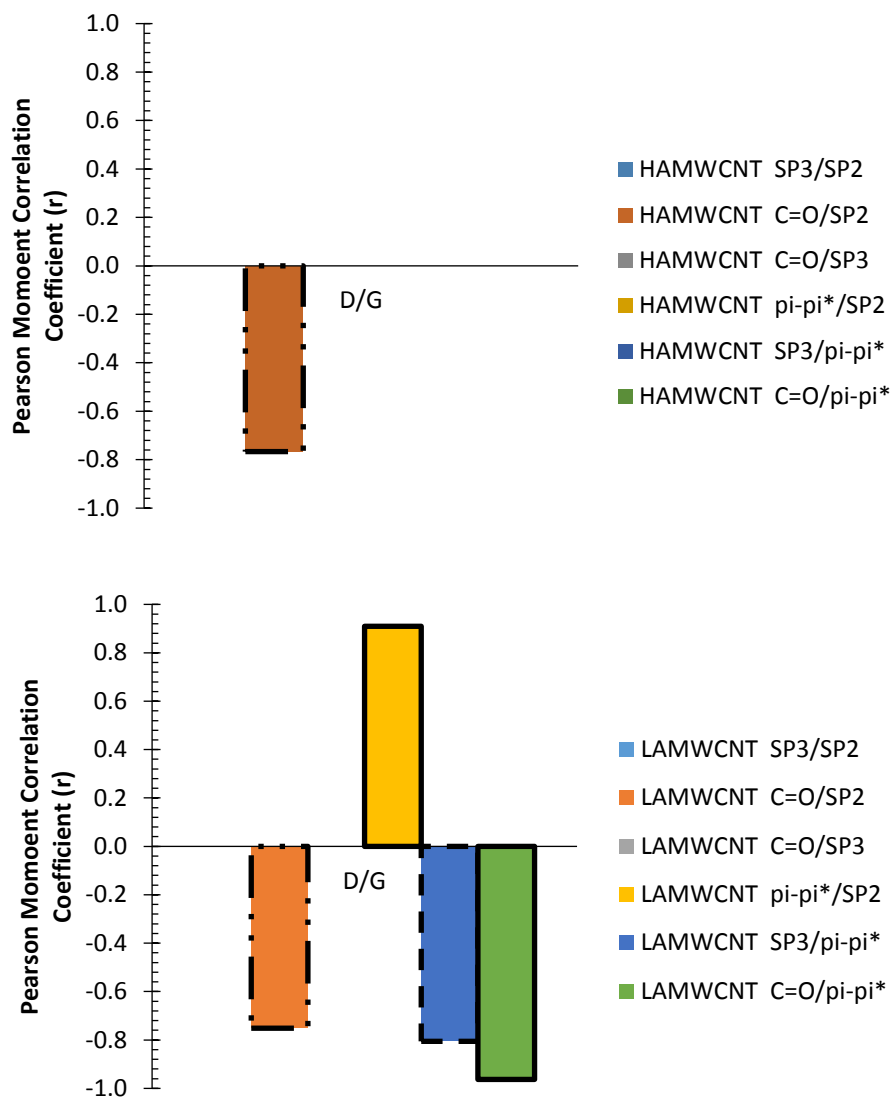


Figure A.11 Pearson product moment correlation coefficient for intensity based Raman spectral properties determined with two deconvoluted peaks as a function of X-ray photoelectron spectral properties for HAMWCNT and LAMWCNT.

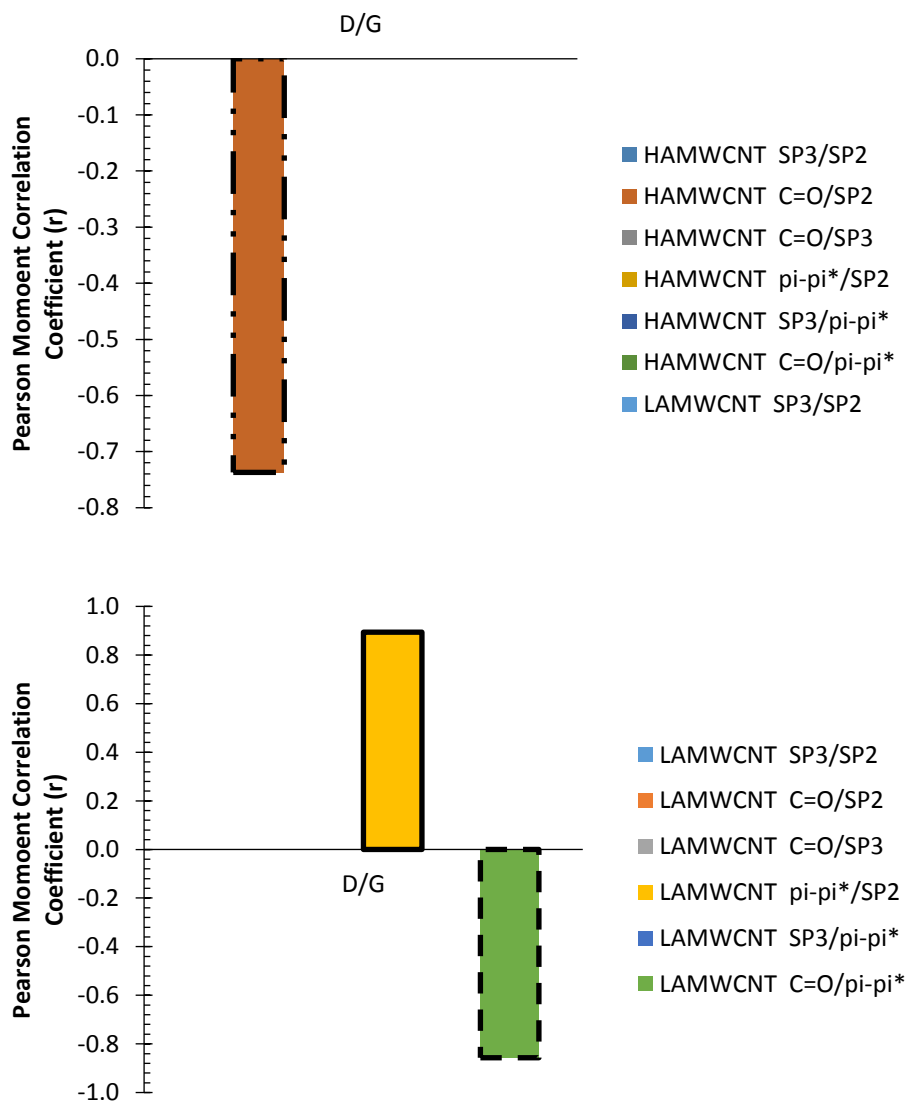


Figure A.12 Pearson product moment correlation coefficient for area based Raman spectral properties determined with two deconvoluted peaks as a function of X-ray photoelectron spectral properties for HAMWCNT and LAMWCNT.

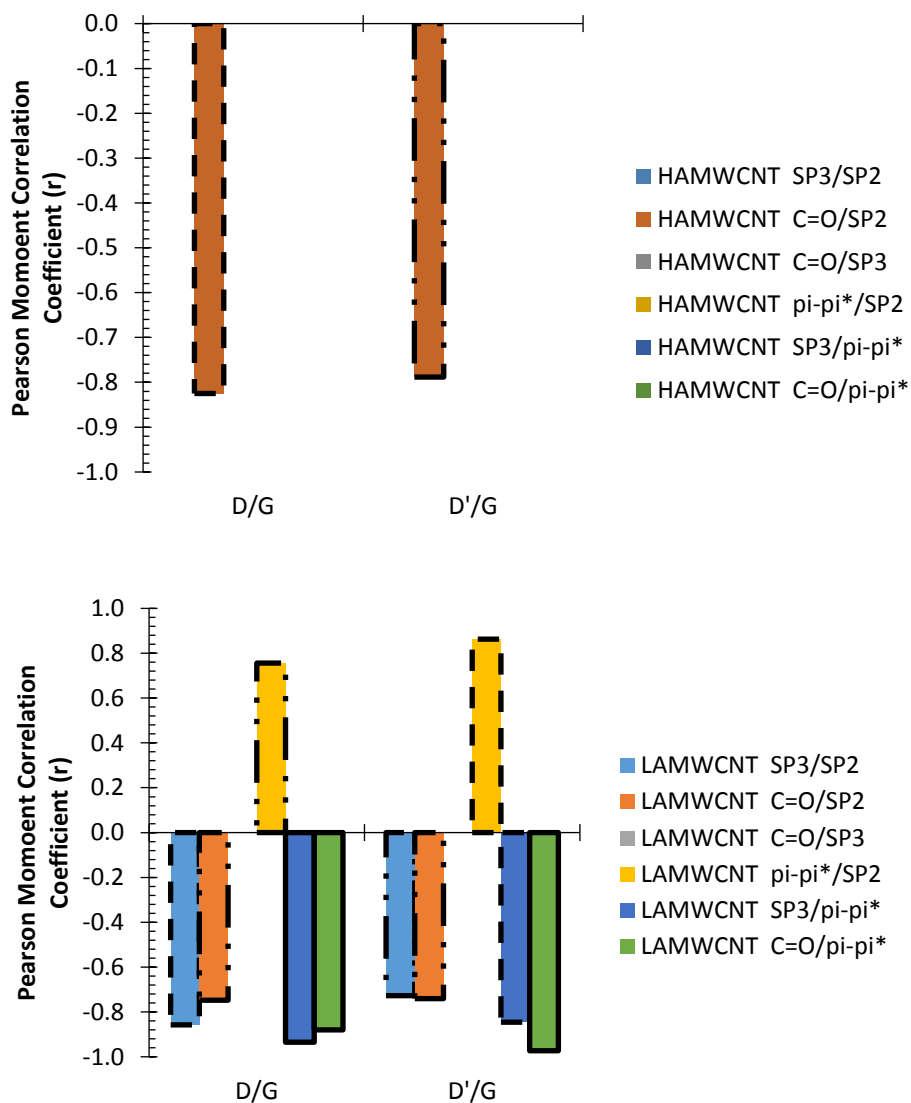


Figure A.13 Pearson product moment correlation coefficient for intensity based Raman spectral properties determined with three deconvoluted peaks as a function of X-ray photoelectron spectral properties for HAMWCNT and LAMWCNT.

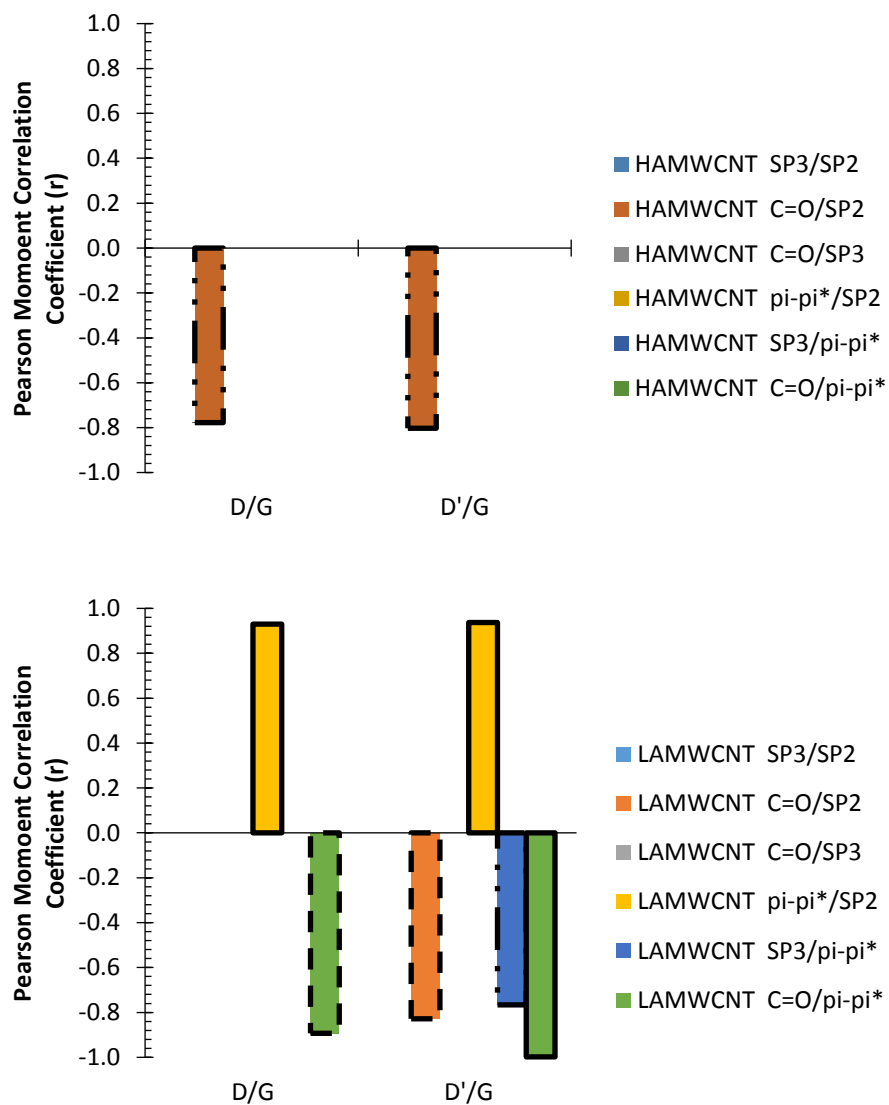


Figure A.14 Pearson product moment correlation coefficient for area based Raman spectral properties determined with three deconvoluted peaks as a function of X-ray photoelectron spectral properties for HAMWCNT and LAMWCNT.

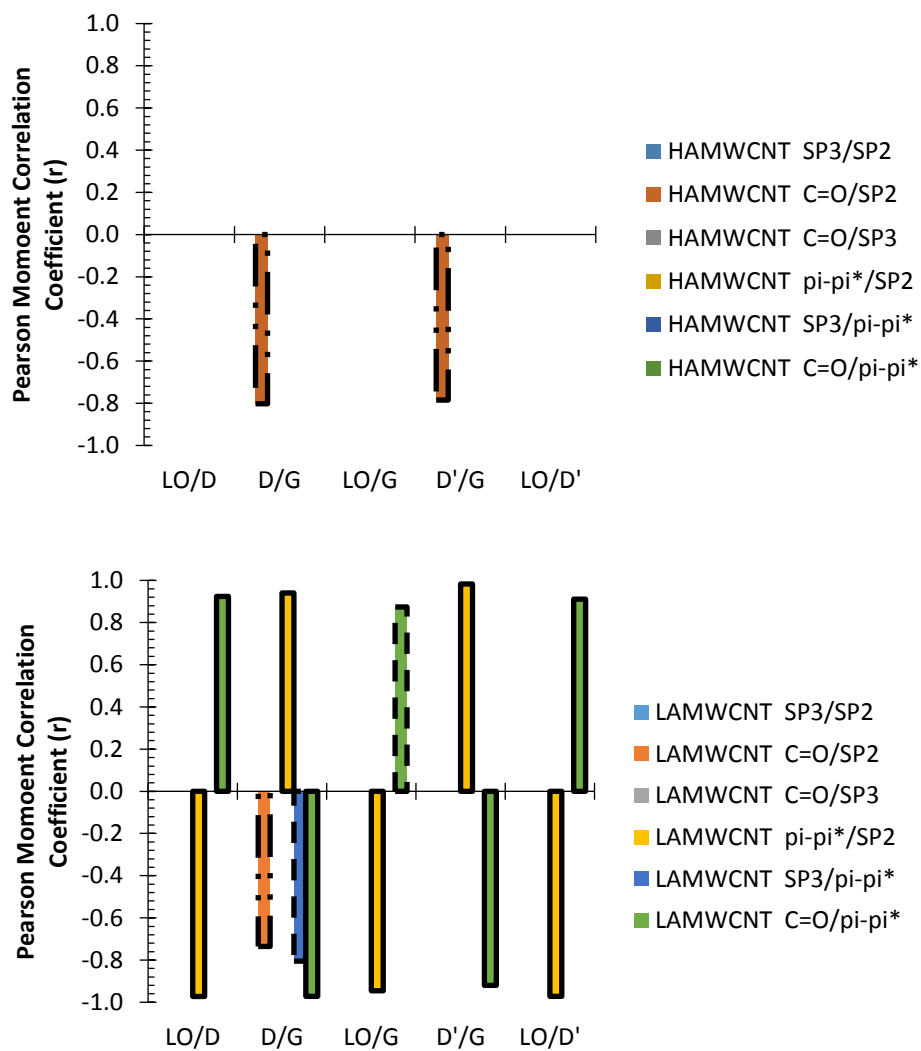


Figure A.15 Pearson product moment correlation coefficient for intensity based Raman spectral properties determined with four deconvoluted peaks as a function of X-ray photoelectron spectral properties for HAMWCNT and LAMWCNT.

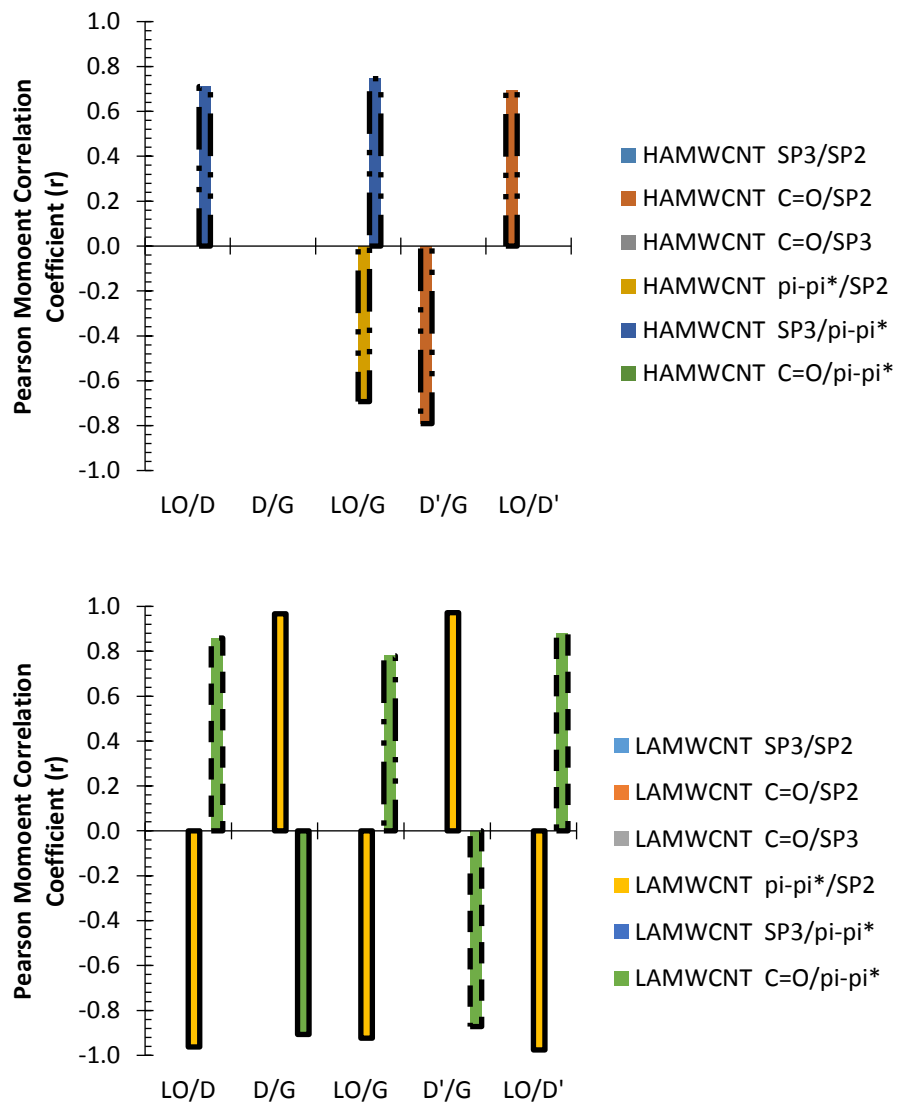


Figure A.16 Pearson product moment correlation coefficient for area based Raman spectral properties determined with four deconvoluted peaks as a function of X-ray photoelectron spectral properties for HAMWCNT and LAMWCNT.

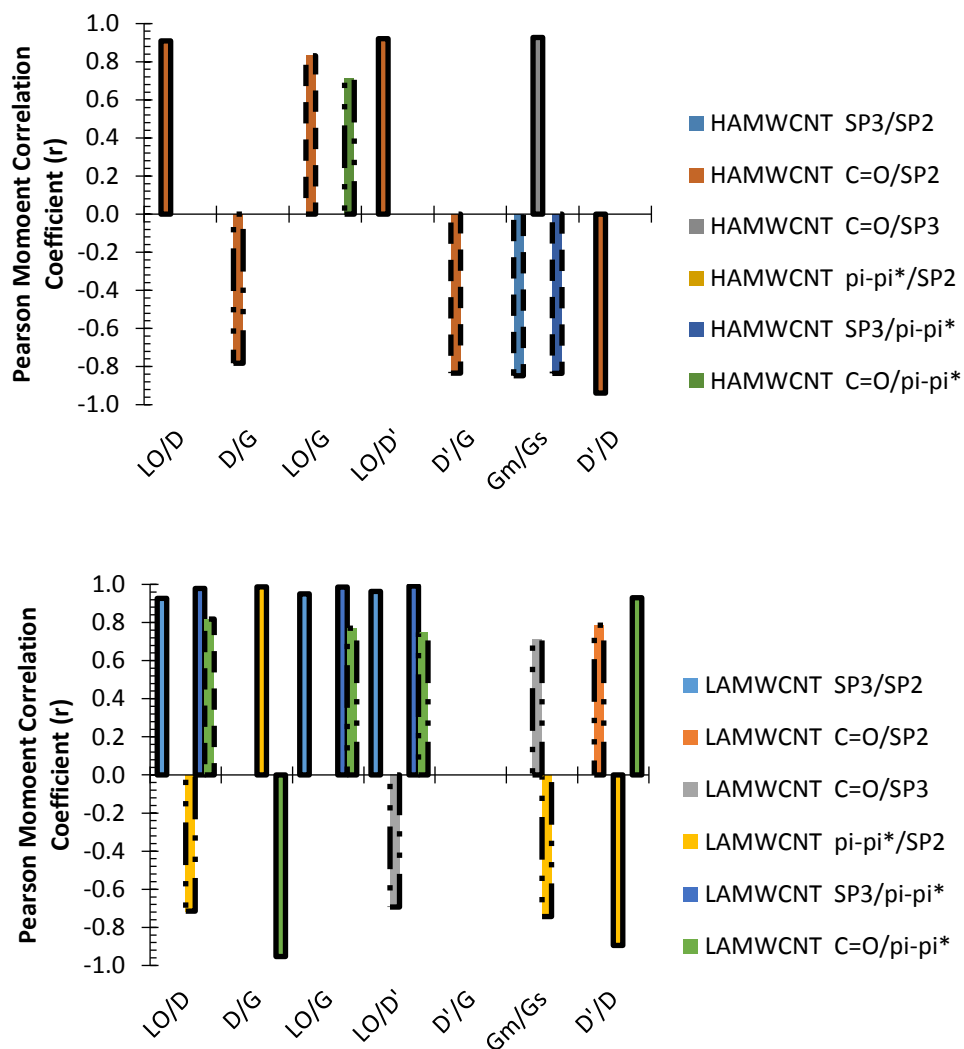


Figure A.17 Pearson product moment correlation coefficient for intensity based Raman spectral properties determined with five deconvoluted peaks as a function of X-ray photoelectron spectral properties for HAMWCNT and LAMWCNT.

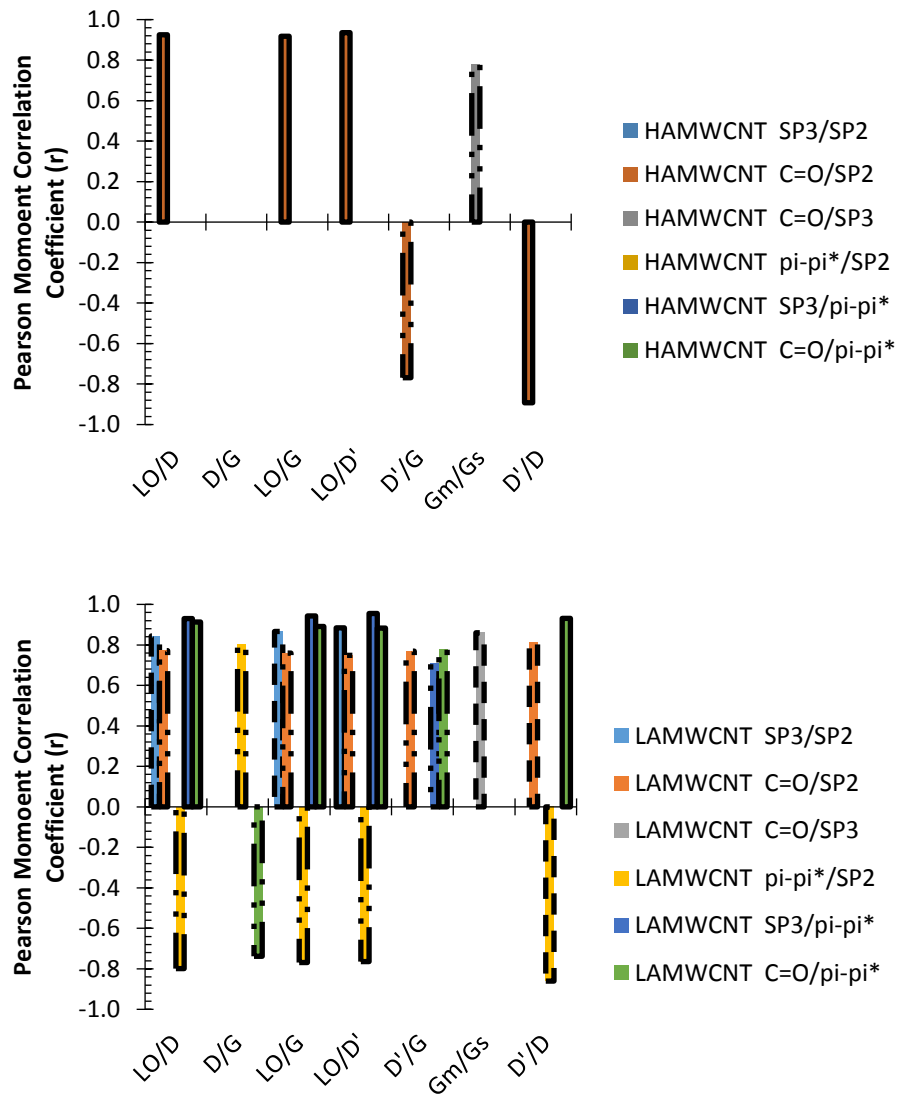


Figure A.18 Pearson product moment correlation coefficient for area based Raman spectral properties determined with five deconvoluted peaks as a function of X-ray photoelectron spectral properties for HAMWCNT and LAMWCNT.

## REFERENCES

1. Furr, N. How Failure Taught Edison to Repeatedly Innovate 2011. <http://www.forbes.com/sites/nathanfurr/2011/06/09/how-failure-taught-edison-to-repeatedly-innovate/#1d0f530b38f5> (accessed 2016 December 11).
2. Koch, G.; Varney, J.; Thompson, N.; Moghissi, O.; Gould, M.; Payer, J. *International Measures of Prevention, Application, and Economics of Corrosion Technologies Study*; NACE International: Houston, 2016.
3. Corrosion Failures: San Francisco Bay Bridge Bolt Failure. <http://www.nace.org/CORROSION-FAILURES-San-Francisco-Bay-Bridge-Bolt-Failure.aspx> (accessed 30 September).
4. Corrosion Failures: Fukushima Nuclear Plant Tank Leak. <http://www.nace.org/CORROSION-FAILURES-Fukushima-Nuclear-Plant-Tank-Leak.aspx> (accessed 30 September).
5. Revie, W. R., *Uhlig's Corrosion Handbook*. 3rd ed.; John Wiley & Sons, Inc.: Hoboken, 2011; p 1253.
6. Sørensen, P. A.; Kiil, S.; Dam-Johansen, K.; Weinell, C. E., Anticorrosive Coatings: A Review. *Journal of Coatings Technology and Research* **2009**, *6* (2), 135-176.
7. Leng, A.; Streckel, H.; Stratmann, M., The Delamination of Polymeric Coatings from Steel. Part 2: First Stage of Delamination, Effect of Type and Concentration of Cations on Delamination, Chemical Analysis of the Interface. *Corrosion Science* **1998**, *41* (3), 579-597.
8. Sander, J.; Kirmaier, L.; Manea, M.; Shchukin, D.; Skorb, E., *Anticorrosive Coatings: Fundamentals and New Concepts*. Vincentz Network GmbH & Co.: Hannover, 2010.
9. *Protective Organic Coatings*. ASM International: Materials Park, OH, 2015; Vol. 5B.
10. Pruna, A., Advances in Carbon Nanotube Technology for Corrosion Applications. In *Handbook of Polymer Nanocomposites. Processing, Performance and Application: Volume B: Carbon Nanotube Based Polymer Composites*, Kar, K. K.; Pandey, K. J.; Rana, S., Eds. Springer Berlin Heidelberg: Berlin, Heidelberg, 2015; pp 335-359.
11. Sharma, S. K.; Peter, A.; Obot, I. B., Potential of Azadirachta Indica as a Green Corrosion Inhibitor against Mild Steel, Aluminum, and Tin: A Review. *Journal of Analytical Science and Technology* **2015**, *6* (1), 1-16.
12. Rani, A. B. E.; Basu, B. B. J., Green Inhibitors for Corrosion Protection of Metals and Alloys: An Overview. *International Journal of Corrosion* **2012**, *2012*, 15.
13. Anonymous, Chromate Primer Alternative Uses Carbon Nanotubes Modified with Corrosion Inhibitors. *Materials Performance* 1 April 2016, 2016.
14. Morsch, S.; Lyon, S.; Greensmith, P.; Smith, S. D.; Gibbon, S. R., Water Transport in an Epoxy–Phenolic Coating. *Progress in Organic Coatings* **2015**, *78*, 293-299.
15. Cotugno, S.; Larobina, D.; Mensitieri, G.; Musto, P.; Ragosta, G., A Novel Spectroscopic Approach to Investigate Transport Processes in Polymers: The Case of Water–Epoxy System. *Polymer* **2001**, *42* (15), 6431-6438.

16. Musto, P.; Ragosta, G.; Mascia, L., Vibrational Spectroscopy Evidence for the Dual Nature of Water Sorbed into Epoxy Resins. *Chemistry of Materials* **2000**, *12* (5), 1331-1341.
17. Soles, C. L.; Yee, A. F., A Discussion of the Molecular Mechanisms of Moisture Transport in Epoxy Resins. *Journal of Polymer Science Part B: Polymer Physics* **2000**, *38* (5), 792-802.
18. Mijović, J.; Zhang, H., Local Dynamics and Molecular Origin of Polymer Network–Water Interactions as Studied by Broadband Dielectric Relaxation Spectroscopy, Ftir, and Molecular Simulations. *Macromolecules* **2003**, *36* (4), 1279-1288.
19. Takeshita, Y.; Becker, E.; Sakata, S.; Miwa, T.; Sawada, T., States of Water Absorbed in Water-Borne Urethane/Epoxy Coatings. *Polymer* **2014**, *55* (10), 2505-2513.
20. Lee, D. K.; Saito, T.; Benesi, A. J.; Hickner, M. A.; Allcock, H. R., Characterization of Water in Proton-Conducting Membranes by Deuterium Nmr T1 Relaxation. *The Journal of Physical Chemistry B* **2011**, *115* (5), 776-783.
21. Li, L.; Yu, Y.; Su, H.; Zhan, G.; Li, S.; Wu, P., The Diffusion Mechanism of Water Transport in Amine-Cured Epoxy Networks. *Applied Spectroscopy* **2010**, *64* (4), 458-466.
22. Barati Farimani, A.; Aluru, N. R., Existence of Multiple Phases of Water at Nanotube Interfaces. *The Journal of Physical Chemistry C* **2016**, *120* (41), 23763-23771.
23. Geise, G. M.; Paul, D. R.; Freeman, B. D., Fundamental Water and Salt Transport Properties of Polymeric Materials. *Progress in Polymer Science* **2014**, *39* (1), 1-42.
24. Dias, C. R.; Rosa, M. J.; de Pinho, M. N., Structure of Water in Asymmetric Cellulose Ester Membranes — and Atr-Ftir Study. *Journal of Membrane Science* **1998**, *138* (2), 259-267.
25. Posner, R.; Titz, T.; Wapner, K.; Stratmann, M.; Grundmeier, G., Transport Processes of Hydrated Ions at Polymer/Oxide/Metal Interfaces: Part 2. Transport on Oxide Covered Iron and Zinc Surfaces. *Electrochimica Acta* **2009**, *54* (3), 900-908.
26. Kropman, M. F.; Bakker, H. J., Dynamics of Water Molecules in Aqueous Solvation Shells. *Science* **2001**, *291* (5511), 2118-2120.
27. Gao, X.; Zhao, T.; Li, Z., Effects of Ions on the Diffusion Coefficient of Water in Carbon Nanotubes. *Journal of Applied Physics* **2014**, *116* (5), 054311.
28. Murphy, D.; de Pinho, M. N., An Atr-Ftir Study of Water in Cellulose Acetate Membranes Prepared by Phase Inversion. *Journal of Membrane Science* **1995**, *106* (3), 245-257.
29. Deyab, M. A., Effect of Carbon Nano-Tubes on the Corrosion Resistance of Alkyd Coating Immersed in Sodium Chloride Solution. *Progress in Organic Coatings* **2015**, *85*, 146-150.
30. Jeon, H.; Park, J.; Shon, M., Corrosion Protection by Epoxy Coating Containing Multi-Walled Carbon Nanotubes. *Journal of Industrial and Engineering Chemistry* **2013**, *19* (3), 849-853.
31. Cubides, Y.; Castaneda, H., Corrosion Protection Mechanisms of Carbon Nanotube and Zinc-Rich Epoxy Primers on Carbon Steel in Simulated Concrete Pore Solutions in the Presence of Chloride Ions. *Corrosion Science* **2016**, *109*, 145-161.

32. Butyrskaya, E. V.; Nechaeva, L. S.; Zapryagaev, S. A., Theoretical Study of the Corrosion Protection Mechanism by Carbon Nanotubes. *Computational and Theoretical Chemistry* **2016**, *1090*, 1-5.
33. Gergely, A.; Pászti, Z.; Hakkel, O.; Drotár, E.; Mihály, J.; Kálmán, E., Corrosion Protection of Cold-Rolled Steel with Alkyd Paint Coatings Compositated with Submicron-Structure Types Polypyrrole-Modified Nano-Size Alumina and Carbon Nanotubes. *Materials Science and Engineering: B* **2012**, *177* (18), 1571-1582.
34. Burchell, T. D., *Carbon Materials for Advanced Technologies*. Elsevier: Amsterdam, 1999; p 558.
35. Burghard, M., Electronic and Vibrational Properties of Chemically Modified Single-Wall Carbon Nanotubes. *Surface Science Reports* **2005**, *58* (1-4), 1-109.
36. Chou, T.-W.; Gao, L.; Thostenson, E. T.; Zhang, Z.; Byun, J.-H., An Assessment of the Science and Technology of Carbon Nanotube-Based Fibers and Composites. *Composites Science and Technology* **2010**, *70* (1), 1-19.
37. Spitalsky, Z.; Tasis, D.; Papagelis, K.; Galiotis, C., Carbon Nanotube-Polymer Composites: Chemistry, Processing, Mechanical and Electrical Properties. *Progress in Polymer Science* **2010**, *35* (3), 357-401.
38. Gergely, A.; Pászti, Z.; Mihály, J.; Drotár, E.; Török, T., Galvanic Function of Zinc-Rich Coatings Facilitated by Percolating Structure of the Carbon Nanotubes. Part II: Protection Properties and Mechanism of the Hybrid Coatings. *Progress in Organic Coatings* **2014**, *77* (2), 412-424.
39. Khun, N. W.; Frankel, G. S., Cathodic Delamination of Polyurethane/Multiwalled Carbon Nanotube Composite Coatings from Steel Substrates. *Progress in Organic Coatings* **2016**, *99*, 55-60.
40. Starkova, O.; Buschhorn, S. T.; Mannov, E.; Schulte, K.; Aniskevich, A., Water Transport in Epoxy/Mwcnt Composites. *European Polymer Journal* **2013**, *49* (8), 2138-2148.
41. Curtzwiler, G. W.; Williams, E. B.; Konecki, C. M.; Wand, S. W.; Rawlins, J. W., Comparison of the Added Value for Corrosion Performance of Chemically Modified Multiwall Carbon Nanotube Epoxy-Amine Coating Systems on Steel Substrates. In *The Waterborne Symposium*, New Orleans, LA, 2016.
42. Iijima, S., Helical Microtubules of Graphitic Carbon. *Nature (London)* **1991**, *354*, 56-8.
43. Kyrylyuk, A. V.; Hermant, M. C.; Schilling, T.; Klumperman, B.; Koning, C. E.; van, d. S. P., Controlling Electrical Percolation in Multicomponent Carbon Nanotube Dispersions. *Nature Nanotechnology* **2011**, *6*, 364-369.
44. Li, X.; Wong, S. Y.; Tjiu, W. C.; Lyons, B. P.; Oh, S. A.; He, C. B., Non-Covalent Functionalization of Multiwalled Carbon Nanotubes and Their Application for Conductive Composites. *Carbon* **2008**, *46*, 829-831.
45. Bose, S.; Khare, R. A.; Moldenaers, P., Assessing the Strengths and Weaknesses of Various Types of Pre-Treatments of Carbon Nanotubes on the Properties of Polymer/Carbon Nanotubes Composites: A Critical Review. *Polymer* **2010**, *51* (5), 975-993.
46. Hernández-Pérez, A.; Avilés, F.; May-Pat, A.; Valadez-González, A.; Herrera-Franco, P. J.; Bartolo-Pérez, P., Effective Properties of Multiwalled Carbon

- Nanotube/Epoxy Composites Using Two Different Tubes. *Composites Science and Technology* **2008**, *68* (6), 1422-1431.
47. Ma, P.-C.; Siddiqui, N. A.; Marom, G.; Kim, J.-K., Dispersion and Functionalization of Carbon Nanotubes for Polymer-Based Nanocomposites: A Review. *Composites Part A: Applied Science and Manufacturing* **2010**, *41* (10), 1345-1367.
  48. Lajoie, E.; Bridges, L., Innovation Decisions: Using the Gartner Hype Cycle. *Library Leadership & Management* **2014**, *28* (4), 7.
  49. Anonymous Gartner Hype Cycle. <http://www.gartner.com/technology/research/methodologies/hype-cycle.jsp> (accessed 12/01/2015).
  50. Duchesne, L. Graphene Is Here to Stay. <http://investorintel.com/technology-metals-intel/graphene-is-here-to-stay/> (accessed 12/1/2015).
  51. Anonymous Graphene, 2d Materials and Carbon Nanotubes: Markets, Technologies and Opportunities 2015-2025. <http://www.prnewswire.com/news-releases/graphene-2d-materials-and-carbon-nanotubes-markets-technologies-and-opportunities-2015-2025-300180496.html> (accessed 12/01/2015).
  52. Multi Walled Carbon Nanotubes Products. <https://www.cheaptubes.com/product-category/multi-walled-carbon-nanotubes/> (accessed 26 October).
  53. Grossiord, N.; Loos, J.; Regev, O.; Koning, C. E., Toolbox for Dispersing Carbon Nanotubes into Polymers to Get Conductive Nanocomposites. *Chemistry of Materials* **2006**, *18* (5), 1089-1099.
  54. Leonard, F., *Physics of Carbon Nanotube Devices*. William Andrew: 2009.
  55. Gojny, F. H.; Nastalczyk, J.; Roslaniec, Z.; Schulte, K., Surface Modified Multi-Walled Carbon Nanotubes in Cnt/Epoxy-Composites. *Chemical Physics Letters* **2003**, *370* (5-6), 820-824.
  56. Butt, H.-J.; Graf, K.; Kappl, M., *Physics and Chemistry of Interfaces*. John Wiley and Sons Inc: New York, NY, 2006.
  57. Morrison, I.; Ross, S., *Colloidal Dispersion: Suspension, Emulsion, and Foams*. Wiley and Sons Inc: New York, NY, 2002.
  58. Fontana, M., *Corrosion Engineering*. 3 ed.; McGraw-Hill, Inc: Singapore, 1986.
  59. Cheng, H. K. F.; Basu, T.; Sahoo, N. G.; Li, L.; Chan, S. H., Current Advances in the Carbon Nanotube/Thermotropic Main-Chain Liquid Crystalline Polymer Nanocomposites and Their Blends. *Polymers* **2012**, *4* (2), 889-912.
  60. Bonard, J.-M., Carbon Nanostructures by Hot Filament Chemical Vapor Deposition: Growth, Properties, Applications. *Thin Solid Films* **2006**, *501*, 8-14.
  61. Hernadi, K.; Ljubović, E.; Seo, J. W.; Forró, L., Synthesis of Mwnt-Based Composite Materials with Inorganic Coating. *Acta Materialia* **2003**, *51* (5), 1447-1452.
  62. Ryan, K. P.; Cadek, M.; Nicolosi, V.; Walker, S.; Ruether, M.; Fonseca, A.; Nagy, J. B.; Blau, W. J.; Coleman, J. N., Multiwalled Carbon Nanotube Nucleated Crystallization and Reinforcement in Poly (Vinyl Alcohol) Composites. *Synthetic Metals* **2006**, *156* (2-4), 332-335.
  63. Kim, Y. A.; Kakegawa, H.; Fujisawa, K.; Shimamoto, D.; Muramatsu, H.; Kim, J. H.; Jung, Y. C.; Hayashi, T.; Endo, M.; Terrones, M.; Dresselhaus, M. S., Sensitive G-Band Raman Features for the Electrical Conductivity of Multi-Walled Carbon Nanotubes. *Journal Nanoscience Nanotechnology* **2010**, *10*, 3940-3944.

64. DiLeo, R. A.; Landi, B. J.; Raffaele, R. P., Purity Assessment of Multiwalled Carbon Nanotubes by Raman Spectroscopy. *Journal of Applied Physics* **2007**, *101* (6), 064307.
65. Dresselhaus, M. S.; Dresselhaus, G.; Saito, R.; Jorio, A., Raman Spectroscopy of Carbon Nanotubes. *Physics Reports* **2005**, *409* (2), 47-99.
66. Dresselhaus, M. S.; Jorio, A.; Saito, R., Characterizing Graphene, Graphite, and Carbon Nanotubes by Raman Spectroscopy. *Annual Review of Condensed Matter Physics* **2010**, *1* (1), 89-108.
67. Grady, B. P., *Carbon Nanotube-Polymer Composites Manufacture, Properties, and Applications*. Wiley: Hoboken, N.J., 2011; p 352.
68. Saito, R.; Dresselhaus, G.; Dresselhaus, M. S., *Physical Properties of Carbon Nanotubes*. Imperial College Press: London, 1998; p 259.
69. Singh, L. T.; Nanda, K. K., General Theories for the Electrical Transport Properties of Carbon Nanotubes. *Nanotechnology* **2011**, *22* (31), 315705.
70. Lehman, J. H.; Terrones, M.; Mansfield, E.; Hurst, K. E.; Meunier, V., Evaluating the Characteristics of Multiwall Carbon Nanotubes. *Carbon* **2011**, *49* (8), 2581-2602.
71. Dresselhaus, M. S.; Jorio, A.; Souza Filho, A. G.; Saito, R., Defect Characterization in Graphene and Carbon Nanotubes Using Raman Spectroscopy. *Philosophical Transactions of the Royal Society A: Mathematical, Physical and Engineering Sciences* **2010**, *368* (1932), 5355-5377.
72. Chakrapani, N.; Curran, S.; Wei, B.; Ajayan, P. M.; Carrillo, A.; Kane, R. S., Spectral Fingerprinting of Structural Defects in Plasma-Treated Carbon Nanotubes. *Journal of Materials Research* **2011**, *18* (10), 2515-2521.
73. Tuinstra, F.; Koenig, J. L., Raman Spectrum of Graphite. *The Journal of Chemical Physics* **1970**, *53* (3), 1126-1130.
74. Tuinstra, F.; Koenig, J. L., Characterization of Graphite Fiber Surfaces with Raman Spectroscopy. *Journal of Composite Materials* **1970**, *4*, 492-9.
75. Osswald, S.; Havel, M.; Gogotsi, Y., Monitoring Oxidation of Multiwalled Carbon Nanotubes by Raman Spectroscopy. *Journal of Raman Spectroscopy* **2007**, *38* (6), 728-736.
76. Cançado, L. G.; Takai, K.; Enoki, T.; Endo, M.; Kim, Y. A.; Mizusaki, H.; Jorio, A.; Coelho, L. N.; Magalhaes-Paniago, R.; Pimenta, M. A., General Equation for the Determination of the Crystallite Size  $L_{[Sub a]}$  of Nanographite by Raman Spectroscopy. *Applied Physics Letters* **2006**, *88* (16), 163106-3.
77. Singh, C.; Srivastava, S.; Ali, M. A.; Gupta, T. K.; Sumana, G.; Srivastava, A.; Mathur, R. B.; Malhotra, B. D., Carboxylated Multiwalled Carbon Nanotubes Based Biosensor for Aflatoxin Detection. *Sensors and Actuators B: Chemical* **2013**, *185* (0), 258-264.
78. Wang, Y.-H.; Chang, C.-M.; Liu, Y.-L., Benzoxazine-Functionalized Multi-Walled Carbon Nanotubes for Preparation of Electrically-Conductive Polybenzoxazines. *Polymer* **2012**, *53* (1), 106-112.
79. Chen, X.; Zhou, M.; Hou, Q.; Tu, X.; Wu, X., Active Poly(4-Chloromethyl Styrene)-Functionalized Multiwalled Carbon Nanotubes. *Macromolecular Chemistry and Physics* **2013**, *214* (16), 1829-1835.

80. Pelalak, R.; Baniadam, M.; Maghrebi, M., Controllable Purification, Cutting and Unzipping of Multi-Walled Carbon Nanotubes with a Microwave Method. *Applied Physics A* **2013**, *111* (3), 951-957.
81. Donato, M. G.; Messina, G.; Santangelo, S.; Galvagno, S.; Milone, C.; Pistone, A., Aid of Raman Spectroscopy in Diagnostics of Mwcnt Synthesised by Fe-Catalysed Cvd. *Journal of Physics: Conference Series* **2007**, *61*, 931-935.
82. Lefrant, S.; Buisson, J. P.; Schreiber, J.; Chauvet, O.; Baibarac, M.; Baltog, I., Raman Studies of Carbon Nanotubes and Polymer Nanotube Composites. *Molecular Crystals and Liquid Crystals* **2004**, *415* (1), 125-132.
83. Mkhabela, V. J.; Mishra, A. K.; Mbianda, X. Y., Thermal and Mechanical Properties of Phosphorylated Multiwalled Carbon Nanotube/Polyvinyl Chloride Composites. *Carbon* **2011**, *49* (2), 610-617.
84. Kar, P.; Choudhury, A., Carboxylic Acid Functionalized Multi-Walled Carbon Nanotube Doped Polyaniline for Chloroform Sensors. *Sensors and Actuators B: Chemical* **2013**, *183* (0), 25-33.
85. Pumera, M.; míd, B.; etislav; Veltruská, K.; ina, Influence of Nitric Acid Treatment of Carbon Nanotubes on Their Physico-Chemical Properties. *Journal of Nanoscience and Nanotechnology* **2009**, *9* (4), 2671-2676.
86. Wepasnick, K. A.; Smith, B. A.; Schrote, K. E.; Wilson, H. K.; Diegelmann, S. R.; Fairbrother, D. H., Surface and Structural Characterization of Multi-Walled Carbon Nanotubes Following Different Oxidative Treatments. *Carbon* **2011**, *49* (1), 24-36.
87. Bokova, S. N.; Obraztsova, E. D.; Grebenyukov, V. V.; Elumeeva, K. V.; Ishchenko, A. V.; Kuznetsov, V. L., Raman Diagnostics of Multi-Wall Carbon Nanotubes with a Small Wall Number. *physica status solidi (b)* **2010**, *247* (11-12), 2827-2830.
88. Awasthi, K.; Kumar, R.; Tiwari, R. S.; Srivastava, O. N., Large Scale Synthesis of Bundles of Aligned Carbon Nanotubes Using a Natural Precursor: Turpentine Oil. *Journal of Experimental Nanoscience* **2010**, *5* (6), 498-508.
89. Lachman, N.; Sui, X.; Bendikov, T.; Cohen, H.; Wagner, H. D., Electronic and Mechanical Degradation of Oxidized Cnts. *Carbon* **2012**, *50* (5), 1734-1739.
90. Ling, X.; Wei, Y.; Zou, L.; Xu, S., The Effect of Different Order of Purification Treatments on the Purity of Multiwalled Carbon Nanotubes. *Applied Surface Science* **2013**, *276* (0), 159-166.
91. Chang, C.-M.; Liu, Y.-L., Functionalization of Multi-Walled Carbon Nanotubes with Furan and Maleimide Compounds through Diels–Alder Cycloaddition. *Carbon* **2009**, *47* (13), 3041-3049.
92. Zhao, Z.; Yang, Z.; Hu, Y.; Li, J.; Fan, X., Multiple Functionalization of Multi-Walled Carbon Nanotubes with Carboxyl and Amino Groups. *Applied Surface Science* **2013**, *276* (0), 476-481.
93. Hussain, S.; Shah, K.; Islam, S. S., Investigation of Effects Produced by Chemical Functionalization in Single-Walled and Multi-Walled Carbon Nanotubes Using Raman Spectroscopy. *Materials Science-Poland* **2013**, *31* (2), 276-280.
94. Amiri, A.; Memarpoor-Yazdi, M.; Shanbedi, M.; Eshghi, H., Influence of Different Amino Acid Groups on the Free Radical Scavenging Capability of Multi

Walled Carbon Nanotubes. *Journal of Biomedical Materials Research Part A* **2013**, *101A* (8), 2219-2228.

95. Ran, M.; Sun, W.; Liu, Y.; Chu, W.; Jiang, C., Functionalization of Multi-Walled Carbon Nanotubes Using Water-Assisted Chemical Vapor Deposition. *Journal of Solid State Chemistry* **2013**, *197* (0), 517-522.

96. Farbod, M.; Tadavani, S. K.; Kiasat, A., Surface Oxidation and Effect of Electric Field on Dispersion and Colloids Stability of Multiwalled Carbon Nanotubes. *Colloids and Surfaces A: Physicochemical and Engineering Aspects* **2011**, *384* (1-3), 685-690.

97. Luo, Z.; Cai, X.; Hong, R. Y.; Li, J. H.; Wei, D. G.; Luo, G. H.; Li, H. Z., Surface Modification of Multiwalled Carbon Nanotubes Via Gliding Arc Plasma for the Reinforcement of Polypropylene. *Journal of Applied Polymer Science* **2013**, *127* (6), 4756-4763.

98. Qian, W.; Liu, T.; Wei, F.; Yuan, H., Quantitative Raman Characterization of the Mixed Samples of the Single and Multi-Wall Carbon Nanotubes. *Carbon* **2003**, *41* (9), 1851-1854.

99. Vix-Guterl, C.; Couzi, M.; Dentzer, J.; Trinquecoste, M.; Delhaes, P., Surface Characterizations of Carbon Multiwall Nanotubes: Comparison between Surface Active Sites and Raman Spectroscopy. *The Journal of Physical Chemistry B* **2004**, *108* (50), 19361-19367.

100. Andrade, N.; Martinez, D.; Paula, A.; Silveira, J.; Alves, O.; Souza Filho, A., Temperature Effects on the Nitric Acid Oxidation of Industrial Grade Multiwalled Carbon Nanotubes. *Journal of Nanoparticle Research* **2013**, *15* (7), 1-11.

101. Delhaes, P.; Couzi, M.; Trinquecoste, M.; Dentzer, J.; Hamidou, H.; Vix-Guterl, C., A Comparison between Raman Spectroscopy and Surface Characterizations of Multiwall Carbon Nanotubes. *Carbon* **2006**, *44* (14), 3005-3013.

102. Yang, D.-Q.; Rochette, J.-F.; Sacher, E., Controlled Chemical Functionalization of Multiwalled Carbon Nanotubes by Kilolectronvolt Argon Ion Treatment and Air Exposure. *Langmuir* **2005**, *21* (18), 8539-8545.

103. Baitinger, E. M.; Vekesser, N. A.; Kovalev, I. N.; Ryabkov, Y. I.; Viktorov, V. V., Defect Structure of Multiwalled Carbon Nanotubes Studied by Raman Spectroscopy. *Inorganic Materials* **2011**, *47* (5), 471-474.

104. Schönfelder, R.; Avilés, F.; Bachmatiuk, A.; Cauich-Rodriguez, J. V.; Knupfer, M.; Büchner, B.; Rummeli, M. H., On the Merits of Raman Spectroscopy and Thermogravimetric Analysis to Assess Carbon Nanotube Structural Modifications. *Applied Physics A* **2012**, *106* (4), 843-852.

105. Chen, C.; Liang, B.; Ogino, A.; Wang, X.; Nagatsu, M., Oxygen Functionalization of Multiwall Carbon Nanotubes by Microwave-Excited Surface-Wave Plasma Treatment. *The Journal of Physical Chemistry C* **2009**, *113* (18), 7659-7665.

106. Santangelo, S.; Messina, G.; Faggio, G.; Lanza, M.; Pistone, A.; Milone, C., Calibration of Reaction Parameters for the Improvement of Thermal Stability and Crystalline Quality of Multi-Walled Carbon Nanotubes. *Journal of Materials Science* **2010**, *45* (3), 783-792.

107. Murphy, H.; Papakonstantinou, P.; Okpalugo, T. I. T., Raman Study of Multiwalled Carbon Nanotubes Functionalized with Oxygen Groups. *Journal of Vacuum*

- Science & Technology B: Microelectronics and Nanometer Structures* **2006**, 24 (2), 715-720.
108. Santangelo, S.; Messina, G.; Faggio, G.; Lanza, M.; Milone, C., Evaluation of Crystalline Perfection Degree of Multi-Walled Carbon Nanotubes: Correlations between Thermal Kinetic Analysis and Micro-Raman Spectroscopy. *Journal of Raman Spectroscopy* **2011**, 42 (4), 593-602.
109. Judek, J.; Jastrzebski, C.; Malolepszy, A.; Mazurkiewicz, M.; Stobinski, L.; Zdrojek, M., Laser Induced Temperature Effects in Multi-Walled Carbon Nanotubes Probed by Raman Spectroscopy. *physica status solidi (a)* **2012**, 209 (2), 313-316.
110. Repalle, S.; Chen, J.; Drozd, V.; Choi, W., The Raman Spectroscopic Studies of Aligned Mwcnts Treated under High Pressure and High Temperature. *Journal of Physics and Chemistry of Solids* **2010**, 71 (8), 1150-1153.
111. Kumar, S.; Kaur, I.; Dharamvir, K.; Bharadwaj, L. M., Controlling the Density and Site of Attachment of Gold Nanoparticles onto the Surface of Carbon Nanotubes. *Journal of Colloid and Interface Science* **2012**, 369 (1), 23-27.
112. Gohil, S.; Ghosh, S., Surface Enhanced Raman Scattering from Multiwalled Carbon Nanotubes at Low Temperatures. *Applied Physics Letters* **2010**, 96 (14), 143108.
113. Sooin, N.; Roy, S. S.; Ray, S. C.; McLaughlin, J. A., Excitation Energy Dependence of Raman Bands in Multiwalled Carbon Nanotubes. *Journal of Raman Spectroscopy* **2010**, 41 (10), 1227-1233.
114. de los Arcos, T.; Garnier, M. G.; Oelhafen, P.; Seo, J. W.; Domingo, C.; García-Ramos, J. V.; Sánchez-Cortés, S., In Situ Assessment of Carbon Nanotube Diameter Distribution with Photoelectron Spectroscopy. *Physical Review B* **2005**, 71 (20), 205416.
115. Datsyuk, V.; Kalyva, M.; Papagelis, K.; Parthenios, J.; Tasis, D.; Siokou, A.; Kallitsis, I.; Galiotis, C., Chemical Oxidation of Multiwalled Carbon Nanotubes. *Carbon* **2008**, 46 (6), 833-840.
116. Stobinski, L.; Lesiak, B.; Kövér, L.; Tóth, J.; Biniak, S.; Trykowski, G.; Judek, J., Multiwall Carbon Nanotubes Purification and Oxidation by Nitric Acid Studied by the Ftir and Electron Spectroscopy Methods. *Journal of Alloys and Compounds* **2010**, 501 (1), 77-84.
117. Tan, P.; An, L.; Liu, L.; Guo, Z.; Czerw, R.; Carroll, D. L.; Ajayan, P. M.; Zhang, N.; Guo, H., Probing the Phonon Dispersion Relations of Graphite from the Double-Resonance Process of Stokes and Anti-Stokes Raman Scatterings in Multiwalled Carbon Nanotubes. *Physical Review B* **2002**, 66 (24), 245410.
118. Lee, S.; Peng, J.-W.; Liu, C.-H., Probing Plasma-Induced Defect Formation and Oxidation in Carbon Nanotubes by Raman Dispersion Spectroscopy. *Carbon* **2009**, 47 (15), 3488-3497.
119. Rao, A. M.; Jorio, A.; Pimenta, M. A.; Dantas, M. S. S.; Saito, R.; Dresselhaus, G.; Dresselhaus, M. S., Polarized Raman Study of Aligned Multiwalled Carbon Nanotubes. *Physical Review Letters* **2000**, 84 (8), 1820-1823.
120. Pietraß, T.; Dewald, J. L.; Clewett, C. F. M.; Tierney, D.; Ellis, A. V.; Dias, S.; Alvarado, A.; Sandoval, L.; Tai, S.; Curran, S. A., Electron Spin Resonance and Raman Scattering Spectroscopy of Multi-Walled Carbon Nanotubes: A Function of Acid Treatment. *Journal of Nanoscience and Nanotechnology* **2006**, 6 (1), 135-140.

121. Behler, K.; Osswald, S.; Ye, H.; Dimovski, S.; Gogotsi, Y., Effect of Thermal Treatment on the Structure of Multi-Walled Carbon Nanotubes. *Journal of Nanoparticle Research* **2006**, *8* (5), 615-625.
122. Safibonab, B.; Reyhani, A.; Nozad Golikand, A.; Mortazavi, S. Z.; Mirershadi, S.; Ghoranneviss, M., Improving the Surface Properties of Multi-Walled Carbon Nanotubes after Irradiation with Gamma Rays. *Applied Surface Science* **2011**, *258* (2), 766-773.
123. Antunes, E. F.; Lobo, A. O.; Corat, E. J.; Trava-Airoldi, V. J.; Martin, A. A.; Veríssimo, C., Comparative Study of First- and Second-Order Raman Spectra of Mwcnt at Visible and Infrared Laser Excitation. *Carbon* **2006**, *44* (11), 2202-2211.
124. Zhao, X.; Ando, Y.; Qin, L.-C.; Kataura, H.; Maniwa, Y.; Saito, R., Multiple Splitting of G-Band Modes from Individual Multiwalled Carbon Nanotubes. *Applied Physics Letters* **2002**, *81* (14), 2550-2552.
125. Frielinghaus, R.; Goss, K.; Trelenkamp, S.; Houben, L.; Schneider, C. M.; Meyer, C., Comprehensive Characterization of an Individual Carbon Nanotube Transport Device. *Phys. Status Solidi B* **2011**, *248*, 2660-2663.
126. Yuan, S.; Zhang, Q.; You, Y.; Shen, Z.-X.; Shimamoto, D.; Endo, M., Correlation between in Situ Raman Scattering and Electrical Conductance for an Individual Double-Walled Carbon Nanotube. *Nano Letters* **2008**, *9* (1), 383-387.
127. Singh, D. K.; Iyer, P. K.; Giri, P. K., Diameter Dependence of Interwall Separation and Strain in Multiwalled Carbon Nanotubes Probed by X-Ray Diffraction and Raman Scattering Studies. *Diamond and Related Materials* **2010**, *19* (10), 1281-1288.
128. Nanot, S.; Millot, M.; Raquet, B.; Broto, J.-M.; Magrez, A.; Gonzalez, J., Doping Dependence of the G-Band Raman Spectra of an Individual Multiwall Carbon Nanotube. *Physica E: Low-dimensional Systems and Nanostructures* **2010**, *42* (9), 2466-2470.
129. Vollebregt, S.; Ishihara, R.; Tichelaar, F. D.; Hou, Y.; Beenakker, C. I. M., Influence of the Growth Temperature on the First and Second-Order Raman Band Ratios and Widths of Carbon Nanotubes and Fibers. *Carbon* **2012**, *50* (10), 3542-3554.
130. Jeet, K.; Jindal, V. K.; Bharadwaj, L. M.; Bhandari, R.; Dharamvir, K., Three-Stage Structural Modification of Carbon Nanotubes by Swift Heavy Ion Irradiation. *Nuclear Instruments and Methods in Physics Research Section B: Beam Interactions with Materials and Atoms* **2012**, *285* (0), 30-36.
131. Ritter, U.; Scharff, P.; Siegmund, C.; Dmytrenko, O. P.; Kulish, N. P.; Prylutskyy, Y. I.; Belyi, N. M.; Gubanov, V. A.; Komarova, L. I.; Lizunova, S. V.; Poroshin, V. G.; Shlapatskaya, V. V.; Bernas, H., Radiation Damage to Multi-Walled Carbon Nanotubes and Their Raman Vibrational Modes. *Carbon* **2006**, *44* (13), 2694-2700.
132. Puech, P.; Anwar, A. W.; Flahaut, E.; Dunstan, D. J.; Bassil, A.; Bacsa, W., Raman G and D Band in Strongly Photoexcited Carbon Nanotubes. *Physical Review B* **2009**, *79* (8), 085418.
133. Piscanec, S.; Lazzeri, M.; Robertson, J.; Ferrari, A. C.; Mauri, F., Optical Phonons in Carbon Nanotubes: Kohn Anomalies, Peierls Distortions, and Dynamic Effects. *Physical Review B* **2007**, *75* (3), 035427.
134. Van der Heide, P., *X-Ray Photoelectron Spectroscopy: An Introduction to Principles and Practices*. John Wiley & Sons, Inc.: Hoboken, 2012; p 241.

135. Ballard, R. E., Empirical Mean Free Path Curves for Electron Scattering in Solids. *Journal of Electron Spectroscopy and Related Phenomena* **1982**, 25 (1), 75-78.
136. Pirlot, C.; Willems, I.; Fonseca, A.; Nagy, J. B.; Delhalle, J., Preparation and Characterization of Carbon Nanotube/Polyacrylonitrile Composites. *Advanced Engineering Materials* **2002**, 4 (3), 109-114.
137. Okpalugo, T. I. T.; Papakonstantinou, P.; Murphy, H.; McLaughlin, J.; Brown, N. M. D., High Resolution Xps Characterization of Chemical Functionalised Mwcnts and Swcnts. *Carbon* **2005**, 43 (1), 153-161.
138. Ago, H.; Kugler, T.; Cacialli, F.; Salaneck, W. R.; Shaffer, M. S. P.; Windle, A. H.; Friend, R. H., Work Functions and Surface Functional Groups of Multiwall Carbon Nanotubes. *The Journal of Physical Chemistry B* **1999**, 103 (38), 8116-8121.
139. Mattevi, C.; Eda, G.; Agnoli, S.; Miller, S.; Mkhoyan, K. A.; Celik, O.; Mastrogiovanni, D.; Granozzi, G.; Garfunkel, E.; Chhowalla, M., Evolution of Electrical, Chemical, and Structural Properties of Transparent and Conducting Chemically Derived Graphene Thin Films. *Advanced Functional Materials* **2009**, 19 (16), 2577-2583.
140. Li, M.; Boggs, M.; Beebe, T. P.; Huang, C. P., Oxidation of Single-Walled Carbon Nanotubes in Dilute Aqueous Solutions by Ozone as Affected by Ultrasound. *Carbon* **2008**, 46 (3), 466-475.
141. Wang, H.; Zhou, A.; Peng, F.; Yu, H.; Yang, J., Mechanism Study on Adsorption of Acidified Multiwalled Carbon Nanotubes to Pb(II). *Journal of Colloid and Interface Science* **2007**, 316 (2), 277-283.
142. Meng, L.-Y.; Park, S.-J., Preparation and Characterization of Reduced Graphene Nanosheets Via Pre-Exfoliation of Graphite Flakes. *Bulletin of the Korean Chemical Society* **2012**, 33 (1), 209-214.
143. Belin, T.; Epron, F., Characterization Methods of Carbon Nanotubes: A Review. *Materials Science and Engineering: B* **2005**, 119 (2), 105-118.
144. Moulder, J. F., *Handbook of X-Ray Photoelectron Spectroscopy*. Physical Electronics: Eden Praire, 1992.
145. Fouquet, M.; Telg, H.; Maultzsch, J.; Wu, Y.; Chandra, B.; Hone, J.; Heinz, T. F.; Thomsen, C., Longitudinal Optical Phonons in Metallic and Semiconducting Carbon Nanotubes. *Physical Review Letters* **2009**, 102 (7), 075501.
146. Gupta, A.; Chen, G.; Joshi, P.; Tadigadapa, S.; Eklund, Raman Scattering from High-Frequency Phonons in Supported N-Graphene Layer Films. *Nano Letters* **2006**, 6 (12), 2667-2673.
147. Arepalli, S.; Freiman, S.; Hooker, S.; Migler, D, Measurement Issues in Single-Wall Carbon Nanotubes. *NIST Recommended Practice Guide* **2008**.
148. Weathington, B. L.; Cunningham, C. J. L.; Pittenger, D. J., *Understanding Business Research*. John Wiley & Sons, Inc.: Hoboken, 2012; p 492.
149. D'Souza, F.; Kadish, K., *Handbook of Carbon Nano Materials: Synthesis and Supramolecular Systems*. World Scientific Publishing Co. Pte. Ltd.: Hackensack, 2011; Vol. 1.
150. Morishita, K.; Takarada, T., Gasification Behavior of Carbon Nanotubes. *Carbon* **1997**, 35 (7), 977-981.

151. Liao, Y.-H.; Marietta-Tondin, O.; Liang, Z.; Zhang, C.; Wang, B., Investigation of the Dispersion Process of Swnts/Sc-15 Epoxy Resin Nanocomposites. *Materials Science and Engineering: A* **2004**, *385* (1–2), 175-181.
152. Grady, B. P., Effects of Carbon Nanotubes on Polymer Physics. *Journal of Polymer Science Part B: Polymer Physics* **2012**, *50* (9), 591-623.
153. Zhu, J.; Peng, H.; Rodriguez-Macias, F.; Margrave, J. L.; Khabashesku, V. N.; Imam, A. M.; Lozano, K.; Barrera, E. V., Reinforcing Epoxy Polymer Composites through Covalent Integration of Functionalized Nanotubes. *Advanced Functional Materials* **2004**, *14* (7), 643-648.
154. Coleman, J. N.; Khan, U.; Blau, W. J.; Gun'ko, Y. K., Small but Strong: A Review of the Mechanical Properties of Carbon Nanotube–Polymer Composites. *Carbon* **2006**, *44* (9), 1624-1652.
155. Pötschke, P.; Bhattacharyya, A. R.; Janke, A., Melt Mixing of Polycarbonate with Multiwalled Carbon Nanotubes: Microscopic Studies on the State of Dispersion. *European Polymer Journal* **2004**, *40* (1), 137-148.
156. Sandler, J.; Shaffer, M. S. P.; Prasse, T.; Bauhofer, W.; Schulte, K.; Windle, A. H., Development of a Dispersion Process for Carbon Nanotubes in an Epoxy Matrix and the Resulting Electrical Properties. *Polymer* **1999**, *40* (21), 5967-5971.
157. Combessis, A.; Mazel, C.; Maugin, M.; Flandin, L., Optical Density as a Probe of Carbon Nanotubes Dispersion in Polymers. *Journal of Applied Polymer Science* **2013**, *130* (3), 1778-1786.
158. Haslam, M. D.; Raeymaekers, B., A Composite Index to Quantify Dispersion of Carbon Nanotubes in Polymer-Based Composite Materials. *Composites Part B: Engineering* **2013**, *55* (0), 16-21.
159. Eckel, D. F.; Balogh, M. P.; Fasulo, P. D.; Rodgers, W. R., Assessing Organo-Clay Dispersion in Polymer Nanocomposites. *Journal of Applied Polymer Science* **2004**, *93* (3), 1110-1117.
160. Villmow, T.; Pötschke, P.; Pegel, S.; Häussler, L.; Kretzschmar, B., Influence of Twin-Screw Extrusion Conditions on the Dispersion of Multi-Walled Carbon Nanotubes in a Poly(Lactic Acid) Matrix. *Polymer* **2008**, *49* (16), 3500-3509.
161. Gao, Y.; Li, Z.; Lin, Z.; Zhu, L.; Tannenbaum, A.; Bouix, S.; Wong, C. P., Automated Dispersion and Orientation Analysis for Carbon Nanotube Reinforced Polymer Composites. *Nanotechnology* **2012**, *23* (43), 435706-435706.
162. *Polymer Nanotubes Nanocomposites Synthesis, Properties and Applications*. 2 ed.; Scrivener Publishing: Beverly, MA 2014; p 470.
163. Gojny, F. H.; Schulte, K., Functionalisation Effect on the Thermo-Mechanical Behaviour of Multi-Wall Carbon Nanotube/Epoxy-Composites. *Composites Science and Technology* **2004**, *64* (15), 2303-2308.
164. Koo, J.; Shin, K.; Seo, Y.-S.; Koga, T.; Park, S.; Satija, S.; Chen, X.; Yoon, K.; Hsiao, B. S.; Sokolov, J. C.; Rafailovich, M. H., Stabilizing Thin Film Polymer Bilayers against Dewetting Using Multiwalled Carbon Nanotubes. *Macromolecules* **2007**, *40* (26), 9510-9516.
165. Xu, X.; Thwe, M. M.; Shearwood, C.; Liao, K., Mechanical Properties and Interfacial Characteristics of Carbon-Nanotube-Reinforced Epoxy Thin Films. *Applied Physics Letters* **2002**, *81* (15), 2833-2835.

166. Yu, J.; Grossiord, N.; Koning, C. E.; Loos, J., Controlling the Dispersion of Multi-Wall Carbon Nanotubes in Aqueous Surfactant Solution. *Carbon* **2007**, *45*, 618-623.
167. Farrokhpay, S.; Morris, G. E.; Fornasiero, D.; Self, P., Titania Pigment Particles Dispersion in Water-Based Paint Films. *JCT Research* **2006**, *3* (4), 275-283.
168. Pazokifard, S.; Farrokhpay, S.; Mirabedini, M.; Esfandeh, M., Surface Treatment of Tio<sub>2</sub> Nanoparticles Via Sol–Gel Method: Effect of Silane Type on Hydrophobicity of the Nanoparticles. *Progress in Organic Coatings* **2015**, *87*, 36-44.
169. Farrokhpay, S., Application of Spectroscopy and Microscopy Techniques in Surface Coatings Evaluation: A Review. *Applied Spectroscopy Reviews* **2012**, *47* (3), 233-243.
170. Kovacs, J. Z.; Andresen, K.; Pauls, J. R.; Garcia, C. P.; Schossig, M.; Schulte, K.; Bauhofer, W., Analyzing the Quality of Carbon Nanotube Dispersions in Polymers Using Scanning Electron Microscopy. *Carbon* **2007**, *45* (6), 1279-1288.
171. Zhao, M.; Ming, B.; Kim, J.-W.; Gibbons, L. J.; Gu, X.; Nguyen, T.; Park, C.; Lillehei, P. T.; Villarrubia, J. S.; Vladar, A.; Liddle, J. A. *New Insights into Subsurface Imaging of Carbon Nanotubes in Polymer Composites Via Scanning Electron Microscopy*; National Institute of Standards and Technology: 2015.
172. Grossiord, N.; Loos, J.; Meuldijk, J.; Regev, O.; Miltner, H. E.; Van, M. B.; Koning, C. E. In *Conductive Carbon-Nanotube/Polymer Composites: Spectroscopic Monitoring of the Exfoliation Process in Water and the Crucial Role of Wetting*, Nano Science and Technology Institute: 2006; pp 222-225.
173. Ferreira, T.; Paiva, M.; Pontes, A., Dispersion of Carbon Nanotubes in Polyamide 6 for Microinjection Moulding. *Journal of Polymer Research* **2013**, *20* (11), 1-9.
174. Jurewicz, I.; Worajittiphon, P.; King, A. A.; Sellin, P. J.; Keddie, J. L.; Dalton, A. B., Locking Carbon Nanotubes in Confined Lattice Geometries--a Route to Low Percolation in Conducting Composites. *Journal Physical Chemistry B* **2011**, *115* (20), 6395-400.
175. Vandervorst, P.; Lei, C. H.; Lin, Y.; Dupont, O.; Dalton, A. B.; Sun, Y. P.; Keddie, J. L., The Fine Dispersion of Functionalized Carbon Nanotubes in Acrylic Latex Coatings. *Progress in Organic Coatings* **2006**, *57* (2), 91-97.
176. Curtzwiler, G.; Costanzo, P. J.; Fernando, R.; Danes, J. E.; Vorst, K., Thermal-Initiated Hydroxyethyl Methacrylate Functionalization of Multiwalled Carbon Nanotubes. *Journal of Applied Polymer Science* **2011**, *121* (2), 964-969.
177. Rastogi, R.; Kaushal, R.; Tripathi, S. K.; Sharma, A. L.; Kaur, I.; Bharadwaj, L. M., Comparative Study of Carbon Nanotube Dispersion Using Surfactants. *Journal of Colloid and Interface Science* **2008**, *328* (2), 421-428.
178. Bakshi, S. R.; Batista, R. G.; Agarwal, A., Quantification of Carbon Nanotube Distribution and Property Correlation in Nanocomposites. *Composites Part A: Applied Science and Manufacturing* **2009**, *40* (8), 1311-1318.
179. Kashiwagi, T.; Fagan, J.; Douglas, J. F.; Yamamoto, K.; Heckert, A. N.; Leigh, S. D.; Obrzut, J.; Du, F.; Lin-Gibson, S.; Mu, M.; Winey, K. I.; Haggenueller, R., Relationship between Dispersion Metric and Properties of Pmma/Swnt Nanocomposites. *Polymer* **2007**, *48* (16), 4855-4866.

180. Sul, I. H.; Youn, J. R.; Song, Y. S., Quantitative Dispersion Evaluation of Carbon Nanotubes Using a New Analysis Protocol. *Carbon* **2011**, *49* (4), 1473-1478.
181. Sharif Sh, M.; Golestani Fard, F.; Khatibi, E.; Sarpoolaky, H., Dispersion and Stability of Carbon Black Nanoparticles, Studied by Ultraviolet–Visible Spectroscopy. *Journal of the Taiwan Institute of Chemical Engineers* **2009**, *40* (5), 524-527.
182. Goldschmidt, A.; Streitberger, H.-J., *Basics of Coating Technology*. 2nd ed.; Vincentz Network: Hannover, 2007.
183. Koleske, J. V., *Paint and Coating Testing Manual*. 15th ed.; ASTM International: West Conshohocken, 2012.
184. Nsib, F.; Ayed, N.; Chevalier, Y., Selection of Dispersants for the Dispersion of Carbon Black in Organic Medium. *Progress in Organic Coatings* **2006**, *55* (4), 303-310.
185. Gordon Carbon Blackness [My], Jetness [Mc], Undertone [Dm] and Tint Strength [T]. <https://measuretruecolor.hunterlab.com/2015/06/02/carbon-blackness-my-jetness-mc-undertone-dm-and-tint-strength-t/> (accessed April 4).
186. Xia, H.; Qiu, G.; Wang, Q., Polymer/Carbon Nanotube Composite Emulsion Prepared through Ultrasonically Assisted in Situ Emulsion Polymerization. *J. Appl. Polym. Sci.* **2006**, *100* (Copyright (C) 2012 American Chemical Society (ACS). All Rights Reserved.), 3123-3130.
187. Grossiord, N.; Loos, J.; Meuldijk, J.; Regev, O.; Miltner, H. E.; Van Mele, B.; Koning, C. E., Conductive Carbon-Nanotube/Polymer Composites: Spectroscopic Monitoring of the Exfoliation Process in Water. *Composites Science and Technology* **2007**, *67* (5), 778-782.
188. Grossiord, N.; Regev, O.; Loos, J.; Meuldijk, J.; Koning, C. E., Time-Dependent Study of the Exfoliation Process of Carbon Nanotubes in Aqueous Dispersions by Using Uv-Visible Spectroscopy. *Analytical Chemistry* **2005**, *77*, 5135-5139.
189. Singh, P.; Campidelli, S.; Giordani, S.; Bonifazi, D.; Bianco, A.; Prato, M., Organic Functionalisation and Characterisation of Single-Walled Carbon Nanotubes. *Chemical Society Reviews* **2009**, *38* (8), 2214-2230.
190. Anonymous Carbon Blackness [My], Jetness [Mc], Undertone [Dm] and Tint Strength [T]. <http://measuretruecolor.hunterlab.com/2015/06/02/carbon-blackness-my-jetness-mc-undertone-dm-and-tint-strength-t/> (accessed February 1).
191. Ellison, S.; Barwick, V.; Trevor, F., *Practical Statistics for the Analytical Scientist: A Bench Guide*. 2nd ed.; The Royal Society of Chemistry: Cambridge, 2009.
192. Baxbaum, G.; Pfaff, G., *Industrial Inorganic Pigments*. 3rd ed.; Wiley-VCH Verlag GmbH & Co. KGaA: Weinheim, 2005.
193. Barzegar-Bafrooei, H.; Ebadzadeh, T.; Tazike, M., A Survey on Dispersion Mechanisms of Multi-Walled Carbon Nanotubes in an Aqueous Media by Uv-Vis, Raman Spectroscopy, Tga, and Ftir. *Journal of Dispersion Science and Technology* **2011**, *33* (7), 955-959.
194. Li, Q.; Church, J. S.; Kafi, A.; Naebe, M.; Fox, B. L., An Improved Understanding of the Dispersion of Multi-Walled Carbon Nanotubes in Non-Aqueous Solvents. *Journal of Nanoparticle Research* **2014**, *16* (7), 2513.
195. Ganguli, S., Effect of Loading and Surface Modification of Mwcnts on the Fracture Behavior of Epoxy Nanocomposites. *Journal of Reinforced Plastics and Composites* **2005**, *25* (2), 175-188.

196. Yaping, Z.; Aibo, Z.; Qinghua, C.; Jiaoxia, Z.; Rongchang, N., Functionalized Effect on Carbon Nanotube/Epoxy Nano-Composites. *Materials Science and Engineering: A* **2006**, *435–436* (0), 145-149.
197. Granier, A.; Nguyen, T.; Steffens, K. L.; Lee, H.-J.; Shapiro, A.; Martin, J. W. In *A Novel Method to Covalently Functionalize Carbon Nanotubes with Isocyanate for Polyurethane Nanocomposite Coatings*, International Coatings Expo: Clean-Lean-Green: Innovative Solutions for the Global Coatings Community, Toronto, ON, Canada, Federation of Societies for Coatings Technology: Toronto, ON, Canada, 2007; pp 41/1-41/21.
198. Xiong, J.; Zhou, D.; Zheng, Z.; Yang, X.; Wang, X., Fabrication and Distribution Characteristics of Polyurethane/Single-Walled Carbon Nanotube Composite with Anisotropic Structure. *Polymer* **2006**, *47* (6), 1763-1766.
199. Itkis, M. E.; Perea, D. E.; Jung, R.; Niyogi, S.; Haddon, R. C., Comparison of Analytical Techniques for Purity Evaluation of Single-Walled Carbon Nanotubes. *Journal of the American Chemical Society* **2005**, *127* (10), 3439-3448.
200. Peng, Z.; Feng, C.; Luo, Y.; Yi, Z.; Kong, L., Structure and Properties of Self-Assembled Natural Rubber/Multi-Walled Carbon Nanotube Composites. *Journal of Wuhan University of Technology--Materials Science Edition* **2011**, *26* (5), 807-811.
201. Cobley, A., Ultrasound Sonochemistry – a More Sustainable Approach to Surface Modification? *Surface Engineering* **2013**, *25* (8), 559-564.
202. Suslick, K. S.; Price, G. J., Applications of Ultrasound to Materials Chemistry. *Annual Review of Materials Science* **1999**, *29* (1), 295-326.
203. Mason, T. J.; Cobley, A. J.; Graves, J. E.; Morgan, D., New Evidence for the Inverse Dependence of Mechanical and Chemical Effects on the Frequency of Ultrasound. *Ultrason Sonochem* **2011**, *18* (Copyright (C) 2012 U.S. National Library of Medicine.), 226-30.
204. Xia, H.; Wang, Q.; Liao, Y.; Xu, X.; Baxter, S. M.; Slone, R. V.; Wu, S.; Swift, G.; Westmoreland, D. G., Polymerization Rate and Mechanism of Ultrasonically Initiated Emulsion Polymerization of N-Butyl Acrylate. *Ultrasonics Sonochemistry* **2002**, *9* (3), 151-158.
205. Doktycz, S. J.; Suslick, K. S., Interparticle Collisions Driven by Ultrasound. *Science (Washington, D. C.)* **1990**, *247*, 1067-9.
206. Cobley, A.; Mason, T. J.; Paniwnyk, L.; Saez, V. In *Aspects of Ultrasound and Materials Science*, CRC Press: 2012; pp 41-73.
207. Petrier, C.; Jeunet, A.; Luche, J. L.; Reverdy, G., Unexpected Frequency Effects on the Rate of Oxidative Processes Induced by Ultrasound. *Journal of the American Chemical Society* **1992**, *114* (8), 3148-3150.
208. Gojny, F. H.; Wichmann, M. H. G.; Köpke, U.; Fiedler, B.; Schulte, K., Carbon Nanotube-Reinforced Epoxy-Composites: Enhanced Stiffness and Fracture Toughness at Low Nanotube Content. *Composites Science and Technology* **2004**, *64* (15), 2363-2371.
209. Burnett, D. J.; Garcia, A. R.; Thielmann, F., Measuring Moisture Sorption and Diffusion Kinetics on Proton Exchange Membranes Using a Gravimetric Vapor Sorption Apparatus. *Journal of Power Sources* **2006**, *160* (1), 426-430.
210. International, A., Standard Practice for Evaluating Degree of Rusting on Painted Steel Surfaces. In *ASTM D610-08(2012)* West Conshohocken, 2012.

211. Franks, F., *The Physics and Physical Chemistry of Water*. Springer: London, 1972; Vol. 1, p 596.
212. Mullins, E., *Statistics for the Quality Control Chemistry Laboratory*. The Royal Society of Chemistry: Cambridge, 2003.
213. Foster, S. F.; Hoff, E. A.; Curtzwiler, G. W.; Williams, E. B.; Davis, K. B.; Patton, D. L.; Rawlins, J. W., Chemorheology Investigation of a Glassy Epoxy Thermoset on Tensile Plastic Flow and Fracture Morphology. *Journal of Polymer Science Part B: Polymer Physics* **2015**, n/a-n/a.
214. Schadler, L. S.; Giannaris, S. C.; Ajayan, P. M., Load Transfer in Carbon Nanotube Epoxy Composites. *Applied Physics Letters* **1998**, *73* (26), 3842-3844.
215. Dusek, K., *Epoxy Resins and Composites II*. Springer-Verlag: New York, 1986.
216. Ni, Z. H.; Yu, T.; Lu, Y. H.; Wang, Y. Y.; Feng, Y. P.; Shen, Z. X., Uniaxial Strain on Graphene: Raman Spectroscopy Study and Band-Gap Opening. *ACS Nano* **2008**, *2* (11), 2301-2305.
217. Eitan, A.; Fisher, F. T.; Andrews, R.; Brinson, L. C.; Schadler, L. S., Reinforcement Mechanisms in Mwcnt-Filled Polycarbonate. *Composites Science and Technology* **2006**, *66* (9), 1162-1173.
218. Hiemenz, P.; Lodge, T., Glass Transition. In *Polymer Chemistry*, 2 ed.; Taylor and Francis Group: Boca Raton, FL, 2007.
219. Curtzwiler, G.; Early, M.; Gottschalk, D.; Konecki, C.; Peterson, R.; Wand, S.; Rawlins, J. W., The World of Surface Coatings Is Centered around the Glass Transition Temperature but Which One? Part 2. *JCT CoatingsTech* **2014**, *11*, 40-51.
220. Curtzwiler, G.; Early, M.; Gottschalk, D.; Konecki, C.; Peterson, R.; Wand, S.; Rawlins, J. W., The World of Surface Coatings Is Centered around the Glass Transition Temperature but Which One? Part I. *JCT CoatingsTech* **2014**, *11*, 28-38.
221. Prolongo, S. G.; Gude, M. R.; Urena, A., Water Uptake of Epoxy Composites Reinforced with Carbon Nanofillers. *Composites, Part A* **2012**, *43*, 2169-2175.
222. Choudalakis, G.; Gotsis, A. D., Free Volume and Mass Transport in Polymer Nanocomposites. *Current Opinion in Colloid & Interface Science* **2012**, *17* (3), 132-140.
223. Silva, J.; Ribeiro, S.; Lanceros-Mendez, S.; Simões, R., The Influence of Matrix Mediated Hopping Conductivity, Filler Concentration, Aspect Ratio and Orientation on the Electrical Response of Carbon Nanotube/Polymer Nanocomposites. *Composites Science and Technology* **2011**, *71* (5), 643-646.
224. Politano, A.; Chiarello, G., The Nature of Free O-H Stretching in Water Adsorbed on Carbon Nanosystems. *The Journal of Chemical Physics* **2013**, *139* (6), 064704.
225. Thomas, J. A.; McGaughey, A. J. H., Density, Distribution, and Orientation of Water Molecules inside and Outside Carbon Nanotubes. *The Journal of Chemical Physics* **2008**, *128* (8), 084715.
226. Martí, J.; Gordillo, M. C., Structure and Dynamics of Liquid Water Adsorbed on the External Walls of Carbon Nanotubes. *The Journal of Chemical Physics* **2003**, *119* (23), 12540-12546.
227. Gordillo, M. C.; Martí, J., Water on the Outside of Carbon Nanotube Bundles. *Physical Review B* **2003**, *67* (20), 205425.

228. Lyon, S. B.; Bingham, R.; Mills, D. J., Advances in Corrosion Protection by Organic Coatings: What We Know and What We Would Like to Know. *Progress in Organic Coatings* **2017**, *102*, 2-7.
229. Standard Practice for Operating Salt Spray (Fog) Apparatus. In *ASTM B117 - 11*, ASTM International: West Conshohocken, 2011.
230. Schneider, A.; Hommel, G.; Blettner, M., Linear Regression Analysis: Part 14 of a Series on Evaluation of Scientific Publications. *Deutsches Arzteblatt International* **2010**, *107* (44), 776-82.
231. Starkova, O.; Chandrasekaran, S.; Prado, L. A. S. A.; Tölle, F.; Mülhaupt, R.; Schulte, K., Hydrothermally Resistant Thermally Reduced Graphene Oxide and Multi-Wall Carbon Nanotube Based Epoxy Nanocomposites. *Polymer Degradation and Stability* **2013**, *98* (2), 519-526.
232. Wielant, J.; Posner, R.; Hausbrand, R.; Grundmeier, G.; Terryn, H., Cathodic Delamination of Polyurethane Films on Oxide Covered Steel – Combined Adhesion and Interface Electrochemical Studies. *Corrosion Science* **2009**, *51* (8), 1664-1670.
233. Marsh, J.; Scantlebury, J. D.; Lyon, S. B., The Effect of Surface/Primer Treatments on the Performance of Alkyd Coated Steel. *Corrosion Science* **2001**, *43* (5), 829-852.
234. Harun, M. K.; Marsh, J.; Lyon, S. B., The Effect of Surface Modification on the Cathodic Disbondment Rate of Epoxy and Alkyd Coatings. *Progress in Organic Coatings* **2005**, *54* (4), 317-321.
235. Khun, N. W.; Troconis, B. C. R.; Frankel, G. S., Effects of Carbon Nanotube Content on Adhesion Strength and Wear and Corrosion Resistance of Epoxy Composite Coatings on Aa2024-T3. *Progress in Organic Coatings* **2014**, *77* (1), 72-80.
236. Mil-Prf-23377j, Performance Specification: Primer Coatings: Epoxy, High-Solids. Defense, D. o., Ed. 2005.
237. Yan, X.; Su, X. G., *Linear Regression Analysis: Theory and Computing*. World Scientific Publishing: Hackensack, NJ, 2009; p 349.
238. Siamphukdee, K.; Collins, F.; Zou, R., Sensitivity Analysis of Corrosion Rate Prediction Models Utilized for Reinforced Concrete Affected by Chloride. *Journal of Materials Engineering and Performance* **2013**, *22* (6), 1530-1540.
239. Yalçyn, H.; Ergun, M., The Prediction of Corrosion Rates of Reinforcing Steels in Concrete. *Cement and Concrete Research* **1996**, *26* (10), 1593-1599.
240. Otieno, M.; Beushausen, H.; Alexander, M., Prediction of Corrosion Rate in Reinforced Concrete Structures – a Critical Review and Preliminary Results. *Materials and Corrosion* **2012**, *63* (9), 777-790.
241. Suleiman, I. Y.; Oloche, O. B.; Yaro, S. A., The Development of a Mathematical Model for the Prediction of Corrosion Rate Behaviour for Mild Steel in 0.5% Sulphuric Acid. *ISRN Corrosion* **2013**, *2013*, 9.
242. Otieno, M.; Beushausen, H.; Alexander, M., Prediction of Corrosion Rate in Rc Structures - a Critical Review. In *Modelling of Corroding Concrete Structures: Proceedings of the Joint Fib-Rilem Workshop Held in Madrid, Spain, 22–23 November 2010*, Andrade, C.; Mancini, G., Eds. Springer Netherlands: Dordrecht, 2011; pp 15-37.